



Institute of Automation and Control
Graz University of Technology



Dipl.-Ing. Stefan Richard Kaltenbacher

Water Distribution Networks

MODELING, OBSERVATION, ROUGHNESS IDENTIFICATION AND ITS APPLICATION

Doctoral Thesis

to achieve the university degree of
DOKTOR DER TECHNISCHEN WISSENSCHAFTEN
(DOCTOR OF TECHNICAL SCIENCES)

the doctoral school of
ELECTRICAL ENGINEERING

under the supervision of
ASS.-PROF. MARTIN STEINBERGER
PROF. MARTIN HORN

in collaboration with the
INSTITUTE OF URBAN WATER MANAGEMENT

Graz, September, 2019

AFFIDAVIT

STATUTORY DECLARATION

I declare that I have authored this thesis independently, that I have not used other than the declared sources / resources and that I have explicitly marked all material which has been quoted either literally or by content from the used sources.

Ich erkläre an Eides statt, dass ich die vorliegende Arbeit selbstständig verfasst, andere als die angegebenen Quellen/Hilfsmittel nicht benutzt und die den benutzten Quellen wörtlich und inhaltlich entnommenen Stellen als solche kenntlich gemacht habe.

.....

Date / Datum

.....

Signature / Unterschrift

Abstract

With a rather off-mainstream view on the modeling and parameter-identification, this thesis offers a completely new set of tools which, ultimately, aim to identify losses in water distribution networks.

Allowing flow dynamics to be part of the mathematical network description, the traditional steady-state modeling approach is put into question as it has actually not been improved upon in the last 40 years. Apart from the additional dynamic information, this methodology allows a more physically suitable consideration of the water consumption in simulation which enables it to be decreased inherently if not enough pressure is available. Benchmarked on a real experimental network at *Graz University of Technology*, strengths and weaknesses of these developed models are discussed when compared to measurements.

Influenced by a control-theoretical background, this additional dynamic model information is then utilized to deduce more general statements about the observability of the model's states of the hydraulic network. Unsurprisingly and completely analogous to the steady state, unknown friction parameters yield to be the major unknowns. The derived dynamic models thereby feature the same mathematical description of friction as the conventional steady-state one, enabling an easily portable framework.

Motivated by the observability analysis, the identification of individual friction parameters per pipe in the network received most dedication. In particular the proper formulation but also the developed solving-algorithms for this friction parameter identification problem can be considered core findings of this work. This problem formulation basically relies on the steady-state model inversion and requires a whole set of assumptions to be uniquely solvable. The solving, in general, proves to be specifically challenging. The developed methods, however, enable the solving to be robust to an extent which not only allows to find individual friction parameters, but also to identify faults in the network itself. A claim which is supported by the results when applying the developed friction parameter identification scheme on a real-world drinking water network.

Kurzfassung

Mit einer unkonventionellen Sicht auf die Modellierung und Parameteridentifikation bietet diese Arbeit eine Reihe von neuen Ansätzen, die letztendlich darauf abzielen, Verluste in Wasserverteilungsnetzen zu identifizieren.

Durch Hinzunahme einer Strömungsdynamik als Teil der mathematischen Netzwerkbeschreibung wird der traditionell stationäre Modellierungsansatz, der praktisch 40 Jahre unverändert blieb, in Frage gestellt. Abgesehen von der zusätzlichen Information durch die nun berücksichtigte Dynamik, ermöglichen diese Modelle eine physikalisch sinnvolle Einbettung des Wasserverbrauchs in die Simulation. So wird dieser automatisch und auf Basis physikalischer Zusammenhänge verringert wenn nicht genügend Druck vorhanden ist. Anhand von Messungen an einem experimentellen Netzwerkaufbau der *Technischen Universität Graz* werden Stärken und Schwächen dieser entwickelten Modelle diskutiert.

Ausgehend von regelungs- und systemtheoretischen Überlegungen werden die dynamischen Modelle verwendet, um allgemein gültige Aussagen über die Beobachtbarkeit der Modellzustände des hydraulischen Netzwerks abzuleiten. Wenig überraschend und völlig analog zum stationären Fall bereiten unbekannt Reibungsparameter die größten Probleme.

Motiviert durch diese Beobachtbarkeitsanalyse steht die Identifizierung von Rauigkeitsparametern je Rohr im speziellen Fokus. Insbesondere die dazu passende Problemformulierung, aber auch die dafür entwickelten Lösungsverfahren sind Kernergebnisse dieser Arbeit. Diese Problemformulierung beruht im Wesentlichen auf der Inversion des stationären Modells und erfordert eine Reihe von Annahmen und Voraussetzungen zur eindeutigen Lösbarkeit. Obwohl sich das Lösen als generell schwierig entpuppt, weisen die entwickelten Lösungsmethoden eine Robustheit auf, die es nicht nur ermöglicht einzelne Reibungsparameter zu finden, sondern auch Fehler in der Netzwerkkonfiguration selbst zu identifizieren. Ein Resultat das sich auf Ergebnisse der Anwendung der entwickelten Rauigkeitsidentifikation an einem realen Trinkwassernetz stützt.

Acknowledgment

The writing of this thesis may be best compared, as with presumably every other, a battle impossible to win solely on my own. Ad ultimum, the final sentences are dedicated to those who fought along with me in this once seemed never-ending battle.

Most gratitude was without doubt earned by Martin Steinberger, without whom this thesis would have never found an end. Something to declare with absolute certainty. One might say his support was *necessary* and *sufficient* for the successful completion. Due to his dedication to really dig deep into details, countless parts could be corrected and be made understandable in the first place. All the hours spent together on discussing these details were an absolute pleasure from which I undoubtedly learned the most. Thank you !

Special thanks to Martin Horn who guided this work not only on the technical front but made the circumstances possible under which this thesis could be brought into being. Also, the evaluation and testing of the developed methodologies were only possible through the collaboration of the *Institute of Urban Water Management* which basically held the practical expertise in the laboratory and field. It is rare that rather deep theoretical assessments can indeed be evaluated with real-world data and measurements when larger water networks are involved. These data was provided by Daniela Fuchs-Hanusch who supervised my esteemed colleagues: Markus Günther, David B. Steffelbauer, and David Camhy at that time. Many thanks to you all! Gratitude was also earned by my direct colleagues at the institute, their kindness and willingness to immediate help is something immensely valuable.

A huge thanks to my parents who always supported me in all ways possible and kept faith in my competence, something I am not particularly good at. Finally, I basically ran out of words for thanking a special person in my life. A person who endured my numerous requests to correct my English. A person who helped me regain motivation when lost in never-ending pondering. A person who not only endured my quickly changing temper during long hours of writing but always stood by my side. Thank you, Nadja.

Contents

1	Introduction	1
1.1	Outline	1
1.2	Comments on the State of the Art	3
1.3	Publications	4
2	Preliminaries	5
2.1	Hydraulics	5
2.1.1	Water Density ρ and Dynamic Water Viscosity η	5
2.1.2	Pressure	6
2.1.3	Fluid Flow and Velocity	6
2.1.4	Friction	7
2.1.5	The <i>Lambert</i> Function	12
2.1.6	An Explicit Solution of Colebrook-White	13
2.2	Notation and Mathematical Tools	16
2.2.1	Notation	16
2.2.2	Hadamard Product	17
2.2.3	Index Transformation with Unity Vectors	17
2.2.4	Derivatives Along Vectors	18
2.2.5	Remarks and References	19
3	Network Hydraulics: A Primarily Steady-State Perspective	21
3.1	Steady-State Network Formulation	21
3.1.1	Conservation of Mass	22
3.1.2	Conservation of Energy	24
3.1.3	Extraction of Cycle Matrix \mathbf{S} out of Incidence Matrix \mathbf{A}	25
3.1.4	Network Model	27
3.1.5	Uniqueness and Solvability	28
3.2	Full Transient Equations	30
4	Network Hydraulics: A Dynamic Yet Rigid Approach	33
4.1	Rigid Water Column Theory	33
4.2	Network Formulation	34
4.3	Pressure-Driven Demand	36
4.3.1	Rapid Valve Opening in the Two-Cycle Network	39
4.4	How to Deal With Consumption?	41

4.4.1	Linear Consumption Dynamics	41
4.4.2	Incorporation in Model Equations	42
4.4.3	Discussion	44
4.4.4	Illustrative Example	45
4.5	Steady-State Properties	50
4.6	Notes on Stability	52
4.7	Coupling With Dynamic Elements	54
4.7.1	Air Vessel	54
4.7.2	Surge Tanks	55
5	Experimental Model Evaluation: Rapid Dynamics	57
5.1	Friction Parameters via Optimization	58
5.2	One Consumer Configuration	63
5.3	Two Consumer Configuration	66
5.4	Conclusions	67
6	Observability Analysis	69
6.1	Concept of State Reconstruction	69
6.2	Pressure Measurements	72
6.3	Flow Measurements	74
6.4	The Need to Identify Friction	77
7	Roughness Identification: The Full Turbulent Case	81
7.1	Configuration	81
7.2	Introductory Example: 3-Cycle Network	83
7.3	Explicit Problem Formulation	84
7.3.1	Turbulent Flow in Steady-State	85
7.3.2	Full Turbulent Set-Up	86
7.3.3	Optimization vs. Root Finding	86
7.4	Newton - Raphson	87
7.4.1	First Turbulent Flow Derivatives	88
7.4.2	Step Length	89
7.4.3	Initial Values and Range	94
7.5	Illustrative Example	96
7.6	Tensor Method	100
7.6.1	Second Turbulent Flow Derivatives	101
7.6.2	Tensor Equation	103
7.6.3	Motivating Examples	106
7.6.4	Degenerate Tensor Equation	109
7.6.5	The Factorization of a Conic Section as Exemplification	114
7.6.6	Final Observations	116
7.7	Illustrative Comparison	121
8	Transitional Water Flow in Steady-State	127
8.1	Notation	127
8.2	Transitional - Turbulent Boundary	128
8.3	Derivation of the Transitional Flow	130
8.3.1	Choice of $\gamma_1(\epsilon, \Delta h)$	130
8.3.2	Choice of $\gamma_2(\epsilon, \Delta h)$	132
8.3.3	Choice of $\gamma_3(\epsilon, \Delta h)$	133
8.4	Comparison to <i>Dunlop's</i> Cubic Interpolation	136

8.5	Summary of Steps to Obtain γ	138
9	Roughness Identification: Consideration of All Flow Regimes	139
9.1	Complete Problem Set-Up	139
9.2	Derivatives of the Combined Flow	141
9.3	3-Cycle Network Example	144
9.3.1	Configuration	144
9.3.2	Results	147
9.3.3	Discussion	154
10	Roughness Identification on a Real Network	157
10.1	Topology Simplification	158
10.2	Sensor Readings and First Assessments	162
10.3	Initial Values	165
10.4	Results and Discussion	168
10.5	Conclusions	171
11	Outlook	173
A	Proof of Proposition 3.6	175
B	Proof of Proposition 3.11	177
C	Proof of Proposition 8.2	179
D	Proof of Proposition 8.6	181
E	Bibliography	183

Introduction

Whether *steady* or *unsteady state modeling*, *state observation*, *roughness identification*, *leakage detection* or *localization*, this thesis combines a whole range of disciplines in the context of water distribution networks. Although the focus is set on water, the developed methods are applicable to *Newtonian* fluids generally, meaning those whose density and viscosity are functions on temperature only.

Among the first things to agree on is the utmost importance to maintain water supply security. Intermediate water supply as it happens in South Africa or even in California, for instance, puts a lot of strain on the local industry and households, raising water prices while decreasing the standard of living. However, the severity of this problem has yet to be recognized. When following the current climate trajectory, increasing temperatures will exacerbate water scarcity to an extent which has yet to be discovered. Knowing that a significant amount of the anyway scarce water is lost during the distribution enforces the problem and raises the need for efficiency improvements. According to the *International Water Association*, the non-revenue water accounts for 25 to 50 percent of the total amount of water supplied when put into a global measure, while it makes up to a staggering 75 percent in the so-called emerging markets [IWA]. These numbers are right in line what the author experienced first-hand when taking measurements in a pilot area of a Chinese town. The terminology “non-revenue water” with its afflicted market-jargon simply characterizes all the water for which no money can be charged, because it never reached any registered consumer. In other words, non-revenue water also accounts for water which is stolen from unregistered consumers, so-called water thieves, and thus is formally *not* lost in the distribution. Actually, the author expects that authorities tend to draw attention to this stolen amount misleadingly, just to obscure and downplay the need for investment in water infrastructure. On the mathematical front, no distinction is made between water which is lost or stolen as both cases are actually treated in the same manner. Effectively, all non-revenue water is referred to as leakage, an expression which is treated as synonym for leaking water in this thesis.

In short, this thesis is written on the premise to develop a framework for leakage detection and localization strategies, although it does *not* deal with either one of these topics explicitly.

1.1 Outline

In this outline a proper connection among all included topics is established and thereby serves as introductory motivation to objectify the chosen methodologies.

Starting with modeling, the derived network description turns out to be predominantly characterized by hydraulic friction which is covered in a compact discourse to be found in the preliminaries (chapter 2). In the course of a pure steady-state consideration in chapter

3, the conventional hydraulic network equations are derived and build the basis for all other chapters to come. Not only contained in the steady-state network hydraulics, friction is the central component upon which this thesis is built. Due to its generally nonlinear character, the network formulation yields strong differences to, for instance, the description of an electric circuit although *Kirchhoff*-type equations are the common building block. The characteristic which sets the analysis of steady-state network hydraulics, in the opinion of the author, apart from others is the deeper mathematical focus. As an example, the solution's uniqueness of the steady-state description, which is not guaranteed inherently due to nonlinear model parts, is proven, putting available literature into a digestible format. Interestingly, the tools used in this proof will turn out substantially useful when allowing some dynamics to be part of the network hydraulics.

Regarding dynamics, after discussions on the weaknesses involved in the steady-state description, flow dynamics per pipe in the network are introduced in chapter 4. The computational effort is contained to an extent which makes the dynamic simulations readily computable on today's standard PCs. This is achieved by assuming the water to remain incompressible, an assumption which prohibits to represent elastic effects, water density fluctuations for instance, on the flip side. Also, a central discussion revolves around the handling of water consumption in the network which is generally distinguished between a pressure-driven and demand-driven methodology in literature (in-depth explanations to be found in chapters 3 and 4). What makes the introduction of flow dynamics valuable is, essentially, not only the additional dynamic information, but how it enables consumption values to be handled in a manner such that they are decreased inherently if there is not enough pressure available. This is only possible with a physically suitable description of the consumption which allows it to be pressure-dependent. Embedded in an *exact linearization* of the dynamic hydraulic model, the introduction of linear consumption dynamics will be key in this context. In this course, the equivalence of the equilibrium of the dynamic model(s) to the now unique solution of the steady-state hydraulic network equations is proven. Also, certain stability properties of the dynamic model(s) can be proven by means of the tools applied for the uniqueness proof of the steady-state network-equation's solution which will turn out valuable for the observability analysis later.

Comparing measurements on a real experimental network with simulation results during fast transient events in chapter 5, friction parameters remain the major uncertainties while the qualitative behavior shows satisfactory agreement, despite the fact that the introduced dynamics intend to model slow transient behavior primarily. These unknown friction parameters express themselves in an offset-like deviation from the measurements as all dynamic friction components are neglected consistently. In principle, the elementary connection between the steady-state and dynamic network models used in this thesis is provided by the same friction description.

The observability analysis in chapter 6 yields that the derived dynamic models turn out to be observers in a strict control-theoretic sense under some circumstances. These circumstances require (among other things) the knowledge of friction parameters, a requirement which is strongly supported by the comparison of simulations to measurements. In the course of this analysis, very general questions are raised and essentially concern the finding of sensors best suitable to satisfy the circumstances under which these models turn out to be observers.

Given this sensor configuration, the author then utilizes the steady-state hydraulic network equations in chapter 7 and inverts them, so to speak, along the friction parameters (roughness values per pipe). Thereby, *Colebrook & White's* formula as implicit description of pressure losses is utilized to express the pipe flow as two dimensional function on the pressure loss along the pipe and the pipe's roughness. The resulting set of equations is initially only valid if all pipe flows are in the turbulent flow regime, a harsh assumption which requires considerable effort to be relieved later on. The developed scheme to identify individual pipe roughnesses by only using sensors at a subset of nodes distributed throughout the network is actually completely based on nodal *Kirchhoff* equations. This equation set-up then requires special treatment to retrieve as many

equations as unknowns, a key point in the entire procedure. The solving, nonetheless, turns out to be particularly challenging. Starting with a modified *Newton-Raphson* type approach in chapter 7.4, customized measures in addition to a set of assumptions are required to enable the roughness identification problem to become uniquely solvable. However, a more advanced solving strategy known as the *Tensor-Method*, basically an extension of *Newton-Raphson*'s method, is also applied in chapter 7.6. Although this method requires a nonlinear system of equations to solve in order to obtain a search direction, it allows some deeper mathematical assessments about the roughness identification problem. Supported by several examples, the working principle of the roughness identification by means of the developed solving strategies is demonstrated successfully.

The relieve of the assumption that all pipe flows have to be in turbulent regime receives the dedicated chapters 8 and 9. As it is impossible to distinguish all pipe flows a-priori between the laminar, transitional and turbulent flow regime, this procedure is motivated by the idea that the roughness identification algorithm shall be capable to automatically converge to the correct flow regime inherently. However, in order to do so, an explicit description of the steady-state water flow in the transitional *Reynolds* regime had to be derived, essentially, what is accomplished in this chapter 8. The necessity to preserve smoothness at the boundary to the turbulent *Colebrook & White* flow as well as to the one of laminar flow in addition to the normal boundary conditions, result in a set of requirements which are remarkably tricky yet feasible to satisfy with sufficient degree of accuracy.

The roughness identification problem formulation is then extended to all flow regimes in chapter 9 by making use of the derived explicit description of the transitional steady-state water flow. The solving techniques applied to solve the full turbulent problem in chapter 7 thereby turn out to be applicable to this complete problem formulation. All theoretical assessments obtained when applying the *Tensor-Method* on the full turbulent roughness identification problem can be easily extended to the complete case. Given the developed solving techniques, the influence of disturbances such as measurement noise and the partial violation of the taken assumptions is studied on examples which include pipe flows with varying flow regimes.

This thesis concludes by applying the developed roughness identification scheme on the real drinking water distribution network of *Graz-Ragnitz* in chapter 10 making use of an already existing data set provided by the *Institute of Urban Water Management* (Graz University of Technology). This application can be considered valuable insofar as the taken assumptions in order for the roughness identification problem to be solvable are put up to real-world test. The problems encountered with the measurement data and the configuration are discussed in detail to clarify the circumstances on which the results can be improved upon. Nonetheless, the obtained results not only demonstrate the applicability of the developed algorithms for roughness identification, but the identification and localization of inconsistencies in the data as caused by leakage for instance.

1.2 Comments on the State of the Art

Generally, a discussion of the literature and existing methodologies with analogies to the ones developed is provided directly in each of the separate chapters. The author thereby believes to best highlight the differences between the included subjects such as modeling, leakage detection and localization or parameter identification.

Apart from literature, the introductory statement that this thesis promises to enhance and develop strategies for detection and localization of leakages needs some clarification. In this field of research modeling, parameter identification, which is often referred to as calibration, leakage detection as well as leakage localization are usually kept separate. Is this the right approach? The quality of the model severely influences the parameter identification, whereas the obtained

model parameters strongly influence if a leakage may be detected. Once detected, a localization algorithm is launched operating on the basis of discrepancies between measurements and the simulation output of the calibrated model. In the opinion of the author, all these topics can be brought together under the umbrella of a traditional observer design as it is known from control theory. In this context, the observability analysis chapter 6 serves the purpose to logically connect all the individual topics and underlines the validity of the conventional steady-state hydraulic network description to be used for calibration among other things.

To sum it up, in the opinion of the author there is a solid chance that leakages are found inherently with a sophisticated parameter identification algorithm built on the basis of the developed models. This is the premise upon which this thesis is founded on.

1.3 Publications

The following papers have been published (or accepted for publication) in chronological order and prior to the final completion of this thesis.

■ [Cattani et al., 2017]:

Cattani, M., Boano, C. A., Steffelbauer, D., Kaltenbacher, S., Günther, M., Römer, K., Fuchs-Hanusch, D., and Horn, M. «*Adige: An Efficient Smart Water Network Based on Long-range Wireless Technology*». In Proceedings of the 3rd International Workshop on Cyber- Physical Systems for Smart Water Networks, pages 3–6, New York, NY, USA, 2017.

■ [Kaltenbacher et al., 2017]:

Kaltenbacher, S., Steffelbauer, D., Cattani, M., Fuchs-Hanusch, D., Horn, M., and Roemer, K. «*A Dynamic Model for Smart Water Distribution Networks*». Computing and Control for the Water Industry, Sheffield, 2017.

■ [Kaltenbacher et al., 2018]:

Kaltenbacher, S., Steinberger, M., and Horn, M. «*Modeling Hydraulic Networks for Control: How to Deal With Consumption?*». IEEE Control Systems Letters, 2(4):671–676, Oct 2018.

■ [Kaltenbacher et al., 2020]:

Kaltenbacher, S., Steinberger, M., and Horn, M. «*Transitional Water Flow in Steady-State*». Journal of Applied Mathematical Modelling, 77:478 – 490, 2020.

Reference [Cattani et al., 2017] was published at a workshop, [Kaltenbacher et al., 2017] at a conference and [Kaltenbacher et al., 2018] as journal and conference paper (Decision and Control 2018) simultaneously. Also, reference [Kaltenbacher et al., 2020] was accepted for journal publication at the time of writing. The content of [Kaltenbacher et al., 2017] was largely used among other things in chapter 4.2 and 4.3, the content of [Kaltenbacher et al., 2018] in part in chapter 4.4 and 4.5, and the content of [Kaltenbacher et al., 2020] in chapter 8. The author of this thesis is simultaneously first author of the last three publications.

2.1 Hydraulics

The modeling of water supply networks is still a fairly active field of research and may be distinguished between steady-state and unsteady-state, i.e. transient, approaches. However, the complexity needed for a whole network description already sets the framework of the modeling procedure as computational effort, application purposes as well as practicability generally restrict the selection of different model types featuring different levels of accuracy. Though, before launching a more genuine discussion about where difficulties with transient models meet inaccuracies in steady-state ones, a common baseline is established. This section introduces the very basic quantities in the context of the water flow in tubes.

2.1.1 Water Density ρ and Dynamic Water Viscosity η

Although the change in density due to temperature and pressure fluctuations is neglected in the majority of cases, small variations in parameters like the density possibly lead to non negligible changes in pressure.

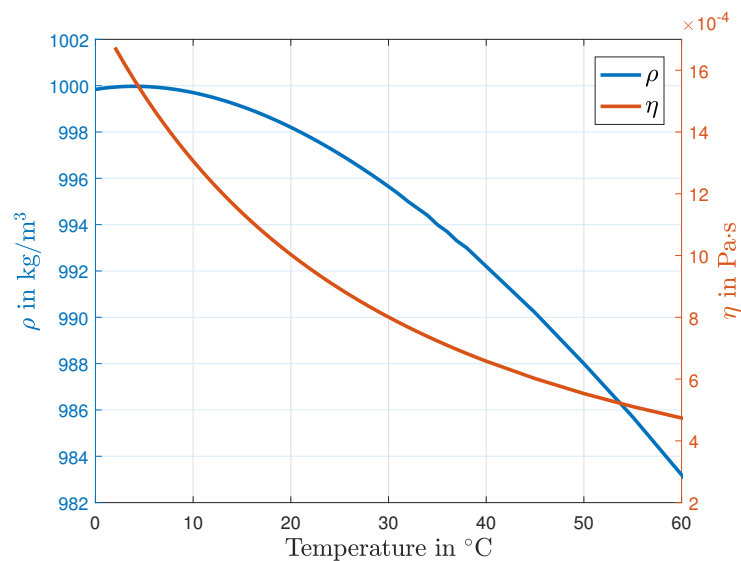


FIGURE 2.1: Water density [Kell, 1969] and dynamic viscosity [Korson et al., 1975] over temperature.

The viscosity η is of particular concern in this regard as it varies drastically in the range of 10° to 30°C in which drinking water is usually distributed. Using look-up tables according to figure 2.1 to accommodate for these parameter variations, temperature is treated as an input variable. Actually, one would need to take local differences in temperature into account as the water temperature, e.g., at sources of the distribution network may be critically different to the one at consumers. A solid argument against this potentially unnecessary complication is that as long as a distributed network consumption ensures a continuous and comprehensive water exchange, local differences in temperature are balanced quickly. In addition, water features a high thermal conductivity and so transports heat even if there is no notable flow. To restrict the model complexity, local temperature variations are neglected, however, it shall be noted that the developed models can be extended to also account for different temperatures per pipe.

In principle, the dependency of water density and viscosity on pressure is sufficiently weak, so, e.g, there is a change of only (regarding density) $\Delta\rho < 0.5\%$ if the pressure increases from 1 to 10 bar (see [Cho et al., 2002]). Nevertheless, this is only half of the truth as in the event of high excitation, a rapid valve opening for instance, elastic effects come into play. These elastic effects, commonly known under the term *waterhammer*, become visible in the form of very high pressure peaks which ultimately cause oscillating flows. Such conditions are very harmful to the water distribution infrastructure and measurement equipment and thus must be avoided under all circumstances. Effectively, variations especially in water density also contribute to these oscillations in flow during those events.

2.1.2 Pressure

Generally, pressure p is considered to be the perpendicular force applied to a body which is in contact with a fluid in the present case. Therefore, the static pressure varies with the water depth for fluids at rest

$$p = g\rho h \quad (2.1)$$

depending on the gravitational acceleration $g \approx 9.81 \text{ m/s}^2$, the density ρ (which also depends on temperature according to figure 2.1) and the water height h with regard to a specified datum (in a tank for instance). In the field of water management the expression *head* instead of *pressure* (measured in *Pascal* $\text{Pa} \hat{=} \text{N/m}^2 \hat{=} \text{kg m}^{-1}\text{s}^{-2} \hat{=} 10^{-5} \text{ bar}$) is established which is equivalent to the water height measured in *meters* according to (2.1). Pressure head values are related to the *gage* pressure (unless otherwise stated) which is relative to the atmospheric pressure of 101325 Pa, whereas the absolute pressure is defined as the sum of the gage and the atmospheric component.

2.1.3 Fluid Flow and Velocity

The velocity of the flow through a pipe is not constant, but will vary over the cross section area A . As a consequence, the integral mean velocity v (m/s) over A as well as the integral mean volumetric flow rate Q (m^3/s) over A (which will be simply called flow for the rest of this thesis)

$$v = \frac{Q}{A} = \frac{\dot{m}}{A\rho} \quad (2.2)$$

are commonly utilized. Q , in turn, can be expressed by the mass flow rate \dot{m} and constant density ρ .

Reynolds Number. Osborne Reynolds is an important figure when it comes to understanding the flow behavior in tubes. In experiments he managed to color areas with high flow velocities in tubes by injecting specific substances. Today, the dimensionless *Reynolds* number for circular

pipes with diameter d

$$Re = \frac{|v| \rho d}{\eta} = \frac{|Q| \rho d}{A \eta} = \frac{|\dot{m}| d}{A \eta} \quad (2.3)$$

helps to distinguish between three different flow regimes, which in general heavily affect the hydraulic behavior in particular the friction, i.e. pressure head losses. For non-circular pipes diameter d is replaced by hydraulic diameter $d_h = 4A/P$, whereas P characterizes the perimeter of this pipe.

A smooth distribution of the velocity profile over the cross section area can be seen in the **laminar flow** condition, where the innermost part moves with the highest and the outermost part with the lowest velocity. The appearance of vortices and eddies makes the flow behavior somewhat unpredictable in the **turbulent flow** condition. A combination of laminar and turbulent areas is simply called **transitional flow**, where the smooth, *laminar* velocity profile starts to scatter and loose its shape. Thanks to Osborne Reynolds, three regimes according to table 2.1

flow condition	Reynolds number
laminar	$Re \leq 2000$
transitional	$2000 < Re < 4000$
turbulent	$Re \geq 4000$

TABLE 2.1: Flow conditions according to Reynolds.

can be specified. The boundary $Re = 2000$ for the transition to the *transitional* or *critical* flow regime appears to be about the lowest value obtainable on a rough pipe entrance, whereas transition values between 2000 and 13000 depending on the smoothness of the entry conditions are possible (cf. [Schneider, 2007] and [Fung, 1990, p. 172]). As the boundaries for flow regimes vary in literature, this thesis sticks to the ones used, e.g., in [White, 2016; Bhave, 1991; Walski et al., 2003] (referring to the *Moody-Diagram*, displayed in figure 2.2).

2.1.4 Friction

Two general types of friction losses in pipes are well known, losses occurring at the surface of the pipe's inner wall (also accounting for viscosity effects), which are proportional to the pipe's length, and so-called minor losses which can be attributed to a specific point in the network rather than an entire pipe.

The former one can actually be separated between a steady-state and an unsteady-state component (see [Chaudhry, 2014; Covas et al., 2005]), whereas the unsteady component is usually neglected, also in the classical waterhammer analysis. However, this is only valid for slow transients and low pulsating frequencies [Covas et al., 2005]. Since this thesis puts focus on slow transient and steady-state modeling, the unsteady part is neglected.

Referring to the steady-state component, one would think that the scientific community already agreed on a common formulation defining the pressure drop due to friction at the pipe's inner surface as far as water networks are concerned, but quite the opposite is the case. Effectively, one disagrees whether to use the *Hazen-Williams* equation (see [Walski et al., 2003]) or the *Darcy-Weisbach* equation [Brown, 2002], although both sides agree that the description of *Darcy-Weisbach* together with the friction factor according to *Colebrook & White* [Colebrook and White, 1937] is more accurate and physically related. A paper by Walski and Ormsbee with the title "*No Calm in West Palm*" [Ormsbee and Walski, 2016] specifically addresses this debate. The error made by *Hazen-Williams* in comparison to *Darcy-Weisbach* is allegedly so minor that its simplicity outweighs its inaccuracy. In this context, *Hazen-Williams* is only valid on a narrow range of Re values [Brown, 2002]. Since the application of *Darcy-Weisbach* requires the solving of an implicit equation according to *Colebrook & White*, iterative methods are usually applied.

However, to avoid any kind of iteration, a variety of different explicit equations (see [Bhave, 1991; Genić et al., 2011; Mohsenabadi et al., 2014]) approximating *Colebrook & White's* friction factor are in use. In this thesis it is shown that no iterative methods are required when applying a few terms in series solving the so-called *Lambert* function which can be used to express *Colebrook & White's* friction factor. Due to its strong physical relation but also to improve accuracy, the description by *Darcy-Weisbach* is utilized in this thesis to express friction at the pipe's inner surface.

Characterized by a constant coefficient, the treatment of minor losses appears to be much simpler. This type of friction occurs at fittings, valves (fully opened), 90 degree bends, at appurtenances in general which provoke turbulences and thus additional head loss.

Darcy-Weisbach

The force acting in the opposite direction to the flow propagation due to friction at the inner pipe's surface and viscosity effects is actually called *shear stress*, usually specified with Greek letter τ and measured in *Newton* per square meter. The magnitude of this force depends on the speed of the fluid, the internal roughness of the pipe and the pipe's dimensions. Presented within the *Darcy-Weisbach* equation, it relates the head loss Δh_{DW} along a pipe with specific length l to the averaged (over A) flow Q

$$\Delta h_{\text{DW}} = \lambda_{\text{DW}} \frac{l|Q|Q}{2dgA^2} = \lambda_{\text{DW}} k_{\text{DW}} |Q|Q \quad (2.4)$$

using the friction factor λ_{DW} . This factor actually depends on material properties and the dimensionless *Reynolds* number (2.3) and therefore has to be distinguished for the three flow regimes according to table 2.1. The *Re* number in turn can be interpreted as a function on the flow Q , the density ρ and the viscosity η , whereas ρ and η can also be considered to be functions of the local temperature. As a remark, instead of using a quadratic dependency on the flow in (2.4), expression $|Q|Q$ helps to maintain the right sign of head losses in case of negative Q values, which simply indicate a change of the flow direction. It is understood that the cross section area A as well as the diameter d are held constant for the pipe segment for which the head loss Δh_{DW} is calculated.

Laminar Area. For the laminar regime, the friction factor

$$\lambda_{\text{DW}} = \frac{64}{Re} \quad \text{for} \quad Re \leq 2000 \quad (2.5)$$

is known as *Hagen-Poiseuille* law and is an exact mathematical result derivable from the fluid equations of motion [White, 2016].

Turbulent Area. In the turbulent area the *Colebrook-White* equation [Brown, 2002]

$$F_{cw}(\lambda_{\text{DW}}) = \frac{1}{\sqrt{\lambda_{\text{DW}}}} + \frac{2}{\ln 10} \ln \left(\frac{\epsilon_{\text{DW}}}{3.7d} + \frac{2.51}{Re\sqrt{\lambda_{\text{DW}}}} \right) = 0 \quad \text{for} \quad Re \geq 4000 \quad (2.6)$$

is based on some 10000 experiments from various sources and describes the friction factor as the positive real solution of the implicit equation $F_{cw}(\lambda_{\text{DW}}) = 0$ in the turbulent region. *Moody* developed a simple diagram (see figure 2.2) where he displayed solutions of $F_{cw}(\lambda_{\text{DW}}) = 0$ over the *Reynolds* number up to an relative roughness of $\epsilon_{\text{DW}}/d = 5\%$. As a remark, factor $1/3.71$ instead of $1/3.7$ at the relative roughness ϵ_{DW}/d in (2.6) is often used, meaning that roughness values can simply be translated by multiplying with $3.7/3.71$.

The implicit Colebrook & White function F_{cw} is semi-empirical and can actually be related to the partial differential *Continuity* and *Momentum* equations [White, 2016] (based on the

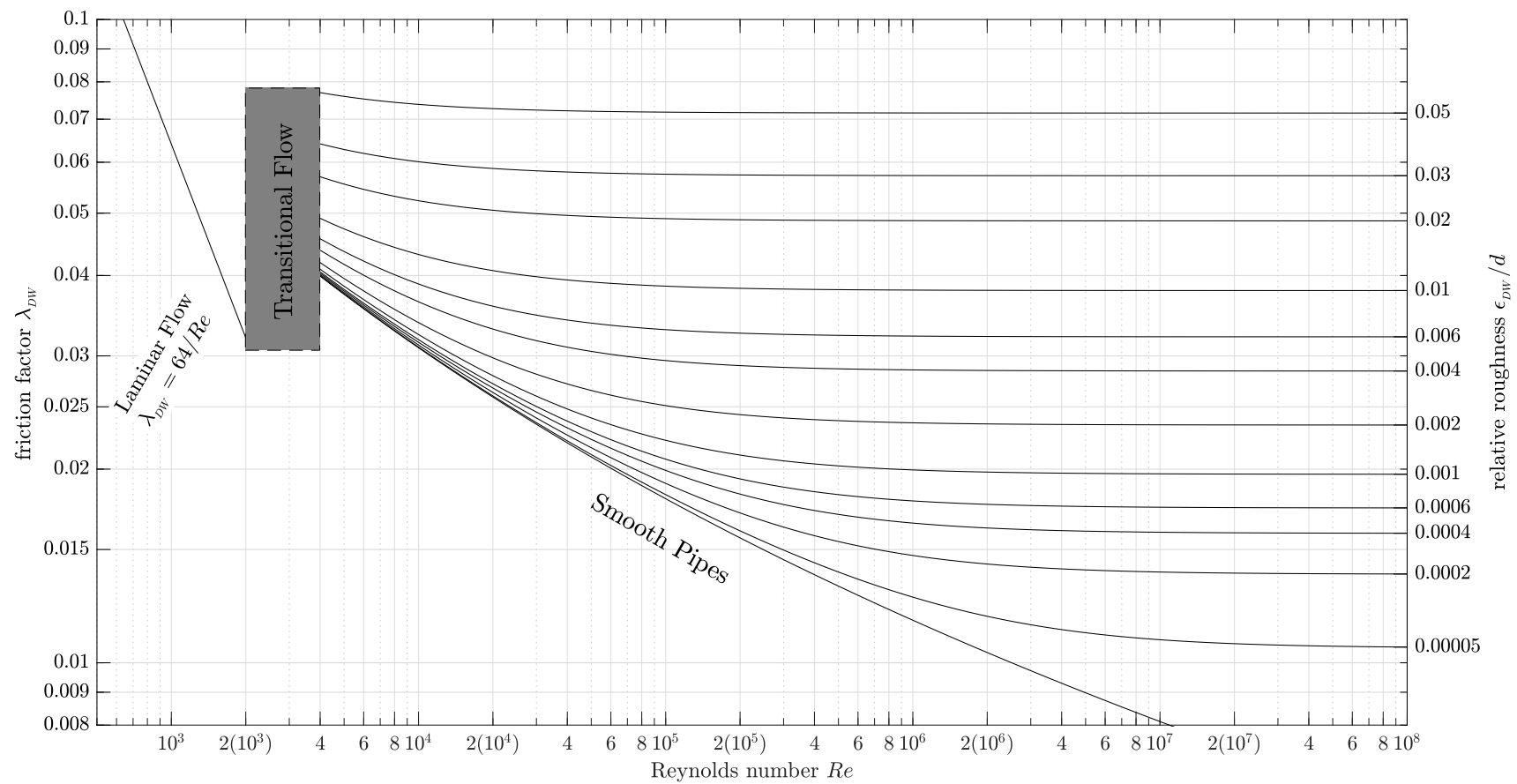


FIGURE 2.2: The reproduced Moody Chart for a temperature of about 18°C according to figure 2.1.

principle of conservation of mass and momentum). It is extensively considered in literature and widely established in the field of fluid mechanics. However, more recent experiments by [Shockling et al., 2006] (in addition to experiments, e.g., by [Nikuradse, 1933]) indicate that the real turbulent friction factor deviates from F_{cw} in the transition area from fully smooth ($\epsilon_{DW} = 0$) to fully rough, at least as far as the so called sand grain roughness is concerned. This type of roughness is produced artificially in laboratories by gluing grains of sand at the inner pipe's wall. Nevertheless, Colebrook and White argue that they used data from commercial pipes instead of artificially roughened ones, although the difference remains unclear at this point (see also [Botros, 2016]). Indisputably, (2.4) is not only considered to deliver an accurate description of the head loss in steady-state but it is widely popular as it combines physical and experimental considerations in one compact equation.

The roughness height (or roughness in short) ϵ_{DW} , usually specified in *millimeters*, accounts for differences in materials, the pipe's age and the amount of dirt and corrosion that accumulates at the inner wall. However, characterizing pressure losses along the inner pipe's surface with a single roughness parameter certainly is a vast simplification. Actually, one would need to model the inner surface of a pipe in three-dimensional space and then apply the full transient, partial differential flow equations, including those of *Navier-Stokes*. Though, the amount of details, let alone the computational effort needed to do so is overwhelming, whereas the information gained is very minor, particularly in the context of a distribution network. Interestingly, the roughness parameter ϵ_{DW} as it is utilized in (2.6) seems to be more related to the root-mean-square roughness of a pipe as one would rather commonly think of the mean roughness over the length and the cross section area (see [Afzal, 2007]).

The *Swamee-Jain* equation (cf. [Walski et al., 2003])

$$\tilde{\lambda}_{DW} = \frac{\left(\frac{\ln(10)}{2}\right)^2}{\ln^2\left(\frac{\epsilon_{DW}}{3.7d} + \frac{5.74}{Re^{0.9}}\right)} \quad \text{for} \quad \begin{array}{l} 4000 < Re \leq 10^8 \\ 10^{-6} \leq \epsilon_{DW}/d \leq 10^{-2} \end{array} \quad (2.7)$$

approximating (2.6) with a relative accuracy of $\pm 1.5\%$ (some claim $\pm 1\%$) gained high popularity, particularly due its application in the software EPANET2 [Lewis, 2000]. Although it has the identical physical meaning as (2.6), it is denoted by $\tilde{\lambda}_{DW}$ to clearly distinguish it from λ_{DW} proposed by Colebrook and White.

Transitional or Critical Area. The development of the *Darcy-Weisbach* equation already started in the 18th century and, yet, the pipe flow in the region between $Re = 2000$ and $Re = 4000$ remains mystical. Analogous to the turbulent region there is no common convention of the friction coefficient, whereas the scientific community seems to have agreed that this area can not be (or at least hardly be) scientifically grasped. Hence, the grayed area in the Moody chart in figure 2.2. As an example, Tobias Schneider dedicated his PhD thesis [Schneider, 2007] to the investigation of properties of the transitional pipe flow showing beautiful images coloring the cross section area with different flow velocities. While citing Reynolds

“Although in most ways the exact manner in which water moves is difficult to perceive and still more difficult to define, as are also the forces attending such motion, certain general features both of the forces and motions stand prominently forth, as if to invite or to defy theoretical treatment.”¹

at the beginning of his thesis he also concludes by remarking the difficulty of the subject, hoping that his investigations *“finally even be of some practical relevance”*.

¹ O. Reynolds, An experimental investigation of the circumstances which determine whether the motion of water shall be direct or sinuous and the law of resistance in parallel channels, 1883.

In this thesis, analogous to *EPANET2* [Lewis, 2000], the cubic interpolation [Dunlop, 1991], which actually applies *Swamee-Jain* (see (2.7)) at $Re = 4000$, with the following steps²

$$y_2 = \frac{\epsilon_{DW}}{3.7d} + \frac{5.74}{Re^{0.9}}, \quad y_3 = -0.86859 \ln \left(\frac{\epsilon_{DW}}{3.7d} + \frac{5.74}{4000^{0.9}} \right)$$

$$f_a = y_3^{-2}, \quad f_b = f_a \left(2 - \frac{0.00514215}{y_2 y_3} \right) \quad (2.8a)$$

$$x_1 = 7f_a - f_b, \quad x_2 = 0.128 - 17f_a + 2.5f_b$$

$$x_3 = -0.128 + 13f_a - 2f_b + \frac{Re}{2000}(0.032 - 3f_a + 0.5f_b)$$

$$\lambda_{DW} = x_1 + \frac{Re}{2000} \left(x_2 + \frac{Re}{2000} x_3 \right) \quad \text{for } 2000 < Re < 4000 \quad (2.8b)$$

is considered at some parts.

Minor Losses

One decisive aspect when dealing with minor losses is that each appurtenance creating some sort of head loss is unique and highly depends on the shape penetrating the pipe. In general, one would have to determine minor head losses

$$\Delta h_m = k_m \left| Q^{n_m - 1} \right| Q \quad (2.9)$$

by finding suitable coefficients k_m for each pipe in the entire network. Equation (2.9) is a very generous formulation due to the unspecified exponent n_m , which gives an additional parameter to adjust with the aim to match minor head losses over a wide range of Q values.

Corresponding with the *Darcy-Weisbach* equation (2.4) a quadratic $n_m = 2$ expression will help to avoid additional unknowns in a network to be found. Indeed, the value $n_m = 2$ has a physical origin. For instance, when calculating the velocity v of the outflow from an open pipe by equating potential- to kinetic energy

$$mgh = \frac{mv^2}{2} \quad (2.10)$$

the quadratic relation between the head h and the discharge (resp. flow) velocity $v = Q/A$ can be seen, whereas the influence of mass m cancels out. After simple manipulations

$$h = \frac{Q^2}{2gA^2} \quad (2.11)$$

the origin of the *Darcy-Weisbach* equation becomes apparent.

²Please mind that $x_1, x_2, x_3, y_1, y_2, y_3, f_a, f_b$ are just auxiliary variables used for (2.8) only.

2.1.5 The *Lambert* Function

The *Lambert* function $W(x)$ solves the equation

$$W \exp(W) = x \quad (2.12)$$

and is the basis for an explicit solution of (2.6). Provided that x is real, the *Lambert* function has two possible real solutions (called *branches*) if $-1/e < x < 0$ denoting $e = \exp(1)$. The one satisfying $W(x) \geq -1$, denoted by $W_0(x)$, is called the *principle branch*, whereas the branch satisfying $W(x) \leq -1$ is denoted by $W_{-1}(x)$. As in figure 2.3, $W(x \geq 0) = W_0(x \geq 0)$ has a unique real solution if $x \geq 0$.

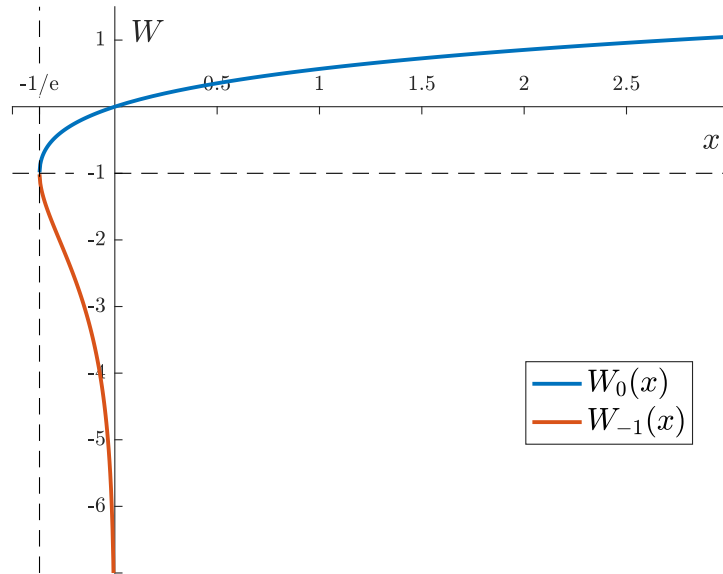


FIGURE 2.3: The *Lambert* function for real-valued arguments x .

However, if argument x is complex there are multiple solutions [Corless et al., 1996] usually denoted by $W_k(x)$.

Property 2.1. For a positive and real argument $x > 0$, the principle branch of Lambert function $W(x > 0) = W_0(x > 0)$

$$\underbrace{W \exp(W)}_{>0} = x > 0 \quad \Rightarrow \quad W > 0 \quad (2.13)$$

has a positive real solution $W_0(x > 0) > 0$.

In fact, the *Lambert* function has a variety of potential applications [Corless et al., 1996], although its appearance often remains unnoticed. An interesting one, especially from a control perspective, may be that it provides a solution for a linear delay equation such as

$$\dot{y}(t) = ay(t - \tau) \quad \text{for} \quad \tau > 0. \quad (2.14)$$

Considering the ansatz $y = \exp(st)$ one obtains

$$s \exp(st) = a \exp(st) \exp(-s\tau) \quad \Rightarrow \quad s\tau \exp(s\tau) = \tau a \quad (2.15)$$

where the scaled *Lambert* function $s = W(\tau a)/\tau$ turns out to be a solution for s . Due to linearity

$$y = \sum_{k=-\infty}^{\infty} c_k \exp\left(\frac{W_k(\tau a)}{\tau} t\right) \quad (2.16)$$

a linear combination of all *Lambert* solutions also solves (2.15). Also, stability is inherently connected to $W_k(\tau a)/\tau$ as y grows exponentially with every positive real part of $W_k(\tau a)/\tau$. For instance, this can also be extended to solve

$$\dot{y}(t) = ay(t - \tau) + by(t). \quad (2.17)$$

With the same ansatz as before one obtains

$$s = a \exp(-s\tau) + b \quad \Rightarrow \quad \ln\left(\frac{s-b}{a}\right) = -s\tau, \quad (2.18)$$

when adding τb and again taking $\exp(\cdot)$ on each side of the equation while multiplying with τ

$$\frac{\exp(\tau b)}{a} \tau(s-b) = \tau \exp(-\tau(s-b)) \quad \Rightarrow \quad \tau(s-b) \exp(\tau(s-b)) = \tau \exp(-\tau b) a \quad (2.19)$$

one already recognizes the connection to the *Lambert* function where $W = \tau(s-b)$ and $x = \tau \exp(-\tau b) a$. This simple concept can be extended to matrices

$$\dot{\mathbf{y}}(t) = \mathbf{A}\mathbf{y}(t - \tau) + \mathbf{B}\mathbf{y}(t) \quad (2.20)$$

with square \mathbf{A}, \mathbf{B} when considering the matrix *Lambert* function $\mathbf{W} \exp(\mathbf{W}) = \mathbf{X}$. Nevertheless, the general matrix *Lambert* equation is a hard problem to solve, though, there are some cases (concerning properties of \mathbf{A}, \mathbf{B}) which could be of special interest (Corless et al. [1996] cites [Bellman and Cooke, 1963; Corless, 1994; Wright, 1949]).

Definition 2.2. *For ongoing investigations only the positive part of the Lambert function in the principle branch is of interest, therefore $W : x \in]0, \infty] \rightarrow]0, \infty]$ is considered only.*

Proposition 2.3. *Given Property 2.1, the Lambert function according to (2.12) and Definition 2.2 is strictly monotonically increasing.*

Proof. Denoting $F_l(W, x) = W \exp(W) - x = 0$, it is clear that

$$\frac{\partial F_l}{\partial x} + \frac{\partial F_l}{\partial W} \frac{\partial W}{\partial x} = 0 \quad \Rightarrow \quad \frac{\partial W}{\partial x} = -\frac{\partial F_l}{\partial x} \left(\frac{\partial F_l}{\partial W} \right)^{-1} = \frac{1}{\exp(W)(1+W)} > 0 \quad \forall x(>0) \quad (2.21)$$

since $W > 0$ (for $x > 0$) according to Property 2.1. ■

2.1.6 An Explicit Solution of Colebrook-White

Denoting³

$$a = \frac{\epsilon_{\text{DW}}}{3.7d} \quad b = \frac{2.51}{Re} \quad c = \frac{2}{\ln(10)} \quad y = \frac{1}{\sqrt{\lambda_{\text{DW}}}} \quad (2.22)$$

Colebrook-White's equation for the friction factor (2.6) turns into $y + c \ln(a + by) = 0$. When multiplied with b and adding a on the left and right hand side

$$(a + by) + bc \ln(a + by) = a, \quad (2.23)$$

then dividing (2.23) by bc

$$\frac{a + by}{bc} + \ln(a + by) = \frac{a}{bc} \quad (2.24)$$

taking $\exp(\cdot)$ on the left and right hand side of (2.24) and again dividing by bc results in

$$\exp\left(\frac{a + by}{bc}\right) \frac{a + by}{bc} = \frac{1}{bc} \exp\left(\frac{a}{bc}\right) \quad (2.25)$$

³Note the definition change of parameters $a, b, c, s, y, \mathbf{A}, \mathbf{B}$, also in other sections.

where one can see the equivalence to problem (2.12) relating $W = \frac{a+by}{bc}$ and $x = \frac{1}{bc} \exp\left(\frac{a}{bc}\right)$. Considering these few steps to reveal the connection, one major reason why the *Lambert* function is hardly applied in hydraulics is that

$$x = \frac{1}{bc} \exp\left(\frac{a}{bc}\right) = \frac{\ln(10)}{2} \frac{Re}{2.51} \exp\left(\frac{\ln(10)}{2} \frac{Re}{2.51} \frac{\epsilon_{DW}}{3.7d}\right) \quad (2.26)$$

increases with growing Re such that is not displayable with current double floating point precision, for instance when $Re = 10 \times 10^5$ and $\epsilon_{DW}/d = 0.02$, then $x = 4.7577 \times 10^{107}$. Note that *Reynolds* numbers are high in the turbulent regime $Re \geq 4000$. This problem, however, can be circumvented elegantly when applying the absolute convergent series [Corless et al., 1996]

$$W(x) = L_1 - L_2 + \sum_{k=0}^{\infty} \sum_{m=1}^{\infty} c_{km} L_2^m L_1^{-k-m} \quad (2.27)$$

where $L_1 = \ln(x) = \frac{a}{bc} - \ln(bc)$ and $L_2 = \ln(\ln(x))$ and thus only the logarithm of argument x of the *Lambert* function is needed. Parameter c_{km} denotes the Stirling number

$$c_{km} = \frac{1}{m!} (-1)^k \binom{k+m}{k+1} = \frac{1}{m!} (-1)^k \frac{(k+m)!}{(k+1)!(m-1)!} \quad (2.28)$$

which leads to the following terms

$$\begin{aligned} W(x) = L_1 - L_2 + \frac{L_2}{L_1} + \frac{L_2(L_2 - 2)}{2L_1^2} + \frac{L_2(6 - 9L_2 + 2L_2^2)}{6L_1^3} \\ + \frac{L_2(-12 + 36L_2 - 22L_2^2 + 3L_2^3)}{14L_1^4} + \mathcal{O}\left(\left\{\frac{L_2}{L_1}\right\}^5\right) = W_{cw}(x) + \mathcal{O}\left(\left\{\frac{L_2}{L_1}\right\}^5\right), \end{aligned} \quad (2.29)$$

where the last term indicates the remaining error which, effectively, depends on L_2/L_1 to the power of 5. When taking the first terms $W_{cw}(x)$ to approximate the Colebrook-White equation, the accuracy is unmatched by any other empirical equation.

Accuracy. Not only from the physical context, but due to $x = \frac{\ln(10)}{2} \frac{Re}{2.51} \exp\left(\frac{\ln(10)}{2} \frac{Re}{2.51} \frac{\epsilon_{DW}}{3.7d}\right) > 0$, it is evident that the Colebrook-White equation (2.6) has a unique and positive solution within the *principle branch* of the *Lambert* function (see figure 2.3). The smallest W and x value obtainable in the transitional regime is located at $Re = 4000$, $\epsilon_{DW}/d = 0$

$$x_{min} = \frac{\ln(10)}{2} \frac{Re}{2.51} \exp\left(\frac{\ln(10)}{2} \frac{Re}{2.51} \frac{\epsilon_{DW}}{3.7d}\right) = \frac{\ln(10)}{2} \frac{4000}{2.51} \quad (2.30)$$

as a direct consequence of $W(x)$, in reference to Definition 2.2, being strictly monotonically increasing according to Property 2.1. The maximal error in the approximation $W_{cw}(x)$ of $W(x)$ occurs at $W(x_{min})$ as higher orders of series (2.29) depend on $\ln(\ln(x)) / \ln(x)$ which becomes largest at $x = x_{min}$. Subsequently, the largest possible relative error is close to

$$\frac{|W(x_{min}) - W_{cw}(x_{min})|}{W(x_{min})} \approx 2.5224 \times 10^{-6} = 0.00025224\%, \quad (2.31)$$

where $W_{min} = W(x_{min})$ was calculated numerically to a precision of $W_{min} \exp(W_{min}) - x_{min} \approx 1.82 \times 10^{-12}$. This provides that error \mathcal{O} in (2.29) is directly proportional to L_2/L_1 . When considering figure 2.4 where the course of friction factor λ_{DW} is compared between the approximated *Lambert* solution W_{cw} (2.29), the *Swamme-Jain* (2.7) equation and the real *Colebrook-White* solution (2.6) (calculated numerically), one can see that (2.7) produces a particularly high error at low turbulent Re numbers, whereas no visible distinction between W_{cw} and the real λ_{DW} can be seen.

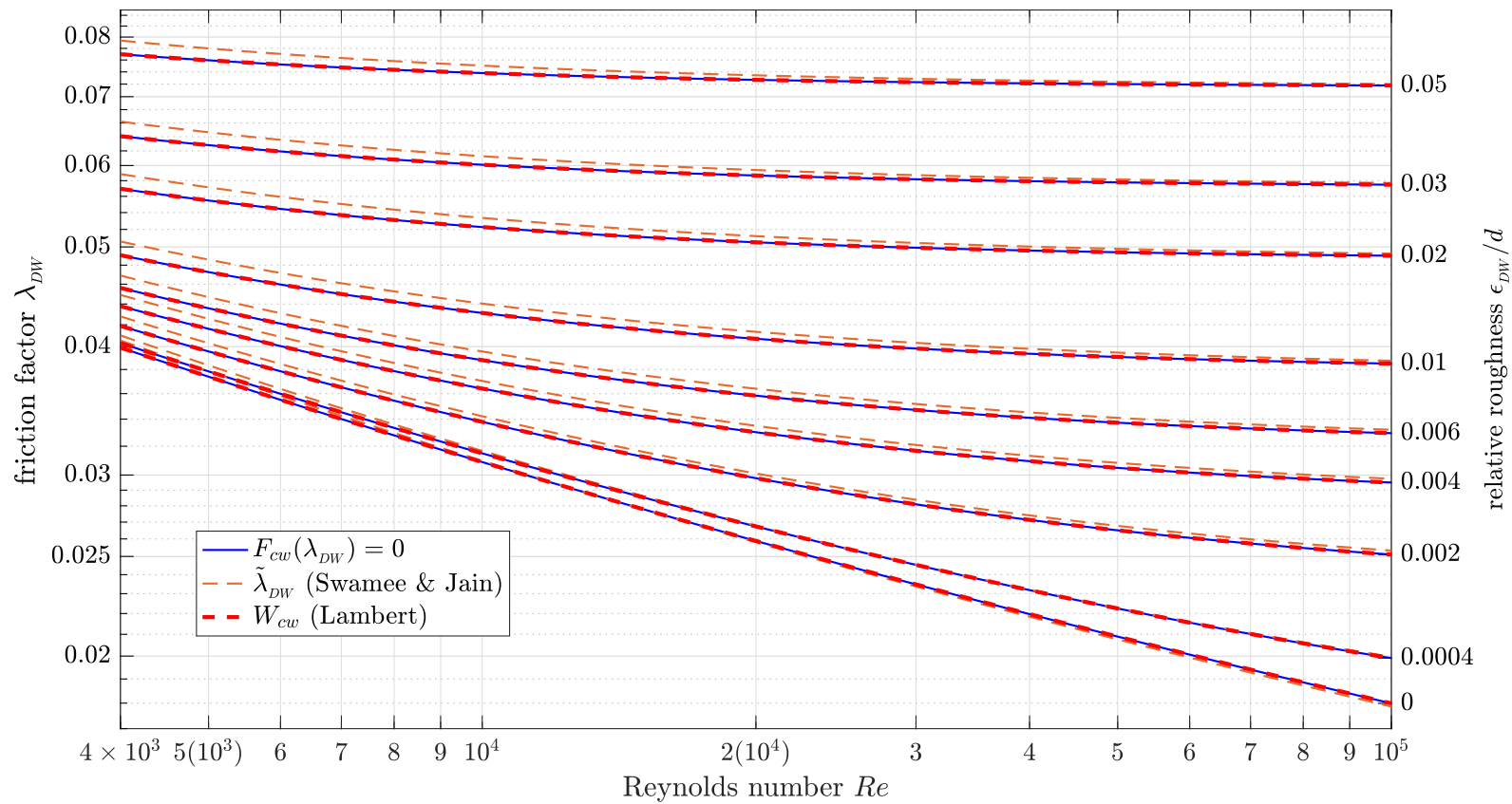


FIGURE 2.4: A *Moody*-type comparison of the friction factor λ_{DW} according to Colebrook-White (2.6) (calculated numerically), *Swamee-Jain* (2.7) and first terms W_{cw} of series (2.29) displaying (2.6) within the *principle branch* of the *Lambert* function.

2.2 Notation and Mathematical Tools

A brief introduction to the applied mathematical tools and notations is given in the following.

2.2.1 Notation

Symbols. The utilization of the symbols discussed below is actually unnecessary from a strict mathematical perspective but intends to improve readability by providing additional context information.

1. Symbol “:=” in $\text{ex}_1 := \text{ex}_2$ assigns the expression on the side of the equality-sign, i.e. ex_2 , to the variable on the side of the double-dots, i.e. ex_1 . For instance, $ax^2 + bx + c =: f(x)$ introduces quadratic function $f(x)$ on variable x with parameters a, b, c .
2. Symbol “ $\stackrel{!}{=}$ ” in $\text{ex}_1 \stackrel{!}{=} \text{ex}_2$ formulates a requirement whereas the validity of this statement has yet to be verified, i.e. expression ex_1 and ex_2 should be equivalent. For instance, the requirement $f(0) \stackrel{!}{=} 1$ leads to $c = 1$.
3. Analogously, symbol “ \equiv ” in $\text{ex}_1 \equiv \text{ex}_2$ embraces the equality of expression ex_1 and ex_2 concerning all their arguments. For instance, suppose that $g(x) := df/dx$. Then, the statement $g \equiv 2$ (one could also write $g \stackrel{!}{=} 2$) is synonymous for $g(x) = 2 \forall x$. This then leads to two equations for parameters a, b , resulting in $a = 0$ and $b = 2$.

Please mind that these symbols are only utilized if the author really believes to thereby improve readability.

Vectors and Matrices. Generally, vectors and matrices are highlighted bold and italic and are consistently assigned to variables featuring lower- and upper-case letters respectively.

1. Bold $\mathbf{1}_x$ and $\mathbf{0}_x$ with size x characterize a matrix or vector filled with ones or zeros, whereas size x is only provided if it is unclear from the context. For instance, $\mathbf{1}_3 = [1 \ 1 \ 1]^T$ or

$$\mathbf{0}_{2 \times 3} = \begin{bmatrix} 0 & 0 & 0 \\ 0 & 0 & 0 \end{bmatrix}.$$

2. The bracket-operator $[\mathbf{A}]_{ij} = A_{ij}$ applied on matrix $\mathbf{A} \in \mathbb{K}^{n \times m}$ of a number field \mathbb{K} , e.g. $\mathbb{K} = \mathbb{R}$ or $\mathbb{K} = \mathbb{C}$, selects element A_{ij} of matrix \mathbf{A} in the $i \in \{1, 2, \dots, n\}$ row and the $j \in \{1, 2, \dots, m\}$ column.
3. Concerning block-matrices, the *blank* block-entries characterize those which can be filled up with zero-matrix $\mathbf{0}$ of corresponding size. For instance, suppose that $\mathbf{A}_1, \mathbf{A}_2 \in \mathbb{K}^{n \times m}$, then one can write

$$\mathbf{A} = \begin{bmatrix} \mathbf{A}_1 & \\ & \mathbf{A}_2 \end{bmatrix} = \begin{bmatrix} \mathbf{A}_1 & \mathbf{0} \\ \mathbf{0} & \mathbf{A}_2 \end{bmatrix} = \begin{bmatrix} \mathbf{A}_1 & \mathbf{0}_{n \times m} \\ \mathbf{0}_{n \times m} & \mathbf{A}_2 \end{bmatrix} \in \mathbb{K}^{2n \times 2m}.$$

4. Bold letter \mathbf{e}_i utilizing index $i \in \mathbb{N}$ characterizes a unity vector $\mathbf{e}_i = [0 \ \dots \ 0 \ 1 \ 0 \ \dots \ 0]^T$ with variable size where $[\mathbf{e}_i]_j = 0 \ \forall i \neq j$ but $[\mathbf{e}_i]_i = 1$.
5. Upper-case and bold $\mathbf{I}_x = \text{diag}(\mathbf{1}_x)$ characterizes the unity matrix where its size x is only provided if it is unclear from the context.

2.2.2 Hadamard Product

Definition: Hadamard Product. Let $\mathbf{A}, \mathbf{B} \in \mathbb{C}^{n \times m}$. The *Hadamard* product of \mathbf{A} and \mathbf{B} is defined by $[\mathbf{A} \odot \mathbf{B}]_{ij} = A_{ij}B_{ij}$ for all $1 \leq i \leq n, 1 \leq j \leq m$.

This *Hadamard* operator [Million, 2007] is also utilized to display element-wise exponentiations as well as inversions in a more compact manner, for instance

$$\begin{aligned} [\mathbf{A}^{\odot 2}]_{ij} &= A_{ij}^2 \\ [\mathbf{A}^{\odot 1/2}]_{ij} &= A_{ij}^{1/2} \\ [\mathbf{A}^{\odot -1}]_{ij} &= A_{ij}^{-1} \end{aligned} \quad \forall 1 \leq i \leq n, 1 \leq j \leq m$$

which certainly provides that $[\mathbf{A}]_{ij} = A_{ij} \neq 0 \forall i, j$ in the context of the inversion $\mathbf{A}^{\odot -1}$ and that $\mathbf{A} \in \mathbb{R}^{n \times m}$ in the context of the square root $\mathbf{A}^{\odot 1/2}$. Also, suppose $\beta \in \mathbb{C}$ and $\mathbf{A}, \mathbf{B}, \mathbf{C} \in \mathbb{C}^{n \times m}$ the operator is commutative $\mathbf{A} \odot \mathbf{B} = \mathbf{B} \odot \mathbf{A}$ as well as linear, thus additive $\mathbf{C} \odot (\mathbf{A} + \mathbf{B}) = \mathbf{C} \odot \mathbf{A} + \mathbf{C} \odot \mathbf{B}$ and homogeneous $\beta(\mathbf{A} \odot \mathbf{B}) = (\beta\mathbf{A}) \odot \mathbf{B} = \mathbf{A} \odot (\beta\mathbf{B})$. Further interesting properties in terms of *Singular Value Decompositions* and the *Schur Product* can be obtained when applying the *Hadamard Product* on diagonal matrices, see [Million, 2007].

2.2.3 Index Transformation with Unity Vectors

Unity vectors in the form of $\mathbf{e}_i \in \mathbb{Z}_{\{0,1\}}^n$, which are comprised of zeros $[\mathbf{e}_i]_j = 0 \forall i \neq j$ and a single one $[\mathbf{e}_i]_i = 1$ only, are applied several times in this thesis to separate a vector $\mathbf{x} \in \mathbb{K}^n$ with entries x_i corresponding to indices $i \in \{1, 2, \dots, n\} = \mathfrak{J}$ into parts

$$[\mathbf{x}]_k = x_k \quad \text{for} \quad k \in \{k_1, k_2, \dots, k_p\} = \mathfrak{K} \subseteq \mathfrak{J} \quad (2.32a)$$

$$[\mathbf{x}]_{\bar{k}} = x_{\bar{k}} \quad \text{for} \quad \bar{k} \in \{\bar{k}_1, \bar{k}_2, \dots, \bar{k}_q\} = \bar{\mathfrak{K}} \subseteq \mathfrak{J} \quad (2.32b)$$

such that $\mathfrak{K} \cup \bar{\mathfrak{K}} = \mathfrak{J}$ and $\mathfrak{K} \cap \bar{\mathfrak{K}} = \{\}$. Hence, $p + q = n$. This separation is then accomplished by matrices

$$\mathbf{R} = \begin{bmatrix} \mathbf{e}_{k_1} & \mathbf{e}_{k_2} & \dots & \mathbf{e}_{k_p} \end{bmatrix}^T \quad \text{and} \quad \bar{\mathbf{R}} = \begin{bmatrix} \mathbf{e}_{\bar{k}_1} & \mathbf{e}_{\bar{k}_2} & \dots & \mathbf{e}_{\bar{k}_q} \end{bmatrix}^T \quad (2.33)$$

resulting in $[\mathbf{R}\mathbf{x}]_k = x_k$ with $k \in \mathfrak{K}$ and $[\bar{\mathbf{R}}\mathbf{x}]_{\bar{k}} = x_{\bar{k}}$ with $\bar{k} \in \bar{\mathfrak{K}}$ analogously. The following properties hold.

Property 2.4. *Matrices \mathbf{R} and $\bar{\mathbf{R}}$ satisfy:*

$$\begin{aligned} \mathbf{R}\mathbf{R}^T &= \mathbf{I}_p & \bar{\mathbf{R}}\bar{\mathbf{R}}^T &= \mathbf{I}_q & \mathbf{R}\bar{\mathbf{R}}^T &= \mathbf{0}_{p \times q} \\ \mathbf{R}^T\mathbf{R} + \bar{\mathbf{R}}^T\bar{\mathbf{R}} &= \mathbf{I}_n \end{aligned}$$

Proof. One can write $[\mathbf{R}\mathbf{R}^T]_{ij} = \mathbf{e}_{k_i}^T \mathbf{e}_{k_j}$ for all $i, j \in \{1, 2, \dots, p\}$ and $[\bar{\mathbf{R}}\bar{\mathbf{R}}^T]_{ij} = \mathbf{e}_{\bar{k}_i}^T \mathbf{e}_{\bar{k}_j}$ for all $i, j \in \{1, 2, \dots, q\}$. Since $\mathbf{e}_i^T \mathbf{e}_j = 0$ for all $i \neq j$ and $\mathbf{e}_i^T \mathbf{e}_i = 1$ for $i = j$, it is evident that $\mathbf{R}\mathbf{R}^T = \mathbf{I}_p$ and $\bar{\mathbf{R}}\bar{\mathbf{R}}^T = \mathbf{I}_q$. In analogy, $[\mathbf{R}\bar{\mathbf{R}}^T]_{ij} = \mathbf{e}_{k_i}^T \mathbf{e}_{\bar{k}_j} = 0$ for $1 \leq i \leq p$ and $1 \leq j \leq q$ as $\mathfrak{K} \cap \bar{\mathfrak{K}} = \{\}$. However, $\mathbf{R}^T\mathbf{R} + \bar{\mathbf{R}}^T\bar{\mathbf{R}} = \mathbf{e}_{k_1}^T \mathbf{e}_{k_1}^T + \mathbf{e}_{k_2}^T \mathbf{e}_{k_2}^T + \dots + \mathbf{e}_{k_p}^T \mathbf{e}_{k_p}^T + \mathbf{e}_{\bar{k}_1}^T \mathbf{e}_{\bar{k}_1}^T + \dots + \mathbf{e}_{\bar{k}_q}^T \mathbf{e}_{\bar{k}_q}^T = \mathbf{e}_1 \mathbf{e}_1^T + \dots + \mathbf{e}_n \mathbf{e}_n^T = \mathbf{I}_n$. ■

Actually, separation (2.32) is not only applicable to vector \mathbf{x} , but also to a matrix $\mathbf{A} = [\mathbf{a}_1 \ \mathbf{a}_2 \ \dots \ \mathbf{a}_n]^T \in \mathbb{K}^{n \times m}$ in order to select $\mathbf{e}_i^T \mathbf{A} = \mathbf{a}_i^T$, i.e. one of the $i \in \{1, 2, \dots, n\} = \mathfrak{J}$ rows of \mathbf{A} . Applying matrices such as (2.33) on \mathbf{A} , then yields subset \mathfrak{K} or $\bar{\mathfrak{K}}$ of the rows $i \in \mathfrak{J}$ of \mathbf{A} , i.e. $\mathbf{R}\mathbf{A} = [\mathbf{a}_{k_1} \ \dots \ \mathbf{a}_{k_p}]^T$ or $\bar{\mathbf{R}}\mathbf{A} = [\mathbf{a}_{\bar{k}_1} \ \dots \ \mathbf{a}_{\bar{k}_q}]^T$.

In case the index-set \mathfrak{J} is separated into three sets or more, instead of only \mathfrak{K} and $\bar{\mathfrak{K}}$, similar properties (referring to Property 2.4) can be derived.

2.2.4 Derivatives Along Vectors

First-Order Derivatives. The derivative of the scalar function $h(\mathbf{x}) : \mathbb{K}^n \rightarrow \mathbb{K}$ operating on a field \mathbb{K} with respect to vector $\mathbf{x} = [x_1 \ \dots \ x_n]^T$ is defined to result in the row-vector

$$\frac{\partial h(\mathbf{x})}{\partial \mathbf{x}} := \left[\frac{\partial h}{\partial x_1} \quad \frac{\partial h}{\partial x_2} \quad \dots \quad \frac{\partial h}{\partial x_n} \right] =: (\nabla_{\mathbf{x}} h)^T$$

whereas its gradient $\nabla_{\mathbf{x}} h$, which is exclusively denoted by the *Nabla* operator ∇ , is defined to yield a column-vector. As a remark, the function argument of h , that is \mathbf{x} , is only provided in the operator $\nabla_{\mathbf{x}} \hat{=} \nabla$ if clarification about the partial derivatives is needed. When considering the vector-field $\mathbf{f}(\mathbf{x}) = [f_1(\mathbf{x}) \ \dots \ f_m(\mathbf{x})]^T : \mathbb{K}^n \rightarrow \mathbb{K}^m$ the derivative along the vector \mathbf{x} is defined to result in

$$\frac{\partial \mathbf{f}(\mathbf{x})}{\partial \mathbf{x}} := \begin{bmatrix} \frac{\partial f_1(\mathbf{x})}{\partial x_1} & \frac{\partial f_1(\mathbf{x})}{\partial x_2} & \dots & \frac{\partial f_1(\mathbf{x})}{\partial x_n} \\ \frac{\partial f_2(\mathbf{x})}{\partial x_1} & \frac{\partial f_2(\mathbf{x})}{\partial x_2} & \dots & \frac{\partial f_2(\mathbf{x})}{\partial x_n} \\ \vdots & \vdots & \ddots & \vdots \\ \frac{\partial f_m(\mathbf{x})}{\partial x_1} & \frac{\partial f_m(\mathbf{x})}{\partial x_2} & \dots & \frac{\partial f_m(\mathbf{x})}{\partial x_n} \end{bmatrix},$$

the *Jacobian*.

Second-Order Derivatives. The second-order derivative of the scalar function $h(\mathbf{x})$ with respect to \mathbf{x} yields

$$\frac{\partial^2 h(\mathbf{x})}{\partial \mathbf{x}^2} = \mathcal{H}(h)(\mathbf{x}) := \begin{bmatrix} \frac{\partial^2 h}{\partial x_1^2} & \frac{\partial^2 h}{\partial x_2 \partial x_1} & \dots & \frac{\partial^2 h}{\partial x_n \partial x_1} \\ \frac{\partial^2 h}{\partial x_1 \partial x_2} & \frac{\partial^2 h}{\partial x_2^2} & \dots & \frac{\partial^2 h}{\partial x_n \partial x_2} \\ \vdots & \vdots & \ddots & \vdots \\ \frac{\partial^2 h}{\partial x_1 \partial x_n} & \frac{\partial^2 h}{\partial x_2 \partial x_n} & \dots & \frac{\partial^2 h}{\partial x_n^2} \end{bmatrix} =: \nabla_{\mathbf{x}}^2 h,$$

the *Hessian* which is also denoted by the square of the *Nabla* operator, i.e. $\mathcal{H}(h)(\mathbf{x}) = \nabla_{\mathbf{x}}^2 h$. A sufficient condition for the *Hessian* to be symmetric, i.e. $\mathcal{H}(h)(\mathbf{x}) = \mathcal{H}(h)(\mathbf{x})^T$ or $\nabla_{\mathbf{x}}^2 h = (\nabla_{\mathbf{x}}^2 h)^T$, is that $h(\mathbf{x})$ must be two-times continuously differentiable (*Schwarz-Clairaut Theorem*), i.e. $h \in C^2$.

Now suppose that the scalar function h depends on a second set of variables combined in vector $\mathbf{y} = [y_1 \ y_2 \ \dots \ y_c]^T \in \mathbb{K}^c$, i.e. $h = h(\mathbf{x}, \mathbf{y})$. Then, the mixed derivative yields

$$\frac{\partial^2 h}{\partial \mathbf{x} \partial \mathbf{y}} = \frac{\partial}{\partial \mathbf{x}} \left(\frac{\partial h}{\partial \mathbf{y}} \right)^T = \frac{\partial}{\partial \mathbf{x}} (\nabla_{\mathbf{y}} h) = \begin{bmatrix} \frac{\partial^2 h}{\partial x_1 \partial y_1} & \frac{\partial^2 h}{\partial x_2 \partial y_1} & \dots & \frac{\partial^2 h}{\partial x_n \partial y_1} \\ \frac{\partial^2 h}{\partial x_1 \partial y_2} & \frac{\partial^2 h}{\partial x_2 \partial y_2} & \dots & \frac{\partial^2 h}{\partial x_n \partial y_2} \\ \vdots & \vdots & \ddots & \vdots \\ \frac{\partial^2 h}{\partial x_1 \partial y_c} & \frac{\partial^2 h}{\partial x_2 \partial y_c} & \dots & \frac{\partial^2 h}{\partial x_n \partial y_c} \end{bmatrix},$$

and in case $h(\mathbf{x}, \mathbf{y})$ is two-times continuously differentiable, one can write

$$\frac{\partial^2 h}{\partial \mathbf{y} \partial \mathbf{x}} = \left(\frac{\partial^2 h}{\partial \mathbf{x} \partial \mathbf{y}} \right)^T = \frac{\partial}{\partial \mathbf{y}} \left(\frac{\partial h}{\partial \mathbf{x}} \right)^T = \frac{\partial}{\partial \mathbf{x}} \left(\frac{\partial h}{\partial \mathbf{y}} \right)^T.$$

The second-order derivatives of a vector-field such as $\mathbf{f}(\mathbf{x})$ can no longer be represented compactly by a single matrix and will be discussed in detail when needed.

2.2.5 Remarks and References

Apart from the above mathematical tools, stability notions on ordinary differential equations are used such as they are established in the field of control-theory. Reference [Khalil, 2002] or [Adamy, 2014] are recommended in the context of *asymptotic stability* of equilibria, *Ljapunov* functions etc. Adamy [2014], for instance, thereby also gives a nice introduction to the method of *exact linearization* which is utilized once in its simplest form.

Coming back to the applied notation concerning indices, in specific the notation as it is used on natural numbers, e.g. $n \in \mathbb{N}$. Variable n is commonly utilized to denote the number of things like nodes in a graph, referring to n_j . Please mind that these subscripts of n , that is “j” (associated with *junctions*) in the case of n_j , are *never* used to denote another index but different variable-names. This is contradictory to other variables like k , as it is used in (2.32) for instance, where the subscripts indeed represent other indices not variable-names. Another example is n_ℓ which consistently denotes the number of edges in a graph, whereas subscript “ ℓ ” was originally associated with the graph’s links.

Network Hydraulics: A Primarily Steady-State Perspective

Generally, there are two essentially different approaches for modeling water networks which are broadly established in the scientific community. One dealing with a full transient description [Chaudhry, 2014], effectively, a particular form of *Navier-Stokes* (as part of the fluid dynamic equations), and the other one a pure steady-state consideration only applying the fundamentals, the *conservation of mass and energy* [Todini and Pilati, 1987; Walski et al., 2003]. Actually, the former one predominantly serves the purpose of analysis, providing the ability to model the water distribution as accurate and detailed as possible, while the steady-state one turns out to be especially handy for manipulation, meaning water management methods for leak detection/localization, pressure control, calibration, consumer demand prediction and further. The arguably most popular ones mainly rely on optimizations, whereas the application of computationally-intensive solvers, particularly genetic algorithms, also gain popularity. On the transient front, the utilization of *inverse transients* for the detection and localization of leaks (see e.g. [Covas and Ramos, 2001]) is often prone to fail as a result of the number of additional parameters needed for the transient description. For solving the transient model equations, the application of the *method of characteristics* [Chaudhry, 2014] apart from *finite differences* is commonly applied to transform the partial differential equations (PDEs) into ordinary ones. Although the author considers the fully transient description to be substantial in every regard, it can hardly be applied as basis for model-based manipulation methods as far as networks are concerned. As a consequence, the PDEs for the full transient description do not receive due attention in this thesis as the emphasis is put on model-based techniques for manipulation.

However, this thesis intends to address subjects with higher relevance in the historical development rather than providing a complete overview, while it sets focus on topics which, in the opinion of the author, have not received adequate attention. Considering the majority of recent articles revolving around the model-based manipulation of water networks, the steady-state formulation as it was proposed by Todini and Pilati [1987] seems to have become the common standard. In their paper they illustrate the equivalence of the solution of *conservation of mass and energy* with the solution of a constrained yet convex optimization problem, where *Lagrange* multipliers turn out to be nodal heads. *Newton-Raphson's* algorithm is applied to solve this nonlinear problem which happens to converge fast due to convexity.

3.1 Steady-State Network Formulation

Averaged flow values Q_i (m^3/s) over the pipe's cross section area of pipe $i \in \mathfrak{P} = \{1, \dots, n_\ell\}$ are located between $k \in \mathfrak{N} = \{1, 2, \dots, n_j + n_s\}$ nodes (cf. figure 3.1). One distinguishes between n_j inner nodes $\mathfrak{I} = \{1, 2, \dots, n_j\}$ and n_s source nodes (also known as fixed head or boundary nodes) $\mathfrak{S} = \{n_j + 1, \dots, n_j + n_s\}$, so $\mathfrak{I} \cup \mathfrak{S} = \mathfrak{N}$. Unknown nodal pressure heads $h_{k \in \mathfrak{I}}$ (m) are

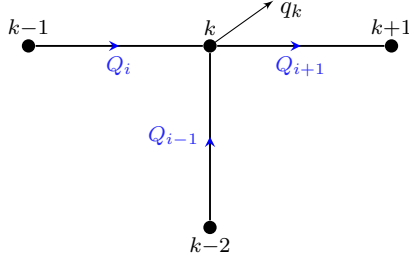


FIGURE 3.1: Hydraulic consumer node comprising three connections.

located at a geographical elevation of $z_{k \in \mathcal{J}}$ (m) respectively. Nodes \mathfrak{S} are usually related to tanks, reservoirs, pumps, and further. It is assumed that the nodal (source) pressure head $h_{k \in \mathfrak{S}}$ at these n_s source nodes \mathfrak{S} , combined in vector $\mathbf{h}_s \in \mathbb{R}_{\geq 0}^{n_s}$, is measured and thus can be directly treated as input. This assumption, however, only serves as simplification, it would certainly be possible to couple, e.g., equations for pumps with the proposed model equations.

The objective is to determine unique flows $\mathbf{x}_Q = [Q_1 \ Q_2 \ \dots \ Q_{n_\ell}]^T \in \mathbb{R}^{n_\ell}$ and nodal pressure heads $\mathbf{h} = [h_1 \ h_2 \ \dots \ h_{n_j}]^T \in \mathbb{R}_{\geq 0}^{n_j}$ while considering nodal elevations $\mathbf{z} = [z_1 \ z_2 \ \dots \ z_{n_j}]^T \in \mathbb{R}_{\geq 0}^{n_j}$ and friction functions $\mathbf{h}_{\text{loss}}(\mathbf{x}_Q) = \Delta \mathbf{h}_{\text{DW}}(\mathbf{x}_Q) + \Delta \mathbf{h}_m(\mathbf{x}_Q) \in \mathbb{R}^{n_\ell}$, comprising a *Darcy-Weisbach* $\Delta \mathbf{h}_{\text{DW}}$ (2.4) and a minor loss $\Delta \mathbf{h}_m$ (2.9) component. Due to reasons which will become apparent later on, \mathbf{h} denotes, as distinguished from literature, nodal pressure heads and not nodal heads $\mathbf{h} + \mathbf{z}$. Individual friction functions $[\mathbf{h}_{\text{loss}}(\mathbf{x}_Q)]_i = h_{\text{loss},i}(Q_i) \ \forall i \in \mathfrak{P}$ thereby only depend on the flow passing through the respective pipe Q_i and actually feature two friction parameters per pipe, roughness $\epsilon_{\text{DW}} \in \mathbb{R}_{\geq 0}^{n_\ell}$ and minor loss values $\mathbf{k}_m \in \mathbb{R}_{\geq 0}^{n_\ell}$, which, in general, can be considered unknown. The nodal consumption $\bar{\mathbf{q}} \in \mathbb{R}_{\geq 0}^{n_j}$ is usually considered to be known as far as the solving of network equations is concerned.

The billing information of customers allows conclusions about their consumption and is utilized to produce consumption patterns which feature a specific course over time. For instance, households usually have a consumption peak in the morning and evening, whereas industries often have quite constant water demand. However, the considered $\bar{\mathbf{q}}$ is indisputably prone to uncertainty and can often be the source of failure. As a consequence, the application of additional sensors, which continuously transmit the water consumption and even pressure to a central processing unit, gains popularity. Big consumers with irregular consumption patterns, such as hospitals or food markets, are of particular interest. In this context, wireless data communication becomes an important part of the drinking water infrastructure as cost-savings, e.g., by avoiding digging for cable installations, are essential for the concept of hydraulic models to be economically viable.

3.1.1 Conservation of Mass

The network's topology is represented by *Kirchhoff's* formulation of nodes

$$\mathbf{A} \mathbf{x}_Q = \bar{\mathbf{q}} \quad (3.1)$$

also known as the principle of the *conservation of mass*. $\mathbf{A} \in \mathbb{Z}_{\{-1,0,1\}}^{n_j \times n_\ell}$, consisting of minus ones, zeros and ones only, represents one part of the graph's incidence matrix $\bar{\mathbf{A}} = [-\mathbf{A}^T \ \tilde{\mathbf{C}}_s]^T \in \mathbb{Z}_{\{-1,0,1\}}^{(n_j+n_s) \times n_\ell}$. Inner nodes \mathcal{J} are represented in \mathbf{A} and the source nodes \mathfrak{S} in $\tilde{\mathbf{C}}_s \in \mathbb{Z}_{\{-1,0,1\}}^{n_\ell \times n_s}$.

Property 3.1. *The sum of the incidence matrix's columns is always zero, i.e.*

$$\sum_{k=1}^{n_j+n_s} [\bar{\mathbf{A}}]_{ki} = 0 \quad \forall i \in \mathfrak{P} \quad (3.2)$$

which means that rows of $\bar{\mathbf{A}}$ are linearly dependent.

To put it into perspective, according to Property 3.1 each flow Q_i is assigned with a unique yet arbitrary number $i \in \mathfrak{P}$ and a direction between exactly two nodes, namely $k_1 \in \mathfrak{N}$ and $k_2 \in \mathfrak{N}$, where $k_1 \neq k_2$ (no self-loops). As flow Q_i is either influent to k_1 and effluent of k_2 or vice versa, Property 3.1 holds.

Two-Cycle Network Example. For illustrative purposes consider figure 3.2,

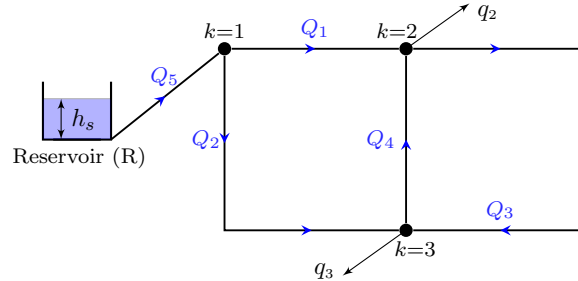


FIGURE 3.2: Two-Cycle/Loop Network.

a network with $n_\ell = 5$ pipes, $n_j = 3$ nodes and one source, i.e. $n_s = 1$, providing constant pressure head h_s from reservoir R. Suppose customers are sitting at nodes 2 and 3 and thereby consume q_2 and q_3 (m^3/s). Then,

$$\underbrace{\begin{bmatrix} -1 & -1 & 0 & 0 & 1 \\ 1 & 0 & -1 & 1 & 0 \\ 0 & 1 & 1 & -1 & 0 \end{bmatrix}}_{\mathbf{A}} \underbrace{\begin{bmatrix} Q_1 \\ \vdots \\ Q_5 \end{bmatrix}}_{\mathbf{x}_Q} = \underbrace{\begin{bmatrix} 0 \\ q_2 \\ q_3 \end{bmatrix}}_{\mathbf{q}}, \quad \tilde{\mathbf{C}}_s = \begin{bmatrix} 0 & 0 & 0 & 0 & 1 \end{bmatrix}^T. \quad (3.3)$$

Considering (3.3), the nodal equations determine the $k \in \mathfrak{J}$ rows in \mathbf{A} , where entries in this row select the corresponding (with the correct sign) entries in flow vector \mathbf{x}_Q . To obtain a unique incidence matrix once flows and nodes are numbered, flows influent to nodes are counted positively, whereas flows effluent of nodes are counted negatively as far as \mathbf{A} is concerned. However, the opposite is the case for matrix $\tilde{\mathbf{C}}_s^T$, where source flows are counted positively if they are (as they should be) influent to the \mathfrak{J} inner nodes which is per definition effluent of the n_s source nodes. This notation may be considered unfortunate as it results in changing signs in the complete incidence matrix $\bar{\mathbf{A}} = [-\mathbf{A}^T \quad \tilde{\mathbf{C}}_s]^T$, but was kept in favor of consistency among publications.

Assumption 3.2 (Graph). *The graph representing the hydraulic network is connected and does not contain self-loops. Also, the network has at least one source node $n_s \geq 1$.*

Lemma 3.3. *Let Assumption 3.2 hold. Then, the incidence matrix has rank $(\bar{\mathbf{A}}) = n_j + n_s - 1$ as a result of Property 3.1.*

Proof. Suppose $\mathbf{x} \in \ker(\bar{\mathbf{A}}^T)$, meaning that $\mathbf{x} \in \mathbb{R}^{n_j+n_s}$ is in the left null space of $\bar{\mathbf{A}}$, that is $\mathbf{x}^T \bar{\mathbf{A}} = \mathbf{0}^T$. Given Property 3.1, $x_i - x_j = 0 \forall i, j \in \mathfrak{N}$ where x_i denotes the i -th entry in vector \mathbf{x} . Subsequently, the kernel of $\bar{\mathbf{A}}^T$ is at most one-dimensional. However, knowing that rows in $\bar{\mathbf{A}}$ are linearly dependent according to Property 3.1, it is evident that $\text{rank}(\bar{\mathbf{A}}) = n_j + n_s - 1$. ■

Corollary 3.4. *Given Property 3.1 and Lemma 3.3, matrix \mathbf{A} representing inner nodes \mathfrak{J} has full (row) rank $(\mathbf{A}) = n_j$ as $\mathfrak{S} \cap \mathfrak{J} = \{\}$. This requires that $n_s > 0$, a necessary condition for the solution of hydraulic network equations to exist.*

Also, Corollary 3.4 implies that $n_j \leq n_\ell$ the number of inner nodes n_j is smaller or equal to the number of pipes n_ℓ which is a direct consequence of $n_s > 0$. For further reading about graphs, reference [Bapat, 2014] is recommended.

3.1.2 Conservation of Energy

The head loss over a pipe must equal the difference in the nodal pressure heads when also considering the nodal elevation. For instance, when considering the left branch in figure 3.1, this means $h_{\text{loss},i}(Q_i) \stackrel{!}{=} (h_{k-1} + z_{k-1}) - (h_k + z_k)$. Applied to a whole network this results in

$$\mathbf{h}_{\text{loss}}(\mathbf{x}_Q) = \underbrace{\begin{bmatrix} -\mathbf{A}^T & \tilde{\mathbf{C}}_s \end{bmatrix}}_{\mathbf{A}^T} \begin{bmatrix} \mathbf{h} + \mathbf{z} \\ f\mathbf{h}_s \end{bmatrix}. \quad (3.4)$$

Remark 3.5. Without losing generality, it is assumed that source nodes are located at zero elevation $z_{k \in \mathfrak{S}} = 0$ in reference to the common datum. However, in case $\mathbf{z}_s \neq \mathbf{0}$, where $[\mathbf{z}_s]_i = z_{(n_j+i) \in \mathfrak{S}}$, one simply replaces \mathbf{h}_s with $\mathbf{h}_s + \mathbf{z}_s$ in the model equations.

For the network in figure 3.2, (3.4) becomes

$$\mathbf{h}_{\text{loss}}(\mathbf{x}_Q) = \begin{bmatrix} 1 & 1 & 0 & 0 & -1 \\ -1 & 0 & 1 & -1 & 0 \\ 0 & -1 & -1 & 1 & 0 \\ 0 & 0 & 0 & 0 & 1 \end{bmatrix}^T \begin{bmatrix} h_1 + z_1 \\ h_2 + z_2 \\ h_3 + z_3 \\ h_s \end{bmatrix} \quad (3.5)$$

where each entry in rows of (3.5) characterizes the difference in nodal heads.

Proposition 3.6. Let $\mathbf{S} \in \mathbb{Z}_{\{-1,0,1\}}^{n_c \times n_\ell}$ be the cycle (or loop) matrix, where n_c characterizes the number of linearly independent cycles in the directed network's graph. Then, \mathbf{S} is orthogonal to

$$\mathbf{S}\mathbf{A}^T = \mathbf{0} \quad (3.6)$$

the transposed incidence matrix \mathbf{A} as long as the graph does not have self-loops. (A Proof is provided in Appendix A and examples of \mathbf{S} , in reference to figure 3.2, are (3.20) and (3.22)).

Proposition 3.6 is equivalent to *Bernoulli's* principle, also called the principle of the *conservation of energy*, which says that there must be no difference in energy between two points in the network regardless of the path taken to connect these points.

$$\mathbf{S}\mathbf{h}_{\text{loss}}(\mathbf{x}_Q) \equiv \mathbf{S}\tilde{\mathbf{C}}_s\mathbf{h}_s \quad (3.7)$$

Regarding term $\mathbf{S}\tilde{\mathbf{C}}_s\mathbf{h}_s$ in (3.7), cycle matrix \mathbf{S} also accounts for linearly independent paths from one source to another such that the sum of head losses along those paths must equal the differences in source pressure heads \mathbf{h}_s , a consequence of source nodes \mathfrak{S} being excluded from \mathbf{A} in reference to (3.4) and (3.6). In literature (e.g. [Bhave, 1991]) the loops connecting different source nodes are denoted as so-called *pseudo-loops* yet there is no need to explicitly account for them in the determination of \mathbf{S} .

Also, important to note is that *Bernoulli's* principle, as it is defined here, only applies for the steady-state $d\mathbf{x}_Q/dt = \mathbf{0}$. When considering (3.7) as a direct consequence of (3.4) and (3.6), the transients $d\mathbf{x}_Q/dt$ also produce an equivalent pressure head loss, resulting in function $\mathbf{h}_{\text{loss}}(\mathbf{x}_Q)$ to be insufficient in describing the head loss in unsteady-state, referring to (3.4).

Remark 3.7. Generally, cycle matrices are not unique and can be linearly dependent when cycles are combined with each other.

However, uniqueness is obtained for the fundamental cycle matrix $\bar{\mathbf{S}} \in \mathbb{Z}_{\{-1,0,1\}}^{n_c \times n_\ell}$ which is expected to satisfy

$$\bar{\mathbf{S}} = \begin{bmatrix} \mathbf{I}_{n_c} & \bar{\mathbf{S}}_{n_\ell - n_c} \end{bmatrix} \quad (3.8)$$

where $\bar{\mathbf{S}}_{n_\ell - n_c} \in \mathbb{Z}_{\{-1,0,1\}}^{n_c \times (n_\ell - n_c)}$. It will be shown that the relation between \mathbf{S} and $\bar{\mathbf{S}}$ is provided by a linear transformation

$$\bar{\mathbf{S}} = \mathbf{S}\mathbf{T} \quad (3.9)$$

where $\mathbf{T} \in \mathbb{Z}_{\{-1,0,1\}}^{n_\ell \times n_\ell}$ has full rank n_ℓ and simply rearranges the numbering of flows Q_i . Actually, cycle matrix \mathbf{S} is not unique as a reason of \mathbf{T} being not unique.

3.1.3 Extraction of Cycle Matrix \mathbf{S} out of Incidence Matrix \mathbf{A}

It is arguably easier to first construct \mathbf{A} and $\tilde{\mathbf{C}}_s^T$ out of, for instance, GIS (geographical information system) data or data from EPANET [Lewis, 2000] by using the EPANET-MATLAB Toolkit [Eliades et al., 2016], and in a second step the cycle matrix if required.

The rearrangement or renumbering of flows is achieved by

$$\mathbf{T} = \begin{bmatrix} \mathbf{e}_{\bar{m}_1} & \mathbf{e}_{\bar{m}_2} & \dots & \mathbf{e}_{\bar{m}_{n_c}} & \mathbf{e}_{m_1} & \mathbf{e}_{m_2} & \dots & \mathbf{e}_{m_{n_\ell - n_c}} \end{bmatrix} \in \mathbb{Z}_{\{0,1\}}^{n_\ell \times n_\ell} \quad (3.10)$$

a matrix which comprises unity vectors in its columns. Indices of those unity vectors $\mathcal{M} = \{m_1, m_2, \dots, m_{n_\ell - n_c}\}$ and $\bar{\mathcal{M}} = \{\bar{m}_1, \bar{m}_2, \dots, \bar{m}_{n_c}\}$ satisfy $\mathcal{M} \cap \bar{\mathcal{M}} = \{\}$ and $\mathcal{M} \cup \bar{\mathcal{M}} = \mathfrak{P}$, where

$$\mathbf{T}_{\bar{t}} = \begin{bmatrix} \mathbf{e}_{\bar{m}_1} & \mathbf{e}_{\bar{m}_2} & \dots & \mathbf{e}_{\bar{m}_{n_c}} \end{bmatrix}, \quad \mathbf{T}_t = \begin{bmatrix} \mathbf{e}_{m_1} & \mathbf{e}_{m_2} & \dots & \mathbf{e}_{m_{n_\ell - n_c}} \end{bmatrix} \quad (3.11)$$

and thus $\mathbf{T} = [\mathbf{T}_{\bar{t}} \quad \mathbf{T}_t]$. According to properties of \mathcal{M} and $\bar{\mathcal{M}}$ it is clear that $\mathbf{T}\mathbf{T}^T = \mathbf{I}_{n_\ell}$ (Property 2.4 in section 2.2.3 for $\mathbf{R} = \mathbf{T}_t^T$, $\bar{\mathbf{R}} = \mathbf{T}_{\bar{t}}^T$, $\mathfrak{K} = \mathcal{M}$ and $\bar{\mathfrak{K}} = \bar{\mathcal{M}}$) while the renumbering of flows via \mathbf{T} applied on \mathbf{A}

$$\mathbf{A}\mathbf{T} = \begin{bmatrix} \mathbf{A}_{\bar{t}} & \mathbf{A}_t \end{bmatrix} \quad (3.12)$$

separates the incidence matrix into two parts $\mathbf{A}_{\bar{t}} \in \mathbb{Z}_{\{-1,0,1\}}^{n_j \times n_c}$ and $\mathbf{A}_t \in \mathbb{Z}_{\{-1,0,1\}}^{n_j \times (n_\ell - n_c)}$ according to (3.11). Knowing that the cycle matrix \mathbf{S} is orthogonal to \mathbf{A}^T (Proposition 3.6),

$$\mathbf{S}\mathbf{A}^T = \mathbf{S}\mathbf{T}\mathbf{T}^T\mathbf{A}^T = \begin{bmatrix} \mathbf{I} & \bar{\mathbf{S}}_{n_\ell - n_c} \end{bmatrix} \begin{bmatrix} \mathbf{A}_{\bar{t}}^T \\ \mathbf{A}_t^T \end{bmatrix} = \mathbf{0} \quad \Rightarrow \quad \mathbf{A}_{\bar{t}}^T + \bar{\mathbf{S}}_{n_\ell - n_c}\mathbf{A}_t^T = \mathbf{0} \quad (3.13)$$

it is evident that \mathbf{A}_t must be non-singular for the transformation to be feasible. As a consequence, the set \mathcal{M} associated with indices of unity vectors in \mathbf{T}_t (3.11) are chosen such that column vectors in $\mathbf{A}_t = [\mathbf{a}_{m_1} \quad \dots \quad \mathbf{a}_{m_{n_\ell - n_c}}]$ are linear independent, i.e.

$$\alpha_1\mathbf{a}_{m_1} + \alpha_2\mathbf{a}_{m_2} + \dots + \alpha_{n_\ell - n_c}\mathbf{a}_{m_{n_\ell - n_c}} = \mathbf{0} \quad (3.14)$$

if and only if $\alpha_1 = \alpha_2 = \dots = \alpha_{n_\ell - n_c} = 0$. Hence, this transformation actually separates an invertible part \mathbf{A}_t from a non-invertible one $\mathbf{A}_{\bar{t}}$ regarding the column vectors of \mathbf{A} .

Corollary 3.8. *As direct consequence of $\text{rank}(\mathbf{A}) = n_j$ according to Corollary 3.4, it is clear that cycle matrix \mathbf{S} has precisely $n_c = n_\ell - n_j$ independent (fundamental) cycles (rows) and is obtained by*

$$\mathbf{S} = \begin{bmatrix} \mathbf{I}_{n_\ell - n_j} & -\left(\mathbf{A}_t^{-1}\mathbf{A}_{\bar{t}}\right)^T \end{bmatrix} \mathbf{T}^T \quad (3.15)$$

reformulating (3.13) such that $\bar{\mathbf{S}}_{n_\ell - n_c} = -\left(\mathbf{A}_t^{-1}\mathbf{A}_{\bar{t}}\right)^T$. As a result of (3.9) and (3.10) $\bar{\mathbf{S}} = \mathbf{S}\mathbf{T} \Rightarrow \mathbf{S} = \bar{\mathbf{S}}\mathbf{T}^T$, i.e. the multiplication with \mathbf{T}^T provides the same numbering of flows as in \mathbf{A} .

Emphasizing on the utilization on not unique indices \mathcal{M} and thus $\bar{\mathcal{M}}$, one just needs to find **one** order in which the columns \mathbf{a}_i for $i \in \mathcal{M}$ are linearly independent as in (3.14). The order in which these n_j independent column vectors are arranged in \mathbf{A}_t is completely irrelevant as a consequence of the possibility to number flows arbitrarily. This is the reason why the transformation matrix \mathbf{T} is not unique when assuming that the incidence matrix \mathbf{A} is not required to have a standardized form (see [Bapat, 2014]). A hint for implementation when using MATLAB, a QR decomposition by means of the qr command can be helpful in this regard.

In this context of the transformation (3.12), \mathbf{A}_t is usually associated with the tree and $\mathbf{A}_{\bar{t}}$ with the co-tree of the network's graph.

Definition 3.9 (Tree and Co-Tree Flow). *The subset of \mathbf{x}_Q*

$$\mathbf{x}_t = \mathbf{T}_t^T \mathbf{x}_Q \quad \Rightarrow \quad [\mathbf{x}_t]_i = [\mathbf{x}_Q]_{m_i} \quad \forall i = 1, \dots, n_j \quad (3.16a)$$

denoted by \mathbf{x}_t is defined as **tree flow** in the hydraulic network and, effectively, corresponds with subset \mathcal{M} of n_j linearly independent columns in \mathbf{A} . The complementary entries in \mathbf{x}_Q

$$\mathbf{x}_{\bar{t}} = \mathbf{T}_{\bar{t}}^T \mathbf{x}_Q \quad \Rightarrow \quad [\mathbf{x}_{\bar{t}}]_i = [\mathbf{x}_Q]_{\bar{m}_i} \quad \forall i = 1, \dots, n_c = n_\ell - n_j \quad (3.16b)$$

denoted by $\mathbf{x}_{\bar{t}}$ are associated with the **co-tree flow** and correspond with $n_\ell - n_j$ linearly dependent columns in \mathbf{A} .

Two-Cycle Network Example. To put it into perspective, the network with $n_\ell - n_j = 2$ cycles in figure 3.2 is considered. For instance, one selects the following columns in \mathbf{A}

$$\mathbf{A} = \begin{bmatrix} m_1=1 & m_2=2 & \bar{m}_1=3 & \bar{m}_2=4 & m_3=5 \\ -1 & -1 & 0 & 0 & 1 \\ 1 & 0 & -1 & 1 & 0 \\ 0 & 1 & 1 & -1 & 0 \end{bmatrix} = [\mathbf{a}_1 \quad \dots \quad \mathbf{a}_5] \quad (3.17)$$

knowing that

$$\alpha_1 \mathbf{a}_{m_1} + \alpha_2 \mathbf{a}_{m_2} + \alpha_3 \mathbf{a}_{m_3} = \mathbf{0} \quad (3.18)$$

if and only if $\alpha_1 = \alpha_2 = \alpha_3 = 0$. Then, the transformation matrix comprises

$$\mathbf{T}_{\bar{t}} = [\mathbf{e}_{\bar{m}_1} \quad \mathbf{e}_{\bar{m}_2}] = \begin{bmatrix} 0 & 0 \\ 0 & 0 \\ 1 & 0 \\ 0 & 1 \\ 0 & 0 \end{bmatrix} \quad \text{and} \quad \mathbf{T}_t = [\mathbf{e}_{m_1} \quad \mathbf{e}_{m_2} \quad \mathbf{e}_{m_3}] = \begin{bmatrix} 1 & 0 & 0 \\ 0 & 1 & 0 \\ 0 & 0 & 0 \\ 0 & 0 & 0 \\ 0 & 0 & 1 \end{bmatrix} \quad (3.19)$$

such that $\mathbf{T} = [\mathbf{T}_{\bar{t}} \quad \mathbf{T}_t]$. According to (3.15) (Corollary 3.8), the cycle matrix \mathbf{S} is obtained by

$$\mathbf{S} = [\mathbf{I}_{n_\ell - n_j} \quad -((\mathbf{A}\mathbf{T}_t)^{-1} \mathbf{A}\mathbf{T}_{\bar{t}})^T] \mathbf{T}^T = \begin{bmatrix} 1 & -1 & 1 & 0 & 0 \\ -1 & 1 & 0 & 1 & 0 \end{bmatrix} \quad (3.20)$$

which can be verified by analyzing the network in figure 3.2. However, when selecting different columns in \mathbf{A} , for instance

$$\mathbf{A} = \begin{bmatrix} m_1=1 & \bar{m}_1=2 & m_2=3 & \bar{m}_2=4 & m_3=5 \\ -1 & -1 & 0 & 0 & 1 \\ 1 & 0 & -1 & 1 & 0 \\ 0 & 1 & 1 & -1 & 0 \end{bmatrix}, \quad (3.21)$$

where $\mathbf{A}_t = \mathbf{A}\mathbf{T}_t = [\mathbf{a}_1 \quad \mathbf{a}_3 \quad \mathbf{a}_5]$ is also invertible, one receives ($\mathbf{A}_{\bar{t}} = \mathbf{A}\mathbf{T}_{\bar{t}}$)

$$\mathbf{S} = [\mathbf{I}_{n_\ell - n_j} \quad -(\mathbf{A}_t^{-1} \mathbf{A}_{\bar{t}})^T] \mathbf{T}^T = \begin{bmatrix} -1 & 1 & -1 & 0 & 0 \\ 0 & 0 & 1 & 1 & 0 \end{bmatrix} \quad (3.22)$$

which is a feasible choice too. Verify the two choices of \mathbf{S} in (3.20) and (3.22) by means of analyzing the network in figure 3.2. In reference to Remark 3.7, the cycle matrix is not unique since there is no need for the transformation to be unique. Nevertheless, once feasible indices $\mathcal{M} = \{m_1, \dots, m_{n_j}\}$ and $\bar{\mathcal{M}} = \{\bar{m}_1, \dots, \bar{m}_{n_\ell - n_j}\}$ are selected, \mathbf{T} and thus \mathbf{S} are uniquely specified.

3.1.4 Network Model

The number of equations in order to obtain a unique solution is the same as, for instance, for an electric network of linear resistors. In contrast, however, the number of (inner) nodal and independent cycle equations $n_j + n_c = n_\ell$ must be solved iteratively for hydraulic networks as the laws of flow resistance are, in general, nonlinear (see section 2.1.4). Interestingly, the number of equations to solve is equivalent to the number of pipes n_ℓ . For instance, the formulation

$$\Gamma : \begin{cases} \mathbf{A}\mathbf{x}_Q = \bar{\mathbf{q}} & (3.23a) \\ \mathbf{S}\mathbf{h}_{\text{loss}}(\mathbf{x}_Q) = \mathbf{S}\tilde{\mathbf{C}}_s\mathbf{h}_s & (3.23b) \end{cases}$$

solves the hydraulic network for flows \mathbf{x}_Q . Considering (3.23b) with $\mathbf{S} \in \mathbb{Z}_{\{-1,0,1\}}^{(n_\ell - n_j) \times n_\ell}$, where $n_\ell > n_j$ as $n_s > 0$, $\tilde{\mathbf{C}}_s\mathbf{h}_s - \mathbf{h}_{\text{loss}}(\mathbf{x}_Q)$ must be expressible within the kernel of \mathbf{S} which is spanned by \mathbf{A}^T , as $\mathbf{S}\mathbf{A}^T = \mathbf{0}$ according to Proposition 3.6. Subsequently, it is apparent that there exists an $\boldsymbol{\alpha} \in \mathbb{R}^{n_\ell}$ for which $\mathbf{A}^T\boldsymbol{\alpha} = \tilde{\mathbf{C}}_s\mathbf{h}_s - \mathbf{h}_{\text{loss}}(\mathbf{x}_Q)$. This parameter $\boldsymbol{\alpha}$ thereby represents the nodal heads $\boldsymbol{\alpha} = (\mathbf{h} + \mathbf{z})$ according to (3.4). As a consequence, the formulation

$$\Gamma_h : \begin{cases} \mathbf{A}\mathbf{x}_Q = \bar{\mathbf{q}} & (3.24a) \\ \mathbf{A}^T(\mathbf{h} + \mathbf{z}) = \tilde{\mathbf{C}}_s\mathbf{h}_s - \mathbf{h}_{\text{loss}}(\mathbf{x}_Q) & (3.24b) \end{cases}$$

as it was proposed, e.g. by Todini and Pilati [1987], is equivalent to (3.23), however it requires to solve an equation system with $n_\ell + n_j$ unknowns (namely \mathbf{h} and \mathbf{x}_Q) instead of n_ℓ unknowns in (3.23). Todini and Rossman [2013] give a broad overview of different implementations of Γ and Γ_h and then apply the *Newton-Raphson* algorithm.

Physical Considerations. Apart from differences in source pressures, referring to Γ (3.23), there are two essential parameters which determine the flow distribution in the network's topology, the nodal consumption $\bar{\mathbf{q}}$ and the friction coefficients (roughness and minor loss values). In case the network completely lacks loops/cycles, however, the friction losses and \mathbf{h}_s are irrelevant (provided the consumption is known), \mathbf{A} would be square and (3.23a) could be inverted. This is fortunately not the case for a real drinking water network, as all consecutive consumers would be cut off at a pipe burst when the network would be set up like a tree. Cycles are an integral part of water networks, providing some redundancy to the distribution.

Network equations Γ (3.23) and Γ_h (3.24) utilize a so-called **demand-driven** consumption and require that the consumption is known to a sufficient level of accuracy. Although this assumption is sometimes feasible, it is not always realistic. It implies that the nodal consumption $\bar{\mathbf{q}}$ is always subtracted from the respective nodes, even if there is not enough pressure to satisfy this consumption. As a result, nodal pressure heads frequently become negative when the considered demand is too high, a rather common experience in, e.g., EPANET Lewis [2000]. However, this is nonsense from a physical perspective. To overcome this problem, there exist various different approaches implementing a **pressure-driven** consumption for the steady-state, e.g. see Giustolisi et al. [2008]; Fujiwara and Li [1998]; Muranho et al. [2014]; Jung et al. [2009]. The implementation, as proposed e.g. by Giustolisi et al. [2008], which reduces the consumption proportionally to the pressure if it can not satisfy the specified $\bar{\mathbf{q}}$, requires an iterative formulation and thereby encounters difficulties. Nevertheless, Piller et al. [2003] prove the solution's uniqueness in this context.

Laminar Network. Suppose all minor loss coefficients are zero $\mathbf{k}_m = \mathbf{0}$ (as they are often neglected), meaning that $\mathbf{h}_{\text{loss}} = \Delta\mathbf{h}_{\text{DW}}$, and the flow is so low that every pipe would be in the laminar regime $Re \leq 2000$ (which is actually never the case). Then, the minimal set of equations

(3.23) becomes linear

$$\begin{bmatrix} \mathbf{A} \\ \mathbf{S} \operatorname{diag}(\bar{\mathbf{w}}) \end{bmatrix} \mathbf{x}_Q = \begin{bmatrix} \bar{\mathbf{q}} \\ \mathbf{S} \tilde{\mathbf{C}}_s \mathbf{h}_s \end{bmatrix} \quad (3.25)$$

considering $[\bar{\mathbf{w}}]_i = 32 \frac{\eta}{\rho} \frac{l_i}{d_i^2 g A_i}$ for all $i \in \mathfrak{P}$ which is obtained when applying (2.3), (2.4) and (2.5). This is an interesting yet primarily academic observation as the flow in pressurized water networks is mostly turbulent [Walski et al., 2003, p. 28], except in the periphery of the network. In a looped network it may also occur that due to a specific consumption-configuration, pressure levels at two adjacent nodes are almost identical which may also lead to laminar flow.

3.1.5 Uniqueness and Solvability

This section is solely dedicated to shed some light on the uniqueness and solvability of the steady-state hydraulic network description. One of the first notes about a proof in context of water networks goes back to Pilati and Todini [1984] mentioned in the paper of Todini and Pilati [1987]. This publication (1984) is written in Italian and hardly accessible today.

Assumption 3.10. *Friction function $\mathbf{h}_{\text{loss}}(\mathbf{x}_Q)$ is strictly monotonically increasing, continuous and at least once continuously differentiable. It further satisfies $\mathbf{h}_{\text{loss}}(\mathbf{0}) = \mathbf{0}$ at the zero point.*

Considering the definition of losses due to friction at the pipe's inner surface (2.4) (*Darcy Weisbach*) and minor losses (2.9), it is clear that zero flow does cause zero head loss $\mathbf{h}_{\text{loss}}(\mathbf{0}) = \mathbf{0}$. Since the *Darcy Weisbach* relation becomes linear (with a slope greater zero $\bar{\mathbf{w}} > \mathbf{0}$ (3.25)) in the laminar regime, it is also evident that the function is strictly monotonically increasing as well as continuously differentiable (in the laminar regime).

Proposition 3.11. *Friction function $\Delta h_{\text{DW}}(Q)$ (2.4) applying friction factor λ_{DW} according to Colebrook-White (2.6) is strictly monotonically increasing for $Q \neq 0$ and thus for the turbulent regime, where $Re \geq 4000$. (A Proof is provided in Appendix B)*

Given Proposition 3.11 it is apparent that $\mathbf{h}_{\text{loss}}(\mathbf{x}_Q)$ is also monotonically increasing in the turbulent regime as minor coefficients are always non-negative $\mathbf{k}_m \geq \mathbf{0}$. While also knowing that $\mathbf{h}_{\text{loss}}(\mathbf{x}_Q)$ is continuous in the laminar and turbulent (see Appendix B) regime, a smooth and continuous description in the transitional area is required.

Proposition 3.12. *Let Assumption 3.2 and 3.10 hold. Then, the network formulation as in (3.23) with inner nodal and independent cycle equations $n_j + n_c = n_\ell$ is sufficient to obtain a unique solution for the steady-state hydraulic network.*

Proof. Utilizing the same separation (3.12) of \mathbf{A} as before $\mathbf{A}\mathbf{T} = [\mathbf{A}_{\bar{t}} \quad \mathbf{A}_t]$ where $\mathbf{T} = [\mathbf{T}_{\bar{t}} \quad \mathbf{T}_t]$ in reference to (3.10), flows are simply renumbered according to indices $\mathcal{M} = \{m_1, \dots, m_{n_j}\} \subseteq \mathfrak{P}$ and $\bar{\mathcal{M}} = \{\bar{m}_1, \dots, \bar{m}_{n_\ell - n_j}\} \subseteq \mathfrak{P}$. Knowing that $\mathbf{T}\mathbf{T}^T = \mathbf{I}_{n_\ell}$, (3.23a) becomes

$$\mathbf{A}\mathbf{x}_Q = \begin{bmatrix} \mathbf{A}_{\bar{t}} & \mathbf{A}_t \end{bmatrix} \begin{bmatrix} \mathbf{T}_{\bar{t}}^T \\ \mathbf{T}_t^T \end{bmatrix} \mathbf{x}_Q = \mathbf{A}_{\bar{t}}\mathbf{x}_{\bar{t}} + \mathbf{A}_t\mathbf{x}_t = \bar{\mathbf{q}}. \quad (3.26)$$

Knowing that $\mathbf{x}_Q = \mathbf{T}_{\bar{t}}\mathbf{x}_{\bar{t}} + \mathbf{T}_t\mathbf{x}_t$ while applying (3.11) to (3.16b), the flow vector \mathbf{x}_Q

$$\mathbf{x}_t = \mathbf{A}_t^{-1}(\bar{\mathbf{q}} - \mathbf{A}_{\bar{t}}\mathbf{x}_{\bar{t}}) \quad \Rightarrow \quad \mathbf{x}_Q = \underbrace{(\mathbf{T}_{\bar{t}} - \mathbf{T}_t\mathbf{A}_t^{-1}\mathbf{A}_{\bar{t}})}_{\mathbf{S}^T} \mathbf{x}_{\bar{t}} + \mathbf{T}_t\mathbf{A}_t^{-1}\bar{\mathbf{q}} \quad (3.27)$$

can be expressed by the co-tree flow $\mathbf{x}_{\bar{t}}$ and the nodal consumption $\bar{\mathbf{q}}$, where $\mathbf{T}_{\bar{t}} - \mathbf{T}_t\mathbf{A}_t^{-1}\mathbf{A}_{\bar{t}} = \mathbf{S}^T$ according to Corollary 3.8. Considering the network formulation (3.23), the equation system is reduced to

$$\mathbf{S}\mathbf{h}_{\text{loss}}\left(\mathbf{S}^T\mathbf{x}_{\bar{t}} + \mathbf{T}_t\mathbf{A}_t^{-1}\bar{\mathbf{q}}\right) - \mathbf{S}\tilde{\mathbf{C}}_s\mathbf{h}_s = \mathbf{0} \quad (3.28)$$

with $n_\ell - n_j$ cycle equations and $n_\ell - n_j$ unknown co-tree flows $\mathbf{x}_{\bar{t}}$ which appear in the argument of function $\mathbf{h}_{\text{loss}}(\mathbf{x}_Q(\mathbf{x}_{\bar{t}}))$. According to the variational principle (cf. Piller and Propato [2006]), formulation (3.28) is equivalent to the optimal solution of the optimization problem

$$\begin{aligned} \min_{\mathbf{x}_{\bar{t}}} \quad & \sum_{i=1}^{n_\ell} \int_0^{Q_i} h_{\text{loss}_i}(\xi_i) d\xi_i - \mathbf{x}_Q^T \tilde{\mathbf{C}}_s \mathbf{h}_s = \min_{\mathbf{x}_{\bar{t}}} f(\mathbf{x}_{\bar{t}}) \\ \text{s.t.} \quad & \mathbf{x}_Q = \mathbf{S}^T \mathbf{x}_{\bar{t}} + \mathbf{T}_t \mathbf{A}_t^{-1} \bar{\mathbf{q}} \end{aligned} \quad (3.29)$$

which is proportional to the total energy required to satisfy specified nodal demands $\bar{\mathbf{q}}$. The optimization problem, similar to (3.29), was first proposed by Collins et al. [1978] and then used by, e.g., Piller and Propato [2006] and Piller et al. [2003]. Then, the gradient of the objective function equals (3.28), i.e.

$$\nabla f(\mathbf{x}_{\bar{t}}) = \left(\frac{\partial f}{\partial \mathbf{x}_Q} \quad \frac{\partial f}{\partial \mathbf{x}_{\bar{t}}} \right)^T = \mathbf{S} \mathbf{h}_{\text{loss}}(\mathbf{x}_Q) - \mathbf{S} \tilde{\mathbf{C}}_s \mathbf{h}_s \stackrel{!}{=} \mathbf{0}. \quad (3.30)$$

As \mathbf{x}_Q is expected to solve (3.30), it is stationary point of the objective function $f(\mathbf{x}_{\bar{t}})$. Denoting $\mathbf{D} = \frac{\partial \mathbf{h}_{\text{loss}}}{\partial \mathbf{x}_Q}$ which is a diagonal matrix where $[\mathbf{D}]_{ii} = \frac{dh_{\text{loss},i}}{dQ_i} > 0$ for all Q_i and $i \in \mathfrak{B}$ as function $\mathbf{h}_{\text{loss}}(\cdot)$ is expected to be strictly monotonically increasing, the *Hessian* matrix

$$\nabla^2 f(\mathbf{x}_{\bar{t}}) = \mathbf{S} \mathbf{D}(\mathbf{x}_Q) \mathbf{S}^T \succ 0 \quad \forall \mathbf{x}_Q \in \mathbb{R}^{n_\ell} \quad (3.31)$$

is globally positive definite as $\mathbf{S} \in \mathbb{Z}_{\{-1,0,1\}}^{(n_\ell - n_j) \times n_\ell}$ has full rank (see Proposition 3.6). The optimality conditions are complete, objective function $f(\mathbf{x}_{\bar{t}})$ of optimization problem (3.29) is strictly convex. This is the result of the *Hessian* matrix $\mathbf{S} \mathbf{D}(\mathbf{x}_Q) \mathbf{S}^T$ (3.31) of $f(\mathbf{x}_{\bar{t}})$ being positive definite for all $\mathbf{x}_Q \in \mathbb{R}^{n_\ell}$ (see e.g. [Beck, 2014, Theorem 7.13]). Subsequently, \mathbf{x}_Q is the global minimum of (3.29) and thus unique solution of (3.28) and subsequently (3.23) and (3.24). ■

Remark 3.13. *Since the optimality condition for strict convexity concerning the Hessian (3.31) is sufficient only, Proposition 3.12 does actually hold for monotonically increasing $\mathbf{h}_{\text{loss}}(\cdot)$ also, referring to Assumption 3.10. This is the result of Piller [1995] which utilizes a modification of $f(\mathbf{x}_{\bar{t}})$ in the vicinity of zero.*

Note that Piller et al. [2003] (see also Piller and Propato [2006]) proves uniqueness of the pressure-driven equations, where the nodal consumption $\bar{\mathbf{q}}$ is expressed as a function on the nodal pressure \mathbf{h} such that $\bar{\mathbf{q}}(\mathbf{h})$. Analogous to the $\mathbf{h}_{\text{loss}}(\cdot)$, the k -th component of function $q_k = q_k(h_k)$ for $k \in \mathfrak{J}$ also solely depends on k -th nodal pressure head h_k .

Actually, convexity allows the set of nonlinear equations $\mathbf{\Gamma}$ (3.23) and $\mathbf{\Gamma}_h$ (3.24) to be solved for large problems. A water distribution network with several thousand nodes and pipes might otherwise never converge.

Strictly speaking, the solution's uniqueness can only be guaranteed if a smooth and continuous description of the transitional pressure head loss in the transitional regime $2000 < Re < 4000$ is found. In this strict context, the expression (2.8) is only, if at all, suitable if the *Swamee-Jain* equation (2.7) is utilized for the turbulent regime. In practice, however, it turned out that (2.8) in combination with *Colebrook-White* (2.6) leads to very reasonable results, which are slightly different to the one when applying *Swamee-Jain* (2.7) in the turbulent regime. Nevertheless, these differences are in the majority of cases so small that they presumably are within the uncertainty band of pressure and flow sensors with standard-accuracy.

Besides, the flow through the network follows the path of least action, where the least energy is spent. In a looped network, where there is, e.g., only one percent error at the first junction, the error possibly accumulates at the consecutive junctions. Also, knowing that laws of pressure head loss are nonlinear, one percent error in the head loss, may lead to more distinct deviation in the flow.

3.2 Full Transient Equations

In this section a brief introduction of the full transient or elastic modeling approach is given which then also serves as basis for the derivation of the *rigid water column* theory. For more background information, references [Chaudhry, 2014; Wylie and Streeter, 1978; Fox, 1977; Larock et al., 1999] are recommended.

Regarding figure 3.3, the forces acting on a fluid moving with velocity v in an inclined yet infinitesimal small volume with length Δs , cross section area ΔA and diameter D is considered.

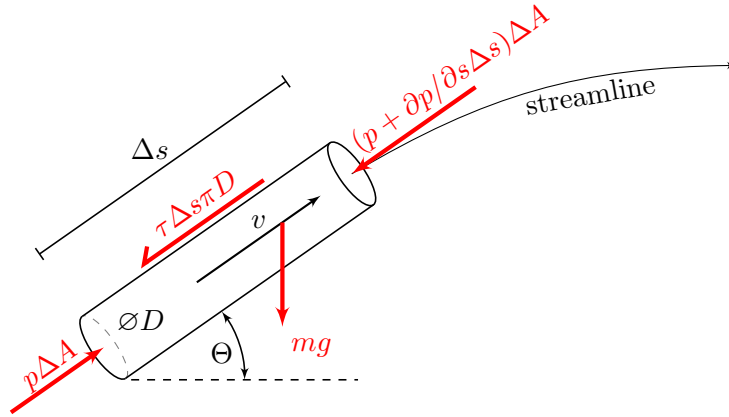


FIGURE 3.3: Forces acting on a fluid in an inclined, infinitesimal small pipe segment (c.f. [Larock et al., 1999, Figure 7.4]).

Pressure $p + \frac{\partial p}{\partial s} \Delta s$, acting against the streamline in figure 3.3, is obtained by a *Taylor* series which is truncated after the linear term, a feasible procedure as only an infinitesimal small volume is considered. The balance of forces according to *Newton's* second law of motion is the starting point:

$$m \frac{dv}{dt} = p\Delta A - \left(p + \frac{\partial p}{\partial s} \Delta s \right) \Delta A - mg \sin(\Theta) - \tau \Delta s \pi D \quad (3.32)$$

The force $p\Delta A$ accelerates the fluid upstream, whereas the opponent $\left(p + \frac{\partial p}{\partial s} \Delta s \right) \Delta A$, gravity $mg \sin(\Theta)$ and friction along the pipe surface $\tau \Delta s \pi D$ are acting against the fluid's acceleration, hence against the total derivative of the velocity $\frac{dv}{dt}$. Gravity equals mass $m = \rho \Delta A \Delta s$ times the constant gravitational acceleration g . Initially, $\frac{\Delta s}{mg} = \frac{1}{g\rho\Delta A}$ is multiplied to equation (3.32).

$$\frac{\Delta s}{g} \frac{dv}{dt} = - \frac{\partial p}{\partial s} \frac{\Delta s}{g\rho} - \underbrace{\tau \frac{D\pi\Delta s}{g\rho\Delta A}}_{\rightarrow \Delta h_{DW}} - \Delta s \sin(\Theta) \quad (3.33)$$

Elastic Approach. As the fluid's velocity $v = v(t, s)$ can be interpreted as a function on time t and space s , whereas space in turn is considered to be a function on time $v(t, s) = v(t, s(t))$, the total derivative reads as

$$\frac{dv}{dt} = \frac{\partial v}{\partial t} + \frac{\partial v}{\partial s} \frac{\partial s}{\partial t} \quad \text{where} \quad v = \frac{\partial s}{\partial t} . \quad (3.34)$$

Expanding the infinitesimal small volume to that of the entire pipe by simply replacing Δs with the pipe's length l , ΔA with the real cross section A and D by d , the expression including shear stress τ is replaced by the *Darcy-Weisbach* equation. Actually, one would also need to account for the unsteady-state component of friction which is not mentioned here (see Chaudhry [2014]). Knowing that $\Delta h_{DW} = \lambda_{DW} \frac{l}{2dg} v|v|$ (2.4), (3.33) yields the *Momentum* equation [Chaudhry,

2014]

$$\frac{\partial v}{\partial t} + v \frac{\partial v}{\partial s} + \frac{\partial p}{\partial s} \frac{1}{\rho} + g \sin \Theta + \lambda_{\text{DW}}(v) \frac{v|v|}{2d} = 0. \quad (3.35)$$

The density is often considered in the derivative $\frac{\partial p}{\partial s} \frac{1}{\rho} \approx \frac{\partial h}{\partial s} \frac{1}{g}$ assuming that the fluid is only slightly compressible and the conduit walls only slightly deformable. However, one accounts for variations in ρ and A by considering the wave velocity a_v to be finite which itself appears in the so-called *Continuity* equation (an elastic version of the conservation of mass)

$$\frac{\partial p}{\partial t} + v \frac{\partial p}{\partial x} + \rho a_v^2 \frac{\partial v}{\partial x} = 0. \quad (3.36)$$

A derivation of (3.36) is provided, e.g., in Chaudhry [2014]. In the majority of engineering applications, the convective acceleration terms $v \partial p / \partial s$ and $v \partial v / \partial s$ are neglected [Chaudhry, 2014] leading to (by taking (3.35) and (3.36))

$$\frac{\partial h}{\partial t} + \frac{a_v^2}{gA} \frac{\partial Q}{\partial x} = 0 \quad (3.37a)$$

$$\frac{\partial Q}{\partial t} + gA \frac{\partial h}{\partial s} + \lambda_{\text{DW}}(Q) \frac{Q|Q|}{2dA} + gA \sin \Theta = 0 \quad (3.37b)$$

considering that $Q = vA$ and $p = g\rho h$.

Network Hydraulics: A Dynamic Yet Rigid Approach

‘Now that computers are available, a very great improvement has been made to the quality of analytic techniques that can be used and it is no longer necessary to confine the mathematical modeling of a network to that of steady state.’

– J. A. Fox, *Hydraulic Analysis of Unsteady Flow in Pipe Networks*, 1977

More than 40 years later the situation has not changed much though, a sign of poor progress in this area, especially considering the progress made in computation and semiconductors. The sheer size of supply networks makes the solving of large sets of nonlinear equations, aside from the physical perspective, a matter of convergence. The industry, however, caught up in part as several software packages (look for e.g. WANDA, KYPIPE, HIDRA) provide transient simulation capabilities, though, they are radically limited in network size and complexity. Also, the mentioned simulation tools are not open-source and usually come with considerable license costs and thus often aggravate or even prohibit further development. If resources are spent on the modification and development of open-source software like EPANET, which is arguably considered as industry standard, development might be accelerated substantially. EPANET, first published in 1993, was developed with the help of public funding by the United States *Environmental Protection Agency* which is faced with severe cost cutting under the recent administration.

In the opinion of the author, the right spot for a new generation of simulation software is based on a model which accounts for some sort of pressure-driven consumption but also for slow transients. Avoiding the complexity needed within partial differential equations as in (3.37), a model which assumes the water to be incompressible reduces the computational effort for larger networks to an extent, which may make it manageable for today’s standard computers. Interestingly, this spot arguably is also the right one for the basis of a model-based control design, possibly applying observer-based methods for monitoring, holistic control methods for control valves and, perhaps, fault detection and isolation methods for leaks.

The content of the publication [Kaltenbacher et al., 2017] was largely used among other things in section 4.2 and 4.3, whereas the content of [Kaltenbacher et al., 2018] was used in part in section 4.4 and 4.5 of this chapter.

4.1 Rigid Water Column Theory

The mentioned modeling approach in question is known under the so-called *rigid water column* theory which will be the major subject for further analysis in this chapter. The confinement to ordinary differential equations (ODEs) within this theory was also an important selection criterion as it may also be the right choice for a model-based control design.

The starting point of this consideration is figure 3.3 depicting the forces acting on a fluid in an infinitesimal small volume as part of a pipe. *Newton's* second law of motion is applied and summarized in (3.32) and modified in (3.33). Concerning (3.33), the constant slope of the pipe's inclination $\sin(\Theta) = \frac{\partial z}{\partial s}$ is replaced by the appropriate derivative, including elevation $z(s)$. Then, pressure p is replaced by the pressure head h considering the fluid's specific weight $\rho g = p/h$ while dividing (3.33) by Δs .

$$\frac{1}{g} \frac{dv}{dt} = -\frac{\partial h}{\partial s} - \frac{\partial z}{\partial s} - \underbrace{\tau \frac{D\pi\Delta s}{g\rho\Delta A}}_{\rightarrow \Delta h_{\text{DW}}} \frac{1}{\Delta s} \quad (4.1)$$

However, by considering the density inside the derivative of $\partial p/\partial s$, ρ is treated as constant along Δs , also assuming that wave velocity is infinite (in contrast to (3.37a)). This simplification depicts the major difference between the rigid and the elastic approach. Now, the infinitesimal small control volume in figure 3.3 is expanded to that of a pipe by replacing Δs with the pipe's length l , ΔA with A and D by d .

$$\frac{1}{g} \frac{dv}{dt} = -\frac{\partial h}{\partial s} - \frac{\partial z}{\partial s} - \frac{\Delta h_{\text{DW}}(v)}{l} \quad (4.2)$$

Also, if it is assumed that the cross section area over the considered pipe section does not vary, it is feasible to substitute velocity v with the flow Q by pulling A out of the time derivative on the left hand side of equation (4.2). The final form of the elementary equation describing the incompressible flow behavior through the conduit can be obtained when integrating equation (4.2) over the length l of the pipe

$$\frac{l}{gA} \frac{dQ}{dt} = (h+z)|_{s=0} - (h+z)|_{s=l} - \lambda_{\text{DW}} \frac{l|Q|Q}{2dgA^2} \quad (4.3)$$

and thereby forcing the flow Q to remain constant over l .

Physical Considerations. By using the rigid column theory, the water inside a pipe is very much treated as a solid body, which itself consists of particles. When a force is acting on one side of the body and thereby on the first layer of particles, it will be transferred to adjacent layers of particles successively, until it reaches the other end of the body. In reality, the velocity of this force propagating through the body will be finite, especially in fluids but even in solid bodies. As in the description of Fox [1977], "*most bodies are not sufficiently long for the wave of compressive stress to be in any way significant but the effect is always present*".

Concluding, if the stress or pressure wave propagating through a pipe is considerably fast, whereas the length of the segment relatively small, the rigid column theory is capable of describing such motions sufficiently accurate. For instance, considering the high speed of sound in water ~ 1500 m/s [Cutnell and Johnson, 2012] (which varies with pipe parameters) in a single pipe, a total length of about 150 m is needed to possibly see any deviations due to the pressure propagation with a sampling time of 0.1s. However, as the wave is reflected in other parts of the network it travels back and forth while its amplitude gradually attenuates.

4.2 Network Formulation

Using the rigid column approach as a basis for network formulations is nothing revolutionary, yet its application can hardly be considered popular. To this point in time, there is no common convention on how to efficiently combine network and differential equations. However, Japanese colleagues early pushed the development towards a common network formulation [Onizuka, 1986; Shimada, 1989, 1993] which also attracted control applications as in Kumar et al. [2009] and

even led to the attempt to explore the application of H_∞ control [Terra et al., 2002]. Also, Ivanov and Bournaski [1996] early proposed using the ODEs for more complex networks as well as Axworthy [1997] made efforts towards a systematic network approach in his PhD thesis.

Nevertheless, these efforts were not broadly pursued, the results of *Onizuka* and *Shimada* were not addressed in any popular books (at least with English translation) dealing with hydraulics as far as the author is aware. For instance, as in *Hydraulics of Pipeline Systems* (1999) [Larock et al., 1999], appropriate sections seem to be extensions of [Watters, 1979] in *Modern Analysis and Control of Unsteady Flow in Pipelines*. There, the formulation within *algebraic differential equations* makes the solving of large networks somewhat complicated. Even more recently [Boulos et al., 2006], the attempt to use cycle equations to combine the flows' ODEs (4.3), presumably analogous to the *Loop Method* mentioned in Onizuka [1986], seems to be impractical.

Network Equations. The same notation as for the steady-state is applied (see section 3.1). Introducing

$$\mathbf{c}_l = g \left[\frac{A_1}{l_1} \quad \dots \quad \frac{A_{n_\ell}}{l_{n_\ell}} \right]^T \in \mathbb{R}_{>0}^{n_\ell} \quad (4.4)$$

the networks' ODEs can already be specified (in reference to (4.3) and section 3.1.2)

$$\frac{d\mathbf{x}_Q}{dt} = \text{diag}(\mathbf{c}_l) \left(\tilde{\mathbf{C}}_s \mathbf{h}_s - \mathbf{A}^T (\mathbf{h} + \mathbf{z}) - \mathbf{h}_{\text{loss}}(\mathbf{x}_Q) \right) \quad (4.5)$$

where friction function $\mathbf{h}_{\text{loss}}(\mathbf{x}_Q) = \Delta \mathbf{h}_{\text{DW}}(\mathbf{x}_Q) + \Delta \mathbf{h}_m(\mathbf{x}_Q)$ also accounts for minor losses in addition to friction at the inner pipe's surface and viscosity-effects. The conservation of mass (same as in steady state, see section 3.1.1) is utilized to calculate nodal pressure heads \mathbf{h} which are still unknown in (4.5). When differentiating the nodal *Kirchhoff* equations $\mathbf{A}\mathbf{x}_Q = \bar{\mathbf{q}}$ with respect to time, ODEs (4.5) can be inserted. The result is then inverted in terms of nodal heads $\mathbf{h} + \mathbf{z}$ yielding

$$\mathbf{h} + \mathbf{z} = \left(\mathbf{A} \text{diag}(\mathbf{c}_l) \mathbf{A}^T \right)^{-1} \left[\mathbf{A} \text{diag}(\mathbf{c}_l) \left(\tilde{\mathbf{C}}_s \mathbf{h}_s - \mathbf{h}_{\text{loss}}(\mathbf{x}_Q) \right) - \frac{d\bar{\mathbf{q}}}{dt} \right]. \quad (4.6)$$

However, (4.6) requires the time derivative of the nodal consumption $\bar{\mathbf{q}}$ to be known which is rather problematic as the values used for $\bar{\mathbf{q}}$ are, generally, less confident.

Proposition 4.1. *Given Corollary 3.4, $\mathbf{L} = \mathbf{A} \text{diag}(\mathbf{c}_l) \mathbf{A}^T \succ 0$ is positive definite and thus invertible.*

Proof. Knowing that $\mathbf{A} \in \mathbb{Z}_{\{-1,0,1\}}^{n_j \times n_\ell}$ has full rank $\text{rank}(\mathbf{A}) = n_j$ according to Corollary 3.4, where $n_j < n_\ell$ as a reason of $n_s > 0$, the left null space or the kernel of the transpose of the incidence matrix is zero, i.e. $\ker \mathbf{A}^T = \{\mathbf{0}_{n_j}\}$. Subsequently, $\mathbf{y} = \mathbf{A}^T \mathbf{x} \neq \mathbf{0}$ for all $\mathbf{x} \neq \mathbf{0}$ resulting in $\mathbf{y}^T \text{diag}(\mathbf{c}_l) \mathbf{y} > 0$ for all $\mathbf{y} \neq \mathbf{0}$ as $\mathbf{c}_l \in \mathbb{R}_{>0}^{n_\ell}$ in reference to (4.4). ■

One possibility to avoid approximating the time derivatives of nodal consumption $\bar{\mathbf{q}}$ in (4.6), as its behavior is only known rudimentarily, is to move $\bar{\mathbf{q}}$ into the derivative of \mathbf{x}_Q . Inserting expression (4.6) into the ODEs (4.5) and then moving $\frac{d\bar{\mathbf{q}}}{dt}$ to the left hand side yields

$$\frac{d}{dt} \left(\mathbf{x}_Q - \text{diag}(\mathbf{c}_l) \mathbf{A}^T \mathbf{L}^{-1} \bar{\mathbf{q}} \right) = \left(\mathbf{I} - \text{diag}(\mathbf{c}_l) \mathbf{A}^T \mathbf{L}^{-1} \mathbf{A} \right) \text{diag}(\mathbf{c}_l) \left(\tilde{\mathbf{C}}_s \mathbf{h}_s - \mathbf{h}_{\text{loss}}(\mathbf{x}_Q) \right) \quad (4.7)$$

which is feasible as $\text{diag}(\mathbf{c}_l) \mathbf{A}^T \mathbf{L}^{-1}$ is constant. After solving (4.7), the result is increased by $\text{diag}(\mathbf{c}_l) \mathbf{A}^T \mathbf{L}^{-1} \bar{\mathbf{q}}$ to obtain \mathbf{x}_Q .

Assumption 4.2. *Initial states $\mathbf{x}_Q(t_0)$ for (4.7) and (4.5) are consistent $\mathbf{A}\mathbf{x}_Q(t_0) \stackrel{!}{=} \bar{\mathbf{q}}(t_0)$, which is a non-trivial requirement as this set of equations usually has multiple solutions. However, $\mathbf{x}_Q(t_0) = \mathbf{0}$ and $\bar{\mathbf{q}}(t_0) = \mathbf{0}$ obviously are always feasible initial states.*

Formulation Characteristics. For the purpose of analysis, suppose there are no cycles/loops concerning \mathbf{A} , meaning that $n_j = n_\ell$. Then, the matrix of the right hand side of (4.7) yields

$$\mathbf{I} - \text{diag}(\mathbf{c}_l) \mathbf{A}^T \left(\mathbf{A} \text{diag}(\mathbf{c}_l) \mathbf{A}^T \right)^{-1} \mathbf{A} \stackrel{n_j=n_\ell}{=} \mathbf{0} \quad (4.8)$$

zero and thus results in the complete loss of dynamics. Analogous to the steady-state, nodal *Kirchhoff* equations are sufficient for solving the network in case $n_\ell = n_j$.

Formulation (4.7) is also considered to be **demand-driven** in terms of nodal consumption $\bar{\mathbf{q}}$ (see section 3.1.4) as the specified $\bar{\mathbf{q}}$ is always subtracted from the respective nodes even there is not enough pressure to satisfy this demand. Also, the influence of the nodal elevation \mathbf{z} cancels out completely which can be seen in the set-up of pressure heads (4.6). However, this is no unique property, also in the steady-state formulation, the nodal elevation has no direct effect on the network equations as in $\mathbf{\Gamma}$ (3.23). This problem is usually being bypassed by subtracting \mathbf{z} after the nodal head vector has been calculated. It is shown in the following sections that the reason why the nodal elevation \mathbf{z} has no influence on the model equations is inherently connected with the demand-driven character.

4.3 Pressure-Driven Demand

The problems involved within specifying explicit demands are well known and communities already focused on modifications such that the specified consumption $\bar{\mathbf{q}}$ is expressed in terms of target or reference values. Regarding the steady-state model, various references (see section 3.1.4) propose extensions by introducing quantities like the desired pressure (for satisfying the specified target consumption) or available pressure at the respective node. In this thesis a different approach is pursued which ultimately leads, in the opinion of the author, to a more natural incorporation of a pressure-driven demand.

In reality, the consumer outflow q depends on the local pressure head h and on the cross section area of the consumer's pipe opening A_q . When equating potential- to kinetic energy, in analogy to section 2.1.4, the discharge relation

$$q = r(\alpha) A_q \sqrt{2gh} \quad (4.9)$$

extended by an additional multiplier $r(\alpha)$ (also known as discharge or orifice coefficient) is obtained. This multiplier is capable of adjusting the consumption much like one regulates the water flow by opening or closing a water tap. In this context α represents the degree of tap opening. In case the water tap is completely open, r becomes $r \approx \pi/(\pi + 2) = 0.611$ at least for a sharp edged orifice in the turbulent flow regime [Jelali and Kroll, 2003]. Although several empirical relations for calculating r depending on the flow condition and on the *Reynolds* number (see [Jelali and Kroll, 2003]) have been identified, another approach is pursued. After adding the orifice equation (4.9) to the network formulation, the focus is set on the control of \mathbf{q}^1 to follow a specified target (desired) consumption $\mathbf{q}_d(t)$ by manipulating \mathbf{r} . As it makes less sense to use complex empiric relations for finding suitable orifice coefficients if the tap opening α is not known anyway, a suitable control will adjust coefficient $r \in]0, 1]$ in its physical bounds.

Assumption 4.3. *Denoting $\mathbf{1} = [1 \ \dots \ 1]^T$, discharge coefficients $\mathbf{r} \in \mathbb{R}_{[\epsilon_r, 1]}^{n_q}$ of n_q consumers are bounded $\mathbf{1}\epsilon_r \leq \mathbf{r} \leq \mathbf{1}$ in order to ensure solvability of the pressure-driven network equations.*

¹note the change in notation $\mathbf{q} \neq \bar{\mathbf{q}}$

Pressure-Driven Network Formulation. In order to incorporate a pressure-dependent consumption, n_q consumer nodes, consuming $\mathbf{q} \in \mathbb{R}_{>0}^{n_q}$ (m^3/s), are separated from $n_j - n_q$ nodes with no consumers withdrawing water (non-consumer nodes). The separation is achieved by applying matrices $\mathbf{R}_q \in \mathbb{Z}_{\{0,1\}}^{n_q \times n_j}$ and $\bar{\mathbf{R}}_q \in \mathbb{Z}_{\{0,1\}}^{(n_j - n_q) \times n_j}$ such that

$$\mathbf{R}_q \bar{\mathbf{q}} = \mathbf{q} \quad \bar{\mathbf{R}}_q \bar{\mathbf{q}} = \mathbf{0} \quad (4.10)$$

which select the appropriate nodes from nodal equations $\mathbf{A}\mathbf{x}_Q = \bar{\mathbf{q}}$. To properly define \mathbf{R}_q and $\bar{\mathbf{R}}_q$, unity vector $\mathbf{e}_k^T \in \mathbb{Z}_{\{0,1\}}^{1 \times n_j}$ with a single one entry in the k -th column is utilized. As a remark, these column vectors have length n_j in contrast to the ones used for transformation (3.10) which have length n_ℓ .

Definition 4.4. The subset \mathcal{K} of inner nodes \mathcal{J} defines **consumer nodes**

$$\mathcal{K} = \{k \in \mathcal{J} \mid \mathbf{e}_k^T \bar{\mathbf{q}} > 0\} = \{k_1, \dots, k_{n_q}\} \subseteq \mathcal{J} \quad (4.11a)$$

where the consumption is strictly greater zero. The complementary set

$$\bar{\mathcal{K}} = \{k \in \mathcal{J} \mid \mathbf{e}_k^T \bar{\mathbf{q}} = 0\} = \{\bar{k}_1, \dots, \bar{k}_{n_j - n_q}\} \subseteq \mathcal{J} \quad (4.11b)$$

defines **non-consumer nodes** where no water is withdrawn. These two sets thereby satisfy $\mathcal{K} \cap \bar{\mathcal{K}} = \{\}$ and $\mathcal{K} \cup \bar{\mathcal{K}} = \mathcal{J}$.

According to Definition 4.4, one obtains

$$\mathbf{R}_q = [\mathbf{e}_{k_1} \quad \dots \quad \mathbf{e}_{k_{n_q}}]^T \quad \bar{\mathbf{R}}_q = [\mathbf{e}_{\bar{k}_1} \quad \dots \quad \mathbf{e}_{\bar{k}_{n_j - n_q}}]^T \quad (4.12)$$

which then have the following properties.

Property 4.5. Matrices \mathbf{R}_q and $\bar{\mathbf{R}}_q$ satisfy: (A proof is provided in section 2.2.3 applying Property 2.4 for $\mathbf{R} = \mathbf{R}_q$, $\bar{\mathbf{R}} = \bar{\mathbf{R}}_q$, $\mathfrak{K} = \mathcal{K}$ and $\bar{\mathfrak{K}} = \bar{\mathcal{K}}$)

$$\begin{aligned} \mathbf{R}_q \mathbf{R}_q^T &= \mathbf{I}_{n_q} & \bar{\mathbf{R}}_q \bar{\mathbf{R}}_q^T &= \mathbf{I}_{n_j - n_q} & \mathbf{R}_q \bar{\mathbf{R}}_q^T &= \mathbf{0} \\ \mathbf{R}_q^T \mathbf{R}_q + \bar{\mathbf{R}}_q^T \bar{\mathbf{R}}_q &= \mathbf{I}_{n_j} \end{aligned} \quad (4.13)$$

In the context of (4.9), $\mathbf{a}_q = [A_{q,k_1} \quad \dots \quad A_{q,k_{n_q}}]^T \in \mathbb{R}_{>0}^{n_q}$ characterizes the n_q cross section areas of maximal consumer openings (e.g. connected pipe with the largest diameter). $\mathbf{R}_q \mathbf{h} = \mathbf{h}_q \in \mathbb{R}_{\geq 0}^{n_q}$ represents n_q elements of pressure head \mathbf{h} at consumer nodes, whereas $\bar{\mathbf{R}}_q \mathbf{h} = \bar{\mathbf{h}}$ specifies $n_j - n_q$ elements of \mathbf{h} at non-consumer nodes. In reference to (4.9), the orifice equation yields

$$\mathbf{q} = \sqrt{2g} \mathbf{r} \odot \mathbf{a}_q \odot \mathbf{h}_q^{\odot 1/2} \quad (4.14)$$

when applying the *Hadamard* operator (see section 2.2.2). By inverting (4.14) with respect to \mathbf{h}_q , the coefficients \mathbf{r} appear in the denominator, meaning that the pressure at consumers could potentially become infinite if this coefficient tends to zero, i.e. if consumer openings are intended to close completely. To circumvent this case, the range of \mathbf{r} is bounded appropriately.

Remark 4.6. With the intention to simulate $q_k = 0$ while $h_k \neq 0$ at consumer node $k \in \mathcal{K}$, the error in the consumption $\epsilon_{q,k} = \epsilon_r A_{q,k} \sqrt{2gh_k}$ is negligible as long as a sufficiently small $\epsilon_r > 0$ is selected.

The aim is to express pressure head values \mathbf{h} in ODEs (4.5) by applying the vector orifice equation (4.14). Considering (4.10), one separates the *Kirchhoff* equations

$$\mathbf{R}_q \mathbf{A}\mathbf{x}_Q = \sqrt{2g} \left(\mathbf{r} \odot \mathbf{a}_q \odot \mathbf{h}_q^{\odot 1/2} \right) \quad (4.15a)$$

$$\bar{\mathbf{R}}_q \mathbf{A}\mathbf{x}_Q = \mathbf{0} \quad (4.15b)$$

into a consumer and a non-consumer part. Given Assumption 4.3, the inversion of (4.15a) in terms of \mathbf{h}_q , i.e.

$$\mathbf{h}_q = \frac{1}{2g} \mathbf{r}^{\odot -2} \odot \mathbf{a}_q^{\odot -2} \odot (\mathbf{R}_q \mathbf{A} \mathbf{x}_Q)^{\odot 2} \stackrel{!}{=} \frac{1}{2g} \mathbf{r}^{\odot -2} \odot \mathbf{a}_q^{\odot -2} \odot (\mathbf{R}_q \mathbf{A} \mathbf{x}_Q) \odot |\mathbf{R}_q \mathbf{A} \mathbf{x}_Q| \quad (4.16)$$

is feasible and already leads to n_q elements of \mathbf{h} . Emphasizing on $\mathbf{q} \stackrel{!}{=} \mathbf{q} \odot |\mathbf{q}|$ in (4.16), the restriction $\mathbf{q} = \mathbf{R}_q \mathbf{A} \mathbf{x}_Q > \mathbf{0}$ allows the pressure heads to remain $\mathbf{h} > \mathbf{0}$ (whereas $\mathbf{h} = \mathbf{0}$ also implies $\mathbf{q} = \mathbf{0}$) as long as a proper value for the boundary, e.g. $\epsilon_r = 10^{-5}$, is selected. However, the infeasible case were $\mathbf{q} < \mathbf{0}$ would result in a physical nonsense, \mathbf{h}_q would be positive for a negative consumption (4.16) if considering $\mathbf{q}^{\odot 2}$ instead of $\mathbf{q} \odot |\mathbf{q}|$ in (4.16).

Remark 4.7. *In principle, the pressure-driven consumption $\mathbf{q} = \mathbf{R}_q \mathbf{A} \mathbf{x}_Q$ and therefore \mathbf{h}_q could still become negative if source pressure \mathbf{h}_s is so low that it fails to satisfy (close to) zero consumption, in which case the appropriate discharge coefficients become $r_k = \epsilon_r$ at $k \in \mathcal{K}$.*

The simulation shall be aborted if $\mathbf{q} = \mathbf{R}_q \mathbf{A} \mathbf{x}_Q$ becomes negative (consumers would become sources). In this case one can, for instance, increase \mathbf{h}_s , decrease the consumption in total $\sum_{i=1}^{n_q} q_{d,k_i}$ or decrease q_k at the right (neighboring) consumer-nodes $k \in \mathcal{K}$ by manipulating r_k . Emphasizing once again on this scenario, this only occurs if sources, concerning \mathbf{h}_s , are unable to satisfy (close to) **zero** consumption via q_k at any consumer node $k \in \mathcal{K}$, in which case the discharge coefficient becomes ϵ_r (orifices can not be completely shut). It will **not** occur if \mathbf{h}_s only fails to satisfy target values $q_d > \epsilon_q > \mathbf{0}$, where $[\epsilon_q]_i = \epsilon_{q,k_i} = \epsilon_r A_{q,k_i} \sqrt{2gh_{k_i}}$.

The remaining non-consumer pressure heads $\bar{\mathbf{h}}$ in addition to (4.16) are obtained by differentiating (4.15b) with respect to time $\bar{\mathbf{R}}_q \mathbf{A} \frac{d\mathbf{x}_Q}{dt} = \mathbf{0}$ while inserting (4.5).

$$\bar{\mathbf{R}}_q \mathbf{L} \mathbf{h} = \bar{\mathbf{R}}_q \mathbf{A} \text{diag}(\mathbf{c}_l) \left(\tilde{\mathbf{C}}_s \mathbf{h}_s - \mathbf{A}^T \mathbf{z} - \mathbf{h}_{\text{loss}}(\mathbf{x}_Q) \right) \quad (4.17)$$

According to Properties 4.5 and (4.12) $\mathbf{h} = \bar{\mathbf{R}}_q^T \mathbf{h}_q + \bar{\mathbf{R}}_q^T \bar{\mathbf{h}}$, which leads to

$$\bar{\mathbf{h}} = \left(\bar{\mathbf{R}}_q \mathbf{L} \bar{\mathbf{R}}_q^T \right)^{-1} \bar{\mathbf{R}}_q \left[\mathbf{A} \text{diag}(\mathbf{c}_l) \left(\tilde{\mathbf{C}}_s \mathbf{h}_s - \mathbf{h}_{\text{loss}}(\mathbf{x}_Q) \right) - \mathbf{L} \left(\mathbf{R}_q^T \mathbf{h}_q + \mathbf{z} \right) \right]. \quad (4.18)$$

Corollary 4.8. *Given Proposition 4.1 and (4.12), $\bar{\mathbf{R}}_q \mathbf{L} \bar{\mathbf{R}}_q^T \succ \mathbf{0}$ is positive definite as $\mathbf{x}^T \bar{\mathbf{R}}_q \mathbf{L} \bar{\mathbf{R}}_q^T \mathbf{x} > \mathbf{0}$ for all $\mathbf{x} \in \mathbb{R}^{n_j - n_q} \neq \mathbf{0}$, where $\bar{\mathbf{R}}_q^T \mathbf{x}$ results in a vector with all components of \mathbf{x} and additional zeros.*

Combining (4.5), (4.16) and (4.18) one obtains the ODEs

$$\frac{d\mathbf{x}_Q}{dt} = \text{diag}(\mathbf{c}_l) \left(\tilde{\mathbf{C}}_s \mathbf{h}_s - \mathbf{A}^T (\mathbf{R}_q^T \mathbf{h}_q + \bar{\mathbf{R}}_q^T \bar{\mathbf{h}} + \mathbf{z}) - \mathbf{h}_{\text{loss}}(\mathbf{x}_Q) \right) \quad (4.19a)$$

$$\mathbf{h}_q = \frac{1}{2g} \mathbf{a}_q^{\odot -2} \odot (\mathbf{R}_q \mathbf{A} \mathbf{x}_Q)^{\odot 2} \odot \mathbf{r}^{\odot -2} \quad (4.19b)$$

$$\bar{\mathbf{h}} = \left(\bar{\mathbf{R}}_q \mathbf{L} \bar{\mathbf{R}}_q^T \right)^{-1} \bar{\mathbf{R}}_q \left[\mathbf{A} \text{diag}(\mathbf{c}_l) \left(\tilde{\mathbf{C}}_s \mathbf{h}_s - \mathbf{h}_{\text{loss}}(\mathbf{x}_Q) \right) - \mathbf{L} \left(\mathbf{R}_q^T \mathbf{h}_q + \mathbf{z} \right) \right] \quad (4.19c)$$

which actually resemble differential algebraic equations. However, when inserting (4.19b) into (4.19a) and the result of (4.19b) \rightarrow (4.19c) into (4.19a), the compact form

$$\frac{d\mathbf{x}_Q}{dt} = (\mathbf{I} - \mathbf{B}) \text{diag}(\mathbf{c}_l) \left[\tilde{\mathbf{C}}_s \mathbf{h}_s - \mathbf{h}_{\text{loss}}(\mathbf{x}_Q) - \mathbf{A}^T \left(\frac{1}{2g} \mathbf{R}_q^T \left(\mathbf{a}_q^{\odot -2} \odot (\mathbf{R}_q \mathbf{A} \mathbf{x}_Q)^{\odot 2} \odot \mathbf{r}^{\odot -2} \right) + \mathbf{z} \right) \right] \quad (4.20)$$

with $\mathbf{B} = \text{diag}(\mathbf{c}_l) \mathbf{A}^T \bar{\mathbf{R}}_q^T \left(\bar{\mathbf{R}}_q \mathbf{L} \bar{\mathbf{R}}_q^T \right)^{-1} \bar{\mathbf{R}}_q \mathbf{A}$ confirms its ODE nature.

Formulation Characteristics. In contrast to (4.8) (demand-driven), the dynamics

$$\mathbf{I} - \text{diag}(c_l) \mathbf{A}^T \bar{\mathbf{R}}_q^T \left(\bar{\mathbf{R}}_q \mathbf{A} \text{diag}(c_l) \mathbf{A}^T \bar{\mathbf{R}}_q^T \right)^{-1} \bar{\mathbf{R}}_q \mathbf{A} \stackrel{n_j=n_\ell}{\neq} \mathbf{0} \quad (4.21)$$

of this formulation generally remain intact in case the number of pipes equals the number of nodes. This holds true with exception of the case $n_q = 0 \Rightarrow \bar{\mathbf{R}}_q = \mathbf{I}_{n_j}$, when there are no consumers, resulting in $\mathbf{I} - \mathbf{B} \stackrel{n_j=n_\ell \wedge n_q=0}{=} \mathbf{0}$. Although nodal equations $\mathbf{A} \mathbf{x}_Q = \bar{\mathbf{q}}$ would be sufficient in case $n_\ell = n_j$, the situation changes when considering pressure-driven demands. Provided that the network completely lacks cycles/loops, steady-state models retain legitimacy although the dynamic character further revealed by the pressure-dependent demands and the consumer separation. Also, the nodal elevations \mathbf{z} first appear in the network equations (4.20) in contrast to (4.7), where \mathbf{z} canceled out completely. As distinguished from literature, this is the reason why nodal pressure heads were denoted by \mathbf{h} and not nodal pressure heads $\mathbf{h} + \mathbf{z}$.

4.3.1 Rapid Valve Opening in the Two-Cycle Network

For illustrative purposes, consider the two-cycle network in figure 3.2 with $n_\ell = 5$ pipe flows, $n_j = 3$ nodes and one ($n_s = 1$) reservoir R. Suppose $h_s = 30$ m, nodal elevations are $\mathbf{z} = [z_1 \ z_2 \ z_3]^T = [0 \ 10 \ 5]^T$ m and the two consumers at node $k = 2$ and $k = 3$ are consuming $q_2 = 1$ l/s and $q_3 = 0.7$ l/s. Nodal equations, consumer and non-consumer equations are defined as follows.

$$\underbrace{\begin{bmatrix} -1 & -1 & 0 & 0 & 1 \\ 1 & 0 & -1 & 1 & 0 \\ 0 & 1 & 1 & -1 & 0 \end{bmatrix}}_{\mathbf{A}} \underbrace{\begin{bmatrix} Q_1 \\ \vdots \\ Q_5 \end{bmatrix}}_{\mathbf{x}_Q} = \underbrace{\begin{bmatrix} 0 \\ q_2 \\ q_3 \end{bmatrix}}_{\bar{\mathbf{q}}}, \quad \underbrace{\begin{bmatrix} 0 & 1 & 0 \\ 0 & 0 & 1 \end{bmatrix}}_{\mathbf{R}_q} \underbrace{\begin{bmatrix} q_2 \\ q_3 \end{bmatrix}}_{\mathbf{q}}, \quad \underbrace{\begin{bmatrix} 1 & 0 & 0 \end{bmatrix}}_{\mathbf{R}_q} \bar{\mathbf{q}} = 0$$

Considering parameter vector $\mathbf{c}_l = 9.81 \times 0.04^2 \pi / 4 \times ([10 \ 20 \ 30 \ 10 \ 10]^T)^{\ominus 1}$, the pipes' cross section area $A_1 = \dots = A_5 = 0.04^2 \pi / 4$ as well as length $l_2 = 20$ m, $l_3 = 30$ m, $l_1 = l_4 = l_5 = 10$ m are defined. Maximal consumer openings \mathbf{a}_q are selected by simply equating them to cross section areas of adjacent pipes $\mathbf{a}_q = [A_2 \ A_3]^T$. Minor loss coefficients are set to zero $\mathbf{k}_m = \mathbf{0}$, whereas roughness coefficients are $\epsilon_{\text{DW}} = [3 \ 0.0015 \ 0.0015 \ 3 \ 0.0015]^T$ mm.

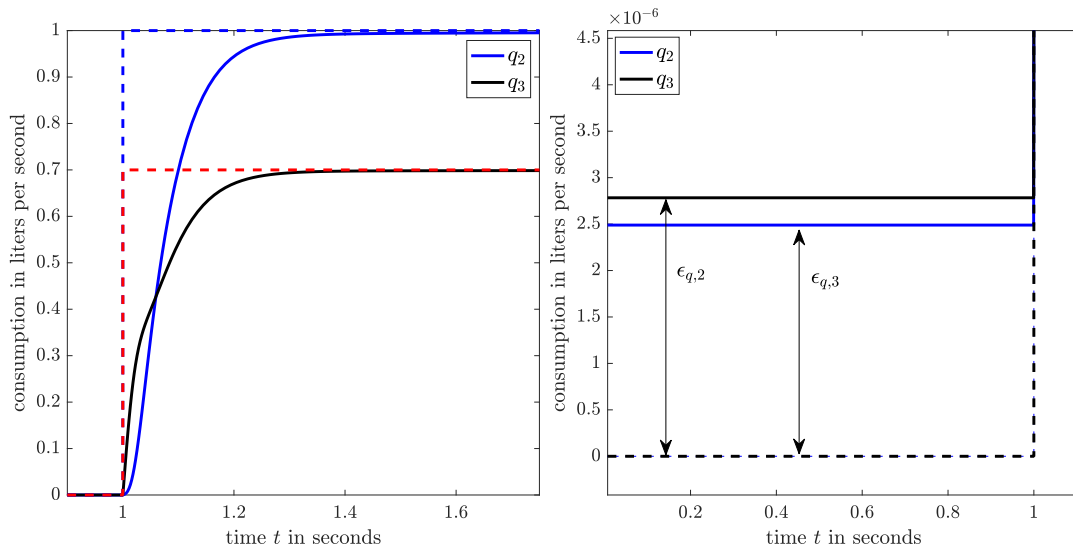


FIGURE 4.1: Simulated \mathbf{q} for the steady-state model (3.24) via EPANET2 (dashed line) and for the dynamic one (4.19) via MATLAB (solid line).

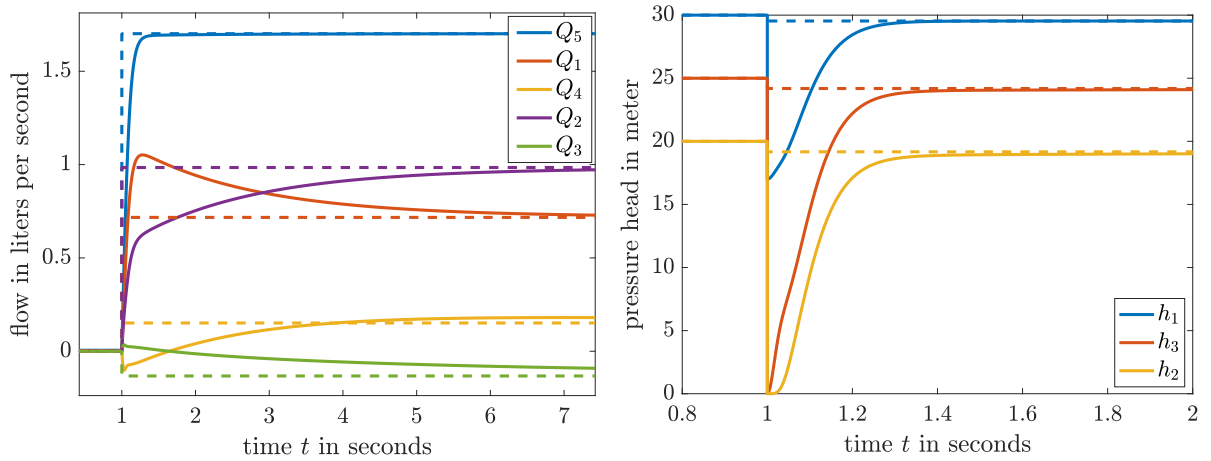


FIGURE 4.2: Simulated \mathbf{x}_Q and \mathbf{h} for the steady-state model (3.24) via EPANET2 (dashed) and for the dynamic one (4.19) via MATLAB (solid).

For friction factors λ_{DW} the Swamee-Jain equation (2.7) is utilized while expression (2.8) serves for the description of the transitional head loss. These choices were made in order to directly compare results of (4.19) with results of EPANET2. Also, a coherent temperature of 18°C is assumed. A step response is simulated where orifice coefficients are increased instantaneously at $t = 1\text{s}$ from $\mathbf{r} = [1 \ 1]^T \epsilon_r = [1 \ 1]^T \times 10^{-7}$ to $\mathbf{r} = [0.041 \ 0.026]^T$ which are chosen such that respective demands $q_2 = 1, q_3 = 0.7 \text{ l/s}$ are achieved.

Regarding Figure 4.1, the sudden increase in orifice coefficients \mathbf{r} causes the water mass inside the network to react inertially such that the consumption gradually reaches desired values. The mutual influence of q_2 and q_3 during their transition to steady-state can be seen at $t \approx [1, 1.03]\text{s}$, where q_3 increases rapidly until q_2 reaches maximal slope and forces q_3 to slow down. Hereby consumption q_3 presumably starts off first as pipe $i = 1$ and $i = 4$ have significantly higher roughness coefficients. Furthermore, as distance $\mathbb{R} \xrightarrow{i=5} k = 1 \xrightarrow{i=2} k = 3 \xrightarrow{i=3} k = 2$ is twice the distance $\mathbb{R} \xrightarrow{i=5} k = 1 \xrightarrow{i=2} k = 3$, h_2 recovers slower than h_3 ($t \approx [1, 1.03]\text{s}$) from the sudden pressure decrease when opening consumers (see Figure 4.2). One can also recognize the rigid character of the ODEs (4.19) as in a real hydraulic network a sudden excitation by valve openings, physically equivalent to the sudden increase in \mathbf{r} , would certainly cause oscillations which are not present here. Such oscillations would be the result of elastic effects meaning, for instance, the pipe's elasticity and variations in water density.

Starting from initial states $\mathbf{x}_Q(t_0) = \mathbf{0}$ and $\mathbf{q}(t_0) = \mathbf{0}$, in reference to Assumption 4.2, one can see that the consumption immediately becomes $\mathbf{q}(t < 1\text{s}) > \mathbf{0}$ as orifice coefficients are $\mathbf{r} > \mathbf{0}$ according to Assumption 4.3. Though, one can see on the right hand side of Figure 4.1 that the lower boundaries $\epsilon_{q,2} = \epsilon_r A_2 \sqrt{2gh_2}(t < 1\text{s}) \approx 2.5 \cdot 10^{-6} \text{ l/s}$ and $\epsilon_{q,3} = \epsilon_r A_3 \sqrt{2gh_3}(t < 1\text{s}) \approx 2.8 \cdot 10^{-6} \text{ l/s}$ in \mathbf{q} are sufficiently small and thus insignificant for the simulation results, referring to Remark 4.6. As shown in Figure 4.2, the results of the dynamic model (4.19) converge to the steady-state ones (3.24) computed by EPANET2. The jump in pressure heads can be directly attributed to the jump in coefficients \mathbf{r} which directly influences \mathbf{h}_q in (4.19b). For solving (4.19) the stiff solver ODE15s was applied which is capable of adjusting the step size efficiently in case of rapid changes in a large number of state variables \mathbf{x}_Q .

In the following sections the focus is set on the choice of orifice coefficients \mathbf{r} , which were not determined by chance in this example, such that specified target or desired values $\mathbf{q}_d \in \mathbb{R}_{\geq 0}^{n_q}$ are reached in a manipulated time frame. As a remark, these reference values \mathbf{q}_d are allowed to become zero as long as orifice coefficients \mathbf{r} are bounded appropriately.

4.4 How to Deal With Consumption?

In this section the degree of freedom in unknown orifice coefficients $\mathbf{r} \in \mathbb{R}_{[\epsilon_r, 1]}^{n_q}$ is exploited to make sure that target consumption values \mathbf{q}_d are gradually satisfied in model (4.19) by replacing the pressure-driven (in terms of \mathbf{q}) character with linear consumption dynamics. The results are then incorporated into model equations which will actually simplify their appearance. This is achieved by applying an exact linearization, a method commonly applied in control, which will support the handling of dynamic hydraulic network simulations.

4.4.1 Linear Consumption Dynamics

The selected target is to vary the control variable $\mathbf{u} = \mathbf{r}^{\odot -2}$ in the bounds $\mathbf{u} \in [1, \epsilon_r^{-2}]$ in order to force the consumption to follow \mathbf{q}_d . When taking the first derivative of output $\mathbf{q} = \mathbf{R}_q \mathbf{A} \mathbf{x}_Q$ and inserting the right hand side of (4.20), it becomes apparent that each derivative of selected outputs depends on \mathbf{u} . Manipulability of the output is assured. This is a rather obvious result as it is clear that each consumption can be controlled by its orifice coefficient $q_k = r_k A_{q,k} \sqrt{2gh_k}$ for $k \in \mathcal{K}$. In order to decouple system (4.20), $d\mathbf{q}/dt$ is forced to follow a linear differential equation with eigenvalues $\boldsymbol{\lambda}_q \in \mathbb{R}_{<0}^{n_q}$:

$$\frac{d\mathbf{q}}{dt} = \mathbf{R}_q \mathbf{A} \frac{d\mathbf{x}_Q}{dt} \stackrel{!}{=} \boldsymbol{\lambda}_q \odot \mathbf{q} + \boldsymbol{\alpha}_q \odot \mathbf{q}_d \quad (4.22)$$

Parameters $\boldsymbol{\alpha}_q \in \mathbb{R}^{n_q}$ are chosen such that

$$\lim_{t \rightarrow \infty} \mathbf{q}(t) \stackrel{!}{=} \mathbf{q}_d. \quad (4.23)$$

Applying the *Laplace* transform to (4.22) for constant \mathbf{q}_d

$$\mathcal{L}\{\mathbf{q}(t)\} = \hat{\mathbf{q}}(s) = \frac{(s\mathbf{1} - \boldsymbol{\lambda}_q)^{\odot -1}}{s} \odot \boldsymbol{\alpha}_q \odot \mathbf{q}_d \quad (4.24)$$

and the Laplace final value theorem to (4.23) results in

$$\lim_{s \rightarrow 0} (s\mathbf{1} - \boldsymbol{\lambda}_q)^{\odot -1} \odot \boldsymbol{\alpha}_q \odot \mathbf{q}_d \stackrel{!}{=} \mathbf{q}_d \quad \Rightarrow \quad \boldsymbol{\alpha}_q = -\boldsymbol{\lambda}_q. \quad (4.25)$$

After inserting (4.20) into (4.22) while using (4.25) and $\mathbf{u} = \mathbf{r}^{\odot -2}$, one receives

$$\begin{aligned} \mathbf{u} = 2g \operatorname{diag} \left(\mathbf{q}^{\odot -2} \odot \mathbf{a}_q^{\odot 2} \right) \hat{\mathbf{D}}^{-1} \left[\boldsymbol{\lambda}_q \odot (\mathbf{q} - \mathbf{q}_d) \right. \\ \left. + \mathbf{R}_q \mathbf{A} (\mathbf{I} - \mathbf{B}) \operatorname{diag} (c_l) \left(\mathbf{h}_{\text{loss}}(\mathbf{x}_Q) - \tilde{\mathbf{C}}_s \mathbf{h}_s + \mathbf{A}^T \mathbf{z} \right) \right] \end{aligned} \quad (4.26)$$

where $\hat{\mathbf{D}} = -\mathbf{R}_q \mathbf{A} (\mathbf{I} - \mathbf{B}) \operatorname{diag} (c_l) \mathbf{A}^T \mathbf{R}_q^T = \mathbf{R}_q \mathbf{L} \bar{\mathbf{R}}_q^T \left(\bar{\mathbf{R}}_q \mathbf{L} \bar{\mathbf{R}}_q^T \right)^{-1} \bar{\mathbf{R}}_q \mathbf{L} \mathbf{R}_q^T - \mathbf{R}_q \mathbf{L} \mathbf{R}_q^T$. When taking a closer look at the special form of $\hat{\mathbf{D}}$ by making use of the Schur complement, pleasant properties are revealed.

Proposition 4.9. *Given Proposition 4.1, matrix $-\hat{\mathbf{D}}$ is positive definite ($\hat{\mathbf{D}}$ is negative definite) and thus invertible.*

Proof. $-\hat{\mathbf{D}}$ can be interpreted as Schur complement [Zhang, 2005]

$$\mathbf{M}_s / \mathbf{A}_s = \mathbf{R}_q \mathbf{L} \mathbf{R}_q^T - \mathbf{R}_q \mathbf{L} \bar{\mathbf{R}}_q^T \left(\bar{\mathbf{R}}_q \mathbf{L} \bar{\mathbf{R}}_q^T \right)^{-1} \bar{\mathbf{R}}_q \mathbf{L} \mathbf{R}_q^T \quad (4.27)$$

of block matrix $M_s = \begin{bmatrix} \mathbf{A}_s & \mathbf{B}_s \\ \mathbf{B}_s^T & \mathbf{C}_s \end{bmatrix}$, where

$$M_s = \begin{bmatrix} \mathbf{R}_q \mathbf{L} \mathbf{R}_q^T & \mathbf{R}_q \mathbf{L} \bar{\mathbf{R}}_q^T \\ \bar{\mathbf{R}}_q \mathbf{L} \mathbf{R}_q^T & \bar{\mathbf{R}}_q \mathbf{L} \bar{\mathbf{R}}_q^T \end{bmatrix} = \begin{bmatrix} \mathbf{R}_q \\ \bar{\mathbf{R}}_q \end{bmatrix} \mathbf{L} \begin{bmatrix} \mathbf{R}_q^T & \bar{\mathbf{R}}_q^T \end{bmatrix}. \quad (4.28)$$

Since $\mathbf{L} = \mathbf{A} \text{diag}(\mathbf{c}_l) \mathbf{A}^T$ is positive definite (Proposition 4.1), M_s is positive definite considering that $[\mathbf{R}_q^T \quad \bar{\mathbf{R}}_q^T] \mathbf{x}$ simply rearranges entries in \mathbf{x} according to Property 4.5. Subsequently, $M_s / \mathbf{A}_s = \mathbf{A}_s - \mathbf{B}_s \mathbf{C}_s^{-1} \mathbf{B}_s^T = -\hat{\mathbf{D}}$

$$M_s \succ 0 \Leftrightarrow \mathbf{A}_s \succ 0 \quad \text{and} \quad \mathbf{A}_s - \mathbf{B}_s \mathbf{C}_s^{-1} \mathbf{B}_s^T \succ 0 \quad (4.29)$$

is positive definite thus invertible. ■

It was shown that the control law (4.26) is applicable for all considered network configurations. As a result of the linearization when applying (4.26), the pressure-driven character of network's consumption will be suppressed. By applying (4.26), \mathbf{q} is governed by the differential equation (4.22), its convergence-speed towards \mathbf{q}_d can be adjusted via the eigenvalues $\boldsymbol{\lambda}_q < \mathbf{0}$.

4.4.2 Incorporation in Model Equations

Control law (4.26) is inserted into the model equations (4.19b) and (4.20). One has to be aware that this is only valid if \mathbf{u} or \mathbf{r} remains in its boundaries.

Assumption 4.10. *The network is properly designed such that source pressures \mathbf{h}_s are high enough to satisfy specified demands \mathbf{q}_d . Then, (4.26) remains in the boundary $\mathbf{u}(\mathbf{x}_Q, \mathbf{q}_d, \mathbf{h}_s) \in [1, \epsilon_r^{-2}]$ for chosen eigenvalues $\boldsymbol{\lambda}_q < \mathbf{0}$ and ϵ_r according to Assumption 4.3.*

Theorem 4.11. *Let Assumption 4.10 hold. Then, system (4.19b) and (4.20) with $\mathbf{u} = \mathbf{r}^{\odot -2}$ according to (4.26) is equivalent to flow transients (4.30a) and nodal heads (4.30b)*

$$\frac{d\mathbf{x}_Q}{dt} = \mathbf{G} \left(\tilde{\mathbf{C}}_s \mathbf{h}_s - \mathbf{h}_{\text{loss}}(\mathbf{x}_Q) \right) + \mathbf{M} \left(\mathbf{R}_q \mathbf{A} \mathbf{x}_Q - \mathbf{q}_d \right) \quad (4.30a)$$

$$\mathbf{h} + \mathbf{z} = \mathbf{L}^{-1} \left[\mathbf{A} \text{diag}(\mathbf{c}_l) \left(\tilde{\mathbf{C}}_s \mathbf{h}_s - \mathbf{h}_{\text{loss}}(\mathbf{x}_Q) \right) - \mathbf{R}_q^T \text{diag}(\boldsymbol{\lambda}_q) \left(\mathbf{R}_q \mathbf{A} \mathbf{x}_Q - \mathbf{q}_d \right) \right] \quad (4.30b)$$

applying matrices $\mathbf{G} = (\mathbf{I} - \text{diag}(\mathbf{c}_l) \mathbf{A}^T \mathbf{L}^{-1} \mathbf{A}) \text{diag}(\mathbf{c}_l)$ and $\mathbf{M} = \text{diag}(\mathbf{c}_l) \mathbf{A}^T \mathbf{L}^{-1} \mathbf{R}_q^T \text{diag}(\boldsymbol{\lambda}_q)$.

Proof. First, (4.30a) is proven. Inserting (4.26) into (4.20) yields:

$$\begin{aligned} \frac{d\mathbf{x}_Q}{dt} &= (\mathbf{I} - \mathbf{B}) \text{diag}(\mathbf{c}_l) \left(\tilde{\mathbf{C}}_s \mathbf{h}_s - \mathbf{h}_{\text{loss}}(\mathbf{x}_Q) - \mathbf{A}^T \mathbf{z} \right) \\ &\quad - (\mathbf{I} - \mathbf{B}) \text{diag}(\mathbf{c}_l) \mathbf{A}^T \mathbf{R}_q^T \hat{\mathbf{D}}^{-1} \left[\boldsymbol{\lambda}_q \odot (\mathbf{q} - \mathbf{q}_d) \right. \\ &\quad \left. + \mathbf{R}_q \mathbf{A} (\mathbf{I} - \mathbf{B}) \text{diag}(\mathbf{c}_l) \left(\mathbf{h}_{\text{loss}}(\mathbf{x}_Q) - \tilde{\mathbf{C}}_s \mathbf{h}_s + \mathbf{A}^T \mathbf{z} \right) \right] \end{aligned} \quad (4.31)$$

One may recognize that term $-\mathbf{A}^T \mathbf{z}$ is missing in (4.30a) when compared to (4.31) which can be attributed to special properties of \mathbf{G} , resulting in $\mathbf{G} \mathbf{A}^T = \mathbf{0}$. By collecting terms in front of $(\tilde{\mathbf{C}}_s \mathbf{h}_s - \mathbf{h}_{\text{loss}}(\mathbf{x}_Q) - \mathbf{A}^T \mathbf{z})$ (ii) and $(\mathbf{q} - \mathbf{q}_d)$ (i) in (4.31), one has to prove the two conditions

$$\begin{aligned} \text{(i)} \quad & -(\mathbf{I} - \mathbf{B}) \text{diag}(\mathbf{c}_l) \mathbf{A}^T \mathbf{R}_q^T \hat{\mathbf{D}}^{-1} \stackrel{!}{=} \text{diag}(\mathbf{c}_l) \mathbf{A}^T \mathbf{L}^{-1} \mathbf{R}_q^T, \\ \text{(ii)} \quad & \left(\mathbf{I} + (\mathbf{I} - \mathbf{B}) \text{diag}(\mathbf{c}_l) \mathbf{A}^T \mathbf{R}_q^T \hat{\mathbf{D}}^{-1} \mathbf{R}_q \mathbf{A} \right) (\mathbf{I} - \mathbf{B}) \stackrel{!}{=} \left(\mathbf{I} - \text{diag}(\mathbf{c}_l) \mathbf{A}^T \mathbf{L}^{-1} \mathbf{A} \right) \end{aligned}$$

where $\text{diag}(c_l)$ was already canceled from the left and right hand side of (ii). Matrix

$$\mathbf{Z} = \text{diag}(c_l) \mathbf{A}^T \mathbf{L}^{-1} \left(\mathbf{R}_q^T \mathbf{R}_q + \bar{\mathbf{R}}_q^T \bar{\mathbf{R}}_q \right) \mathbf{A} \quad (4.32)$$

which is invariant in terms of $\mathbf{Z} \text{diag}(c_l) \mathbf{A}^T = \text{diag}(c_l) \mathbf{A}^T$ and $\mathbf{AZ} = \mathbf{A}$ will be helpful. After using the definition of $\mathbf{B} = \text{diag}(c_l) \mathbf{A}^T \bar{\mathbf{R}}_q^T \left(\bar{\mathbf{R}}_q \mathbf{L} \bar{\mathbf{R}}_q^T \right)^{-1} \bar{\mathbf{R}}_q \mathbf{A}$ (below (4.20)) for the left of condition (i)

$$- \text{diag}(c_l) \mathbf{A}^T \left(\mathbf{R}_q^T - \bar{\mathbf{R}}_q^T \left(\bar{\mathbf{R}}_q \mathbf{L} \bar{\mathbf{R}}_q^T \right)^{-1} \bar{\mathbf{R}}_q \mathbf{L} \mathbf{R}_q^T \right) \hat{\mathbf{D}}^{-1} \quad (4.33)$$

and then replacing $\text{diag}(c_l) \mathbf{A}^T$ with $\mathbf{Z} \text{diag}(c_l) \mathbf{A}^T$ in (4.33)

$$- \text{diag}(c_l) \mathbf{A}^T \mathbf{L}^{-1} \mathbf{R}_q^T \left(\mathbf{R}_q \mathbf{L} \mathbf{R}_q^T - \mathbf{R}_q \mathbf{L} \bar{\mathbf{R}}_q^T \left(\bar{\mathbf{R}}_q \mathbf{L} \bar{\mathbf{R}}_q^T \right)^{-1} \bar{\mathbf{R}}_q \mathbf{L} \mathbf{R}_q^T \right) \hat{\mathbf{D}}^{-1} \quad (4.34)$$

it is clear that condition (i) holds, considering the definition of $\hat{\mathbf{D}}$ (below (4.26)).

For the verification of condition (ii) one has to show that

$$\left(\mathbf{I} - \text{diag}(c_l) \mathbf{A}^T \mathbf{L}^{-1} \mathbf{R}_q^T \mathbf{R}_q \mathbf{A} \right) (\mathbf{I} - \mathbf{B}) \stackrel{!}{=} \left(\mathbf{I} - \text{diag}(c_l) \mathbf{A}^T \mathbf{L}^{-1} \mathbf{A} \right) \quad (4.35)$$

where condition (i) was already inserted. Subsequently, for proving (4.35) one has to verify if

$$-\mathbf{B} - \text{diag}(c_l) \mathbf{A}^T \mathbf{L}^{-1} \mathbf{R}_q^T \mathbf{R}_q \mathbf{A} (\mathbf{I} - \mathbf{B}) \stackrel{!}{=} -\text{diag}(c_l) \mathbf{A}^T \mathbf{L}^{-1} \mathbf{A}. \quad (4.36)$$

The definition of \mathbf{B} (below (4.20)) is applied on the left hand side of (4.36)

$$\text{diag}(c_l) \mathbf{A}^T \left[\bar{\mathbf{R}}_q^T \left(\bar{\mathbf{R}}_q \mathbf{L} \bar{\mathbf{R}}_q^T \right)^{-1} \bar{\mathbf{R}}_q + \mathbf{L}^{-1} \mathbf{R}_q^T \mathbf{R}_q - \mathbf{L}^{-1} \mathbf{R}_q^T \mathbf{R}_q \mathbf{L} \bar{\mathbf{R}}_q^T \left(\bar{\mathbf{R}}_q \mathbf{L} \bar{\mathbf{R}}_q^T \right)^{-1} \bar{\mathbf{R}}_q \right] \mathbf{A}. \quad (4.37)$$

When replacing $\text{diag}(c_l) \mathbf{A}^T$ with $\mathbf{Z} \text{diag}(c_l) \mathbf{A}^T$ on the left of (4.37), it becomes evident (with the help of Property 4.5) that condition (ii) holds. ■

Proof. The second part (4.30b), dealing with pressure heads \mathbf{h} , is proven. One inserts (4.26) into (4.19b)

$$\mathbf{h}_q = \hat{\mathbf{D}}^{-1} \left[\lambda_q \odot (\mathbf{q} - \mathbf{q}_d) + \mathbf{R}_q \mathbf{A} (\mathbf{I} - \mathbf{B}) \text{diag}(c_l) \left(\mathbf{h}_{\text{loss}}(\mathbf{x}_Q) - \tilde{\mathbf{C}}_s \mathbf{h}_s + \mathbf{A}^T \mathbf{z} \right) \right] \quad (4.38)$$

and (4.38) into (4.19c) and then collects terms in front of $(\tilde{\mathbf{C}}_s \mathbf{h}_s - \mathbf{h}_{\text{loss}}(\mathbf{x}_Q) - \mathbf{A}^T \mathbf{z})$ (iv) as well as $(\mathbf{q} - \mathbf{q}_d)$ (iii) in expression

$$\mathbf{h} = \mathbf{R}_q^T \mathbf{h}_q + \bar{\mathbf{R}}_q^T \bar{\mathbf{h}} \quad (4.39)$$

which leads to the two conditions

$$\begin{aligned} \text{(iii)} \quad & \left(\mathbf{R}_q^T - \bar{\mathbf{R}}_q^T \left(\bar{\mathbf{R}}_q \mathbf{L} \bar{\mathbf{R}}_q^T \right)^{-1} \bar{\mathbf{R}}_q \mathbf{L} \mathbf{R}_q^T \right) \hat{\mathbf{D}}^{-1} \stackrel{!}{=} -\mathbf{L}^{-1} \mathbf{R}_q^T, \\ \text{(iv)} \quad & \left[- \left(\mathbf{R}_q^T - \bar{\mathbf{R}}_q^T \left(\bar{\mathbf{R}}_q \mathbf{L} \bar{\mathbf{R}}_q^T \right)^{-1} \bar{\mathbf{R}}_q \mathbf{L} \mathbf{R}_q^T \right) \hat{\mathbf{D}}^{-1} \mathbf{R}_q \mathbf{A} (\mathbf{I} - \mathbf{B}) + \bar{\mathbf{R}}_q^T \left(\bar{\mathbf{R}}_q \mathbf{L} \bar{\mathbf{R}}_q^T \right)^{-1} \bar{\mathbf{R}}_q \mathbf{A} \right] \\ & \stackrel{!}{=} \mathbf{L}^{-1} \mathbf{A} \end{aligned}$$

where $\text{diag}(c_l)$ was already canceled from the left and right hand side of (iv). Starting with condition (iii), after multiplying matrix $\mathbf{L}^{-1} \left(\mathbf{R}_q^T \mathbf{R}_q + \bar{\mathbf{R}}_q^T \bar{\mathbf{R}}_q \right) \mathbf{L} = \mathbf{I}$ (see Property 4.5) from the left to the left hand side of (iii)

$$\mathbf{L}^{-1} \left[\bar{\mathbf{R}}_q^T \bar{\mathbf{R}}_q \mathbf{L} \mathbf{R}_q^T - \bar{\mathbf{R}}_q^T \left(\bar{\mathbf{R}}_q \mathbf{L} \bar{\mathbf{R}}_q^T \right) \left(\bar{\mathbf{R}}_q \mathbf{L} \bar{\mathbf{R}}_q^T \right)^{-1} \bar{\mathbf{R}}_q \mathbf{L} \mathbf{R}_q^T - \mathbf{R}_q^T \hat{\mathbf{D}} \right] \hat{\mathbf{D}}^{-1} = -\mathbf{L}^{-1} \mathbf{R}_q^T \quad (4.40)$$

it can be seen condition (iii) is satisfied.

Condition (iii) is now applied on the left hand side of (iv)

$$\left[\mathbf{L}^{-1} \mathbf{R}_q^T \mathbf{R}_q \mathbf{A} (\mathbf{I} - \mathbf{B}) + \bar{\mathbf{R}}_q^T (\bar{\mathbf{R}}_q \mathbf{L} \bar{\mathbf{R}}_q^T)^{-1} \bar{\mathbf{R}}_q \mathbf{A} \right] \text{diag}(\mathbf{c}_l). \quad (4.41)$$

The definition of \mathbf{B} (below (4.20)) and $\mathbf{R}_q^T \mathbf{R}_q = \mathbf{I} - \bar{\mathbf{R}}_q^T \bar{\mathbf{R}}_q$ (Property 4.5) is applied to (4.41).

$$\left[\mathbf{L}^{-1} (\mathbf{I} - \bar{\mathbf{R}}_q^T \bar{\mathbf{R}}_q) (\mathbf{A} - \mathbf{L} \bar{\mathbf{R}}_q^T (\bar{\mathbf{R}}_q \mathbf{L} \bar{\mathbf{R}}_q^T)^{-1} \bar{\mathbf{R}}_q \mathbf{A}) + \bar{\mathbf{R}}_q^T (\bar{\mathbf{R}}_q \mathbf{L} \bar{\mathbf{R}}_q^T)^{-1} \bar{\mathbf{R}}_q \mathbf{A} \right] = \mathbf{L}^{-1} \mathbf{A} \quad (4.42)$$

According to (4.42), condition (iv) holds. \blacksquare

4.4.3 Discussion

Definition 4.12. *To introduce a common terminology of different models distinguished by the implementation of the consumption, table 4.1*

notation	equations	consumption type
DD	(4.6) \wedge (4.7)	demand driven
PD	(4.19)	pressure driven
	(4.19b) \wedge (4.19c) \wedge (4.20)	
LCD	(4.30)	linear consumption dynamics

TABLE 4.1: Model notation with different consumption implementations.

should clarify the connection to the underlying equations. However, as the consumption of LCD is expected to follow the linear differential equation (4.22) exactly, it can also be considered to be demand-driven.

Results before section 4.3 including DD are well known in literature (e.g. see [Piller et al., 2003]), however, the incorporation of a pressure-driven consumption as in PD was not yet considered to the best of the author's knowledge. One may recognize the resemblance of LCD's flow transients (4.30a) with the ones of DD which have been identified early. By writing flow transients of DD (4.7) as follows

$$\frac{d\mathbf{x}_Q}{dt} = \underbrace{(\mathbf{I} - \text{diag}(\mathbf{c}_l) \mathbf{A}^T \mathbf{L}^{-1} \mathbf{A})}_{\mathbf{G}} \text{diag}(\mathbf{c}_l) (\tilde{\mathbf{C}}_s \mathbf{h}_s - \mathbf{h}_{\text{loss}}(\mathbf{x}_Q)) + \text{diag}(\mathbf{c}_l) \mathbf{A}^T \mathbf{L}^{-1} \frac{d\bar{\mathbf{q}}}{dt} \quad (4.43)$$

some interesting implications can be derived.

Corollary 4.13. *By forcing n_q non-zero components \mathbf{q} of nodal consumption $\bar{\mathbf{q}} = \mathbf{R}_q^T \mathbf{q}$ to follow a linear differential equation $\frac{d\bar{\mathbf{q}}}{dt} = \mathbf{R}_q^T \frac{d\mathbf{q}}{dt}$ as in (4.22), flow transients in DD are equivalent to flow transients in LCD (according to Theorem 4.11), which have been obtained by an exact linearization of PD around \mathbf{q} .*

In other words, PD was obtained by the incorporation of (4.14) into DD while coupling consumers with each other via $\mathbf{q} = \mathbf{R}_q \mathbf{A} \mathbf{x}_Q$. The reverse operation is thereby provided by an exact linearization when the consumption dynamics $\frac{d\bar{\mathbf{q}}}{dt}$ in DD are also forced to satisfy (4.22).

Starting from the pure demand-driven DD, where the nodal consumption $\bar{\mathbf{q}}$ is subtracted irrespectively, to the more accurate, pressure-driven PD, where one has to deal with unknown orifice coefficients, back to the demand-driven LCD with few yet distinct advantages. Even if the consumption is not known in great detail, regarding their typically poor time resolution, LCD attenuates discontinuities which would be caused by jumps in the explicit $\bar{\mathbf{q}}$ concerning DD. However, instantaneous changes in \mathbf{r} concerning PD also cause discontinuities in the pressure, resulting in unrealistic jumps. This occurred in the two-cycle network in section 4.3.1 concerning

pressure heads, seen on the right side of figure 4.2. Nevertheless, this may be considered a feature rather than a drawback knowing that the pressure propagates with infinite velocity according to the rigid column theory (see physical considerations on page 34).

What shall be the right implementation for the consumption? Neither of the ones in the list provided in table 4.1, but PD in combination with control law \mathbf{u} (4.26) while saturating the control variable $\mathbf{u} \in [1, \epsilon_r^{-2}]$, or orifice coefficients $\mathbf{r} \in [\epsilon_r, 1]$. As a remark, the only difference to LCD is provided by the saturation of the control variable, which was assumed to never exceed its limits according to Assumption 4.10 regarding LCD (Theorem 4.11).

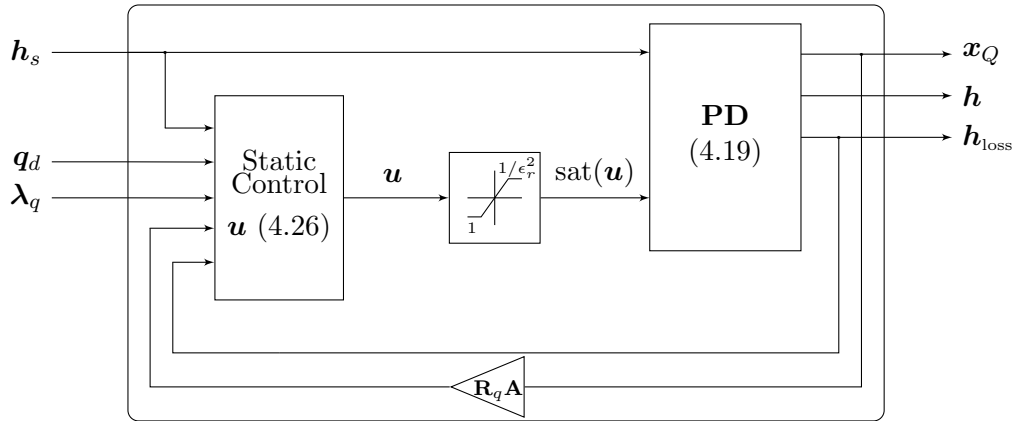


FIGURE 4.3: Block diagram of the model displaying its internal control loop to simulate specified consumptions.

This limitation then physically accounts for a pressure limiting factor of the consumption, meaning that if \mathbf{q}_d requires more pressure than available, orifice coefficients can only open completely $r = 1$ but never exceed “1”. In this context, eigenvalues $\lambda_q \in \mathbb{R}_{<0}^{n_q}$ play an important role. In principle, one can manipulate the time needed for the consumption $\mathbf{q} = \mathbf{R}_q \mathbf{A} \mathbf{x}_Q$ by changing λ_q arbitrarily. However, by decreasing eigenvalues too much (for decreasing the time needed for $\mathbf{R}_q \mathbf{A} \mathbf{x}_Q$ to approach \mathbf{q}_d), the control variable and thus orifice coefficients \mathbf{r} exceed their physical limits (example below). As a consequence, eigenvalues $\lambda_q \in \mathbb{R}_{<0}^{n_q}$ have to be chosen somewhat realistically. Validating experiments on a small-scale replica of a drinking water network, values $\lambda_q \in [-25, -5]$ (s^{-1}) performed reasonably well, this, however, may depend on pipe characteristics such as length and diameter.

Definition 4.14. *Model PD according to table 4.1 is distinguished*

notation	equations	orifice coefficients
PD	(4.19)	\mathbf{r} explicit
PD $_{\mathbf{u}}$	(4.19) \wedge (4.26)	control $\text{sat}(\mathbf{u}) = \mathbf{r}^{\ominus-2}$ (4.26)

TABLE 4.2: Model notation with different consumption implementations.

by either using explicit orifice coefficients \mathbf{r} in PD or control $\text{sat}(\mathbf{u}) = \mathbf{r}^{\ominus-2}$ in PD $_{\mathbf{u}}$ where \mathbf{u} is saturated $\mathbf{u} \in [1, \epsilon_r^{-2}]$.

4.4.4 Illustrative Example

Configuration. In this subsection the two-cycle example as in figure 3.2 with the same configuration (unless of the parameters stated) as section 4.3.1 is considered. While also using PD, orifice coefficients are determined through the saturated control law (4.26), i.e. $\text{sat}(\mathbf{u})$ according to block diagram in figure 4.3. Regarding the saturation of \mathbf{u} , limits are selected as follows

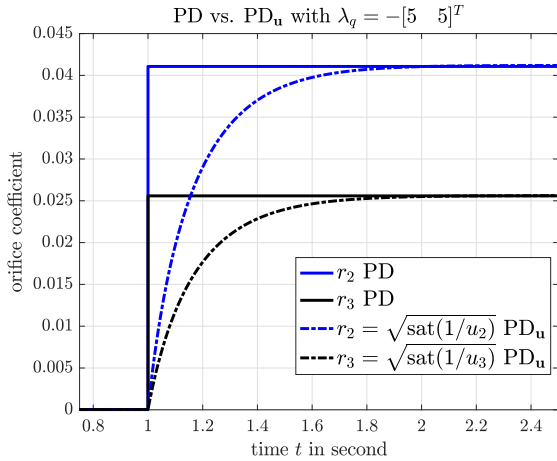
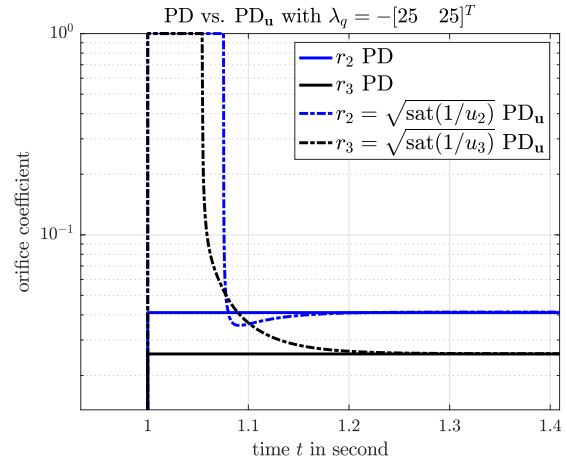
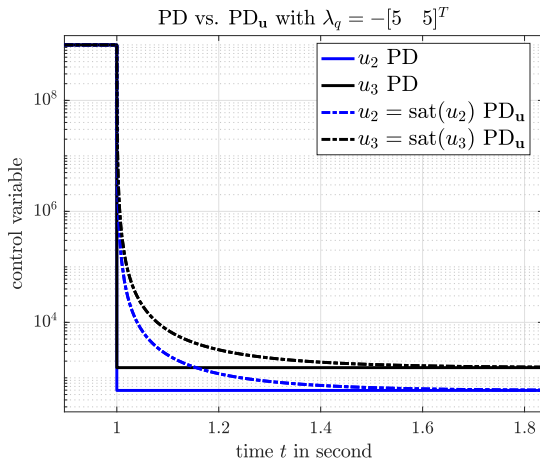
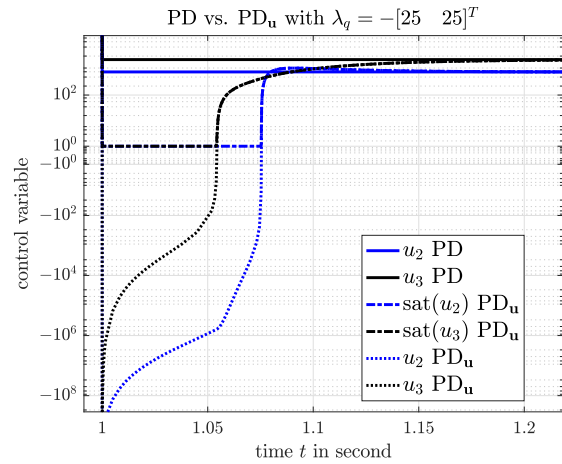
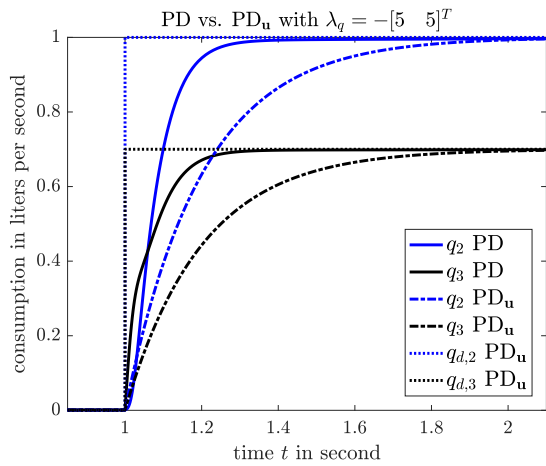
(A) \mathbf{r} according to figure 4.5A.(B) \mathbf{r} according to figure 4.5B.(C) \mathbf{u} according to figure 4.4A.(D) \mathbf{u} according to figure 4.4B.

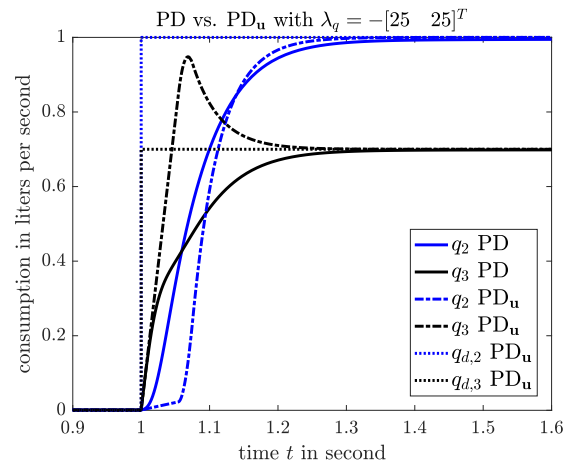
FIGURE 4.4: Comparison of PD simulating a jump in \mathbf{r} (solid lines in figure 4.4A) and $PD_{\mathbf{u}}$ simulating a jump in \mathbf{q}_d with different eigenvalues $\lambda_q = -[5 \ 5]^T$ (left), $\lambda_q = -[25 \ 25]^T$ (right), related to figure 4.5.

$\mathbf{u} \in [1, 10^9]$, meaning that $\epsilon_r = \sqrt{10^{-9}}$. Taking a closer look on the pressure heads of the previous example on the right side of figure 4.2, one can see clearly that the pressure already approaches zero at the time of switching (increasing \mathbf{r} instantaneously at $t = 1$ s). Knowing that the decoupling (in terms of the ODE (4.22)) of consumers through \mathbf{u} (4.26) requires additional effort, the control variable and thus \mathbf{r} will most likely reach its saturation if eigenvalues are chosen too aggressively. In contrast to PD, where \mathbf{r} is increased instantaneously, in $PD_{\mathbf{u}}$ the reference values \mathbf{q}_d are increased instantaneously from $\mathbf{q}_d(t < 1s) = \mathbf{0}$ to $\mathbf{q}_d(t \geq 1) = [1 \ 0.7]^T$ l/s.

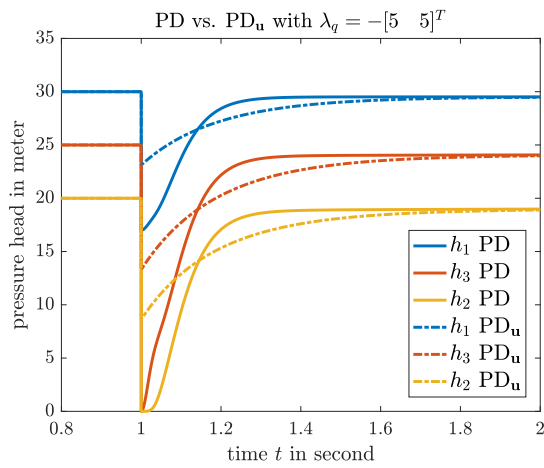
Too Slow and Too Fast. Concerning figure 4.5, the consumption $\mathbf{R}_q \mathbf{A} \mathbf{x}_Q$, pressure heads \mathbf{h} and flows \mathbf{x}_Q are compared when selecting orifice coefficients \mathbf{r} explicitly (best seen in figure 4.4A, solid line) in PD and when \mathbf{r} is determined through the saturated control law \mathbf{u} (4.26) in $PD_{\mathbf{u}}$. In comparison to the step response of PD, eigenvalues of $PD_{\mathbf{u}}$ are chosen too high $\lambda_q = -[5 \ 5]^T$ in figure 4.5A as it takes too long for $\mathbf{q} PD_{\mathbf{u}}$ to reach the desired values $\mathbf{q}_d = [1 \ 0.7]^T$ l/s. The opposite is the case for $\lambda_q = -[25 \ 25]^T$ in figure 4.5B where the control variable has to be saturated substantially (see figure 4.4D, dotted and dash dotted). The reason why the orifice



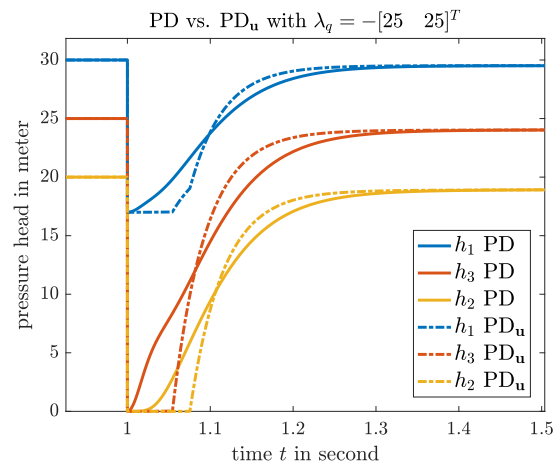
(A) Consumption with (too) slow dynamics.



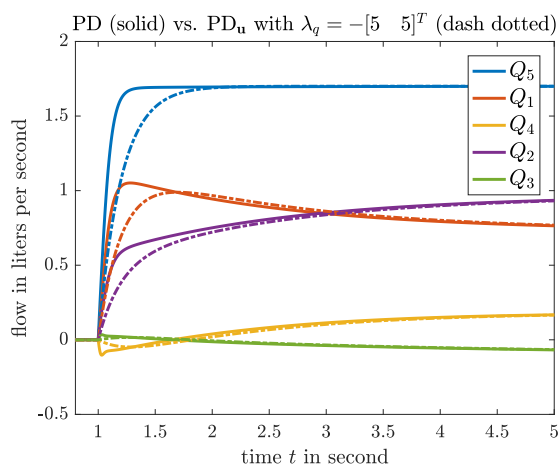
(B) Consumption with (too) fast dynamics.



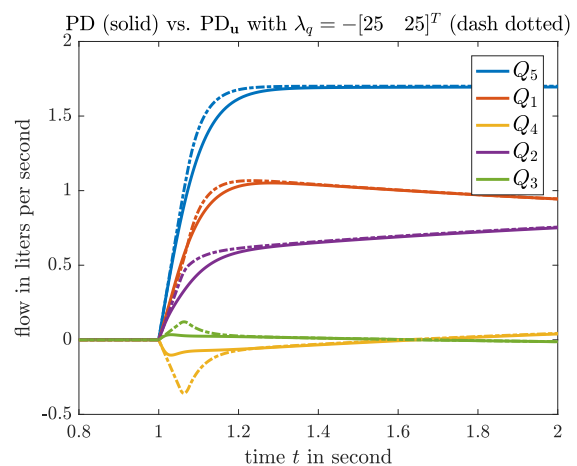
(C) Pressure heads.



(D) Pressure heads.



(E) Flows of PD (solid) and PD_u (dash dotted).



(F) Flows of PD (solid) and PD_u (dash dotted).

FIGURE 4.5: Consumption, pressure heads and flows of PD simulating a jump in r (solid lines in figure 4.4A) and PD_u with different eigenvalues $\lambda_q = -[5 \ 5]^T$ (left), $\lambda_q = -[25 \ 25]^T$ (right).

coefficients i.e. the control variable is in saturation can be best seen in the pressure heads (figure 4.5D), which are prohibited (indirectly) to become negative. Analogous to flows, dynamics are too slow in figure 4.5E and too fast in figure 4.5F, at least as long as one intends to mimic the rapid valve opening (considered for \mathbf{r} PD) by means of a rapid increase in \mathbf{q}_d .

Concerning figure 4.4, both control variable and orifice coefficients had to be plotted in order to visualize the saturation in $\mathbf{u} = \mathbf{r}^{\odot -2}$ as \mathbf{r} would become complex if \mathbf{u} is negative. Negative \mathbf{u} values correspond, loosely speaking, with orifice coefficients greater “1” and therefore lack a physical meaning. This is the reason why only the saturated part $\mathbf{r} = \text{sat}(\mathbf{u})^{\odot -1/2}$ was plotted. However, this effect is only seen in figure 4.4D in comparison to figure 4.4B where fast transients $\lambda_q = -[25 \ 25]^T$ force \mathbf{u} to become far negative, up to $\mathbf{u} \rightarrow -10^9$. In order to visualize the course over this large range figure 4.4B, 4.4C and 4.4D were plotted with logarithmic scale on the y -axes, also accounting for the negative y -axes in figure 4.4D. In conclusion, the built-in saturation which only allows orifice coefficients to be non-negative and smaller or equal to “1” represents a natural pressure-limiting factor in the model equations.

Suitable Eigenvalues. With the intention to implement a pressure-limiting behavior for $\text{PD}_{\mathbf{u}}$ which is close or at least similar to PD, eigenvalues can be adjusted accordingly. Emphasizing once again on the major difference, instead of increasing \mathbf{r} instantaneously at $t = 1\text{s}$ in PD, the desired consumption \mathbf{q}_d is increased instantaneously at $t = 1\text{s}$ in $\text{PD}_{\mathbf{u}}$ which then allows to let orifice coefficients \mathbf{r} be unknown (in comparison to PD).

In figure 4.6 the eigenvalues $\lambda_q = -[9.754 \ 12.8631]^T$ where chosen such that the qualitative behavior of \mathbf{q} $\text{PD}_{\mathbf{u}}$ approximately matches \mathbf{q} PD.

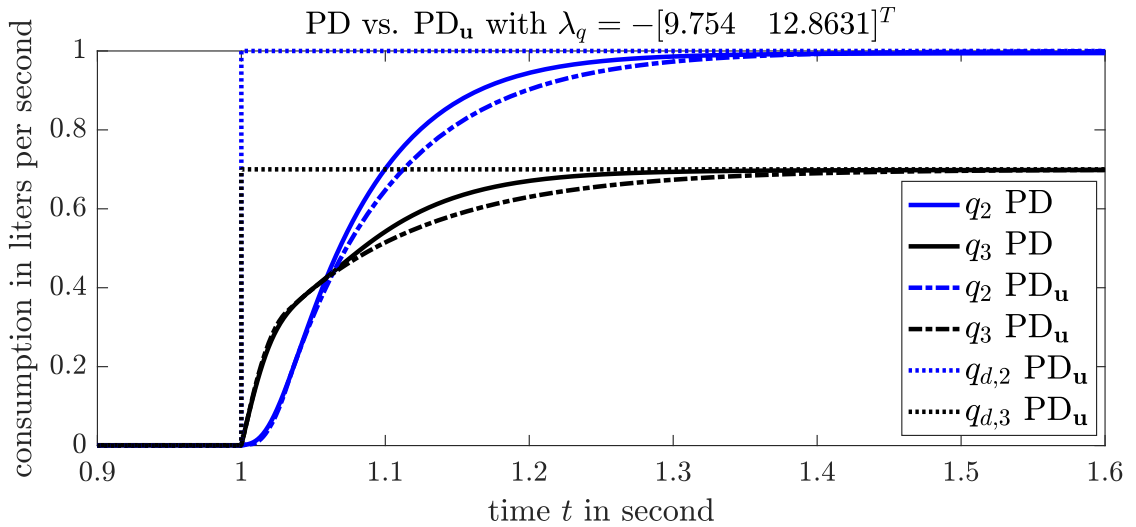


FIGURE 4.6: Consumption \mathbf{q} $\text{PD}_{\mathbf{u}}$ with ideal dynamics in respect to \mathbf{q} PD.

Although the consumption will and also should not look identical, the qualitative reaction to the pressure limit is somehow physically related. While the slope of q_2 PD is decreased substantially at $t \approx [1, 1.03]\text{s}$ after q_3 PD starts to increase due to limited pressure (see figure 4.7A) concerning PD (detailed explanation in section 4.3.1), the effort to compensate this coupling effect by the control variable \mathbf{u} concerning $\text{PD}_{\mathbf{u}}$ is so large that $\mathbf{r} = \text{sat}(\mathbf{u})^{\odot -1/2}$ reaches its physical limit (fully opened consumer orifices). In other words, in this situation the control fails to achieve the decoupling of consumers which is exactly what provides the intended physical limitation.

Particularly in the consumption but also in the flows (figure 4.7B), one can see that the quadratic term $(\mathbf{R}_q \mathbf{A} \mathbf{x}_q)^{\odot 2}$ in the model equations (4.20) causes \mathbf{x}_Q and \mathbf{q} to approach their steady-state values faster in PD compared to $\text{PD}_{\mathbf{u}}$. This is no surprise when knowing that \mathbf{q} $\text{PD}_{\mathbf{u}}$ follows the linear differential equation (4.22), at least when \mathbf{u} is not saturated. However, pressure heads in

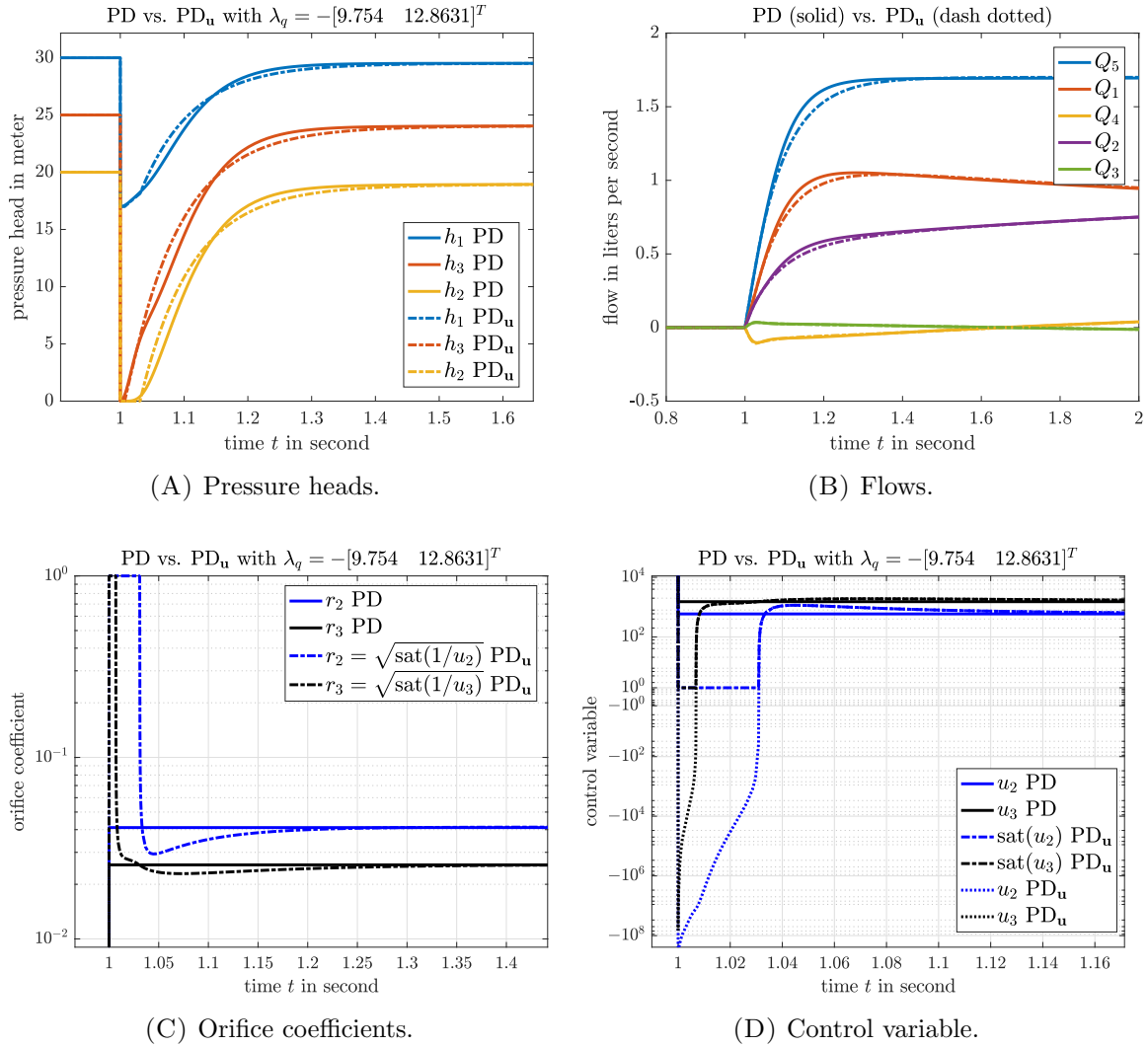


FIGURE 4.7: Pressure heads, flows and orifice coefficients in reference figure to 4.6, comparing PD with PD_u using eigenvalues $\lambda_q = -[9.754 \quad 12.8631]^T$.

figure 4.7A indeed look very similar with some distinct differences in the recovery period from the rapid valve opening. Nevertheless, the unsaturated control variable in figure 4.7D reaches, analogous to the previous results (figure 4.4D) far negative values. This is likely to occur when the consumption is close to zero (it is prohibited to reach zero exactly) and far from the desired values \mathbf{q}_d as a reason of control variable \mathbf{u} being directly proportional to $\mathbf{q}^{\odot -2} = (\mathbf{R}_q \mathbf{A} \mathbf{x}_Q)^{\odot -2}$. Also, the point where \mathbf{u} enters the saturation certainly depends on selected maximal pipe openings \mathbf{a}_q , however, it makes sense physically to equate \mathbf{a}_q to the largest cross section area of the pipe connected to the respective consumer node.

Nevertheless, eigenvalues $\lambda_q = -[9.754 \quad 12.8631]^T$ where chosen for the appropriate consumption $\mathbf{q}_d = [1 \quad 0.7]^T$ 1/s and, as a consequence, by changing (drastically increasing) \mathbf{q}_d also these somewhat ideal eigenvalues might be inappropriate. As shown in figure 4.8, a target consumption with $\mathbf{q}_d = [0.5 \quad 1.5]^T$ 1/s on the left and $\mathbf{q}_d = [1 \quad 2]^T$ 1/s on the right with a consistently higher load on node 3 in comparison to node 2 was simulated. Although the consumption well matches in figure 4.8A, the results are indeed very distinct in figure 4.8B with the total consumption of 3 l/s which forces the control variable into high saturation. In this last example one reaches the very limits of the small hydraulic network with a source pressure of only $h_s = 30$ m.

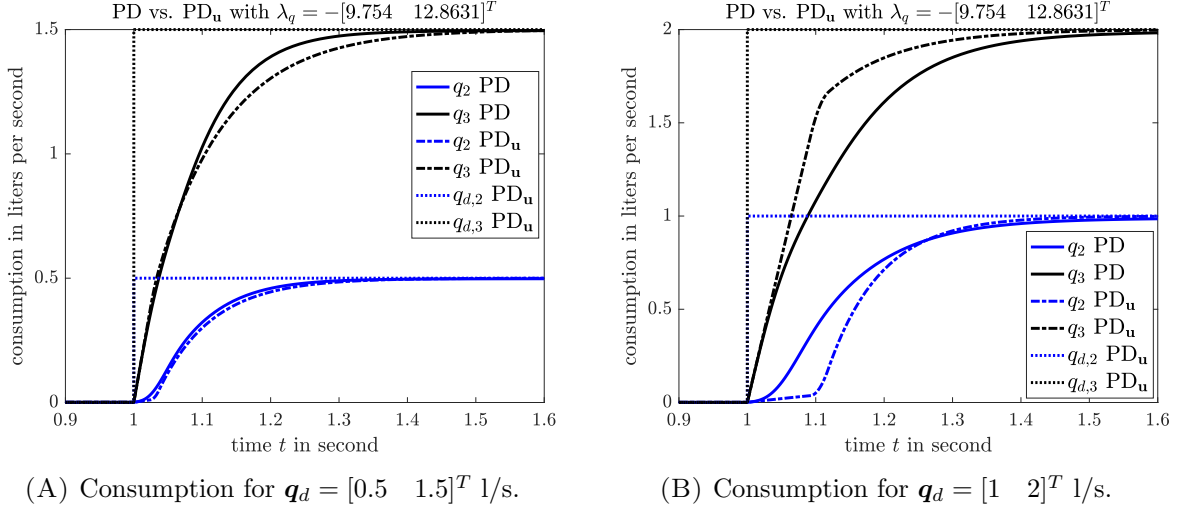


FIGURE 4.8: Comparing PD with $\text{PD}_{\mathbf{u}}$ with different target consumption values while applying eigenvalues $\lambda_q = -[9.754 \ 12.8631]^T$.

4.5 Steady-State Properties

In this section the steady-state properties of LCD are investigated. Since LCD is identical to $\text{PD}_{\mathbf{u}}$ as long as \mathbf{u} remains in the boundaries $\mathbf{1} \leq \mathbf{u} \leq \mathbf{1}\epsilon_r^{-2}$ according Theorem 4.11, the equilibria of LCD and $\text{PD}_{\mathbf{u}}$ are identical if Assumption 4.10 holds. The missing piece in this context is the direct relation to the steady-state hydraulic network equations as in (3.24)

$$\mathbf{A}\mathbf{x}_e = \mathbf{R}_q^T \mathbf{q}_d \quad (4.44a)$$

$$\mathbf{A}^T \mathbf{h} = \tilde{\mathbf{C}}_s \mathbf{h}_s - \mathbf{h}_{\text{loss}}(\mathbf{x}_e) - \mathbf{A}^T \mathbf{z} \quad (4.44b)$$

with equilibrium solution \mathbf{x}_e . Provided Assumption 4.10 holds, the nodal consumption of $\text{PD}_{\mathbf{u}}$ becomes $\bar{\mathbf{q}} = \mathbf{R}_q^T \mathbf{q}_d$ in steady-state (see Properties 4.5).

Theorem 4.15. *Let Assumption 4.2 hold. Then the solution \mathbf{x}_e of the dynamic equations (4.30a) of LCD in the equilibrium $\frac{d\mathbf{x}_Q}{dt} = \mathbf{0}$*

$$\mathbf{f}_Q(\mathbf{x}_e) = \mathbf{G} \left(\tilde{\mathbf{C}}_s \mathbf{h}_s - \mathbf{h}_{\text{loss}}(\mathbf{x}_e) \right) + \mathbf{M} \left(\mathbf{R}_q \mathbf{A} \mathbf{x}_e - \mathbf{q}_d \right) = \mathbf{0} \quad (4.45a)$$

and the resulting pressure heads $\mathbf{h}(\mathbf{x}_e)$ (4.30b)

$$\mathbf{h}(\mathbf{x}_e) = \mathbf{L}^{-1} \left[\mathbf{A} \text{diag}(\mathbf{c}_l) \left(\tilde{\mathbf{C}}_s \mathbf{h}_s - \mathbf{h}_{\text{loss}}(\mathbf{x}_e) - \mathbf{A}^T \mathbf{z} \right) - \mathbf{R}_q^T \text{diag}(\lambda_q) \left(\mathbf{R}_q \mathbf{A} \mathbf{x}_e - \mathbf{q}_d \right) \right] \quad (4.45b)$$

solve the steady-state equations $\Gamma_h(\mathbf{x}_e)$ (4.44) and vice versa.

Remark 4.16. *System (4.45a) is generally underdetermined. It can be uniquely solved if initial conditions according to Assumption 4.2 are considered. Conditions $\bar{\mathbf{R}}_q \mathbf{A} \mathbf{x}_e = \mathbf{0}$ and $\mathbf{f}_Q(\mathbf{x}_e) = \mathbf{0}$ can be combined in*

$$\tilde{\mathbf{f}}_Q(\mathbf{x}_e) = \mathbf{G} \left(\tilde{\mathbf{C}}_s \mathbf{h}_s - \mathbf{h}_{\text{loss}}(\mathbf{x}_e) \right) + \text{diag}(\mathbf{c}_l) \mathbf{A}^T \mathbf{L}^{-1} \text{diag} \left(\mathbf{R}_q^T \lambda_q + \bar{\mathbf{R}}_q^T \mathbf{1}_{n_j - n_q} \right) \left(\mathbf{A} \mathbf{x}_e - \mathbf{R}_q^T \mathbf{q}_d \right) \quad (4.46)$$

when solving $\tilde{\mathbf{f}}_Q(\mathbf{x}_e) = \mathbf{0}$. As $\bar{\mathbf{R}}_q \mathbf{A} \mathbf{f}_Q \equiv \mathbf{0}$ independently from \mathbf{x}_e , (4.46) also forces non-consumer equations to zero (Property 4.5) $\bar{\mathbf{R}}_q \mathbf{A} \tilde{\mathbf{f}}_Q = \bar{\mathbf{R}}_q \mathbf{A} \mathbf{x}_e$ when $\tilde{\mathbf{f}}_Q = \mathbf{0}$. However, since (4.44a) already implies $\bar{\mathbf{R}}_q \mathbf{A} \mathbf{x}_e = \mathbf{0}$, it can be omitted from the following proof.

Proof. It is shown that the following statements end up in contradiction.

- (i) $\mathbf{A}\mathbf{x}_e = \mathbf{R}_q^T \mathbf{q}_d \wedge \mathbf{f}_Q(\mathbf{x}_e) = \mathbf{0} \wedge \mathbf{A}^T \mathbf{h} \neq \tilde{\mathbf{C}}_s \mathbf{h}_s - \mathbf{h}_{\text{loss}}(\mathbf{x}_e) - \mathbf{A}^T \mathbf{z}$
- (ii) $\mathbf{A}\mathbf{x}_e = \mathbf{R}_q^T \mathbf{q}_d \wedge \mathbf{f}_Q(\mathbf{x}_e) \neq \mathbf{0} \wedge \mathbf{A}^T \mathbf{h} = \tilde{\mathbf{C}}_s \mathbf{h}_s - \mathbf{h}_{\text{loss}}(\mathbf{x}_e) - \mathbf{A}^T \mathbf{z}$
- (iii) $\mathbf{A}\mathbf{x}_e \neq \mathbf{R}_q^T \mathbf{q}_d \wedge \mathbf{f}_Q(\mathbf{x}_e) = \mathbf{0} \wedge \mathbf{A}^T \mathbf{h} = \tilde{\mathbf{C}}_s \mathbf{h}_s - \mathbf{h}_{\text{loss}}(\mathbf{x}_e) - \mathbf{A}^T \mathbf{z}$
- (iv) $\mathbf{A}\mathbf{x}_e \neq \mathbf{R}_q^T \mathbf{q}_d \wedge \mathbf{f}_Q(\mathbf{x}_e) \neq \mathbf{0} \wedge \mathbf{A}^T \mathbf{h} \neq \tilde{\mathbf{C}}_s \mathbf{h}_s - \mathbf{h}_{\text{loss}}(\mathbf{x}_e) - \mathbf{A}^T \mathbf{z}$

Concerning (i), system (4.45) is written for $\mathbf{A}\mathbf{x}_e = \mathbf{R}_q^T \mathbf{q}_d \Rightarrow \mathbf{R}_q \mathbf{A}\mathbf{x}_e = \mathbf{q}_d$, \mathbf{A}^T is multiplied to (4.45b) from the left

$$\begin{aligned} \mathbf{0} &= \mathbf{G} \left(\tilde{\mathbf{C}}_s \mathbf{h}_s - \mathbf{h}_{\text{loss}}(\mathbf{x}_e) \right) = \mathbf{G} \left(\tilde{\mathbf{C}}_s \mathbf{h}_s - \mathbf{h}_{\text{loss}}(\mathbf{x}_e) - \mathbf{A}^T \mathbf{z} \right) \\ &\Leftrightarrow \tilde{\mathbf{C}}_s \mathbf{h}_s - \mathbf{h}_{\text{loss}}(\mathbf{x}_e) - \mathbf{A}^T \mathbf{z} = \mathbf{A}^T \mathbf{L}^{-1} \mathbf{A} \text{diag}(\mathbf{c}_l) \left(\tilde{\mathbf{C}}_s \mathbf{h}_s - \mathbf{h}_{\text{loss}}(\mathbf{x}_e) - \mathbf{A}^T \mathbf{z} \right) \end{aligned} \quad (4.47a)$$

$$\mathbf{A}^T \mathbf{h} = \mathbf{A}^T \mathbf{L}^{-1} \mathbf{A} \text{diag}(\mathbf{c}_l) \left(\tilde{\mathbf{C}}_s \mathbf{h}_s - \mathbf{h}_{\text{loss}}(\mathbf{x}_e) - \mathbf{A}^T \mathbf{z} \right) \quad (4.47b)$$

and when inserting (4.47a) into (4.47b)

$$\mathbf{A}^T \mathbf{h} = \tilde{\mathbf{C}}_s \mathbf{h}_s - \mathbf{h}_{\text{loss}}(\mathbf{x}_e) - \mathbf{A}^T \mathbf{z} \quad (4.48)$$

it is apparent that (4.48) contradicts statement (i).

Considering statement (ii) and the definition of \mathbf{G} below (4.30)

$$\begin{aligned} \mathbf{0} &\neq \text{diag}(\mathbf{c}_l) \left(\mathbf{I} - \mathbf{A}^T \mathbf{L}^{-1} \mathbf{A} \text{diag}(\mathbf{c}_l) \right) \left(\tilde{\mathbf{C}}_s \mathbf{h}_s - \mathbf{h}_{\text{loss}}(\mathbf{x}_e) \right) \\ &\Leftrightarrow \mathbf{0} \neq \left(\tilde{\mathbf{C}}_s \mathbf{h}_s - \mathbf{h}_{\text{loss}}(\mathbf{x}_e) - \mathbf{A}^T \mathbf{z} \right) - \mathbf{A}^T \mathbf{L}^{-1} \mathbf{A} \text{diag}(\mathbf{c}_l) \left(\tilde{\mathbf{C}}_s \mathbf{h}_s - \mathbf{h}_{\text{loss}}(\mathbf{x}_e) - \mathbf{A}^T \mathbf{z} \right) \end{aligned} \quad (4.49)$$

the right term on the right hand side of (4.49) is replaced with $\mathbf{A}^T \mathbf{h}$ according to (4.47b) and (4.45b) multiplied with \mathbf{A}^T from the left

$$\mathbf{0} \neq \tilde{\mathbf{C}}_s \mathbf{h}_s - \mathbf{h}_{\text{loss}}(\mathbf{x}_e) - \mathbf{A}^T \mathbf{z} - \mathbf{A}^T \mathbf{h}. \quad (4.50)$$

The contradiction is evident, statement (ii) is false.

Concerning statement (iii), (4.44b) is inserted into (4.45a)

$$\begin{aligned} \mathbf{0} &= \text{diag}(\mathbf{c}_l) \left(\mathbf{I} - \mathbf{A}^T \mathbf{L}^{-1} \mathbf{A} \text{diag}(\mathbf{c}_l) \right) \mathbf{A}^T \mathbf{h} + \mathbf{M} (\mathbf{R}_q \mathbf{A}\mathbf{x}_e - \mathbf{q}_d) \\ &\Leftrightarrow \mathbf{0} = \text{diag}(\mathbf{c}_l) \mathbf{A}^T \mathbf{L}^{-1} \mathbf{R}_q^T \text{diag}(\boldsymbol{\lambda}_q) (\mathbf{R}_q \mathbf{A}\mathbf{x}_e - \mathbf{q}_d). \end{aligned} \quad (4.51)$$

Then, \mathbf{A} is multiplied from the left to (4.51).

$$\mathbf{0} = \mathbf{R}_q^T \text{diag}(\boldsymbol{\lambda}_q) (\mathbf{R}_q \mathbf{A}\mathbf{x}_e - \mathbf{q}_d) \quad (4.52)$$

$$\Leftrightarrow \mathbf{0} = \mathbf{R}_q \mathbf{A}\mathbf{x}_e - \mathbf{q}_d \quad (4.53)$$

When separating (4.52) by multiplying with $\bar{\mathbf{R}}_q$, one gets $\bar{\mathbf{R}}_q \mathbf{R}_q^T = \mathbf{0}$ according to Property 4.5. This is the part where Assumption 4.2 comes into play. As $\bar{\mathbf{R}}_q \mathbf{R}_q^T = \mathbf{0}$ for every \mathbf{x}_e in $\mathbf{f}_Q(\mathbf{x}_e)$, $\bar{\mathbf{R}}_q \mathbf{A}\mathbf{x}_e = \mathbf{0}$ would not be guaranteed within $\mathbf{f}_Q(\mathbf{x}_e) = \mathbf{0}$ without demanding consistent initial states. However, when multiplying with \mathbf{R}_q one gets (4.53), seeing the contradiction with (iii).

Regarding statement *(iv)*, system (4.45) is used once again whereas $\text{diag}(\mathbf{c}_l^{\odot -1})$ is multiplied from the left to (4.45a) and \mathbf{A}^T from the left to (4.45b).

$$\mathbf{0} = \mathbf{A}^T \mathbf{L}^{-1} \mathbf{R}_q^T \text{diag}(\boldsymbol{\lambda}_q) (\mathbf{R}_q \mathbf{A} \mathbf{x}_e - \mathbf{q}_d) + \left(\mathbf{I} - \mathbf{A}^T \mathbf{L}^{-1} \mathbf{A} \text{diag}(\mathbf{c}_l) \right) \left(\tilde{\mathbf{C}}_s \mathbf{h}_s - \mathbf{h}_{\text{loss}}(\mathbf{x}_e) - \mathbf{A}^T \mathbf{z} \right) \quad (4.54)$$

$$\mathbf{A}^T \mathbf{h} = \mathbf{A}^T \mathbf{L}^{-1} \mathbf{A} \text{diag}(\mathbf{c}_l) \left(\tilde{\mathbf{C}}_s \mathbf{h}_s - \mathbf{h}_{\text{loss}}(\mathbf{x}_e) - \mathbf{A}^T \mathbf{z} \right) - \mathbf{A}^T \mathbf{L}^{-1} \mathbf{R}_q^T \text{diag}(\boldsymbol{\lambda}_q) (\mathbf{R}_q \mathbf{A} \mathbf{x}_e - \mathbf{q}_d) \quad (4.55)$$

After looking carefully at the above equations, one may see that (4.55) can in fact be inserted into (4.54), resulting in

$$\mathbf{0} = \left(\tilde{\mathbf{C}}_s \mathbf{h}_s - \mathbf{h}_{\text{loss}}(\mathbf{x}_e) - \mathbf{A}^T \mathbf{z} \right) - \mathbf{A}^T \mathbf{h} \quad (4.56)$$

which is a contradiction to statement *(iv)*. Subsequently, there exists no \mathbf{x}_e which solves $\boldsymbol{\Gamma}_h(\mathbf{x}_e)$ (4.44) but not $\mathbf{f}_Q(\mathbf{x}_e) = \mathbf{0}$ (or vice versa).

The uniqueness of \mathbf{x}_e follows from the fact that $\boldsymbol{\Gamma}_h(\mathbf{x}_e)$ (4.45) has a unique solution according to Proposition 3.12 if function $\mathbf{h}_{\text{loss}}(\mathbf{x}_e)$ is (strictly) monotonically increasing, continuous and once continuously differentiable (see Assumption 3.10 and Remark 3.13). ■

Regarding Remark 4.16, is also important to note that once initial states are chosen such that $\tilde{\mathbf{R}}_q \mathbf{A} \mathbf{x}_Q(t_0) = \mathbf{0}$ the trajectory $\tilde{\mathbf{R}}_q \mathbf{A} \mathbf{x}_Q \equiv \mathbf{0}$ is identical to zero for all $t \geq t_0$ as $\tilde{\mathbf{R}}_q \mathbf{A} \mathbf{f}_Q \equiv \mathbf{0}$. This is the reason why Theorem 4.15 requires Assumption 4.2.

4.6 Notes on Stability

Since hydraulic networks are in general nonlinear, a closer look at the stability of the system's unique equilibrium provides some interesting insights.

Cycle or Co-Tree Flow Dynamics. Considering flow transients of DD (4.43), flows are expressed by co-tree flows and the consumption $\mathbf{x}_Q = \mathbf{S}^T \mathbf{x}_{\bar{t}} + \mathbf{T}_t \mathbf{A}_t^{-1} \bar{\mathbf{q}}$ (see (3.27)).

$$\text{diag}(\mathbf{c}_l^{\odot -1}) \left(\mathbf{S}^T \frac{d\mathbf{x}_{\bar{t}}}{dt} + \mathbf{T}_t \mathbf{A}_t^{-1} \frac{d\bar{\mathbf{q}}}{dt} \right) = \left(\mathbf{I} - \mathbf{A}^T \mathbf{L}^{-1} \mathbf{A} \text{diag}(\mathbf{c}_l) \right) \left(\tilde{\mathbf{C}}_s \mathbf{h}_s - \mathbf{h}_{\text{loss}}(\mathbf{x}_Q) \right) + \mathbf{A}^T \mathbf{L}^{-1} \frac{d\bar{\mathbf{q}}}{dt} \quad (4.57)$$

When multiplying (4.57) with cycle matrix \mathbf{S} from the left one receives

$$\frac{d\mathbf{x}_{\bar{t}}}{dt} = \left(\mathbf{S} \text{diag}(\mathbf{c}_l^{\odot -1}) \mathbf{S}^T \right)^{-1} \mathbf{S} \left(\tilde{\mathbf{C}}_s \mathbf{h}_s - \mathbf{h}_{\text{loss}}(\mathbf{x}_Q) - \text{diag}(\mathbf{c}_l^{\odot -1}) \mathbf{T}_t \mathbf{A}_t^{-1} \frac{d\bar{\mathbf{q}}}{dt} \right) \quad (4.58)$$

knowing that $\mathbf{S} \mathbf{A}^T = \mathbf{0}$ according to Proposition 3.6. ODEs similar to (4.58) are usually known as loop or cycle dynamics as the number of variables $\mathbf{x}_{\bar{t}}$ equals the number of cycles $n_c = n_\ell - n_j$ in the network, however, in this thesis the author refers (4.58) to the co-tree flow dynamics (see Definition 3.9).

Remark 4.17. As $\mathbf{c}_l \in \mathbb{R}_{>0}^{n_\ell}$ (4.4) and $\mathbf{S} \in \mathbb{Z}_{\{-1,0,1\}}^{(n_\ell - n_j) \times n_\ell}$ with full rank $(\mathbf{S}) = n_\ell - n_j$ (Proposition 3.6 and Corollary 3.8), it is evident that $\mathbf{S} \text{diag}(\mathbf{c}_l^{\odot -1}) \mathbf{S}^T \succ 0$ is positive definite.

Interestingly, the same applies for PD. Taking (4.20) while expressing \mathbf{x}_Q by co-tree flows and the consumption

$$\begin{aligned} \text{diag} \left(\mathbf{c}_l^{\odot -1} \right) \left(\mathbf{S}^T \frac{d\mathbf{x}_{\bar{t}}}{dt} + \mathbf{T}_t \mathbf{A}_t^{-1} \frac{d\bar{\mathbf{q}}}{dt} \right) &= \left(\mathbf{I} - \mathbf{A}^T \bar{\mathbf{R}}_q^T \left(\bar{\mathbf{R}}_q \mathbf{L} \bar{\mathbf{R}}_q^T \right)^{-1} \bar{\mathbf{R}}_q \mathbf{A} \text{diag}(\mathbf{c}_l) \right) \\ &\times \left[\tilde{\mathbf{C}}_s \mathbf{h}_s - \mathbf{h}_{\text{loss}}(\mathbf{x}_Q) - \mathbf{A}^T \left(\frac{1}{2g} \mathbf{R}_q^T \left(\mathbf{a}_q^{\odot -2} \odot (\mathbf{R}_q \mathbf{A} \mathbf{x}_Q)^{\odot 2} \odot \mathbf{r}^{\odot -2} \right) + \mathbf{z} \right) \right] \end{aligned} \quad (4.59)$$

all terms different to (4.57) become zero when multiplying cycle matrix \mathbf{S} from the left to (4.59). As a result, the co-tree flow dynamics of DD and PD and thus of LCD are only distinguished by $\frac{d\bar{\mathbf{q}}}{dt}$ the derivative of the nodal consumption. Suppose the nodal consumption $\bar{\mathbf{q}}(t) = \mathbf{A} \mathbf{x}_Q(t)$ remains constant over time $\frac{d\bar{\mathbf{q}}}{dt} = \mathbf{0}$ for $t \geq t_0$. Then,

$$\frac{d\mathbf{x}_{\bar{t}}}{dt} = \left(\mathbf{S} \text{diag} \left(\mathbf{c}_l^{\odot -1} \right) \mathbf{S}^T \right)^{-1} \mathbf{S} \left(\tilde{\mathbf{C}}_s \mathbf{h}_s - \mathbf{h}_{\text{loss}}(\mathbf{x}_Q) \right). \quad (4.60)$$

Now a relation to the optimization problem (3.29), which is proportional to the total energy used in the network, can be drawn (see section 3.1.5). As a direct consequence of Theorem 4.15, the unique solution of this strictly convex optimization problem is the equilibrium of DD and LCD, the same equilibrium which also solves the steady-state network equations (3.23).

Theorem 4.18. *Let Assumption 3.10 hold and suppose the consumption is constant over time $\frac{d\bar{\mathbf{q}}}{dt} = \mathbf{0}$. Then, the equilibrium $\mathbf{x}_e = \mathbf{S}^T \mathbf{x}_{\bar{t}}^* + \mathbf{T}_t \mathbf{A}_t^{-1} \bar{\mathbf{q}}$ with co-tree equilibrium flow $\mathbf{x}_{\bar{t}}^*$ of DD and PD and thus LCD is globally asymptotically stable. $V(\mathbf{x}_{\bar{t}}) = f(\mathbf{x}_{\bar{t}}) - f(\mathbf{x}_{\bar{t}}^*)$, applying function $f(\cdot)$ of problem (3.29), is a strict Lyapunov function.*

Proof. The Lyapunov function was first proposed by Piller and Propato [2006] as far as the author is aware. The strictly convex function satisfies $f(\mathbf{x}_{\bar{t}}) > f(\mathbf{x}_{\bar{t}}^*) \forall \mathbf{x}_{\bar{t}}$. Subsequently, $V = f(\mathbf{x}_{\bar{t}}) - f(\mathbf{x}_{\bar{t}}^*) > 0 \forall \mathbf{x}_{\bar{t}}$ the Lyapunov function is strictly positive. Given Remark 4.17, the derivative of the Lyapunov function

$$\begin{aligned} \frac{dV}{dt} &= \frac{\partial f}{\partial \mathbf{x}_Q} \frac{\partial \mathbf{x}_Q}{\partial \mathbf{x}_{\bar{t}}} \frac{d\mathbf{x}_{\bar{t}}}{dt} = \\ &= - \left(\tilde{\mathbf{C}}_s \mathbf{h}_s - \mathbf{h}_{\text{loss}}(\mathbf{x}_Q) \right)^T \mathbf{S}^T \left(\mathbf{S} \text{diag}(\mathbf{c}_l^{\odot -1}) \mathbf{S}^T \right)^{-1} \mathbf{S} \left(\tilde{\mathbf{C}}_s \mathbf{h}_s - \mathbf{h}_{\text{loss}}(\mathbf{x}_Q) \right) < 0 \quad \forall \mathbf{x}_Q \neq \mathbf{x}_e \end{aligned} \quad (4.61)$$

is smaller zero for all $\mathbf{S}(\tilde{\mathbf{C}}_s \mathbf{h}_s - \mathbf{h}_{\text{loss}}(\mathbf{x}_Q)) \neq \mathbf{0}$. Knowing that this is only the case in the equilibrium itself according to Theorem 4.15 (cf. with steady-state equations $\mathbf{\Gamma}$ (3.23)), it is evident that Theorem 4.18 holds. \blacksquare

Deducing generally valid statements concerning the hydraulic network's stability becomes more delicate when accounting for varying consumption. This is somehow analogous to control theory where one usually also only considers the "autonomous" system, setting the control variable to zero (or to a constant equilibrium control value). Nevertheless, from a physical perspective it is somehow obvious that the system is stable, knowing that consumers are capable to withdraw water only if enough pressure is available. Thereby the system's states, flows in this case, are certainly bounded and, importantly, are zero if the consumption is zero. The fact that there is no flow in the network if the consumption is zero can be directly derived from the principle of least action which is related, mathematically, to the optimization energy-function $f(\mathbf{x}_{\bar{t}})$ regarding problem (3.29).

Considering (4.58), the co-tree flow dynamics would be sufficient to determine all flows in the network, at least when either user DD or LCD. By solving (4.58) one receives $\mathbf{x}_{\bar{t}}$ and in a second step tree flows $\mathbf{x}_t = \mathbf{A}_t^{-1} (\bar{\mathbf{q}} - \mathbf{A}_{\bar{t}} \mathbf{x}_{\bar{t}})$. This, however, requires the explicit knowledge of the consumption, a requirement which can not be fulfilled when accounting for a pressure-driven

consumption. However, concerning LCD one would apply the solution of the linear differential equation (4.22) which provides that neither too high target consumption values nor too low source pressures (or too aggressive eigenvalues) force the network into saturation (Assumption 4.10).

4.7 Coupling With Dynamic Elements

It was assumed that the pressure at all critical elements concerning nodes \mathfrak{S} is measured and treated as input variable by means of \mathbf{h}_s . In this section, models for water tanks and air vessels will turn out to be representable by ODEs which can be coupled with the derived model equations.

Remark 4.19. *In order for control law (4.26) to be compatible with these elements, \mathbf{u} must be extended appropriately, completely analogous to section 4.4.1.*

4.7.1 Air Vessel

If compared to a mechanical system, an air vessel damps pressure peaks in a hydraulic network to prevent the infrastructure from getting harmed. These air chambers are usually installed near pump stations and hydroelectric power plants to safeguard the most expensive components of a water distribution system. Since the lifespan of pipes and fittings also heavily suffer from too rapid pressure changes, the employment of such elements might be crucial from a cost perspective.

Allowing more physical considerations, the chamber typically encloses a compressed gas mix at its top (usually air as in figure 4.9), whereas a non-permeable but flexible membrane separates this mix from the water. At the bottom of the air chamber a connection to the hydraulic network makes it possible to exchange water, whereas the resulting water height is a direct indicator of the vessel pressure h_{av} . The following derivation of the air vessel model is based on the thesis of [Axworthy, 1997] as well as [Wylie and Streeter, 1978] and [Chaudhry, 2014]. The vessel is

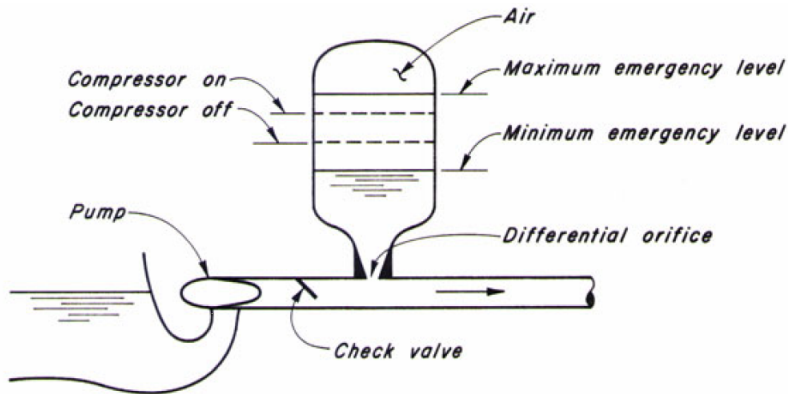


FIGURE 4.9: Air vessel (source [Chaudhry, 2014], Figure 10-2).

connected via an inertia or pipe element to a common network node $n_{av} \in \mathfrak{N}$ with pressure head $h_{n_{av}}$ at elevation $z_{n_{av}}$. Thereby, h_{av} denotes the pressure head at the bottom of the vessel itself and varies with the pressure (head) of the gas mix h_g and with the pressure coming from the network. In this context z_{av} denotes the geographical elevation of the bottom (with respect to the water) of the vessel. Then, the exchange flow Q_{av}

$$\frac{dQ_{av}}{dt} = \underbrace{\frac{gA_{av}}{l_{av}}}_{c_{av}} (h_{n_{av}} + z_{n_{av}} - (h_{av} + z_{av}) - h_{\text{loss},av}(Q_{av})) \quad (4.62)$$

from the network into the vessel and vice versa is given by ODE (4.62). The pressure drop at the differential orifice in figure 4.9 can be included in the head loss $h_{av,loss}$ by increasing its minor loss coefficient appropriately. The pressure head at the bottom of the vessel

$$h_{av} = h_g + z_{H_2O} - h_{atm} \quad (4.63)$$

consists of relative gas pressure $h_g - h_{atm}$ and the head increase coming from the network thereby provoking the water to rise z_{H_2O} meters. After differentiating this equation

$$\frac{dh_{av}}{dt} = \dot{h}_g + \dot{z}_{H_2O} \quad (4.64)$$

the barometric thus constant component h_{atm} disappears. The change in gas pressure h_g results in a contraction or expansion of the gas volume. This relation is specified by the polytropic gas law

$$h_g V_g^{n_g} = c_g \quad (4.65)$$

of an ideal gas, which implies that the product of gas pressure h_g times the gas volume V_g (occupied in the vessel) to the power of the polytropic exponent n_g remains at a constant value c_g . The exponent is usually fixed at $n_g = 1.2$ according practical applications [Axworthy, 1997]. On the basis of the assumption that the water density will approximately remain constant, the change in gas volume and thereby the change of the water height times the cross section area of the vessel A_{av}

$$\frac{dV_g}{dt} = A_{av} \frac{dz_{H_2O}}{dt} = -Q_{av} \quad (4.66)$$

equals the discharge into the network. The derivative of (4.65) yields

$$\dot{h}_g = -\frac{n_g c_g}{V_g^{n_g+1}} \dot{V}_g \quad (4.67)$$

and makes it possible to summarize the three model equations of the air vessel.

$$\begin{aligned} \frac{dQ_{av}}{dt} &= c_{av} (h_{n_{av}} + z_{n_{av}} - (h_{av} + z_{av}) - h_{av,loss}(Q_{av})) \\ \frac{dh_{av}}{dt} &= \left(\frac{n_g c_g}{V_g^{n_g+1}} + \frac{1}{A_{av}} \right) Q_{av} \\ \frac{dV_g}{dt} &= -Q_{av} \end{aligned} \quad (4.68)$$

In the case of a rapid pressure peak somewhere in the network, for instance as a reason of a pipe burst, the pressure wave reaching the vessel will cause the gas volume to contract, which in turn provokes the water to flow from the network into the vessel and thereby damping the wave's amplitude. After the pressure decreases again the water will flow back into the network as the gas volume starts expanding.

The incorporation into the network is simply achieved by adding flow Q_{av} to nodal equations $\mathbf{A}\mathbf{x}_Q = \bar{\mathbf{q}}$ while modifying incidence matrix \mathbf{A} in terms of node n_{av} .

4.7.2 Surge Tanks

In contrast to reservoirs, where the outflow is negligible in comparison to the total amount of water, the source pressure in tanks decreases with increasing outflow. As the total volume of the tank $V_t = A_{\text{tank}} h_{s,t}$ is the product of its cross section area A_{tank} and the water height $h_{s,t}$ or source pressure head, its derivative

$$\frac{dh_{s,t}}{dt} = -\frac{1}{A_{\text{tank}}} Q_t \quad (4.69a)$$

equals the discharge Q_t into the network. This pipe flow follows

$$\frac{l_t}{gA_t} \frac{dQ_t}{dt} = h_t - h_{n_t} - h_{\text{loss},t}(Q_t) \quad (4.69b)$$

and thereby connects the tank with the network at node $n_t \in \mathfrak{N}$ considering the pipe's length l_t and cross section area A_t . The incorporation into the network equations is achieved by extending flow vector \mathbf{x}_Q by Q_t and incidence matrix \mathbf{A} in terms of node n_t .

Experimental Model Evaluation: Rapid Dynamics

Measurements have been taken on a small-scale replica of a water distribution network [Günther et al., 2016] (see figure 5.1) with a total pipe length of about 50m. This pipe network is assembled at the *Institute of Urban Water Management* at Graz University of Technology with the purpose to evaluate and test techniques for leakage detection and localization. The author expresses special thanks to *Markus Günther, David B. Steffelbauer, David Camhy* and *Daniela Fuchs-Hanusch* for their support. These experiments would not have been possible without their help and dedication for software as well as hardware improvements.

Measurements are compared with simulations on PD, associated with a *pressure-driven* consumption, and PD_u (Definition 4.14) as well as LCD (Definition 4.12), associated with linear consumption dynamics. In this context, the measured \mathbf{q} is used for reference \mathbf{q}_d concerning all models thereby utilizing $\lambda_{\mathbf{q}} = -20 \times \mathbf{1}_{n_{\mathbf{q}}}$. The pipe segments highlighted, as exemplification, with blue boxes are treated as consumers and are equipped with a flow meter and a solenoid valve respectively. These solenoid valves can be opened and shut electronically in a few milliseconds. A EPANET-MATLAB toolkit [Eliades et al., 2016] is used to extract topology data and pipe parameters from an existing EPANET [Lewis, 2000] model representing figure 5.1.

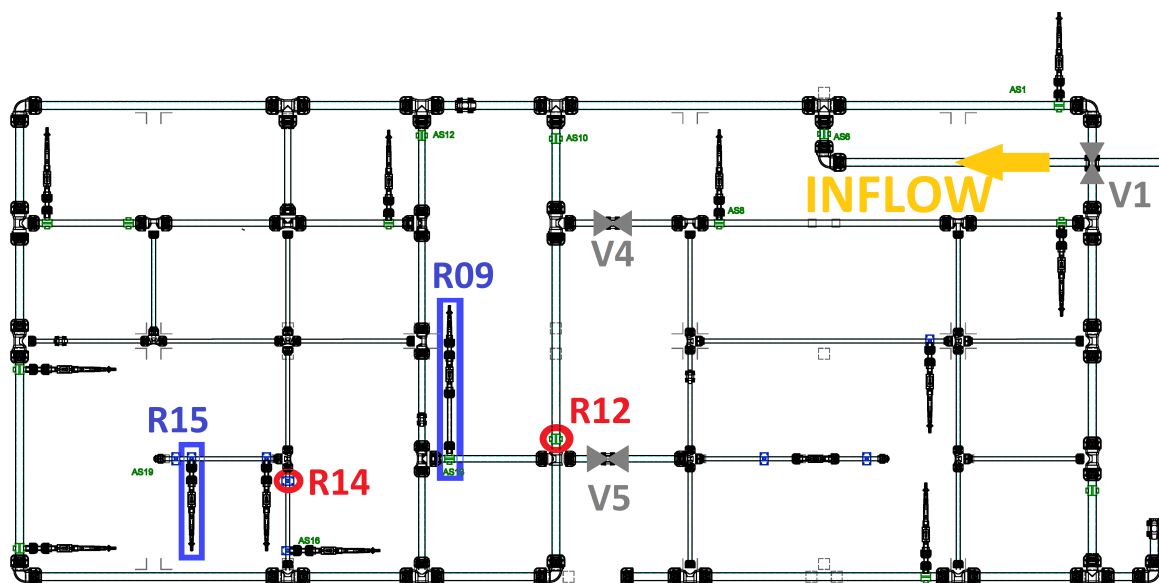


FIGURE 5.1: CAD model of the testbed highlighting two consumer-pipe-segments (blue), two pressure-sensors (red), three manual valves (gray) and the source pipe (gold). A complete sensor-overview can be found in figure 5.3. Credit to Günther et al. [2016].

A pump feeds the network via a 94mm diameter source pipe from the right hand side, as indicated in figure 5.1, producing source pressure h_s which is measured, filtered and fed into model equations.

Considering figure 5.1, the topology was simplified by closing manual valves V1, V4 and V5 to only operate the left part of the network. This was done to limit the complexity for the comparison of derived models with measurements. When considering figure 5.3, where the network with all sensors is represented, this is also the reason why, for instance, no consumption measurements of sensors R17, R18, R23, R25 or pressure-measurements of sensors R03, R26 are shown in the following sections.

Some results of this chapter were also used for publication [Kaltenbacher et al., 2018].

5.1 Friction Parameters via Optimization

The identification of friction parameters, roughness values in specific, will be a major subject of this thesis, however, for the present application a simplified approach was taken. Pipes' roughness coefficients and minor-loss coefficients were adjusted by an optimization attempting to solve the least-square problem

$$\min_{\epsilon, \mathbf{k}_m} (\mathbf{y}_h - \mathbf{C}_h \hat{\mathbf{h}}(\epsilon, \mathbf{k}_m))^T (\mathbf{y}_h - \mathbf{C}_h \hat{\mathbf{h}}(\epsilon, \mathbf{k}_m)). \quad (5.1)$$

Thereby \mathbf{y}_h denotes the vector of pressure measurements at nodes $\{p_1, p_2, \dots, p_{n_p}\} \subseteq \mathcal{J}$ in the network, whereas matrix $\mathbf{C}_h = [\mathbf{e}_{p_1} \ \mathbf{e}_{p_2} \ \dots \ \mathbf{e}_{p_{n_p}}]^T$ comprised of $\mathbf{e}_{p_i} \in \mathbb{Z}_{\{0,1\}}^{n_i}$ (see section 2.2.3) selects those elements of simulated nodal pressure-head vector $\hat{\mathbf{h}}$ (considered as function of the pipe's roughnesses ϵ and minor loss coefficients \mathbf{k}_m) where pressure sensors are present.

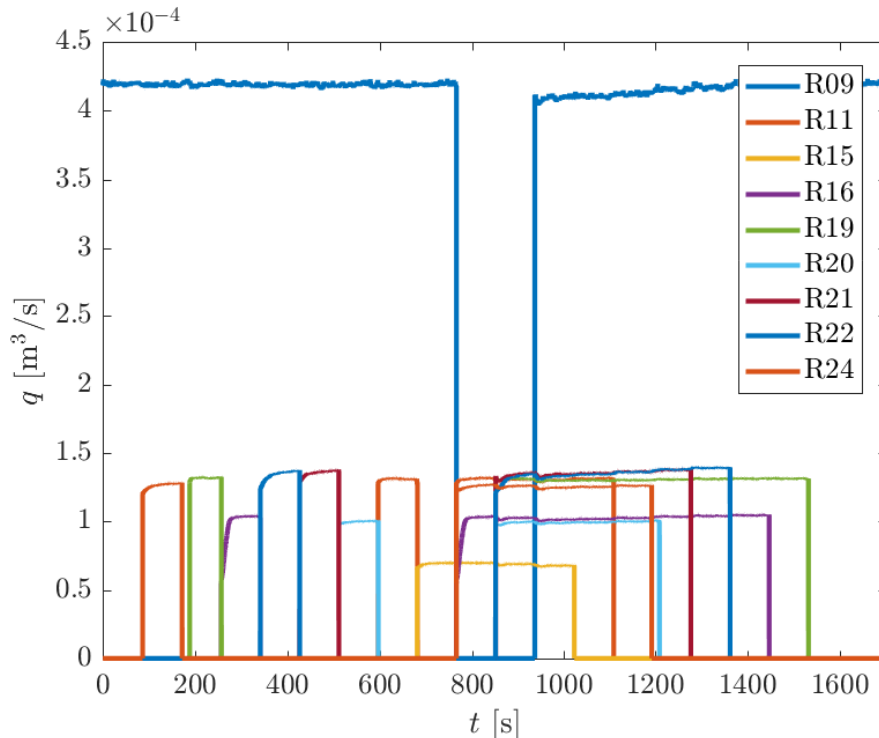


FIGURE 5.2: Measured consumption of respective consumers by inductive flow sensors. This consumption pattern was produced by opening and closing solenoid-consumer-valves. Flow-sensors can be attributed to corresponding consumers when looking at the sensor identifiers, e.g. R09, in figure 5.3 (red boxes).

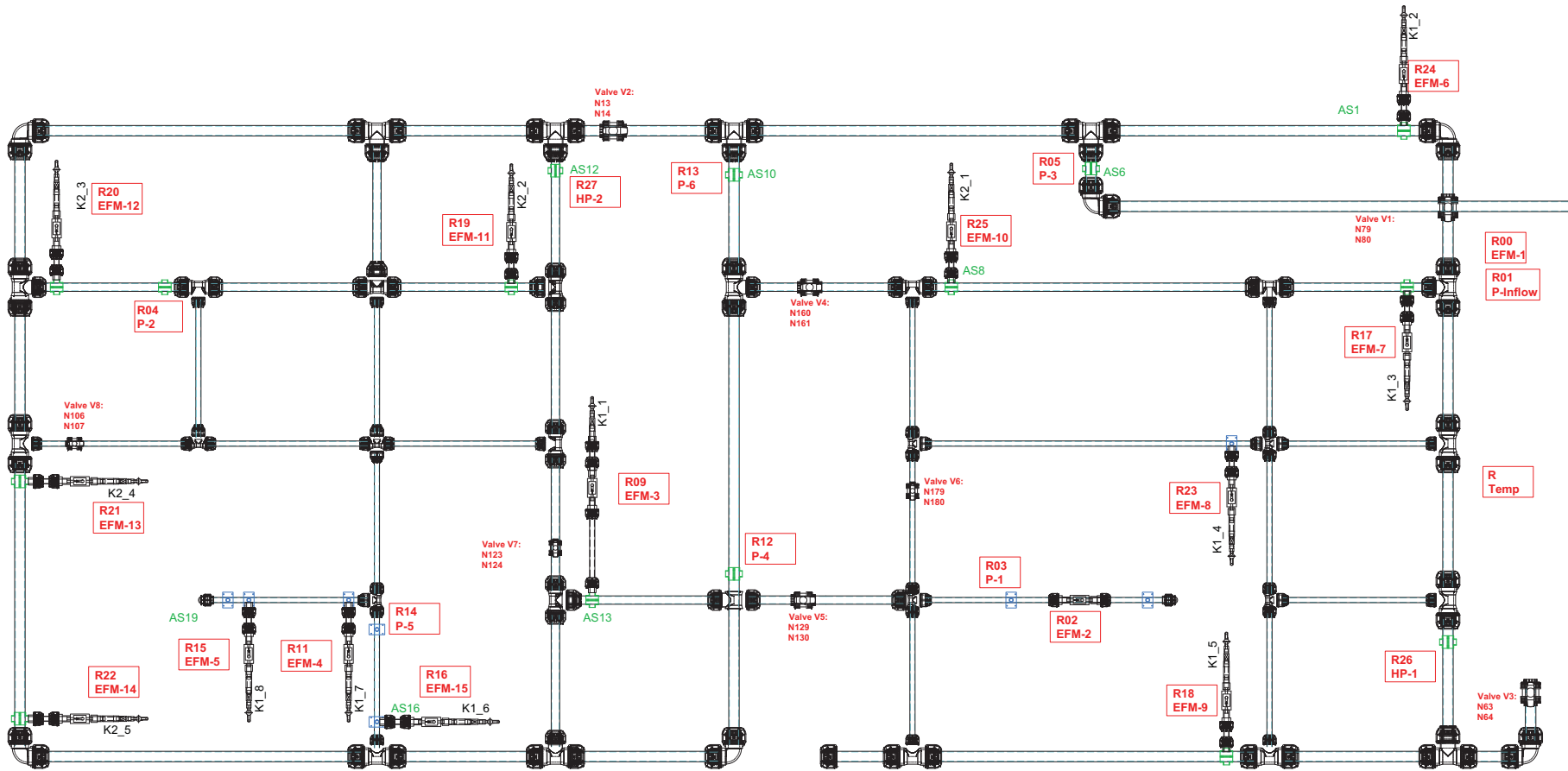


FIGURE 5.3: Complete CAD model of the testbed showing all sensor channels. Sensors identifiers are presented in red boxes, e.g. R01 denotes the pressure sensor reading the pump pressure. The type of sensor can be read off the second line in the red boxes. For instance, inductive flow sensors at consumers have the initial “EFM” whereas pressure sensors have the initial “P” in the second line. Credit to Günther et al. [2016].

However, \mathbf{y}_h and thus $\hat{\mathbf{h}}$ represent a specific point in time of the network only. Ultimately, multiple points in time have been considered according to figure 5.2 for this optimization (5.1). This means \mathbf{y}_h as well as $\hat{\mathbf{h}}$ are replaced by matrices \mathbf{Y}_h and $\hat{\mathbf{H}}$ respectively, where the corresponding columns account for a time-series of measurements in the optimization problem (5.1) such that

$$\min_{\boldsymbol{\epsilon}, \mathbf{k}_m} \sum_{ij} [(\mathbf{Y}_h - \mathbf{C}_h \hat{\mathbf{H}}(\boldsymbol{\epsilon}, \mathbf{k}_m))^{\odot 2}]_{ij} \forall i, j. \quad (5.2)$$

For producing the simulated nodal pressure heads $\hat{\mathbf{h}}$, the DD (purely demand-driven) model was applied (Definition 4.12) for the optimization (5.1). This means the nodal head vector is given by (4.6) utilizing the flows \mathbf{x}_Q as a solution of the ODEs (4.7). This choice was made in order to avoid specifying explicit orifice coefficients \mathbf{r} for PD or eigenvalues $\boldsymbol{\lambda}_q$ for LCD or PD $_{\mathbf{u}}$, at least for calibration of friction parameters $\boldsymbol{\epsilon}$ and \mathbf{k}_m . Nonetheless, the derivative of the consumption in (4.6) had to be approximated qualitatively. Also inequality constraints for the optimization problem have been considered to limit the pipes' roughness- and minor-loss parameters within their physically relevant bounds.

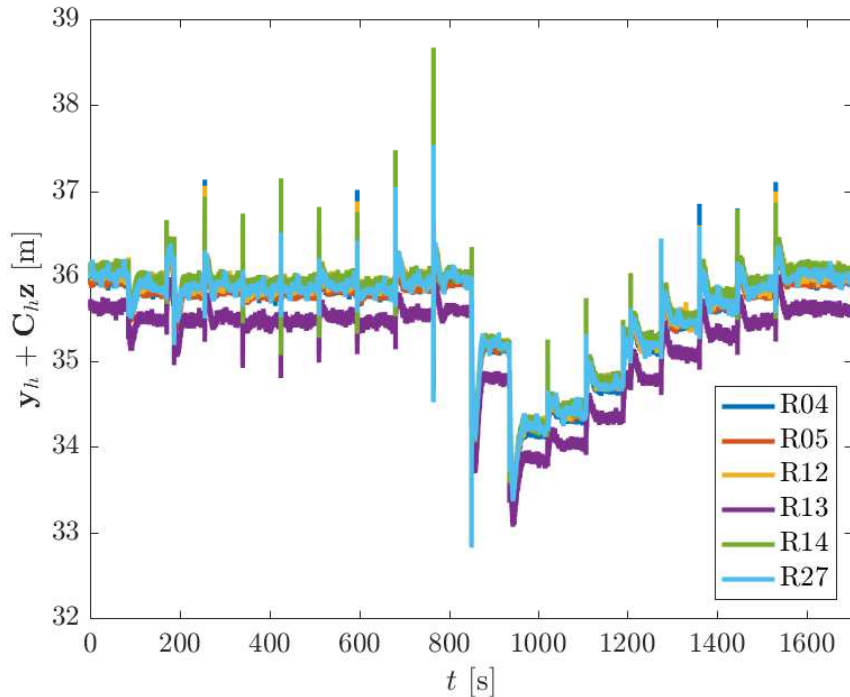


FIGURE 5.4: Measured head at nodes with pressure sensors according to figure 5.3. The measured pressure head values \mathbf{y}_h were increased by the elevation (with respect to the laboratory's floor) at the appropriate nodes $\mathbf{C}_h \mathbf{z}$.

Remark 5.1. *When looking at figure 5.4, it is clear why the identification of individual friction parameters per pipe can not be successful on this experimental network as the head-losses along the pipes are far too small in order to be distinguishable among each other.*

Attempts to increase the flow in the network for producing higher head-losses failed as the deployed inductive flow sensors (at consumers) are only capable to measure flow between $[0.0133, 0.2667]$ l/s with the only exception of the flow sensor at R09 which can measure up to 0.833 l/s (see figure 5.2). Besides, neither the pump nor the rest of the equipment is designed to produce enough flow which would be necessary for the roughness-identification as presented later, in chapter 7 or 9. Also, the pipes are made of PVC material and therefore have low roughness inherently. Knowing that the produced measurement-sets with consumption pattern in figure 5.2 results in insufficient head-loss, the friction parameters to be found were grouped such that

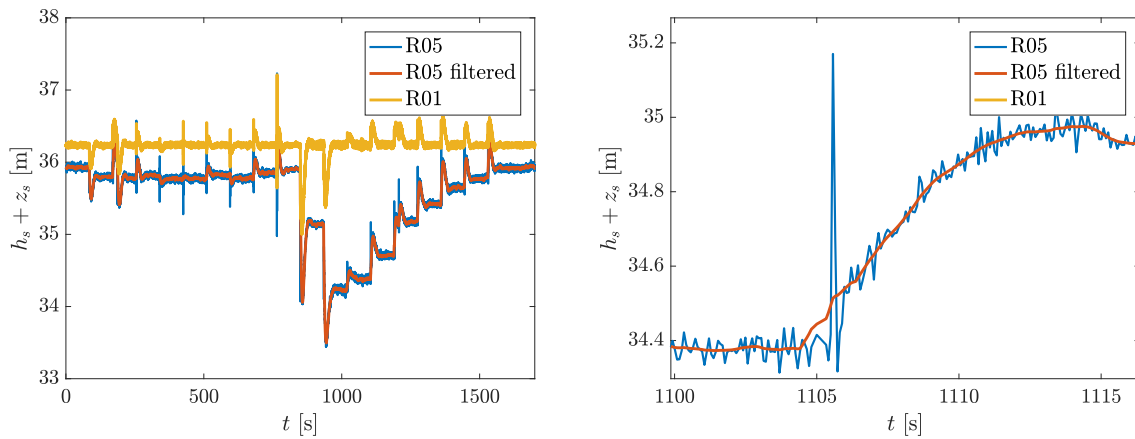


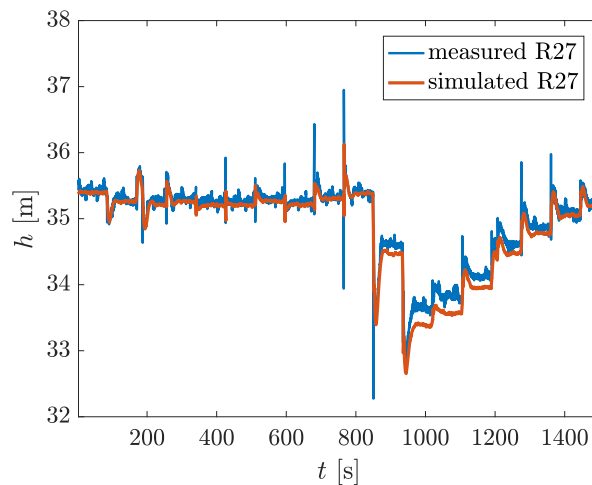
FIGURE 5.5: Filtering of measurements of sensor R05 applied as source pressure h_s and comparison to R01 which is closer to the pump. The elevation of R05 with respect to the laboratory's floor is $z_{R05} = z_s = 0.422\text{m}$ whereas $z_{R01} = 0.17\text{m}$.

pipes with the same diameter are fixed to have the same roughness concerning ϵ . Analogously, certain groups of pipe's where fixed to have the same minor-loss parameters concerning k_m .

The pressure-sensor R05 (see figure 5.3) was taken as reference for the source pressure h_s instead of R01 which would actually be closer to the pump. Seen in figure 5.5, most of the head-loss occurs along the source pipe which is equipped with a filter and has a connection to an air-vessel. The fine-meshed membrane of this filter prevents contamination from the tank, which supplies the pump, to get into the hydraulic network whereas the air-vessel attenuates pressure peaks, a measure to protect the pump. Concerning the high losses over the source pipe, the area between R01 and R05 in figure 5.5 is proportional to the energy primarily needed to overcome the head-loss over this filter.

By filtering h_s (meaning R05), it is ensured that no transients are induced due to the source pressure itself as the transient reactions, seen in figure 5.5, also occur in the unfiltered h_s . At the same time, the pump is pressure controlled and tries to keep about $h_s \approx 36\text{ m}$ (cf. R01 in figure 5.5).

Optimization Results. To allow verification of the obtained friction parameters of this optimization, model $\text{PD}_{\mathbf{u}}$ is applied with eigenvalues $\lambda_q = -20 \times \mathbf{1}_{n_q}$ to be compared with the calibration-measurements (seen in figure 5.2 and 5.4).



(A) Comparing h at R27 (cf. figure 5.3).

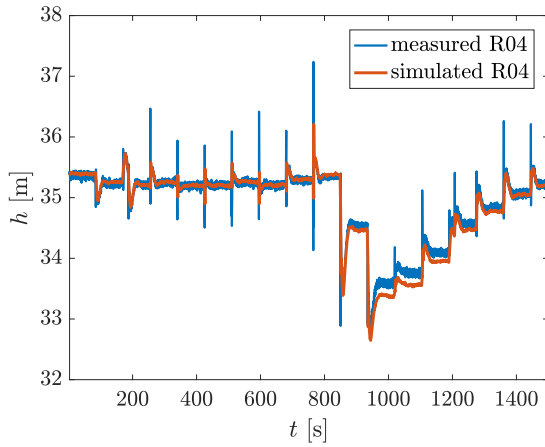
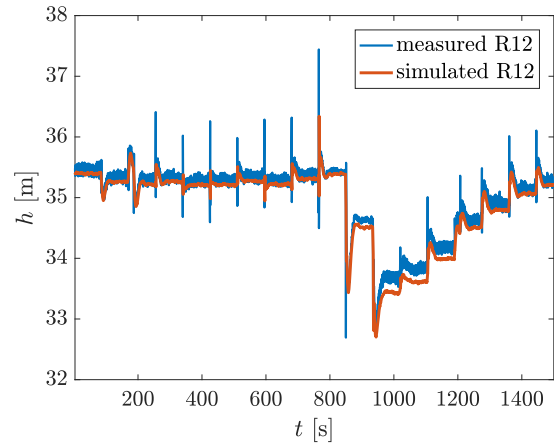
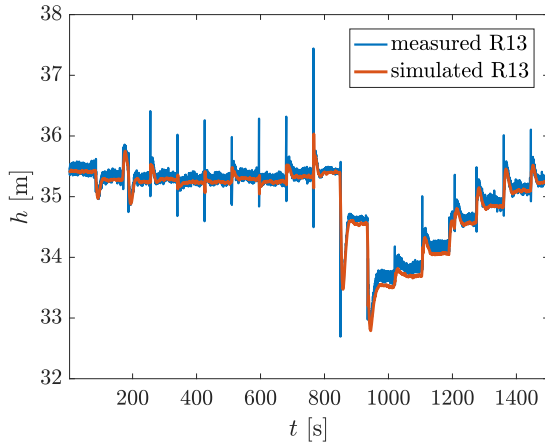
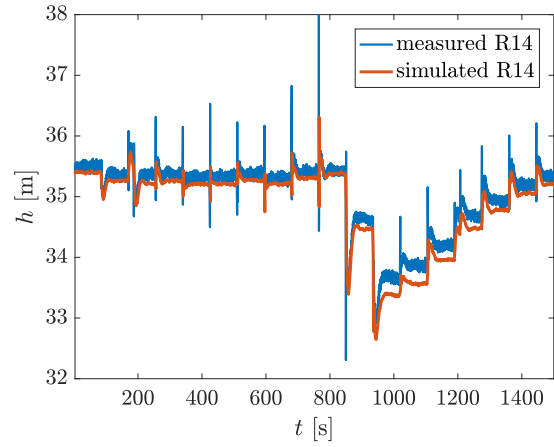
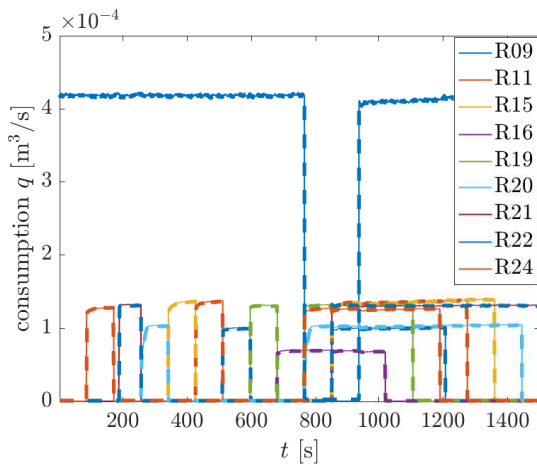
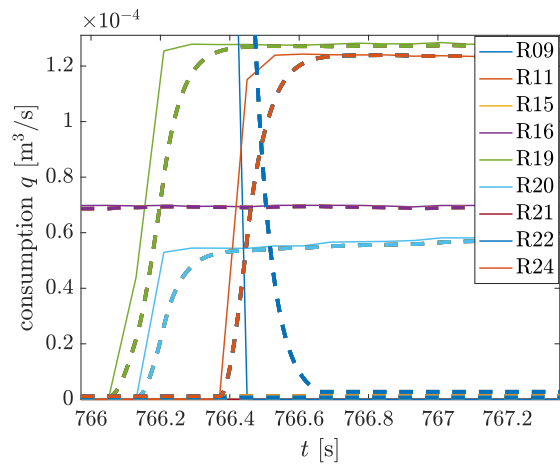
(B) Comparing h at R04 (cf. figure 5.3).(C) Comparing h at R12 (cf. figure 5.3).(D) Comparing h at R13 (cf. figure 5.3).(E) Comparing h at R14 (cf. figure 5.3).

FIGURE 5.6: Comparison of measurements (blue) with simulation results (red) at respective pressure-nodes (Definition 7.8) when applying model $PD_{\mathbf{u}}$ (Definition 4.14) and $\lambda_q = -20 \times \mathbf{1}_{n_q}$.

(A) Simulated and measured q .

(B) Zoom of figure 5.7A showing dynamics.

FIGURE 5.7: Calibration-measurements of q (solid lines) are compared with simulation results (dashed lines) of $PD_{\mathbf{u}}$ where the measured q was selected for reference q_d utilizing $\lambda_q = -20 \times \mathbf{1}_{n_q}$.

In addition to the friction parameters, also the nodal elevations (with respect to the laboratory-floor) needed slight modifications in the centimeter-range. Considering figure 5.6, one has to expect that the obtained friction parameters do not reliably represent the real values due to the minor yet distinct deviations in pressure (particularly in the steady-state time-frames) during peak-consumption ($t \approx 900$ s), where all consumers (solenoid-valves) are open. However, this will not be overly important for this chapter as the qualitative behavior, especially during dynamic events, will be sufficient to identify the strength and weaknesses of the derived models in comparison to measurements.

In this context, the comparison of the consumption during dynamic responses to excitation (valve openings) as in figure 5.7 would indeed be most interesting, given the model techniques applied in chapter 4. The problem is that the flow sensors at consumers need more than one second to adjust to the real physical values according to the product datasheet. This is also the reason why the exact times of valve-switching (either opening or closing) are basically unknown and therefore it is challenging to align the measurements to simulations in the sub-second time-resolution. The comparably long response time is a common problem with flow sensors of all types, including ultrasonic ones, as far as the author is aware. This means that although one can clearly see the dynamic transitions of the consumption in simulated \mathbf{q} in figure 5.7B, the jumps seen in the measured \mathbf{q} are not representative of the real dynamic transition to the steady-state consumption when opening or closing consumer-valves. The only possibility to compare transients is to have a closer look at the pressure peaks as on the right hand side of figure 5.5.

The sampling frequency used to record these measurements (in this section), which were applied for the optimization of friction parameters, was comparably low. This can be seen on the right hand side of figure 5.5 where the time resolution to represent the pressure-peak when closing a consumer-valve is visibly coarse. With some software and hardware improvements achieved by the author's esteemed colleagues from the institute of *Urban Water Management*, the sampling frequency could be increased slightly. For the sake of investigation of dynamics with the higher sampling frequency, the complexity of the following experiments is kept fairly limited in terms of the number of active consumers. Nevertheless, the working principle of model $\text{PD}_{\mathbf{u}}$ when dealing with more complex scenarios was demonstrated successfully in this section while sufficiently accurate friction parameters have been obtained.

5.2 One Consumer Configuration

The solenoid valve at consumer R09 in figure 5.1 is opened and shut periodically while all other consumers remain closed. The pressure-sensor closest to R09, i.e. h at R12, and the outflow q at R09 are monitored. Referring to figure 5.8, a polynomial between $\epsilon_r = 10^{-7}$ and $\max(r)$ in the course of orifice coefficient r PD (at the time of switching) is utilized to imitate the opening/closing of the solenoid-consumer-valve of R09 for model PD, whereas the course of orifice coefficient $r = 1/\sqrt{u}$ for model $\text{PD}_{\mathbf{u}}$ is given by control law (4.26). Effectively, figure 5.8 shows the transition from fully closed to fully open (or vice-versa) of this consumer.

At this point, recall Theorem 4.11 which says that LCD and $\text{PD}_{\mathbf{u}}$ are equivalent as long as Assumption 4.10 holds which is the case for all the conducted measurements on the lab-network (figure 5.3). Nevertheless, the differences between LCD and $\text{PD}_{\mathbf{u}}$ are presented in detail in section 4.4.4. Also, there is not much to be seen in the simulation results of model DD (see Definition 4.12) which also does not have any visible fast dynamics in the pressure since the approximation of the consumption-derivative (as it is needed in (4.6)) from the measured \mathbf{q} just causes some unrealistic peaks due to the sensors' long response time. Effectively, only simulations with model PD and $\text{PD}_{\mathbf{u}}$ respectively are compared with the recorded measurements.

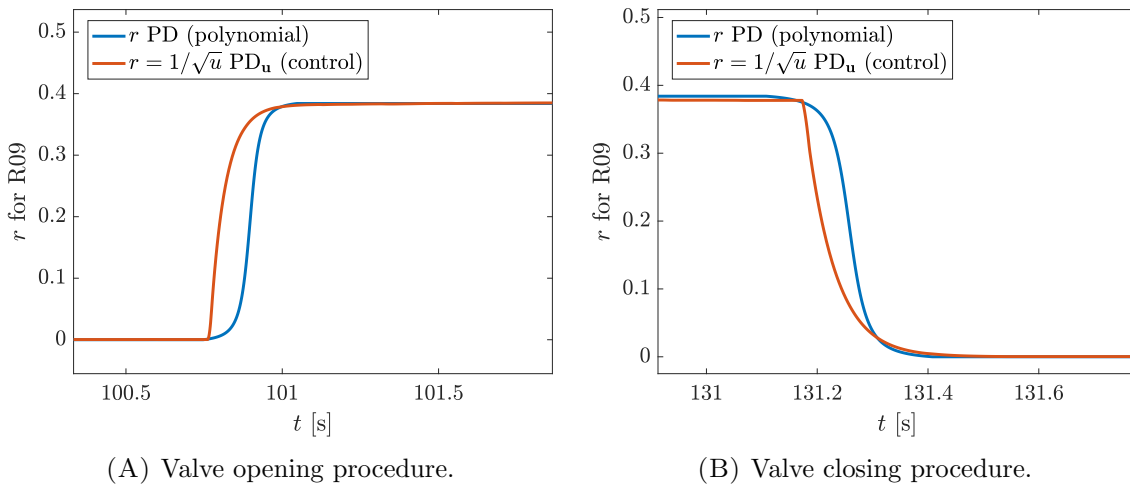


FIGURE 5.8: Assumed polynomial transition of orifice coefficient r for consumer R09 (blue) for model PD, i.e. r PD, and r PD_u given by (4.26) (also see Definition 4.12 and 4.14).

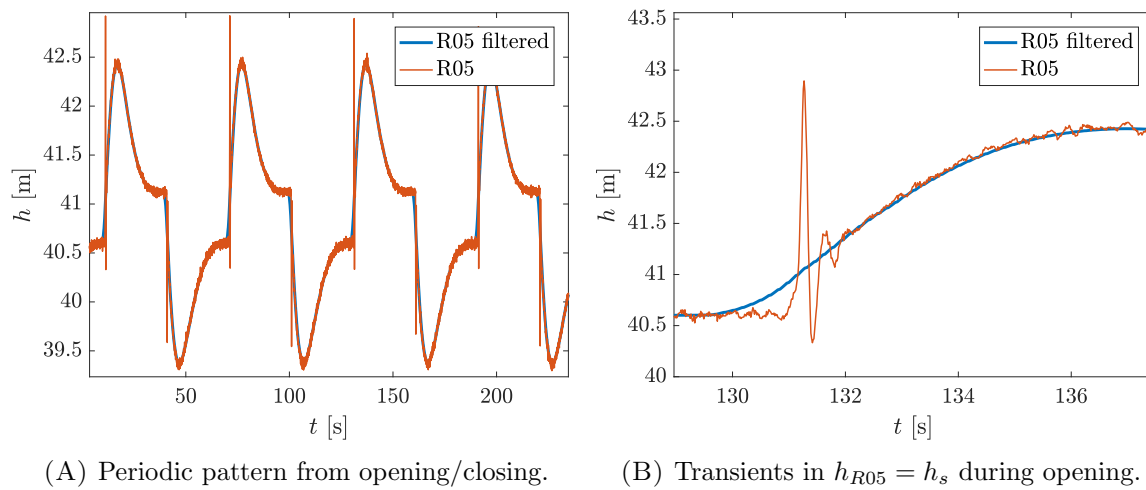
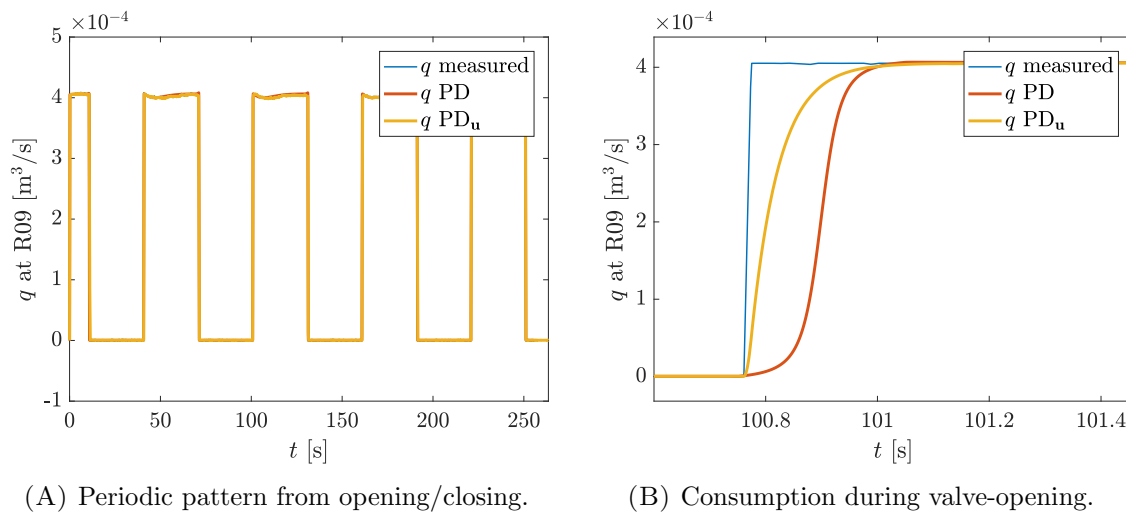


FIGURE 5.9: Measured pressure at R05 which is filtered and then used as h_s .



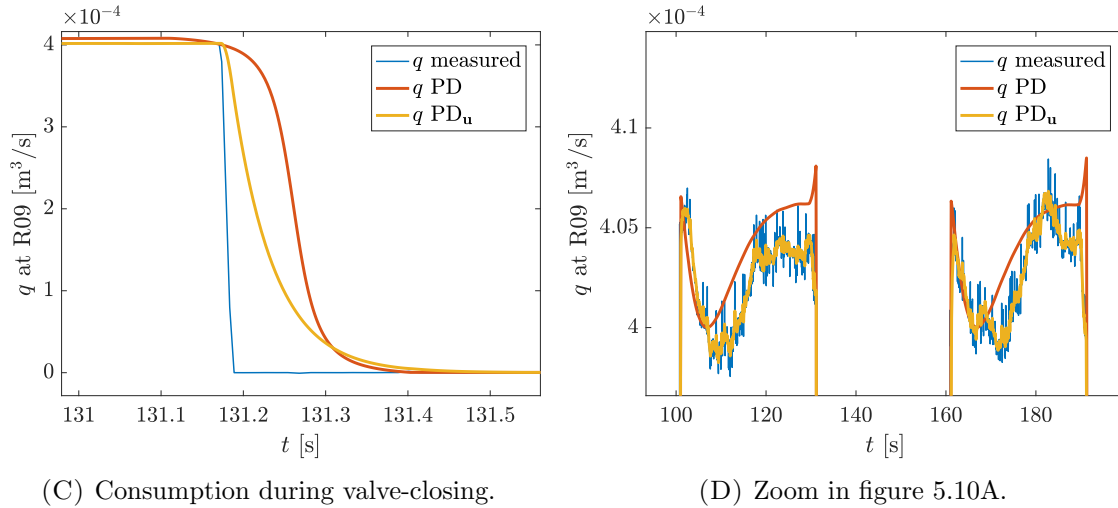


FIGURE 5.10: Measured and simulated consumption at R09.

Considering figure 5.9, the filtered pressure head at R05 which is utilized as h_s , one can see that the increased time resolution improves the reading of the pressure fluctuation as a reaction to the rapid valve closing at $t \approx 131$ s (referring to figure 5.9B). One can also recognize the pump-dynamics in the course of R05 as it tries to keep about 40.75m in source head.

The periodic opening and closing of the consumer-valve R09 can be seen in figure 5.10A. Figure 5.10B and 5.10C demonstrate that q PD $_{\mathbf{u}}$ nicely follows a linear ODE with $\lambda_q = -20 \text{ s}^{-1}$, whereas q PD simply mimics the polynomial transition of the consumer's orifice coefficient (as in figure 5.8). As expected, no fast dynamics are seen in the measured q of R09 in figure 5.10B which is utilized for q_d (the desired consumption) concerning PD $_{\mathbf{u}}$. What can be seen (figure 5.10D) is that the pressure-dependent character (heavily influenced by the pump) of the simulated q quite matches real-world scenarios in both models. The controlled q PD $_{\mathbf{u}}$ quickly follows specified values and filters the high frequency noise of the inductive flow sensor. Things become more interesting when looking at the higher-resolution pressure data in figure 5.11. Primarily, the pressure heads visibly follow h_s (as in figure 5.9) in steady-state, seeing a small misalignment between simulated and measured h at R12. Selected friction coefficients/roughnesses are not perfect. At the time of switching valves, transients are induced, seen in figure 5.11 with a zoom in figure 5.12. These pressure spikes (also seen in the source pressure figure 5.9) depict the commonly known *waterhammer* effect.

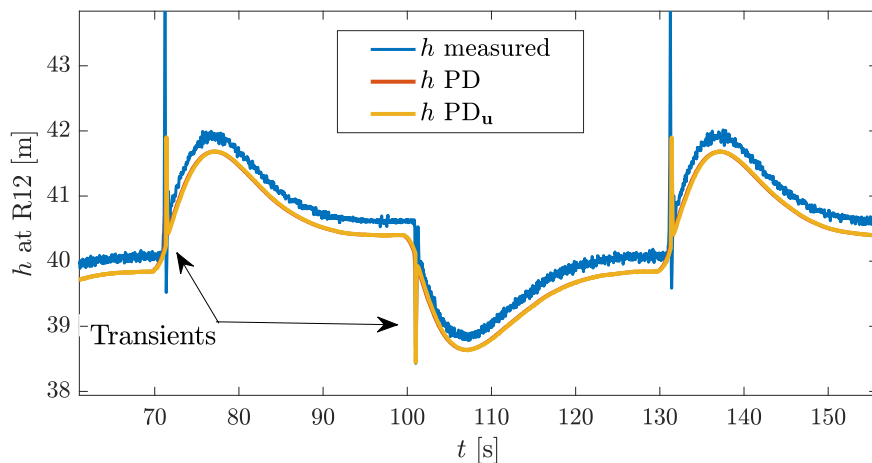


FIGURE 5.11: Comparison of pressure heads at R12.

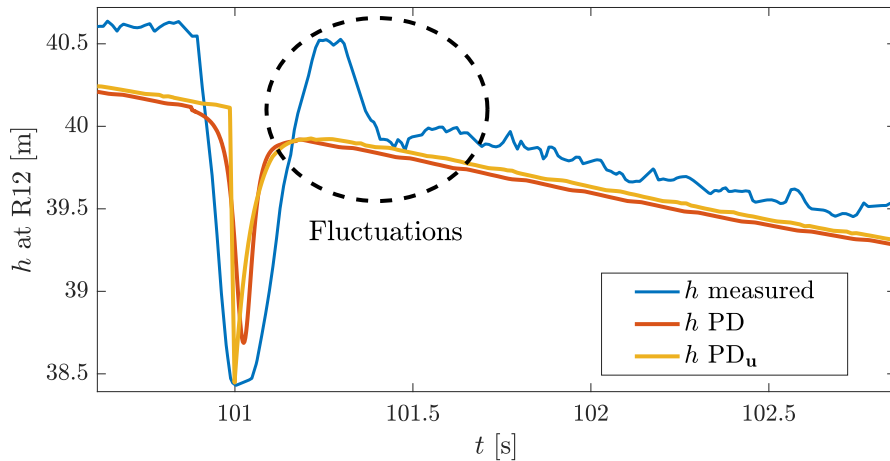


FIGURE 5.12: Zoom of Fig. 5.11 showing transients in an opening operation.

The fact that these induced transients are higher when closing valves (at $t \approx 70\text{s}, 130\text{s}$) compared to the opening operation ($t \approx 100\text{s}$) is remarkable (Fig. 5.11). The water mass is at rest before opening and, despite the rapid opening, has some time to gradually transition to the next steady state, whereas flowing water is abruptly (in a few 10^3 's of *milliseconds*) cut off during the closing operation, leading to higher pressure peaks.

Effectively, when looking at figure 5.12, the zoom of figure 5.11 at an opening operation, one can recognize that it is possible to mimic pressure peaks qualitatively with the help of polynomial transitions in r , concerning PD, and the utilization of linear consumption dynamics regarding PD_u .

5.3 Two Consumer Configuration

For the two-consumer-configuration an ultrasonic sensor is used to also record the flow at R15 (see figure 5.1) in order to exceed the 0.233 l/s limit of the inductive flow-sensor. However, the same notation, namely R15, is used to denote these ultrasonic consumption-recordings to not confuse the reader. Unfortunately, the following measurements have been recorded with the lower sampling-frequency, nonetheless, some interesting conclusions can still be made.

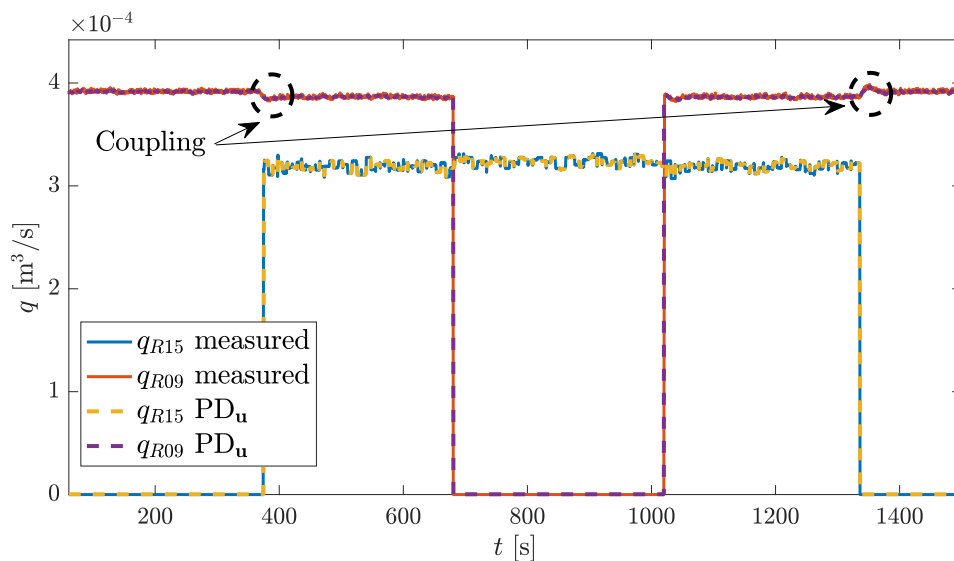


FIGURE 5.13: Consumption and actuation in the *Two Consumer Configuration*.

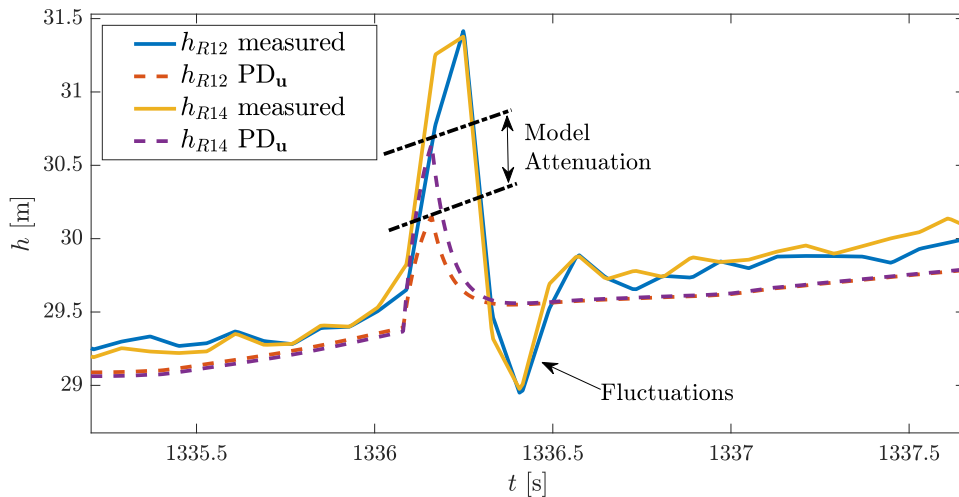


FIGURE 5.14: Closing operation of R15 in the *Two Consumer Configuration*.

Figure 5.13 shows the consumption of active consumers R09 and R15 while actuating their solenoid valves. Mutual coupling effects are visible in q_{R09} when opening/closing the solenoid valve of R15 leading to a *waterhammer* which also effects the consumption at R09 and can be seen in the pressure at R12. As the ultrasonic sensor used for q_{R15} has higher measurement noise, these effects are only seen in q_{R09} .

Concerning the pressure readings, the pump tries to keep $h_s \approx 30\text{m}$ in pressure head at R05 which is filtered and again utilized for source pressure head h_s in the model (completely analogously to figure 5.9). Figure 5.14 displays pressure heads h_{R12} and h_{R14} during a closing operation of R15. As a closing operation in figure 5.14 is monitored, the pressure peak is generally higher (relative to h_s) as in figure 5.12 (see previous section) which leads to higher deviations from the simulation concerning the peak height. Beside of this height difference, an attenuation of the pressure peak due to the physical distance between R12 and R14 can be recognized as pressure-sensor R12 is significantly closer to the consumer-valve of R15. This attenuation is far more aggressive in simulation as it is in reality. Nonetheless, this attenuation can also be seen in the measurements as the peak of h_{R14} *measured* (which has to be higher as the one of h_{R12} *measured*) is apparently cut off due to the lower sampling frequency.

The fluctuations seen in the pressure (figure 5.12 and 5.14) after the opening/closing and the weak attenuation (figure 5.14) are consequences of water density fluctuations and perhaps the pipes' elasticity. To incorporate these effects in the model, partial differential equations within an elastic modeling approach are necessary (see (3.37)).

5.4 Conclusions

Bottom line of these measurements is that one can use the derived models applying the *Rigid Water Column Theory* for the description of transients to mimic these fast transient operations. However, as e.g. in [Shimada, 1989; Axworthy and Karney, 2000; Nault and Karney, 2016] one can actually conclude that this approach is particularly suitable to model slow transient effects. When coupled with the simple ODEs (4.69) to also allow (simulated) dynamics in the tank pressure, the simulation can indeed be improved substantially (see [Axworthy and Karney, 2000] and [Nault and Karney, 2016]).

Observability Analysis

In this chapter the additional slow transient model information is utilized to derive more general statements about observability and detectability. In this context, one can apparently see from the resulting model equations that the focus is inherently placed on the flow and its derivative. It is important to emphasize that this is indeed not intentional, but a result from the underlying physics. Loosely speaking, the pressure propagation is in the range of one order of magnitude faster than the propagation of the flow (for more physical considerations the reader is guided to page 34). On the contrary, flow sensors are in the range of one order of magnitude more expensive than pressure sensors to this point in time. Also, installation costs are often higher as, for instance, inductive flow sensors require to cut the pipe whereas ultrasonic ones, which just need to be in contact with the pipe, are generally most costly. Besides, the response time (minimal sample time) of typical flow sensors is in the range of one second (and beyond) making it impossible (as far as the author is aware) to directly measure fast transient flow behavior.

The application of pressure sensors inside the network is, for reasons mentioned, vastly more popular. After a more genuine discussion about what to measure in this chapter, it is assumed that pressure sensors are the only source of information inside the considered network's area (so called District Metering Areas or DMAs) as far as state reconstruction is concerned. Thereby the source pressure as well as the consumption is assumed to be known. Up till now the latter assumption is, admittedly, unrealistic. However, there is some hope that customers will be equipped with direct measurement devices [Gascón et al., 2004] in the future. In this context, there is little doubt that wireless data transmission is inevitable, driving down maintenance- and installation costs by economies of scale. New network protocols such as LORA [Cattani et al., 2017] which only demand low energy while being able to transmit data over larger distances might be able to accelerate the transition to an integrated monitoring system.

6.1 Concept of State Reconstruction

Definition 6.1 (Observability). *Consider system*

$$\Sigma : \begin{cases} \dot{\mathbf{x}} = \mathbf{f}(\mathbf{x}, \mathbf{u}) \\ \mathbf{y} = \mathbf{g}(\mathbf{x}, \mathbf{u}) \end{cases} \quad \text{with} \quad \mathbf{x}(t_0) = \mathbf{x}_0 \quad (6.1a)$$

$$(6.1b)$$

for $\mathbf{x} \in D_{\mathbf{x}} \subseteq \mathbb{R}^n$, input \mathbf{u} and output \mathbf{y} in the time interval $[t_0, t_1 < \infty]$, denoted by $\mathbf{u}_{[t_0, t_1]}$ and $\mathbf{y}_{[t_0, t_1]}$. Then, system Σ is said to be observable if all initial states $\mathbf{x}_0 \in D_{\mathbf{x}}$ can be uniquely determined from the knowledge of $\mathbf{u}_{[t_0, t_1]}$ and $\mathbf{y}_{[t_0, t_1]}$.

Diffeomorphism. For the purpose of analysis, the same nonlinear-system Σ with a single output $y = g(\mathbf{x}, \mathbf{u})$ is considered. Further suppose that functions $\mathbf{u}(\cdot)$ and $g(\cdot)$ are $n - 1$ times continuously differentiable in the interval $t \in [t_0, t_1]$. Taking the derivatives

$$\begin{aligned} \dot{y} &= \frac{\partial g}{\partial \mathbf{x}} \mathbf{f}(\mathbf{x}, \mathbf{u}) + \frac{\partial g}{\partial \mathbf{u}} \dot{\mathbf{u}} = h_1(\mathbf{x}, \mathbf{u}, \dot{\mathbf{u}}) \\ \ddot{y} &= \frac{\partial h_1}{\partial \mathbf{x}} \mathbf{f}(\mathbf{x}, \mathbf{u}) + \frac{\partial h_1}{\partial \mathbf{u}} \dot{\mathbf{u}} + \frac{\partial h_1}{\partial \dot{\mathbf{u}}} \ddot{\mathbf{u}} = h_2(\mathbf{x}, \mathbf{u}, \dot{\mathbf{u}}, \ddot{\mathbf{u}}) \\ &\vdots \\ y^{(n-1)} &= \frac{\partial h_{n-2}}{\partial \mathbf{x}} \mathbf{f}(\mathbf{x}, \mathbf{u}) + \frac{\partial h_{n-2}}{\partial \mathbf{u}} \dot{\mathbf{u}} + \frac{\partial h_{n-2}}{\partial \dot{\mathbf{u}}} \ddot{\mathbf{u}} + \dots + \frac{\partial h_{n-2}}{\partial \mathbf{u}^{(n-2)}} \mathbf{u}^{(n-1)} = h_{n-1}(\mathbf{x}, \mathbf{u}, \dot{\mathbf{u}}, \dots, \mathbf{u}^{(n-1)}) \end{aligned} \quad (6.2)$$

system Σ with single output y is observable if the mapping

$$\boldsymbol{\zeta} = \mathbf{h}(\mathbf{x}) = \begin{bmatrix} g(\mathbf{x}, \mathbf{u}) \\ h_1(\mathbf{x}, \mathbf{u}, \dot{\mathbf{u}}) \\ h_2(\mathbf{x}, \mathbf{u}, \dot{\mathbf{u}}, \ddot{\mathbf{u}}) \\ \vdots \\ h_{n-1}(\mathbf{x}, \mathbf{u}, \dot{\mathbf{u}}, \dots, \mathbf{u}^{(n-1)}) \end{bmatrix} \quad (6.3)$$

with operator \mathbf{h} is injective, meaning that $\mathbf{x} = \mathbf{h}^{-1}(\boldsymbol{\zeta})$ can be uniquely determined by inverting (6.3). As the mapping does not account for the entire interval $t \in [t_0, t_1]$, observability, in general, does depend on the input. As a consequence, the requirement for the mapping \mathbf{h} to be injective is *necessary* only.

Remark 6.2. *The conditions become sufficient when $\boldsymbol{\zeta} = \mathbf{h}_{[t_0, t_1]}(\mathbf{x})$ remains injective for every instant in $t \in [t_0, t_1]$ which actually depends on the input $\mathbf{u}_{[t_0, t_1]}$ and its derivatives $\dot{\mathbf{u}}_{[t_0, t_1]}, \dots, \mathbf{u}^{(n-1)}_{[t_0, t_1]}$. And, an autonomous system $\dot{\mathbf{x}} = \mathbf{f}(\mathbf{x})$ and $y = g(\mathbf{x})$ is observable if and only if the mapping $\boldsymbol{\zeta} = \mathbf{h}(\mathbf{x})$ (independent of \mathbf{u}) is injective [Adamy, 2014].*

Remark 6.3. *Functions $\mathbf{u}(\cdot)$ and $g(\cdot)$ were assumed to be contained in the domain of $n - 1$ continuously differentiable functions C^{n-1} . However, in case continuity holds for further derivatives, e.g. C^∞ , there is, in principle, no limit to the number of differentiations of y concerning (6.2) to achieve an injective mapping $\mathbf{x} = \mathbf{h}_{[t_0, t_1]}^{-1}(\boldsymbol{\zeta})$.*

In general, observability is very difficult to verify since it requires the inversion of a set (particularly large for hydraulic networks) of nonlinear equations which also depend on the input and its derivatives. Provided that the goal is to reconstruct states in steady-state at least, observability appears to be too restrictive. A less restrictive alternative is contained in the notion of “detectability”. Although very well defined for linear systems, there is no generally agreed definition for this concept in the nonlinear case. Actually, it has not yet been achieved (as far as the author is aware) to state necessary and sufficient conditions for a generally nonlinear input-dependent system such as (6.1), referring to system properties, which guarantee existence of an asymptotic observer or strong observer.

Definition 6.4 (Asymptotic Observer). *A system*

$$\Omega : \dot{\hat{\mathbf{x}}} = \hat{\mathbf{f}}(\hat{\mathbf{x}}, \mathbf{u}, \mathbf{y}) \quad \text{with} \quad \hat{\mathbf{x}}_0 = \hat{\mathbf{x}}(t_0) \quad (6.4)$$

with inputs \mathbf{y}, \mathbf{u} and output $\hat{\mathbf{x}}$ is called asymptotic observer for system Σ if the observer estimation error $\mathbf{x} - \hat{\mathbf{x}}$, specified by the dynamics $\mathbf{f}(\mathbf{x}, \mathbf{u}) - \hat{\mathbf{f}}(\hat{\mathbf{x}}, \mathbf{u}, \mathbf{g}(\mathbf{x}))$, vanishes asymptotically for any $\mathbf{x}_0, \hat{\mathbf{x}}_0$.

Definition 6.5 (Strong Observer). *A system*

$$\Omega^* : \dot{\hat{\mathbf{x}}} = \hat{\mathbf{f}}^*(\hat{\mathbf{x}}, \mathbf{y}) \quad \text{with} \quad \hat{\mathbf{x}}_0 = \hat{\mathbf{x}}(t_0) \quad (6.5)$$

with input \mathbf{y} and output $\hat{\mathbf{x}}$ is called strong observer for system Σ if the observer estimation error $\mathbf{x} - \hat{\mathbf{x}}$, specified by the dynamics $\mathbf{f}(\mathbf{x}, \mathbf{u}) - \hat{\mathbf{f}}^*(\hat{\mathbf{x}}, \mathbf{g}(\mathbf{x}))$, vanishes asymptotically for any $\mathbf{x}_0, \hat{\mathbf{x}}_0$ and \mathbf{u} .

Two particular aspects shall be noticed. First, the crucial difference between Definition 6.4 and 6.5 is the independency of the input \mathbf{u} of the latter. Second, observability (Definition 6.1) is sufficient for the existence of an asymptotic observer in the defined time interval $t \in [t_0, t_1]$ only. For the attentive reader, references [Levine, 2010] [Sontag, 2004] well address the subject of “detectability” for Σ and also draw connections to “input/output to state stability”. In this context, the definitions by [Hautus, 1983] posed for linear systems do also have a distinctive meaning in the nonlinear case. Known as zero-detectability this property does find application in, e.g. [Levine, 2010] or [Sontag, 2004] and references therein.

Definition 6.6 (zero-detectability). Σ is said to be zero-detectable if

$$\mathbf{y} \equiv \mathbf{0} \quad \text{implies that} \quad \lim_{t \rightarrow \infty} \mathbf{x}(t) = \mathbf{0} \quad (6.6)$$

for all inputs \mathbf{u} and initial states \mathbf{x}_0 .

Definition 6.7 (strong zero-detectability). System Σ is said to be strongly zero-detectable if

$$\lim_{t \rightarrow \infty} \mathbf{y}(t) = \mathbf{0} \quad \text{implies that} \quad \lim_{t \rightarrow \infty} \mathbf{x}(t) = \mathbf{0} \quad (6.7)$$

for all inputs \mathbf{u} and initial states \mathbf{x}_0 .

Definitions similar to 6.6 and 6.7 can be found in [Hautus, 1983] and were adapted to the nonlinear case. In reference to this nonlinear case and knowing that observability is only sufficient for the existence of an asymptotic observer, zero-detectability appears to be very appealing in comparison to observability as it is completely independent from the input.

In the linear case, strong zero-detectability (equivalent to “strong* detectable” in Hautus [1983]) guarantees existence of a strong observer (details below). In this context, strong zero-detectability implies zero-detectability, the converse is not necessarily true. Analyzing a “detectable” linear system, the “unobservable” system part, spanned by the kernel of the observability matrix ((6.1) for $\mathbf{u} \equiv \mathbf{0}$ in the linear case where (6.1) yields a linear mapping), forms an asymptotically stable subsystem. For illustrative purposes, the linear case is considered in more detail.

Linear Detectable System. Consider the linear system¹

$$\Sigma_L : \begin{cases} \dot{\mathbf{x}} = \mathbf{A}\mathbf{x} + \mathbf{B}\mathbf{u} \\ \mathbf{y} = \mathbf{C}\mathbf{x} + \mathbf{D}\mathbf{u} \end{cases} \quad \text{with} \quad \mathbf{x}(t_0) = \mathbf{x}_0, \quad (6.8a)$$

$$(6.8b)$$

then the Luenberger-type observer

$$\dot{\hat{\mathbf{x}}} = \mathbf{A}\hat{\mathbf{x}} + \mathbf{B}\mathbf{u} - \mathbf{E}(\mathbf{y} - \mathbf{C}\hat{\mathbf{x}} - \mathbf{D}\mathbf{u}) \quad (6.9)$$

represents an asymptotic observer if and only if matrix $\mathbf{A} + \mathbf{E}\mathbf{C}$ is Hurwitz, meaning that $\mathbf{A} + \mathbf{E}\mathbf{C}$ has eigenvalues with strictly negative real parts only. This can be seen when considering the observer error dynamics

$$\dot{\mathbf{e}} = \dot{\mathbf{x}} - \dot{\hat{\mathbf{x}}} = (\mathbf{A} + \mathbf{E}\mathbf{C})\mathbf{e}. \quad (6.10)$$

¹Please note that matrices $\mathbf{A}, \mathbf{B}, \dots, \mathbf{E}$ are only valid for this paragraph and must not be confused with hydraulic quantities such as the incidence matrix.

Remark 6.8. System Σ_L , or the pair (C, A) of Σ_L is said to be detectable if and only if there exists a matrix E such that $A + EC$ is Hurwitz. Although necessary and sufficient for the existence of an asymptotic observer, this is insufficient yet necessary for the existence of a strong observer.

Here, the fundamental difference between a strong and an asymptotic observer comes into play. The desire to preserve the independence of a strong observer Ω^* from the input \mathbf{u} , as in Definition 6.5, requires a completely different treatment.

Theorem 6.9. System Σ_L has a strong observer if and only if it is strongly zero-detectable. [Hautus, 1983, Theorem 1.12]

Theorem 6.10. System Σ_L is strongly zero-detectable if and only if it is zero-detectable and in addition

$$\text{rank} \begin{bmatrix} CB & D \\ D & 0 \end{bmatrix} = \text{rank}(D) + \text{rank} \begin{bmatrix} B \\ D \end{bmatrix} \quad (6.11)$$

holds [Hautus, 1983, Theorem 1.6].

In comparison to the nonlinear case, i.e. under consideration of system Σ , the notion of zero-detectability is “not well-posed” enough according to Sontag [2004, Chapter 8]. And so, strong zero-detectability of Σ does neither guarantee the existence of a strong nor asymptotic observer in the general nonlinear case. In the linear case, considering Σ_L , zero-detectability guarantees existence of an asymptotic observer nonetheless.

Remark 6.11. However, it is known that zero-detectability is a necessary condition for both, the existence of an asymptotic as well as a strong observer.

In regards to hydraulic networks, by relating flow and pressure measurements to the dynamic hydraulic network equations, a more general discussion about the benefits and drawbacks of using either one of each is launched. Concerning notation, detected or reconstructed (one may say observed) quantities are denoted with a hat, for instance $\hat{\mathbf{x}}_e$ denotes the observed value of equilibrium flow \mathbf{x}_e .

6.2 Pressure Measurements

Assumption 6.12. Pipe characteristics, such as length and diameter as well as the network’s topology and the nodal elevation are known. Also, the source pressure \mathbf{h}_s is assumed to be known.

For the purpose of analysis, consider Assumption 6.12 and suppose all pressure heads \mathbf{h} and thus all pressure head losses

$$\mathbf{A}^T \mathbf{h} = \tilde{\mathbf{C}}_s \mathbf{h}_s - \hat{\mathbf{h}}_{\text{loss}}(\hat{\mathbf{x}}_e) - \mathbf{A}^T \mathbf{z} \quad (6.12)$$

are measured in steady-state while friction parameters are unknown. Although one aims to achieve $\mathbf{h}_{\text{loss}}(\mathbf{x}_e) \stackrel{!}{=} \hat{\mathbf{h}}_{\text{loss}}(\hat{\mathbf{x}}_e)$ (at least at the time of the steady-state measurement), one can not accurately calculate the flow $\hat{\mathbf{x}}_e = \hat{\mathbf{h}}_{\text{loss}}^{-1}(\tilde{\mathbf{C}}_s \mathbf{h}_s - \mathbf{A}^T(\mathbf{h} + \mathbf{z}))$ which would require the inversion of the friction function with unknown parameters. Also, as a result of neglecting the unsteady-state component of friction (see section 2.1.4), it is essential to emphasize that it makes sense to measure the pressures in steady-state only as far as state reconstruction is concerned. In conclusion, measuring the pressure gives no direct information about the flow unless friction coefficients are known.

In reality, however, only some $n_p < n_j$ of the \mathcal{J} inner nodes are equipped with pressure sensors. Denoting these pressure measurements with $\mathbf{y}_h \in \mathbb{R}_{\geq 0}^{n_p}$ one obtains

$$\mathbf{C}_h \mathbf{h} = \mathbf{y}_h \quad (6.13)$$

where $\mathbf{C}_h = [e_{l_1} \ e_{l_2} \ \dots \ e_{l_{n_p}}]^T \in \mathbb{Z}_{\{0,1\}}^{n_p \times n_j}$ comprises unity vectors $e_i^T \in \mathbb{Z}_{\{0,1\}}^{1 \times n_j}$ concerning indices $i \in \{l_1, \dots, l_{n_p}\} \subset \mathcal{I}$. The complementary set, analogous to matrices \mathbf{R}_q and $\bar{\mathbf{R}}_q$ (see Property 4.5), is denoted by $\bar{\mathbf{C}}_h = [e_{\bar{l}_1} \ e_{\bar{l}_2} \ \dots \ e_{\bar{l}_{n_j-n_p}}]^T$ and results in

$$\bar{\mathbf{C}}_h \mathbf{h} = \mathbf{h}_N \in \mathbb{R}_{\geq 0}^{n_j-n_p}, \quad (6.14)$$

i.e. unknown pressure heads \mathbf{h}_N at nodes $\{\bar{l}_1, \dots, \bar{l}_{n_j-n_p}\} \subset \mathcal{I}$ such that $\mathbf{h} = \mathbf{C}_h^T \mathbf{y}_h + \bar{\mathbf{C}}_h^T \mathbf{h}_N$. In terms of head losses $\Delta \mathbf{h} := \mathbf{C}_s \mathbf{h}_s - \mathbf{A}^T (\mathbf{h} + \mathbf{z})$, one can eliminate $n_j - n_p$ nodes of the original network.

Network Transformation Example. To illustrate this procedure, the 2-cycle network as before is considered. Suppose the pressure is measured at node $k = 2$ and $k = 3$. As one can see from figure 6.1, the transformation is not unique and only feasible in terms of pressure heads as the laws of flow resistance are nonlinear. Provided by a fat matrix \mathbf{T}_h (more columns than rows), the head losses of the reduced network are given by $\Delta \tilde{\mathbf{h}} = \mathbf{T}_h \Delta \mathbf{h}$. As a reason of the transformation being not unique, \mathbf{T}_h is apparently not unique.

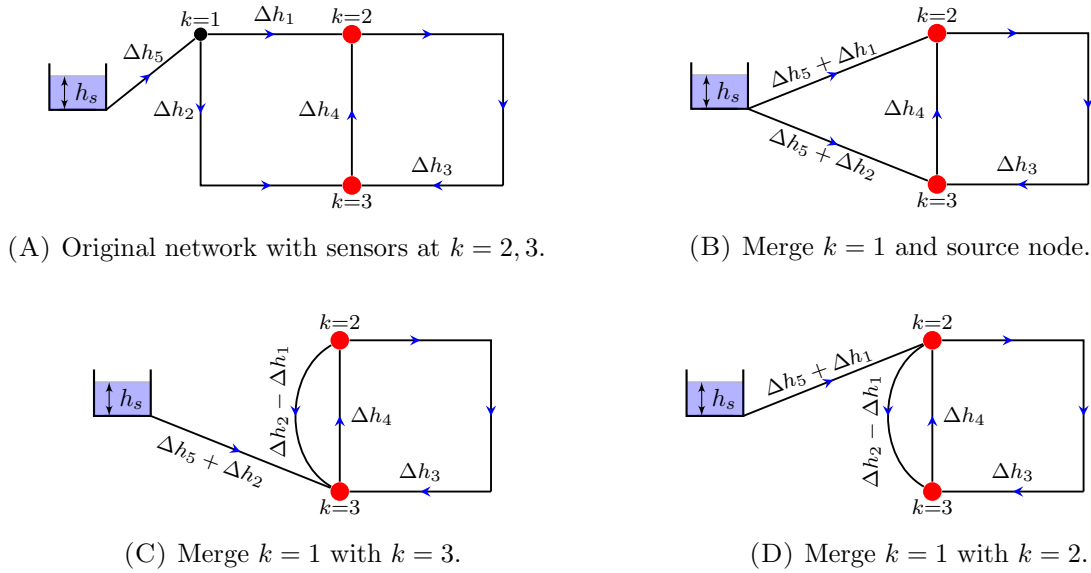


FIGURE 6.1: Network transformation by node elimination.

For instance, the transformation concerning figure 6.1B is given by

$$\Delta \tilde{\mathbf{h}} = \mathbf{T}_h \Delta \mathbf{h} = \begin{bmatrix} 1 & 0 & 0 & 0 & 1 \\ 0 & 1 & 0 & 0 & 1 \\ 0 & 0 & 1 & 0 & 0 \\ 0 & 0 & 0 & 1 & 0 \end{bmatrix} \begin{bmatrix} (h_1 + z_1) - (h_2 + z_2) \\ (h_1 + z_1) - (h_3 + z_3) \\ \vdots \\ h_s - (h_1 + z_1) \end{bmatrix} \quad (6.15)$$

The demonstration concerning figure 6.1 should illustrate that by measuring the subset of pressure heads \mathbf{y}_h in steady-state, one basically measures the linear combination of pressure head losses

$$\mathbf{T}_h \mathbf{h}_{\text{loss}}(\mathbf{x}_e) = -\mathbf{T}_h \left(\mathbf{A}^T \mathbf{C}_h^T \mathbf{y}_h - \bar{\mathbf{C}}_s \mathbf{h}_s + \mathbf{A}^T \mathbf{z} \right) \quad (6.16)$$

in the network which certainly aggravates any conclusion about the flow. The only direct conclusion which can be made in this case is that

$$\mathbf{T}_h \hat{\mathbf{h}}_{\text{loss}}(\hat{\mathbf{x}}_e) = \mathbf{T}_h \mathbf{h}_{\text{loss}}(\mathbf{x}_e) \quad \Leftrightarrow \quad \mathbf{h}_{\text{loss}}(\mathbf{x}_e) - \hat{\mathbf{h}}_{\text{loss}}(\hat{\mathbf{x}}_e) \in \ker(\mathbf{T}_h). \quad (6.17)$$

Remark 6.13. *Although the transformation concerning \mathbf{T}_h is not unique, one can show that the kernels of all feasible transformation matrices \mathbf{T}_h span the equivalent null space.*

Notes About Sensor Placement. The case of either poorly distributed pressure sensors or too few ones where complete cycles are left without sensors has to be highlighted in this context. The transformed network would feature self-loops which have been excluded according to Assumption 3.2. Concerning the transformed network, the orthogonality of cycle matrices to the transposed incidence matrix can not be guaranteed in this case (in reference to Proposition 3.6). In principle, it is reasonable to distribute pressure sensors, or any kind of sensor for that matter, along the cycles, more specifically along the co-tree edges, of the hydraulic network. Also, a solid argument in favor of this statement is that the (real) minimal form of the demand-driven steady-state network equations (3.28) as well as the demand-driven (known consumption and derivative) slow transient network equations (4.58) (co-tree flow dynamics), do only have $n_c = n_\ell - n_j$ states.

However, with popular methods such as sensitivity analysis where one estimates the pressure sensitivity in reference to the *Jacobian* matrix, with respect to different locations, it may occur that cycles are left without sensors due to low pressure sensitivity. If the pressure drop along these cycles is at least greater than the sensor accuracy with some healthy margins, it arguably does make sense to equip these cycles with sensors.

Résumé. By measuring the pressure, one directly measures a linear combination of pressure head losses of the hydraulic network. Since the unsteady-state component of friction, which would require additional unknowns to be found, is neglected, there is little usability of transient pressure peaks for the reconstruction of the original states. Also in steady-state, no immediate relation to the flow can be drawn as long as the friction parameters are unknown and, yet, pressure measurements will turn out necessary to calibrate friction parameters.

6.3 Flow Measurements

The derived slow transient model equations PD (4.20) in an (*Luenberger*) observer-type form,

$$\begin{aligned} \frac{d\hat{\mathbf{x}}_Q}{dt} = & (\mathbf{I} - \mathbf{B}) \text{diag}(\mathbf{c}_l) \left[\tilde{\mathbf{C}}_s \mathbf{h}_s - \hat{\mathbf{h}}_{\text{loss}}(\hat{\mathbf{x}}_Q) - \mathbf{A}^T \left(\frac{1}{2g} \mathbf{R}_q^T \left(\mathbf{a}_q^{\odot -2} \odot (\mathbf{R}_q \mathbf{A} \hat{\mathbf{x}}_Q)^{\odot 2} \odot \hat{\mathbf{r}}^{\odot -2} \right) + \mathbf{z} \right) \right] \\ & - \mathbf{L}_Q (\mathbf{y}_Q - \mathbf{C}_Q \hat{\mathbf{x}}_Q) + \bar{\mathbf{L}}_q \bar{\mathbf{R}}_q \mathbf{A} \hat{\mathbf{x}}_Q = \hat{\mathbf{f}}_Q(\hat{\mathbf{x}}_Q, \hat{\mathbf{u}}, \mathbf{y}_Q) \end{aligned} \quad (6.18)$$

with some flow-measurement candidates $\mathbf{y}_Q \in \mathbb{R}^{n_Q}$, \mathbf{C}_Q comprised of unity vectors (analogous to 6.13 and 6.14) and mapping $\mathbf{L}_Q : \mathbb{R}^{n_Q} \rightarrow \mathbb{R}^{n_\ell}$ as well as $\bar{\mathbf{L}}_q : \mathbb{R}^{n_j - n_q} \rightarrow \mathbb{R}^{n_\ell}$ (linearity not required) are considered.

Assumption 6.14. *Concerning the measurement locations, it is assumed that*

$$\text{rank} \begin{bmatrix} \mathbf{C}_Q \\ \bar{\mathbf{R}}_q \mathbf{A} \end{bmatrix} = n_Q + n_j - n_q \quad (6.19)$$

otherwise some measurement locations are redundant.

For now, (6.18) does not require the consumption to be known which will turn out rather problematic as n_q unknown (orifice coefficients) inputs $\hat{\mathbf{u}} = \hat{\mathbf{r}}^{\odot -2}$ have to be considered. The following observations concerning (6.18) can be made.

- (1) n_q affine inputs $\hat{\mathbf{u}} = \hat{\mathbf{r}}^{\odot -2}$ are unknown.
 - (a) Even if assumed to be known (e.g. out of knowledge of the consumption \mathbf{q}), the derivatives of $\hat{\mathbf{u}} = \mathbf{u}$ introduce vast uncertainties in the diffeomorphism.
- (2) System equations completely lack a linear part in the dynamics.
- (3) Friction function $\hat{\mathbf{h}}_{\text{loss}}(\cdot)$ (satisfying Assumption 3.10) has unknown parameters.
 - (a) It is (strictly) monotonically increasing.
 - (b) Its *Jacobian* is diagonal and globally positive definite.
- (4) Non-consumer nodal equations $\bar{\mathbf{R}}_q \mathbf{A} \mathbf{x}_Q \equiv \mathbf{0}$ can be harnessed as pseudo-measurements.
 - (a) Derivatives of these pseudo-measurements satisfy $\bar{\mathbf{R}}_q \mathbf{A} (\mathbf{I} - \mathbf{B}) = \mathbf{0} \Rightarrow \bar{\mathbf{R}}_q \mathbf{A} \mathbf{f}_Q \equiv \mathbf{0}$.

Arising Questions. Given Assumption 6.12 and 6.14, the author tackles the following questions with respect to flow measurements.

- (i) Assuming the consumption and friction parameters to be unknown, can the dynamic model information be used to reconstruct states?
- (ii) What can be achieved when assuming the consumption to be known and friction parameters to be unknown?

Diffeomorphism. When considering the output of (6.18) with pseudo-measurements (in reference to point (4) of this page)

$$\mathbf{y} = \begin{bmatrix} \mathbf{C}_Q \\ \bar{\mathbf{R}}_q \mathbf{A} \end{bmatrix} \mathbf{x}_Q = \begin{bmatrix} \mathbf{y}_Q \\ \bar{\mathbf{R}}_q \mathbf{A} \mathbf{x}_Q \end{bmatrix} \quad (6.20a)$$

$$\begin{aligned} \mathbf{C}_Q \dot{\mathbf{x}}_Q &= \mathbf{C}_Q (\mathbf{I} - \mathbf{B}) \text{diag}(\mathbf{c}_l) \left[\tilde{\mathbf{C}}_s \mathbf{h}_s - \mathbf{h}_{\text{loss}}(\mathbf{x}_Q) - \mathbf{A}^T \left(\frac{1}{2g} \mathbf{R}_q^T \left(\mathbf{a}_q^{\odot -2} \odot (\mathbf{R}_q \mathbf{A} \mathbf{x}_Q)^{\odot 2} \odot \mathbf{u} \right) + \mathbf{z} \right) \right] \\ &\quad - \frac{1}{2g} \mathbf{C}_Q (\mathbf{I} - \mathbf{B}) \text{diag}(\mathbf{c}_l) \mathbf{A}^T \mathbf{R}_q^T \left(\mathbf{a}_q^{\odot -2} \odot (\mathbf{R}_q \mathbf{A} \mathbf{x}_Q)^{\odot 2} \right) \odot \dot{\mathbf{u}} \end{aligned} \quad (6.20b)$$

and its derivative knowing that $\bar{\mathbf{R}}_q \mathbf{A} \dot{\mathbf{x}}_Q \equiv \mathbf{0}$, one can draw conclusions from the first output derivative (6.20b) (non-zero part). The inverse of the strictly monotone (thus injective) friction function $\mathbf{h}_{\text{loss}}(\cdot)$ is required for the diffeomorphism (compare with (6.1)). Also, the derivative of orifice coefficients \mathbf{u} would be needed. However, since friction parameters are unknown, no output derivatives can be harnessed in this context for such a diffeomorphism, although there is more than one output available (compare to (6.1)). Effectively, steady-state nodal equations

$$\begin{bmatrix} \mathbf{A} & -\mathbf{R}_q^T \end{bmatrix} \begin{bmatrix} \mathbf{x}_Q \\ \mathbf{q} \end{bmatrix} = \mathbf{0} \quad (6.21)$$

are the only source of information as measuring pressure does not allow any direct conclusion about the flow.

Furthermore, in case the consumption $\mathbf{q} = \mathbf{R}_q \mathbf{A} \mathbf{x}_Q$ is unknown, one can not conclude that $\mathbf{y} \equiv \mathbf{0}$ (6.20a) does result in $\lim_{t \rightarrow \infty} \mathbf{x}_Q(t) = \mathbf{0}$ as $\mathbf{x}_Q = \mathbf{0} \Leftrightarrow \mathbf{q} = \mathbf{0}$ and thus $\mathbf{q} \neq \mathbf{0} \Rightarrow \mathbf{x}_Q \neq \mathbf{0}$ in steady-state. However, as zero-detectability is a necessary condition for the existence of an asymptotic or strong observer, one can already answer the first question (i).

Conclusion (i). The dynamic model information can not be harnessed to reconstruct states if friction coefficients and the consumption are unknown.

Actually, the missing zero-detectability is already sufficient to exclude the existence of any observer (strong as well as asymptotic) and thus proves considerations about the diffeomorphism obsolete. The situation barely improves when assuming the consumption to be known. Even if \mathbf{q} is measured, one has to expect the data to feature low time resolution, meaning that no transients may be seen in this data. Also, considering the consumption as output $\mathbf{y} = \mathbf{q}$, the verification of zero-detectability according to Definition 6.6 has to be investigated closely. As zero consumption $\mathbf{y} = \mathbf{q} = \mathbf{0}$ violates Definition 4.4 in reference to Assumption 4.3 and Remark 4.6, where orifice coefficients were restricted to become zero, all nodes are considered as output $\mathbf{y} = \mathbf{A}\mathbf{x}_Q$ which become non-consumer ones in case $\mathbf{y} \equiv \mathbf{0}$.

Corollary 6.15. *Let Assumption 3.10 and 4.2 hold. Consider the output $\mathbf{y} = \mathbf{A}\mathbf{x}_Q$ for PD (4.20) and $\mathbf{y} = \mathbf{A}\mathbf{x}_Q = \mathbf{R}_q^T \mathbf{q}_d$ for LCD (4.30) where the non-consumer nodes $\bar{\mathbf{R}}_q \mathbf{A}\mathbf{x}_Q \equiv \mathbf{0}$ are trivial and thus can be added to the measured consumption $\mathbf{q} = \mathbf{R}_q \mathbf{A}\mathbf{x}_Q$. Then, system LCD (4.30) as well as PD (4.20), hence (4.19), are zero-detectable.*

Proof. This is a direct consequence of Theorem 4.18 which states global asymptotic stability (LCD and PD) for every constant consumption $\frac{d\mathbf{q}}{dt} \equiv \mathbf{0}$. Due to Definition 4.4, $\bar{\mathbf{R}}_q = \mathbf{I}$ leaving $\mathbf{R}_q = \mathbf{0}$. As a consequence, LCD (4.30) is equivalent to PD (4.20) for the current configuration $\mathbf{q}_d \equiv \mathbf{0}$, respectively, $\mathbf{A}\mathbf{x}_Q \equiv \mathbf{0}$ knowing that $\mathbf{G}\mathbf{A}^T = \mathbf{0}$. As a result of Theorem 4.15, the equilibrium of LCD and thus PD is a solution of $\mathbf{\Gamma}$ (3.23). Knowing that $\mathbf{x}_e = \mathbf{0}$ solves $\mathbf{\Gamma}(\mathbf{x}_e)$ (4.15) for zero consumption, as $\mathbf{h}_{\text{loss}}(\mathbf{0}) = \mathbf{0}$ according to Assumption 3.10, and that a solution of $\mathbf{\Gamma}$ has to be unique according to Proposition 3.12, $\mathbf{y} \equiv \mathbf{0}$ implies $\lim_{t \rightarrow \infty} \mathbf{x}_Q(t) = \mathbf{x}_e = \mathbf{0}$ independently of consistent initial states (Assumption 4.2), the source pressure \mathbf{h}_s , the orifice coefficients \mathbf{r} (thus \mathbf{u}) and the elevation \mathbf{z} . ■

Technically, the only feasible solution for the consumption to become $\mathbf{q} \rightarrow \mathbf{0}$ turns out to be at zero pressure $\mathbf{h}_q = \mathbf{0}$ while the orifice coefficients $\mathbf{r} > \mathbf{0} \Leftrightarrow \mathbf{u} > \mathbf{1}$ lose all influence on the system's states. So the analysis in terms of strong zero-detectability appears to be much more puzzling.

Remark 6.16. *Definition 4.4 does not comply with $[\bar{\mathbf{q}}]_k = 0$ for any $k \in \mathcal{K}$ with a-priori determined, or static, \mathbf{R}_q and $\bar{\mathbf{R}}_q$ and would require to make them dependent on the system's states. Indices in sets \mathcal{K} and $\bar{\mathcal{K}}$ would have to swap among the two sets such that if $q_{k_i} \rightarrow 0$ approaches zero, index k_i (and therefore $\mathbf{e}_{k_i}^T$ in (4.12)) would have to make a transition from set \mathcal{K} to $\bar{\mathcal{K}}$ which is associated with switching dimensions of \mathbf{R}_q and $\bar{\mathbf{R}}_q$.*

However, the real problem involved with making \mathbf{R}_q and $\bar{\mathbf{R}}_q$ (or the indices of the unity vectors from which they are built from) dependent on system states, is of technical nature and concerns the implementation of the switching process. One would have to ensure thoroughly that nodal *Kirchhoff* equations are not violated during or after the switching process. As with shrinking consumer orifices, smaller and smaller \mathbf{r} (cf. (4.14)), \mathbf{u} would approach infinity reciprocally to the consumption which shall approach zero. While violating Assumption 4.3, this will certainly cause numerical issues. It is reasonable to assume that this will remain a thought experiment only after all.

Although zero-detectable, there hardly is any chance to design an asymptotic observer when friction function $\mathbf{h}_{\text{loss}}(\cdot)$ is unknown. To illustrate this, consider the purely hypothetical case where the derivative of the nodal consumption $\dot{\bar{\mathbf{q}}}$ is perfectly known (given Assumption 6.12). Then, it can be considered as input in the co-tree flow dynamics (4.58). In a similar observer-type

form

$$\begin{aligned} \frac{d\hat{\mathbf{x}}_{\bar{t}}}{dt} &= \left(\mathbf{S} \operatorname{diag} \left(\mathbf{c}_l^{\odot -1} \right) \mathbf{S}^T \right)^{-1} \mathbf{S} \left(\tilde{\mathbf{C}}_s \mathbf{h}_s - \hat{\mathbf{h}}_{\text{loss}} \left(\mathbf{S}^T \hat{\mathbf{x}}_{\bar{t}} + \mathbf{T}_t \mathbf{A}_t^{-1} \mathbf{R}_q^T \bar{\mathbf{q}} \right) - \operatorname{diag} \left(\mathbf{c}_l^{\odot -1} \right) \mathbf{T}_t \mathbf{A}_t^{-1} \mathbf{R}_q^T \dot{\mathbf{q}} \right) \\ &\quad - \mathbf{L}_{\bar{t}} \left(\mathbf{y}_{\bar{t}} - \mathbf{C}_{\bar{t}} \hat{\mathbf{x}}_{\bar{t}} \right) = \hat{\mathbf{f}}_{\bar{t}} \left(\hat{\mathbf{x}}_{\bar{t}}, \dot{\mathbf{q}}, \mathbf{q}, \mathbf{y}_{\bar{t}} \right) \end{aligned} \quad (6.22)$$

flow measurements $\mathbf{y}_{\bar{t}} = \mathbf{C}_{\bar{t}} \mathbf{x}_{\bar{t}} \in \mathbb{R}^{n_{\bar{t}}}$ at the co-tree branches, selected by $\mathbf{C}_{\bar{t}}$, of the network are considered. The observed error $(\mathbf{y}_{\bar{t}} - \mathbf{C}_{\bar{t}} \hat{\mathbf{x}}_{\bar{t}})$ thereby serves as input to the operator $\mathbf{L}_{\bar{t}} : \mathbb{R}^{n_{\bar{t}}} \rightarrow \mathbb{R}^{n_{\bar{t}} - n_j}$. In this case, however, nodal *Kirchhoff* equations can not be harnessed as *pseudo*-measurements since $\mathbf{A} \mathbf{x}_Q = \mathbf{A} (\mathbf{S}^T \mathbf{x}_{\bar{t}} + \mathbf{T}_t \mathbf{A}_t^{-1} \bar{\mathbf{q}}) = \bar{\mathbf{q}}$ as $\mathbf{A} \mathbf{S}^T = \mathbf{0}$. Nevertheless, in this purely hypothetical case one might be able to stabilize the error dynamics:

$$\dot{\mathbf{e}}_{\bar{t}} = \dot{\mathbf{x}}_{\bar{t}} - \dot{\hat{\mathbf{x}}}_{\bar{t}} = - \left(\mathbf{S} \operatorname{diag} \left(\mathbf{c}_l^{\odot -1} \right) \mathbf{S}^T \right)^{-1} \mathbf{S} \left(\mathbf{h}_{\text{loss}} \left(\mathbf{x}_Q \right) - \hat{\mathbf{h}}_{\text{loss}} \left(\hat{\mathbf{x}}_Q \right) \right) + \mathbf{L}_{\bar{t}} \mathbf{C}_{\bar{t}} \mathbf{e}_{\bar{t}} \quad (6.23)$$

After closer inspection this turns out to be also rather hypothetical. For the purpose of analysis, consider the conceptually simplest form of $\mathbf{h}_{\text{loss}}(\cdot)$, the laminar case where $\mathbf{h}_{\text{loss}}(\mathbf{x}_Q) = \operatorname{diag}(\bar{\mathbf{w}}) \mathbf{x}_Q = \operatorname{diag}(\bar{\mathbf{w}}) (\mathbf{S}^T \mathbf{x}_{\bar{t}} + \mathbf{T}_t \mathbf{A}_t^{-1} \bar{\mathbf{q}})$. Yielding in

$$\dot{\mathbf{e}}_{\bar{t}} = \dot{\mathbf{x}}_{\bar{t}} - \dot{\hat{\mathbf{x}}}_{\bar{t}} = - \left(\mathbf{S} \operatorname{diag} \left(\mathbf{c}_l^{\odot -1} \right) \mathbf{S}^T \right)^{-1} \mathbf{S} \left(\operatorname{diag}(\bar{\mathbf{w}}) \mathbf{S}^T \mathbf{x}_{\bar{t}} - \operatorname{diag}(\hat{\mathbf{w}}) \mathbf{S}^T \hat{\mathbf{x}}_{\bar{t}} \right) \quad (6.24a)$$

$$- \left(\mathbf{S} \operatorname{diag} \left(\mathbf{c}_l^{\odot -1} \right) \mathbf{S}^T \right)^{-1} \mathbf{S} \left(\operatorname{diag}(\bar{\mathbf{w}}) - \operatorname{diag}(\hat{\mathbf{w}}) \right) \mathbf{S}^T \mathbf{T}_t \mathbf{A}_t^{-1} \bar{\mathbf{q}} \quad (6.24b)$$

$$+ \mathbf{L}_{\bar{t}} \mathbf{C}_{\bar{t}} \mathbf{e}_{\bar{t}} \quad (6.24c)$$

while assuming $\bar{\mathbf{w}}$ to be unknown, one would have to compensate (6.24a) and (6.24b) via $\mathbf{L}_{\bar{t}} \mathbf{C}_{\bar{t}} \mathbf{e}_{\bar{t}}$ which would presumably result in the requirement to measure the flow in most (yet not all) co-tree branches of the network.

Conclusion (ii). Assuming the consumption to be known, the co-tree branches of the network are the places to look when searching for possible flow measurement locations. However, in terms of detectability, there hardly is any possibility to stabilize the error dynamics when considering that one can not expect the derivative of the consumption $\dot{\mathbf{q}}$ to be known while nonlinear friction affects each of the observer (-error) states.

6.4 The Need to Identify Friction

The best method to identify the frictional behavior of a pipe is to measure the pressure drop over the entire pipe with two pressure sensors at its ends while an attached flow sensors records different flow conditions. The situation aggravates intensively if one of the three sensors is absent. Before going into detail, suppose (for the purpose of analysis) that friction function $\mathbf{h}_{\text{loss}}(\cdot)$ is known.

Theorem 6.17. *Let Assumption 3.10 as well as 6.12 hold and suppose friction function $\mathbf{h}_{\text{loss}}(\cdot)$ is known. Further suppose that the observed consumption $\hat{\mathbf{q}}(t)$ reaches the real equilibrium consumption \mathbf{q}_e after a finite time. Then, DD, LCD and $PD_{\mathbf{u}}$ respectively (see Definition 4.12 and 4.14) are strong observers for PD (4.19).*

Remark 6.18. *In the opinion of the author, it is not entirely clear whether observer LCD and $PD_{\mathbf{u}}$ shall be called strong or asymptotic in reference to Theorem 6.17. Since it will be shown below that the observer error vanishes asymptotically for all feasible unknown inputs, orifice coefficient $\mathbf{u} = \mathbf{r}^{\odot -2}$, they were called strong. However, the reader shall be reminded that*

\mathbf{u} (different to the real unknown input) was exploited internally to make the state estimation $\mathbf{R}_q \mathbf{A} \hat{\mathbf{x}}_Q$ follow the output, that is consumption \mathbf{q} .

Proof. First, nodal *Kirchhoff* equations do hold for every instant in time concerning DD, PD \mathbf{u} and LCD due to their rigid character (see physical considerations on page 34). Subsequently (compare with (3.27))

$$\mathbf{e}_Q(t) = \mathbf{x}_Q(t) - \hat{\mathbf{x}}_Q(t) = \mathbf{S}^T \underbrace{(\mathbf{x}_{\bar{t}}(t) - \hat{\mathbf{x}}_{\bar{t}}(t))}_{\mathbf{e}_{\bar{t}}(t)} + \mathbf{T}_t \mathbf{A}_t^{-1} \mathbf{R}_q^T (\mathbf{q}(t) - \hat{\mathbf{q}}(t)). \quad (6.25)$$

Provided that the observed equilibrium consumption $\hat{\mathbf{q}}_e$ equals the real equilibrium consumption \mathbf{q}_e after a finite time t_1 such that

$$\mathbf{e}_Q(t > t_1) = \mathbf{S}^T \mathbf{e}_{\bar{t}} \Rightarrow \lim_{t \rightarrow \infty} \mathbf{e}_Q(t) = \lim_{t \rightarrow \infty} \mathbf{S}^T \mathbf{e}_{\bar{t}}(t) \quad (6.26)$$

the error in all flows becomes zero if and only if the error in co-tree flows approaches zero due to $\ker \mathbf{S}^T = \{\mathbf{0}\}$. Second, it was shown in section 4.6 that DD, PD \mathbf{u} and so LCD feature common co-tree flow dynamics (4.58), resulting in the co-tree flow observer error dynamic

$$\frac{d\mathbf{e}_{\bar{t}}}{dt} = - \left(\mathbf{S} \operatorname{diag}(\mathbf{c}_l^{\odot -1}) \mathbf{S}^T \right)^{-1} \mathbf{S} \left(\mathbf{h}_{\text{loss}}(\mathbf{x}_Q) - \mathbf{h}_{\text{loss}}(\hat{\mathbf{x}}_Q) - \operatorname{diag}(\mathbf{c}_l^{\odot -1}) \mathbf{T}_t \mathbf{A}_t^{-1} \mathbf{R}_q^T \frac{d(\mathbf{q} - \hat{\mathbf{q}})}{dt} \right). \quad (6.27)$$

Knowing that $\mathbf{q} - \hat{\mathbf{q}} = \mathbf{0}$ after $t > t_1$, it is sufficient to show that

$$\dot{\mathbf{e}}_{\bar{t}}(t > t_1) = - \left(\mathbf{S} \operatorname{diag}(\mathbf{c}_l^{\odot -1}) \mathbf{S}^T \right)^{-1} \mathbf{S} (\mathbf{h}_{\text{loss}}(\mathbf{x}_Q) - \mathbf{h}_{\text{loss}}(\hat{\mathbf{x}}_Q)) \quad (6.28)$$

is asymptotically stable. Applying the *Mean Value Theorem* on the continuous function $\mathbf{h}_{\text{loss}}(\cdot)$

$$\exists \boldsymbol{\xi} \in [\hat{\mathbf{x}}_Q, \mathbf{x}_Q] : \int_{\hat{\mathbf{x}}_Q}^{\mathbf{x}_Q} \mathbf{h}_{\text{loss}}(\boldsymbol{\zeta}) d\boldsymbol{\zeta} = \mathbf{h}_{\text{loss}}(\boldsymbol{\xi}) \odot \mathbf{e}_Q \Leftrightarrow \mathbf{h}_{\text{loss}}(\mathbf{x}_Q) - \mathbf{h}_{\text{loss}}(\hat{\mathbf{x}}_Q) = \left. \frac{\partial \mathbf{h}_{\text{loss}}(\boldsymbol{\zeta})}{\partial \boldsymbol{\zeta}} \right|_{\boldsymbol{\xi}} \mathbf{e}_Q \quad (6.29)$$

with the diagonal and positive definite Jacobian $\mathbf{D}(\boldsymbol{\xi}) = \left. \frac{\partial \mathbf{h}_{\text{loss}}(\boldsymbol{\zeta})}{\partial \boldsymbol{\zeta}} \right|_{\boldsymbol{\xi}} \succ 0$ for all $\boldsymbol{\xi}$, one reformulates co-tree flow dynamics (6.28) in terms of

$$\dot{\mathbf{e}}_{\bar{t}}(t > t_1) = - \left(\underbrace{\mathbf{S} \operatorname{diag}(\mathbf{c}_l^{\odot -1}) \mathbf{S}^T}_{\mathbf{M}_1} \right)^{-1} \mathbf{S} \mathbf{D}(\boldsymbol{\xi}) \mathbf{S}^T \mathbf{e}_{\bar{t}}. \quad (6.30)$$

Considering the Lyapunov function candidate for the equilibrium $\mathbf{e}_{\bar{t}} = \mathbf{0}$

$$V = \frac{1}{2} \mathbf{e}_{\bar{t}}^T \mathbf{M}_1 \mathbf{e}_{\bar{t}} > 0 \quad \forall \mathbf{e}_{\bar{t}} \neq \mathbf{0} \quad (6.31)$$

with positive definite matrix $\mathbf{M}_1 \succ 0$ (see Remark 4.17 and compare with Proposition 4.1), its derivative

$$\dot{V} = -\mathbf{e}_{\bar{t}}^T \mathbf{M}_1 \mathbf{M}_1^{-1} \mathbf{S} \mathbf{D}(\boldsymbol{\xi}) \mathbf{S}^T \mathbf{e}_{\bar{t}} = -\mathbf{e}_{\bar{t}}^T \mathbf{S} \mathbf{D}(\boldsymbol{\xi}) \mathbf{S}^T \mathbf{e}_{\bar{t}} < 0 \quad \forall \mathbf{e}_{\bar{t}} \neq \mathbf{0} \quad (6.32)$$

is always smaller than zero because of $\mathbf{D}(\boldsymbol{\xi}) \succ 0 \Rightarrow \mathbf{S} \mathbf{D}(\boldsymbol{\xi}) \mathbf{S}^T \succ 0$ being positive definite. As a direct consequence of (6.30) being globally asymptotically stable, matrix

$$\mathbf{M}_2 = \mathbf{M}_1^{-1} \mathbf{S} \mathbf{D}(\boldsymbol{\xi}) \mathbf{S}^T \succ 0 \quad \forall \boldsymbol{\xi} \quad (6.33)$$

has to be positive definite. Subsequently, the only feasible equilibrium which solves $\mathbf{M}_2 \mathbf{e}_{\bar{t},e} = \mathbf{0}$ is $\mathbf{e}_{\bar{t},e} = \mathbf{0}$ since \mathbf{M}_2 has full rank (as a direct consequence of (6.33)). ■

Physical Considerations. Put into a physical perspective, the presented results, in particular Theorem 6.17, follow an indeed natural intuition. As the flow distributes according to the consecutive flow resistance (described by function $\mathbf{h}_{\text{loss}}(\cdot)$), referring to the principle of least action, at the junction and into the cycles of the network, it appears to be rather natural that once the observed flows follow the real consumption $\mathbf{A}\hat{\mathbf{x}}_Q = \mathbf{R}_q^T \mathbf{q}$, the observed flow distribution at the network's cycles will approach the real one when flow resistances are the same.

Résumé. Effectively, two basic characteristics have been identified for a strong observer, in the form of designated models, to function. The first being an obstacle which makes these designated models follow a specified consumption, essentially, the methodology on the basis of an exact linearization developed in chapter 4. The second characteristic being a method to identify friction coefficients. However, this will occupy the rest of this thesis and beyond as it will turn out that the defined circumstances, which make these considerations as realistic as possible, lead to an indeed difficult, in many situations probably insolvable, problem. In the author's opinion, this is the point where this thesis leaves a rather theoretically-intensive part and enters a more engineering-oriented one which is, arguably, even more intense.

Roughness Identification: The Full Turbulent Case

In the observability analysis, conducted in the previous chapter 6, the knowledge of the frictional behavior of individual pipes in the hydraulic network turned out vital for the reconstruction of network's states. Although the literature is vast on the topic of roughness calibration, as far as the determination of steady-state friction parameters is concerned, the subject can not be considered closed. Actually, many fundamentally different methodologies were developed, even an official competition on a real water network was organized [Ostfeld et al., 2012]. The arguably most popular ones competed with each other in this organized calibration challenge. In essence, however, it turned out that practical experience is most important to obtain useful results. The capability to identify errors contained in the measurement data, in the considered topology, in the consumption as well as to find closed valves which were thought to be open etc. is more vital than the pure data processing. Although well aware of the necessity to correct all these errors, which inevitably occur in practice, some basic assumptions have to be made in order to allow theoretical treatment.

Historically, the main research focus shifted from trial and error methods in the rather early appearance of calibration algorithms, as in Bhave [1988]; Walski [1983], over explicit methods, e.g. Boulos and Wood [1990]; Ormsbee and Wood [1986], to implicit methods based on optimization problems, minimizing the error between measured and simulated quantities (early references are, for instance, Ormsbee [1989]; Lansey and Basnet [1991]). Explicit methods characterize those which require to directly solve steady-state hydraulic network equations (referring to the conservation of mass, section 3.1.1, and energy, section 3.1.2) for determination of friction parameters. Admittedly, this thesis does neither provide a complete nor thorough literature review of this subject as this would fill several books readily, but seeks to carefully outline the differences to existing approaches. However, a more thorough literature overview ought to be found in, e.g., [Savic et al., 2009], [Walski et al., 2003] or [Kapelan, 2002].

As distinguished from the usual structure, this thesis emphasizes on the basic idea of the developed approach first, which appears to be intuitively simple, and then refers to differences to existing methods. Followed by some deeper theoretical observations, a better understanding of the original problem is obtained while new research questions arise.

7.1 Configuration

This section briefly summarizes the sensor configuration as well as all necessary assumptions in order for the presented roughness calculation scheme to be applicable. In order to handle a large number of unknowns by means of $n_p < n_j$ pressure sensors only, several sets of measurements, which have to be taken during different loading conditions (concerning \mathbf{h}_s and \mathbf{q}), are needed.

Assumption 7.1 (Linear Independency). *There are n_m sets of linear independent measurements, denoted by $\mathfrak{M} = \{1, 2, \dots, n_m\}$, available. Linear independence can be achieved by a variation of source pressure \mathbf{h}_s and/or the consumption \mathbf{q} .*

Since consumers are currently not equipped with the necessary sensor technology, so-called *fireflow* tests are usually conducted. At the minimum-night-flow, somewhere from 2am to 5am where the regular water consumption is lowest, hydrants are opened systematically. The hydrants' outflow is measured as well as pressure sensors throughout the network record, at least part of, the pressure distribution. Also the source pressure is assumed to be known according to Assumption 6.12. Depending on the amount of the minimum-night-flow, this procedure is, potentially, very problematic for calibration as nodal *Kirchhoff* equations (conservation of mass) are violated when the sum of all considered hydrant flows (fireflows) is lower than the total inflow in the network or *District Metering Area*.

Assumption 7.2 (Steady-State). *These n_m sets of measurements are taken in steady-state of the network.*

In order to avoid distortions due to transient effects, which have not been considered in the modeling procedure, the network has to be in steady-state during the time-frame considered for each of the measurement-sets. Recording a larger time-frame with a number of different measurement values for each sensor in each measurement-set may also be valuable for filtering noise. Applying simple averaging often proves effective in this regard.

Assumption 7.3 (Noise). *The variance of the measurement noise of applied pressure sensors is significantly smaller than the pressure drop, i.e. $[\text{var}(\mathbf{y}_h^{(i)})]_k \ll [\tilde{\mathbf{C}}_s \mathbf{h}_s^{(i)} - \mathbf{A}^T(\mathbf{h}^{(i)} + \mathbf{z})]_j$ for all $k = 1, 2, \dots, n_p$ and $j \in \mathfrak{J}$ in at least one of the $i \in \mathfrak{M}$ measurement-sets (compare with Remark 5.1). This means that the inequality holds for all j, k in at least one of the i -th measurement-sets. Also, the measurement errors in fireflows and pressures have zero mean.*

Without mentioning, flow sensors must also be sufficiently accurate in order to obtain useful results. When considering minor losses (section 2.1.4) also, one would, in principle, have to determine $2n_l$ unknowns. To keep the number of unknowns reasonably small, these minor losses are usually neglected. Besides, according to Walski et al. [2003][Chapter 2, p. 40] “*minor losses are generally much smaller than the head losses due to friction (hence the term “minor”)*”. However, this statement is certainly not always true, partially closed valves, local pipe constrictions, fittings and others may contribute to the pressure loss substantially, especially to pipes with relatively short lengths.

Assumption 7.4 (Minor Losses). *Minor losses of the n_l pipes in the network can be neglected.*

Together with the assumption already taken in the previous chapters, one can sum up.

Assumption	Context
3.2	properties of the graph
3.10	characteristics of $\mathbf{h}_{\text{loss}}(\cdot)$
6.12	pipe dimensions & source pressure
7.1	independency of measurements
7.2	measurements in steady-state
7.3	measurement noise
7.4	negligible minor losses

TABLE 7.1: Summary of assumptions relevant for roughness calibration.

One does not have to be misguided by the comparably large number of assumptions in table 7.1, at second glance they do appear rather general for people familiar with the subject. Nevertheless, several of them are hard or even impossible to verify. Regarding Assumption 7.3 for instance, it is well known that one has to produce high fireflows in order for the measurement noise to be negligible, however, the inequality can not be verified without the full knowledge of all nodal pressure heads \mathbf{h} . Also, the independence of the measurement-sets can also hardly be verified in reference to Assumption 7.1, a concern which will be raised later on.

Sensors. Following the previous chapter, n_p pressure sensors are placed at a subset of the n_j inner nodes \mathcal{J} of the network while the consumption \mathbf{q} of the n_q consumers is expected to be measured, at least during the calibration. Keep in mind that these n_q consumer-nodes are also a subset of \mathcal{J} and can represent, for instance, hydrants. The source pressure was already considered to be known according to Assumption 6.12.

7.2 Introductory Example: 3-Cycle Network

For illustrative purposes, consider a network with $n_j = 5$ nodes, $n_\ell = 8$ pipes and hence $n_c = n_\ell - n_j = 3$ cycles in figure 7.1.

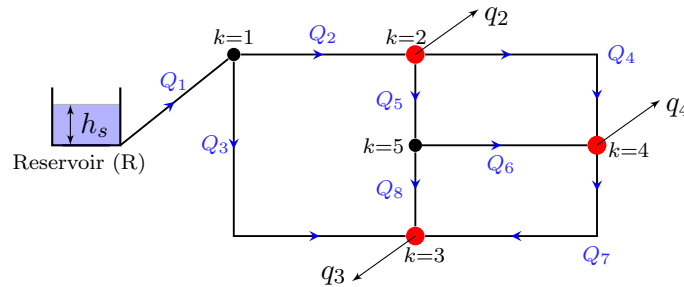


FIGURE 7.1: 3-cycle network with pressure sensors at red colored nodes $k = 2, 3, 4$.

This network, featuring $n_q = 3$ consumers and $n_s = 1$ constant pressure source, is a step-up in complexity compared to the illustrative 2-cycle network in figure 3.2. The fact that the (red colored) nodes equipped with pressure sensors also have consumers is mere chance and does not affect the identification scheme.

The principle of the presented approach starts with the premise to obtain at least as many equations as unknowns. In the first set of measurements, that is $i = 1$, the pressure head at node $k = 1, 5$ as well as roughnesses of n_ℓ pipes are unknown, which makes up to a total number of 10 unknowns. On the contrary, there are $n_j = 5$ nodal equations providing additional information to be used, resulting in a relation of 2:1 regarding unknowns versus equations. Important to note here is that the three independent cycle equations (conservation of energy) have to be used implicitly for the set-up of nodal equations and thus provide no additional information, but more on that later.

The key observation is that the nodal *Kirchhoff* equations in the second set of measurements, i.e. $i = 2$, are independent from the nodal equations from the first measurement-set given Assumption 7.1. However, as in the second measurement-set only two additional unknown pressure heads, in addition to the 10 unknowns (first set) have to be considered, the relation of unknowns versus equations improves to 12:10 (combining the first & second set). After taking the third measurement-set, a break-even point is reached, where in total more (nodal) equations than unknowns are available. Table 7.2 summarizes the comparison of unknowns and equations in reference to the 3-cycle network.

measurement-set	# unknown heads	# unknown roughnesses	# total unknowns	# equations	Δ
1	$n_j - n_p = 2$	$n_\ell = 8$	10	$n_j = 5$	5
2	$2(n_j - n_p) = 4$	$n_\ell = 8$	12	$2n_j = 10$	2
3	$3(n_j - n_p) = 6$	$n_\ell = 8$	14	$3n_j = 15$	-1

TABLE 7.2: Unknowns vs. equations of the 3-cycle network in figure 7.1.

The key here is that the number of nodal equations grows faster than the number of unknown pressure heads $n_j > n_j - n_p$ with each independent measurement-set. In this context, it is trivial to recognize that at least one $n_p > 0$ pressure sensor must be available. Taking a closer look at table 7.2, it is clear that the Δ , the difference between the total number of unknowns and the number of equations, of each measurement-set reduces by 3 with each measurement-set. Given a fixed number of sensors n_p , the minimum number of measurement-sets in order to reach a break-even point is denoted with $n_{m,\min}$. One obtains

$$[n_{m,\min}(n_j - n_p) + n_\ell] - n_{m,\min}n_j < 0$$

$$n_{m,\min} = \left\lceil \frac{n_\ell}{n_p} \right\rceil \quad (7.1)$$

which has to be rounded to the next higher integer. For instance, if only one pressure sensor is available ($n_p = 1$), $n_\ell/n_p = 8$ independent measurement-sets are needed. Interestingly, this requirement is completely independent from the number of nodes, junctions (more than two connections) to be precise, in the network. Though, one should not be deceived by this result since the number of equations grows linearly with n_j , making the solving more difficult due to numerical issues as well as the computational demand.

Remark 7.5. *Moreover, the ability to produce at least $\lceil n_\ell/n_p \rceil$ independent measurement-sets presumably depends on several graph characteristics, in particular on the number of cycles but also on the number of consumers. Experimenting with several network configurations, the number of cycles $n_c = n_\ell - n_j$ turned out to be a good candidate for the smallest feasible n_p .*

From a practical perspective, however, one also has to consider which consumption-configurations can be realized. In reality, it is certainly not possible to vary the consumption arbitrarily, especially on a high consumer-outflow level which is necessary to produce sufficient head loss (in reference to Assumption 7.3). Summarizing the proposed rule of thumb, at least $n_p \geq n_\ell - n_c$ pressure sensors on nodes adjacent to co-tree edges of the hydraulic network (see also page 74) should be deployed.

Up to this point, the consideration of the roughness-calibration was conducted “*en gros*” only, it is not yet clear how the set-up the problem formulation nor how to solve it. The proposed equations in the following section can also be formulated as a multi-objective optimization problem and, in principle, be solved by any sophisticated solver.

7.3 Explicit Problem Formulation

The primary distinguishing aspect of the developed *explicit* calibration-method (algebraic equation system based on the conservation of mass and energy) to existing methods is the direct application of the implicit *Colebrook & White* formula (2.6) for the friction factor λ_{DW} (2.4). Due to two main reasons, this approach is controversial to this point in time.

First, explicit methods seem to be completely off radar from this research area for the time being. In this context, e.g., Savic et al. [2009] only attribute “*historical significance*” to explicit

methods and mention the following major drawbacks: (1) the number of calibration parameters need to be smaller or equal to the number of measurements, (2) measurement errors are not taken into account and (3) it is, allegedly, impossible to quantify the uncertainty of calibrated parameters. This thesis puts (2) and (3) in question while arguing against this ultimate assessment. A counterargument for (1), which certainly contains a correct critique, is that the risk to obtain roughnesses, which are only suitable for the calibration-measurements (measurement taken for calibration), particularly the pressure distribution, is high if requirements as described in the previous section are not met (compare table 7.2 concerning figure 7.1). This holds true independently from the applied calibration-method.

Second, the application of Darcy-Weisbach (2.4) instead of Hazen-Williams (see section 2.1.4) in combination with the friction factor (2.6) is also hardly applied directly for calibration due to its implicit character.

7.3.1 Turbulent Flow in Steady-State

This implicit character, however, is only present in the form

$$\Delta h = \lambda_{\text{DW}} k_{\text{DW}} |Q| Q \quad \Rightarrow \quad Q = \text{sign}(\Delta h) \frac{1}{\sqrt{\lambda_{\text{DW}}}} \sqrt{\frac{|\Delta h|}{k_{\text{DW}}}} \quad (7.2)$$

when expressing the head loss Δh (see (2.6)). Given Assumption 7.4, the total pressure head loss becomes $\Delta h = \Delta h_{\text{DW}}$ in reference to (2.4). The expression in terms of Q in (7.2) is equated with $|Q| = Re \frac{A\eta}{d\rho}$ according to (2.3) to yield the product of the Reynolds number and the (square root of) friction factor

$$Re \sqrt{\lambda_{\text{DW}}} = \frac{d\rho}{A\eta} \sqrt{\frac{|\Delta h|}{k_{\text{DW}}}}. \quad (7.3)$$

When inserting (7.3) into the *Colebrook & White* formula (2.6), i.e.

$$\frac{1}{\sqrt{\lambda_{\text{DW}}}} = -\frac{2}{\ln 10} \ln \left(\frac{\epsilon_{\text{DW}}}{3.7d} + 2.51 \frac{A\eta}{d\rho} \sqrt{\frac{k_{\text{DW}}}{|\Delta h|}} \right) \quad (7.4)$$

and (7.4) into (7.2), the turbulent flow as an *explicit* function on the pressure head loss and the roughness is obtained

$$Q = f_t(\epsilon_{\text{DW}}, \Delta h) = -\text{sign}(\Delta h) \frac{2}{\ln(10)} \sqrt{\frac{|\Delta h|}{k_{\text{DW}}}} \ln \left(\frac{\epsilon_{\text{DW}}}{3.7d} + 2.51 \frac{A\eta}{d\rho} \sqrt{\frac{k_{\text{DW}}}{|\Delta h|}} \right). \quad (7.5)$$

Keep in mind that these simple manipulations, which are well known in literature (e.g. in [Bhave, 1991]), are exact, no approximation was applied so far.

Remark 7.6. For the sake of readability the subscript “DW” of roughnesses ϵ_{DW} as well as of the parameter variable k_{DW} is suppressed from now on.

Assumption 7.7. Suppose temporarily, for the sake of simplicity, that each pipe flow j in each measurement-set i is in the turbulent regime, i.e.

$$Re_j^{(i)} = \frac{|Q_j^{(i)}| d_j \rho}{A_j \eta} \geq 4000 \quad \forall j \in \mathfrak{P} \wedge \forall i \in \mathfrak{M} \quad (7.6)$$

in order for (7.5) to be generally applicable.

The restriction will be relieved under considerable effort after closer inspection of this “full turbulent” case.

7.3.2 Full Turbulent Set-Up

The nodal equations along the i -th measurement-set have the following structure

$$\mathbf{A}\mathbf{x}_Q(\boldsymbol{\epsilon}, \mathbf{h}_N^{(i)}) = \mathbf{R}_q^T \mathbf{q}^{(i)} \quad (7.7a)$$

$$\Delta \mathbf{h}^{(i)} = \tilde{\mathbf{C}}_s \mathbf{h}_s^{(i)} - \mathbf{A}^T \mathbf{C}_h^T \mathbf{y}_h^{(i)} - \mathbf{A}^T \bar{\mathbf{C}}_h^T \mathbf{h}_N^{(i)} - \mathbf{A}^T \mathbf{z} \quad (7.7b)$$

$$[\mathbf{x}_Q(\boldsymbol{\epsilon}, \Delta \mathbf{h}^{(i)})]_j = Q_j^{(i)} \stackrel{(7.5)}{=} f_{t,j}([\boldsymbol{\epsilon}]_j, [\Delta \mathbf{h}^{(i)}]_j) \quad \forall j \in \mathfrak{P} \quad (7.7c)$$

$$\text{for } i \in \{1, 2, \dots, n_m\} = \mathfrak{M}$$

where the j -th flow component (7.7c) used for *Kirchhoff* equations (7.7a) is calculated via (7.5), i.e. the flow in the turbulent regime, thereby applying the conservation of energy (cf. with (3.24b)) for the head losses (7.7b). Effectively, the unknowns of this set of equations are the roughnesses $\boldsymbol{\epsilon} \in \mathbb{R}_{\geq 0}^{n_\ell}$ and the pressure heads at nodes with no sensors $\mathbf{h}_N^{(i)} \in \mathbb{R}_{\geq 0}^{n_j - n_p}$ in the i -th measurement-set. In reference to (7.7b), matrix $\mathbf{C}_h \in \mathbb{Z}_{\{0,1\}}^{n_p \times n_\ell}$ and its complementary part $\bar{\mathbf{C}}_h \in \mathbb{Z}_{\{0,1\}}^{(n_j - n_p) \times n_\ell}$ are comprised of unity vectors as in (6.13) and (6.14) selecting those entries in nodal heads \mathbf{h} where pressure sensors are present $\mathbf{C}_h \mathbf{h} = \mathbf{y}_h$, or absent $\bar{\mathbf{C}}_h \mathbf{h} = \mathbf{h}_N$. This is completely analogous to matrices \mathbf{R}_q and $\bar{\mathbf{R}}_q$ which select consumer and non-consumer nodes respectively.

Definition 7.8 (Pressure Nodes). *The subset \mathcal{P} of inner nodes \mathfrak{I} defines **pressure-nodes**, meaning nodes which are equipped with pressure sensors. The complementary set $\bar{\mathcal{P}}$ defines **non-pressure nodes**, meaning nodes where no pressure sensors are deployed.*

$$\mathcal{P} = \{p_1, p_2, \dots, p_{n_p}\} \subseteq \mathfrak{I} \quad \bar{\mathcal{P}} = \{\bar{p}_1, \bar{p}_2, \dots, \bar{p}_{n_j - n_p}\} \subseteq \mathfrak{I} \quad (7.8)$$

These two sets thereby satisfy $\mathcal{P} \cap \bar{\mathcal{P}} = \{\}$ and $\mathcal{P} \cup \bar{\mathcal{P}} = \mathfrak{I}$.

Following Definition 7.8, one obtains $\mathbf{C}_h = [\mathbf{e}_{p_1} \ \mathbf{e}_{p_2} \ \dots \ \mathbf{e}_{p_{n_p}}]^T$ and $\bar{\mathbf{C}}_h = [\mathbf{e}_{\bar{p}_1} \ \mathbf{e}_{\bar{p}_2} \ \dots \ \mathbf{e}_{\bar{p}_{n_j - n_p}}]^T$ where $\mathbf{e}_l \in \mathbb{Z}_{\{0,1\}}^{n_j}$ for $l \in \mathfrak{I}$.

At this point (7.7) contains, in principle, all information needed to determine all the pipes' roughness, provided that the assumptions in table 7.1 hold. Emphasizing once again on the application of the *Colebrook & White* formula in respect to the explicit turbulent flow expression, (7.5) has not been considered for any explicit or implicit calibration scheme in literature as far as the author is aware. A more recent proposal for an explicit approach applying *Hazen-William's* description of pipe friction can be found in, for instance, [Kun et al., 2018]. However, (7.7) turns out to be particularly difficult to solve even in the unperturbed case when no measurement noise is considered. The reason for that can not only be attributed to the problem's size, which is considerably larger than the steady-state problem Γ_h (3.24), but to the nonlinear dependency of (7.5) on $\mathbf{h}_N^{(i)}$.

7.3.3 Optimization vs. Root Finding

A considerable effort was undertaken to develop and enhance solver strategies in order to cope with (7.7)-type problems. Before going into detail, it should be emphasized that root finding of a multidimensional function, by means of e.g. a *Newton-Raphson* type solver, is generally to favor over a minimization problem where this multidimensional function is collapsed into a single

dimension and then treated as an optimization function [Press et al., 1992]. Once it is collapsed into a single dimension (by taking e.g. the sum of squares) the components of its gradient are not independent whereas the components of the multidimensional function are (Assumption 7.1) and so information gets lost unnecessarily. Nevertheless, the equivalence of an unconstrained optimization problem to finding a solution of $\mathbf{f}(\mathbf{x}) = \mathbf{0}$ with $\mathbf{f} : \mathbb{R}^n \rightarrow \mathbb{R}^n$ (root-finding) can, in principle, be shown as in the proof of Proposition 3.12, if and only if the *antiderivative* of $\mathbf{f}(\mathbf{x})$ is found. However, it is quite unlikely that one manages to find the *antiderivative* of (7.7) which involves the solving of a considerably large set of partial differential equations.

Effectively, the primary weakness of these optimization problems is that the solution space features lots of local minima which are barely distinguishable from the desired global optimum. In reference to Assumption 7.1, it is important to mention that at least $n_{m,\min}$ independent sets of measurements are required to potentially see this global minimum.

Genetic algorithms ought to overcome this weakness for the cost of computational effort and celebrate high popularity in this field of research [Savic and Walters, 1995; Kapelan, 2002; Steffelbauer, 2018]. Up to this point and given the current sensor configuration, these algorithms are, to the best of the author's knowledge, only fed with an (usually scalar) optimization function f_{opt} which depends on the measurement error $\mathbf{y}_h - \mathbf{C}_h \hat{\mathbf{h}}(\boldsymbol{\epsilon})$ such that

$$\min_{\boldsymbol{\epsilon}} f_{opt}(\mathbf{y}_h - \mathbf{C}_h \hat{\mathbf{h}}(\boldsymbol{\epsilon})) \quad \xrightarrow{\text{e.g.}} \quad \min_{\boldsymbol{\epsilon}} (\mathbf{y}_h - \mathbf{C}_h \hat{\mathbf{h}}(\boldsymbol{\epsilon}))^T \mathbf{W}_h (\mathbf{y}_h - \mathbf{C}_h \hat{\mathbf{h}}(\boldsymbol{\epsilon})) \quad (7.9)$$

where $\hat{\mathbf{h}}(\boldsymbol{\epsilon})$ denotes the simulated pressure head vector depending on the roughnesses as a solution of $\boldsymbol{\Gamma}_h$ (3.24) and $\mathbf{W}_h \in \mathbb{R}^{n_p \times n_p}$ a weighting matrix. Optimization problem (7.9) is usually enhanced with a set of inequality constraints. Although the simplicity of this approach is utterly appealing, this formulation lacks *direct* consideration of the conservation of mass (in the objective function) in comparison to (7.7). In the perspective of (7.9) there is little incentive to match the real flows \mathbf{x}_Q , particularly due the fact that the solver only sees a subset of linear combinations of head losses (see section 6.2 and note that $\mathbf{h}_{\text{loss}}(\mathbf{x}_Q) = \Delta \mathbf{h}$ in steady-state $\mathbf{x}_Q = \mathbf{x}_e$) which allows no conclusion about the flow. Remember the network transformation example on page 73 concerning figure 6.1 in this context. To put it into other words, by only measuring a linear subset of pressure head losses as in (6.16) there are multiple different combinations of $\Delta \hat{\mathbf{h}}$ to result in \mathbf{y}_h . These combinations lie in the kernel of the transformation matrix \mathbf{T}_h . Only by considering at least more than $n_{m,\min}$ sets of measurements, one may be able to reconstruct the flows. Formulation (7.7) seems to be much more suitable to do so as it simply inverts the steady-state hydraulic network equations $\boldsymbol{\Gamma}_h$ (3.24) along the roughnesses $\boldsymbol{\epsilon}$ and the unknown pressure heads $\mathbf{h}_N^{(i)}$.

Albeit mathematically sophisticated, it is much more effective to search along a dedicated search direction, obtained via (7.7) featuring more equations than unknowns, as to instruct a genetic algorithm to search in the entire space spanned by a scalar optimization function.

7.4 Newton - Raphson

With the aim to solve a nonlinear set of equations of the form

$$\mathbf{f}(\mathbf{x}) \stackrel{!}{=} \mathbf{0} \quad (7.10)$$

with a smooth and continuous vector function $\mathbf{f} : \mathbb{R}^n \rightarrow \mathbb{R}^n$, the iterative scheme

$$\mathbf{x}_k = \mathbf{x}_{k-1} + \mu \Delta \mathbf{x}_k \quad \text{for } k = 1, 2, \dots \quad (7.11)$$

provides *quadratic* convergence to the real root $\mathbf{x}^* \Rightarrow \mathbf{f}(\mathbf{x}^*) = \mathbf{0}$ if the initial value \mathbf{x}_0 is chosen in vicinity of \mathbf{x}^* . In the original proposal the scalar step length equals $\mu = 1$, whereas the search

direction $\Delta \mathbf{x}_k = \mathbf{x}_k - \mathbf{x}_{k-1}$ is obtained with the help of a *Taylor* series around \mathbf{x}_k

$$\mathbf{f}(\mathbf{x}_k) = \mathbf{f}(\mathbf{x}_{k-1}) + \left. \frac{\partial \mathbf{f}}{\partial \mathbf{x}} \right|_{\mathbf{x}_{k-1}} \Delta \mathbf{x}_k + \mathcal{O}(\Delta \mathbf{x}_k^2) \quad (7.12)$$

where higher order terms $\mathcal{O}(\Delta \mathbf{x}_k^2)$ are neglected. By setting the *Taylor* series to zero, the search direction

$$\Delta \mathbf{x}_k = - \left(\left. \frac{\partial \mathbf{f}}{\partial \mathbf{x}} \right|_{\mathbf{x}_{k-1}} \right)^{-1} \mathbf{f}(\mathbf{x}_{k-1}) = -\mathbf{J}_{k-1}^{-1} \mathbf{f}(\mathbf{x}_{k-1}) \quad (7.13)$$

is obtained, also applying the inverse of *Jacobian* \mathbf{J}_{k-1} . This provides that \mathbf{J}_{k-1} is square and has full rank. However, in the present application (7.7)

$$\mathbf{f}(\mathbf{x}) = \begin{bmatrix} \mathbf{A} & & \\ & \ddots & \\ & & \mathbf{A} \end{bmatrix} \begin{bmatrix} \mathbf{x}_Q(\boldsymbol{\epsilon}, \mathbf{h}_N^{(1)}) \\ \mathbf{x}_Q(\boldsymbol{\epsilon}, \mathbf{h}_N^{(2)}) \\ \vdots \\ \mathbf{x}_Q(\boldsymbol{\epsilon}, \mathbf{h}_N^{(n_m)}) \end{bmatrix} - \begin{bmatrix} \mathbf{R}_q^T \mathbf{q}^{(1)} \\ \mathbf{R}_q^T \mathbf{q}^{(2)} \\ \vdots \\ \mathbf{R}_q^T \mathbf{q}^{(n_m)} \end{bmatrix} \quad \text{with} \quad \mathbf{x}^T = \left[\boldsymbol{\epsilon}^T \quad \mathbf{h}_N^{(1)T} \quad \dots \quad \mathbf{h}_N^{(n_m)T} \right] \quad (7.14)$$

function $\mathbf{f} : \mathbb{R}^{n_m n_j} \rightarrow \mathbb{R}^{n_\ell + n_m(n_j - n_p)}$ has, in general, not the same number of components as the number of variables, i.e. $n_m n_j \neq n_\ell + n_m(n_j - n_p)$. Taking a closer look at its thin (more rows than columns) *Jacobian*

$$\mathbf{J}(\mathbf{x}) = \begin{bmatrix} \mathbf{A} & & \\ & \ddots & \\ & & \mathbf{A} \end{bmatrix} \begin{bmatrix} \frac{\partial \mathbf{x}_Q(\boldsymbol{\epsilon}, \mathbf{h}_N^{(1)})}{\partial \boldsymbol{\epsilon}} & \frac{\partial \mathbf{x}_Q(\boldsymbol{\epsilon}, \mathbf{h}_N^{(1)})}{\partial \mathbf{h}_N^{(1)}} & \mathbf{0} & \dots & \mathbf{0} \\ \frac{\partial \mathbf{x}_Q(\boldsymbol{\epsilon}, \mathbf{h}_N^{(2)})}{\partial \boldsymbol{\epsilon}} & \mathbf{0} & \frac{\partial \mathbf{x}_Q(\boldsymbol{\epsilon}, \mathbf{h}_N^{(2)})}{\partial \mathbf{h}_N^{(2)}} & \dots & \mathbf{0} \\ \vdots & \vdots & & \ddots & \\ \frac{\partial \mathbf{x}_Q(\boldsymbol{\epsilon}, \mathbf{h}_N^{(n_m)})}{\partial \boldsymbol{\epsilon}} & \mathbf{0} & \mathbf{0} & \dots & \frac{\partial \mathbf{x}_Q(\boldsymbol{\epsilon}, \mathbf{h}_N^{(n_m)})}{\partial \mathbf{h}_N^{(n_m)}} \end{bmatrix}, \quad (7.15)$$

where $\mathbf{J} \in \mathbb{R}^{n_m n_j \times n_\ell + n_m(n_j - n_p)}$ is supposed to have full rank ($\mathbf{J}(\mathbf{x}) = n_\ell + n_m(n_j - n_p)$ in reference to Assumption 7.1. Note that $\mathbf{J}_{k-1} := \mathbf{J}(\mathbf{x}_{k-1})$. A quite practical possibility to deal with the non-square form of $\mathbf{J}(\mathbf{x})$ is to take the left inverse

$$\mathbf{J}^+ := (\mathbf{J}^T \mathbf{J})^{-1} \mathbf{J}^T \quad (7.16)$$

which, effectively, inverts $\mathbf{J} \Delta \mathbf{x} = -\mathbf{f}$ (7.13) for any $\mathbf{f} \in \mathbb{R}^{n_m n_j}$ by

$$\min_{\Delta \mathbf{x}} \frac{1}{2} (\mathbf{J} \Delta \mathbf{x} + \mathbf{f})^T (\mathbf{J} \Delta \mathbf{x} + \mathbf{f}) \quad \Rightarrow \quad \frac{1}{2} \frac{\partial}{\partial \Delta \mathbf{x}} (\mathbf{J} \Delta \mathbf{x} + \mathbf{f})^T (\mathbf{J} \Delta \mathbf{x} + \mathbf{f}) = \mathbf{0}^T \quad (7.17a)$$

$$\frac{\partial}{\partial \Delta \mathbf{x}} \frac{1}{2} \left(\Delta \mathbf{x}^T \mathbf{J}^T \mathbf{J} \Delta \mathbf{x} + 2 \mathbf{f}^T \mathbf{J} \Delta \mathbf{x} + \mathbf{f}^T \mathbf{f} \right) = \Delta \mathbf{x}^T \mathbf{J}^T \mathbf{J} + \mathbf{f}^T \mathbf{J} = \mathbf{0}^T \quad (7.17b)$$

$$\Rightarrow \quad \Delta \mathbf{x} = -(\mathbf{J}^T \mathbf{J})^{-1} \mathbf{J}^T \mathbf{f} = -\mathbf{J}^+ \mathbf{f} \quad (7.17c)$$

minimizing the quadratic error of the residual of (7.13) with respect to the search direction $\Delta \mathbf{x}$. This is applicable since one can show that $\mathbf{J}^T \mathbf{J} \succ 0$ for any thin \mathbf{J} with full rank.

7.4.1 First Turbulent Flow Derivatives

In order to build up the *Jacobian* according to (7.15), the derivatives of (7.5) with respect to $\boldsymbol{\epsilon}$ and \mathbf{h}_N are needed. To display these derivatives more compactly, the argument of the natural

logarithm in (7.5)

$$\ell = \ell(\epsilon, \Delta h) = \frac{\epsilon}{3.7d} + 2.51 \frac{\eta A}{\rho d} \sqrt{\frac{k}{|\Delta h|}} \quad (7.18)$$

is denoted with ℓ . Keep in mind that d denotes the diameter, A the cross section area and that $k = \frac{l}{2dgA}^1$, including the length l of the pipe and the gravitational acceleration $g \approx 9.81$ m/s². Also, in reference to Assumption 7.7, remember that $Q = f_t(\epsilon, \Delta h)$ if $Re \geq 4000$ only. Starting with the roughness, one obtains (neglecting indices on the right hand side of (7.19a))

$$\frac{\partial f_{t,i}}{\partial \epsilon_i} =: p_{\epsilon,i}(\epsilon_i, \Delta h_i) \hat{=} \frac{\partial f_t}{\partial \epsilon} = -\frac{2}{\ln(10)} \text{sign}(\Delta h) \sqrt{\frac{|\Delta h|}{k}} \frac{1}{3.7d \ell(\epsilon, \Delta h)} \quad \forall i \in \mathfrak{P} \quad (7.19a)$$

followed by $\frac{\partial f_t}{\partial h_N} = \frac{\partial f_{t,i}}{\partial \Delta h_i} \frac{\partial \Delta h_i}{\partial h_N} =: p_{\Delta h,i}(\epsilon_i, \Delta h_i) \frac{\partial \Delta h_i}{\partial h_N} \quad \forall i \in \mathfrak{P} \wedge j \in \bar{\mathcal{P}} \hat{=}$

$$\frac{\partial f_t}{\partial h_N} = -\frac{1}{\ln(10)} \left(\sqrt{\frac{1}{k|\Delta h|}} \ln(\ell(\epsilon, \Delta h)) - 2.51 \frac{\eta A}{\rho d} \frac{|\Delta h|^{-1}}{\ell(\epsilon, \Delta h)} \right) \frac{\partial \Delta h}{\partial h_N} \quad (7.19b)$$

(neglecting indices) where the partial derivative of Δh in respect to h_N is constant due to

$$\frac{\partial \Delta \mathbf{h}}{\partial \mathbf{h}_N} \stackrel{(7.7b)}{=} -\mathbf{A}^T \bar{\mathbf{C}}_h \quad \text{with} \quad [\Delta \mathbf{h}]_i = [\mathbf{h}_{\text{loss}}(\mathbf{x}_e)]_i = \Delta h_i \quad \forall i \in \mathfrak{P} \quad (7.20)$$

$$[\mathbf{h}_N]_j = [\bar{\mathbf{C}}_h \mathbf{h}]_j = h_{N, \bar{p}_j} \quad \forall \bar{p}_j \in \bar{\mathcal{P}} \wedge j \in \{1, 2, \dots, n_j - n_p\}$$

when considering vector dependencies. As a remark, note that the author assumed that $\frac{\partial}{\partial \Delta h} \text{sign}(\Delta h) = 0$ neglecting the *Dirac-Delta* $\delta(\Delta h)$ function. The scalar partial derivatives (7.19) can now be summarized in vector notation as follows

$$\frac{\partial \mathbf{x}_Q(\epsilon, \Delta \mathbf{h}^{(i)})}{\partial \epsilon} = \text{diag} \left(\mathbf{p}_\epsilon(\epsilon, \Delta \mathbf{h}^{(i)}) \right) \quad \forall i \in \mathfrak{M} = \{1, 2, \dots, n_m\} \quad (7.21)$$

$$\frac{\partial \mathbf{x}_Q(\epsilon, \Delta \mathbf{h}^{(i)})}{\partial \mathbf{h}_N^{(i)}} = -\text{diag} \left(\mathbf{p}_{\Delta h}(\epsilon, \Delta \mathbf{h}^{(i)}) \right) \mathbf{A}^T \bar{\mathbf{C}}_h^T$$

where $[\mathbf{p}_\epsilon]_j \stackrel{(7.19a)}{=} p_{\epsilon,j}(\epsilon_j, \Delta h_j)$ and $[\mathbf{p}_{\Delta h}]_j \stackrel{(7.19b)}{=} p_{\Delta h,j}(\epsilon_j, \Delta h_j)$ for all $j \in \mathfrak{P}$. Strictly speaking, pipe parameters in (7.19) would also require a pipe index, e.g. d_j , as they do certainly vary with each pipe. However, index j was not displayed to improve readability. Actually, one can recognize that the information concerning \mathbf{J} which varies along the i -th measurement-sets can entirely be stored in vectors by means of \mathbf{p}_ϵ and $\mathbf{p}_{\Delta h}$.

7.4.2 Step Length

At this point, one may think that all necessary tools for solving (7.7) have already been obtained, however, this is far from reality. As mentioned earlier, the initial value \mathbf{x}_0 must be sufficiently close to \mathbf{x}^* which can not be evaluated beforehand and so finding suitable \mathbf{x}_0 is a rather hard problem to solve. To somewhat relax the requirement to already start in the vicinity of \mathbf{x}^* a suitable selection of the step length μ_k in each iteration is needed. The author implemented a methodology similar to the one proposed by Press et al. [1992, section 9.7]. The principle shall be described briefly in the following.

The idea is to choose μ_k such that a norm, i.e. $\|\mathbf{f}(\mathbf{x}_k)\|$, decreases with each iteration step, i.e. $\|\mathbf{f}(\mathbf{x}_{k+1})\| < \|\mathbf{f}(\mathbf{x}_k)\|$. Although [Press et al., 1992, section 9.7] proposes to use the \mathcal{L}_2 norm

$$\|\mathbf{f}\|_{\mathcal{L}_2}^2 = f_1^2 + f_2^2 + \dots + f_{n_m n_j}^2 \quad (7.22a)$$

¹Please do not confuse k comprised of pipe parameters with the iteration index k .

also \mathcal{L}_1 and \mathcal{L}_∞ norms in the form

$$\|\mathbf{f}\|_{\mathcal{L}_1} = \sum_{p=1}^{n_m n_j} |f_p| \quad (7.22b)$$

$$\|\mathbf{f}\|_{\mathcal{L}_\infty} = \max_p |f_p| \quad (7.22c)$$

are tested. The 3-cycle network in figure 7.1 was chosen for analysis. $n_m = 4$ measurement-sets were generated with varying consumption. Relative roughnesses were chosen $[\epsilon_1/d_1 \dots \epsilon_8/d_8] = [5 \ 4.37 \ 3.75 \ 3.13 \ 2.50 \ 1.87 \ 1.25 \ 0.63]^T\%$ for the $n_\ell = 8$ pipes. In order to allow graphical representation in 3 dimensions with $n_\ell + n_m(n_j - n_p) = 8 + 4 \times 2 = 16$ unknowns, 14 of these unknowns were fixed in the real root \mathbf{x}^* of (7.7) whereas the solution space concerning (7.22) along the two remaining variables was considered. Figure 7.2 allows comparison of the different norms of $\mathbf{f}(\mathbf{x})$ concerning problem (7.7), where one observation may be particularly important. The limits for the $h_{N,5}^{(3)}$ axes in figure 7.2 were determined with the help of measurements $\mathbf{y}_h^{(3)}$ at node 2, 3, 4 such that $h_{N,5}^{(3)} \in [\min_p(y_{h,p}^{(3)}), \max_p(y_{h,p}^{(3)})]$ which is feasible as no sources are directly connected to node 5, see figure 7.1.

- The norms were designed to be symmetrical along the roughness axes by taking the absolute value of ϵ in function (7.5) concerning $\|\mathbf{f}(\mathbf{x})\|$, and (7.7), to preserve the convex-type shapes in figure 7.2 towards positive thus physical relevant roughnesses.
- There is a particularly weak slope towards \mathbf{x}^* along the ϵ_7/d_7 axes in the \mathcal{L}_2 norm of figure 7.2A, whereas the \mathcal{L}_1 norm in figure 7.2B shows the overall highest slope towards the real root \mathbf{x}^* . This result is consistent, even when varying different roughnesses (one of the n_ℓ pipe roughnesses) and different $h_{N,j}^{(i)}$ in the variable space.

Due to this observation, the \mathcal{L}_1 norm (in contrast to Press et al. [1992]) was selected as quality-measure for the step length. Knowing that every root of $\mathbf{f}(\mathbf{x})$, i.e. \mathbf{x}^* , is a minimum of $v(\mathbf{x}) = \|\mathbf{f}(\mathbf{x})\|_{\mathcal{L}_1}$, it is clear that the *Newton* direction (7.13) (and so (7.17)) represents a *descent* direction of $v(\mathbf{x})$, i.e.

$$\frac{\partial v}{\partial \mathbf{x}} \Delta \mathbf{x} = \frac{\partial v}{\partial \mathbf{f}} \frac{\partial \mathbf{f}}{\partial \mathbf{x}} \Delta \mathbf{x} = -\text{sign}(\mathbf{f})^T \mathbf{J} \mathbf{J}^{-1} \mathbf{f} = -\text{sign}(\mathbf{f})^T \mathbf{f} < 0 \quad \forall \mathbf{f} \neq \mathbf{0}. \quad (7.23)$$

The strategy is comprised of three basic steps.

- (I) try the full $\mu = 1$ Newton step which will provide quadratic convergence eventually
- (II) check at each iteration if the proposed step reduces the norm (or similar criteria)
- (III) if not, backtrack along the Newton direction until an acceptable step is obtained

As the Newton step is indeed a descent direction, it is guaranteed that there must exist a μ_k for which $v(\mathbf{x}_k) < v(\mathbf{x}_{k-1})$. According to [Press et al., 1992], “*this method can still occasionally fail by landing on a local minimum of $v(\mathbf{x})$, but this is quite rare in practice*”.

Linesearch and Backtracking. The goal is to find a $\mu \in [0, 1]$ for which

$$g(\mu) := \|\mathbf{f}(\mathbf{x}_{k-1} + \mu \Delta \mathbf{x}_k)\|_{\mathcal{L}_1} = v(\mathbf{x}_{k-1} + \mu \Delta \mathbf{x}_k) \quad (7.24)$$

decreases sufficiently. There are several problems involved when directly taking the condition $v(\mathbf{x}_k) \leq v(\mathbf{x}_{k-1})$ (see [Press et al., 1992]). If the full Newton step with $\mu = 1$ does not comply with the criterion

$$v(\mathbf{x}_k) \leq v(\mathbf{x}_{k-1}) + \alpha \left. \frac{\partial v}{\partial \mathbf{x}} \right|_{\mathbf{x}_{k-1}} \Delta \mathbf{x}_k \quad (7.25)$$

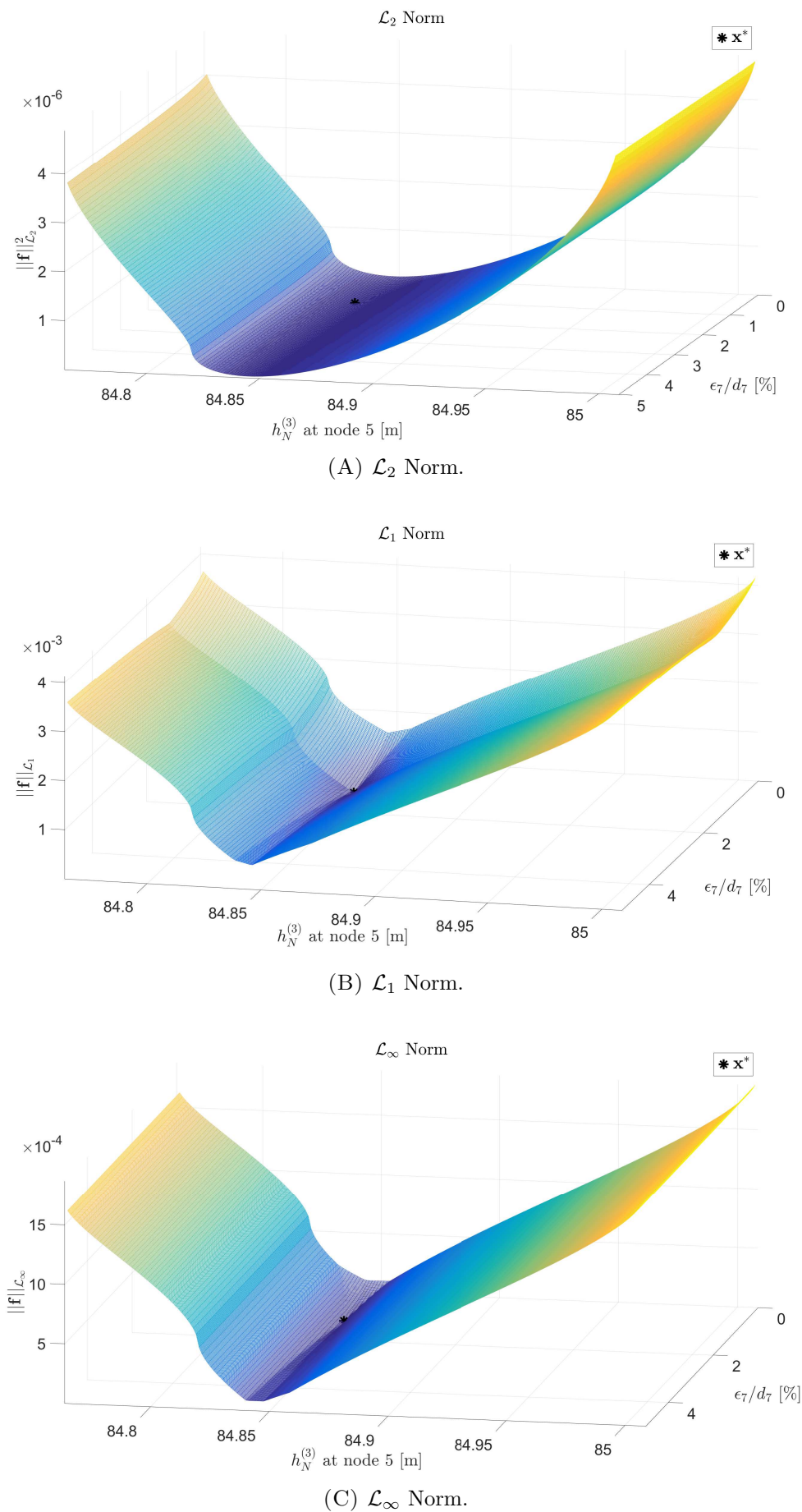


FIGURE 7.2: Norm of $\mathbf{f}(\mathbf{x})$ plotted along the parameter space of ϵ_7/d_7 and $h_{N,5}^{(3)}$ regarding the network in figure 7.1.

which requires the new $v(\mathbf{x}_k)$ to decrease when only going an α -fraction along a linear extrapolation (right hand side of (7.25)), the backtracking routine kicks in. As suggested in Press et al. [1992], the decrease parameter was chosen conservatively as $\alpha = 10^{-4}$. First, $g(0)$ from the previous step at iteration $k - 1$ as well as $g(1)$ from the k -th iteration are already known. Second, the derivative

$$g'(0) = \left. \frac{\partial g(\mathbf{x}_k)}{\partial \mu} \right|_{\mu=0} = \left. \frac{\partial v}{\partial \mathbf{x}} \right|_{\mathbf{x}_{k-1}} \Delta \mathbf{x}_k = -\text{sign}(\mathbf{f}(\mathbf{x}_{k-1}))^T \mathbf{f}(\mathbf{x}_{k-1}) \quad (7.26)$$

is also available. Keep in mind that no additional function calls of $\mathbf{f}(\mathbf{x})$ have been required so far. With these three known function evaluations of $g(\mu)$ one uses the quadratic interpolation

$$g(\mu) \approx \tilde{g}(\mu) = a\mu^2 + b\mu + c \quad \Rightarrow \quad \begin{aligned} g(0) &= c \\ g(1) &= a + b + c \\ g'(0) &= b \end{aligned} \quad (7.27)$$

in the form

$$\tilde{g}(\mu) = (g(1) - g(0) - g'(0))\mu^2 + g'(0)\mu + g(0) \quad (7.28)$$

to determine a μ^* which minimizes (7.28). Looking for a stationary point by taking the derivative of (7.28) and setting it to zero one obtains

$$\mu^* = -\frac{g'(0)}{2(g(1) - g(0) - g'(0))} \quad (7.29)$$

which is chosen for the next iteration. However, to avoid slow convergence the smallest value of μ^* is fixed to $\mu^* \geq \mu_{min} = 0.1$. In case, the new step \mathbf{x}_k (7.11) applying (7.29) still does not comply with (7.25), the additional evaluation of $g(\mu)$, i.e. $g(\mu^*)$, is utilized to interpolate $g(\mu)$ as a cubic polynomial

$$g(\mu) \approx \tilde{g}(\mu) = a\mu^3 + b\mu^2 + g(0)\mu + g'(0) \quad \Rightarrow \quad \begin{aligned} g(1) &= a + b + g'(0) + g(0) \\ g(\mu^*) &= a\mu^{*3} + b\mu^{*2} + g'(0)\mu^* + g(0) \end{aligned} \quad (7.30)$$

where

$$\begin{bmatrix} a \\ b \end{bmatrix} = \frac{1}{\mu^{*2} - \mu^{*3}} \begin{bmatrix} \mu^{*2} & -1 \\ -\mu^{*3} & 1 \end{bmatrix} \begin{bmatrix} g(1) - g'(0) - g(0) \\ g(\mu^*) - g'(0)\mu^* - g(0) \end{bmatrix} \quad (7.31)$$

which is then again minimized in terms of μ . The optimal positive step length in terms of (7.30) yields

$$\mu^+ = \frac{-b + \sqrt{b^2 - 3ag'(0)}}{3a} \quad (7.32)$$

which is applied in the next iteration. The result is saturated in the range [Press et al., 1992]

$$\mu^+ \in [0.1\mu^*, 0.5\mu^*]. \quad (7.33)$$

A summary of the complete algorithm is presented on page 93. The tolerance ϵ_f as well as ϵ_x for the *while* loop of this algorithm have to be adjusted for the network to work with, as the order of the residual of set (7.7) heavily depends on the number of nodes n_j and the quality of the measurement. For the 3-cycle network in figure 7.1 the maximal number of iterations was limited to 1000, whereas $\epsilon_f = 10^{-7}$ and $\epsilon_x = 5 \times 10^{-7}$ were chosen when considering no measurement noise.

Potentially, also important to note is that due to the enforced symmetry along the ϵ -axes (1st bullet point on page 90), the absolute value of n_ℓ components of \mathbf{x}_k (meaning roughnesses ϵ_k) is taken after the Newton step. Taking the absolute value not only in the Algorithm 1 but in (7.5) as part of (7.7) is necessary to preserve the convex-type shape, seen in figure 7.2.

Algorithm 1 Modified *Newton-Raphson* algorithm with step length variation

```

1: procedure NEWTON(FUN,  $\mathbf{x}_0$ )  $\triangleright$  FUN characterizes a pointer on a function returning the
    $\triangleright$  residuum of (7.14) under (7.7) (in the full turbulent case) and  $\mathbf{J}$  (7.15)
   INITIAL PHASE
2:  $[\mathbf{f}_k, \mathbf{J}_k] \leftarrow \text{FUN}(\mathbf{x}_0)$   $\triangleright$  first function call of FUN
3:  $v_k \leftarrow \sum_{p=1}^{n_j n_m} |f_{k,p}|$   $\triangleright$  norm calculation (7.22b)
4:  $v_{k-1} \leftarrow v_k$   $\triangleright$  for initialization purposes only
5:  $\Delta \mathbf{x}_k \leftarrow -(\mathbf{J}_k^T \mathbf{J}_k)^{-1} \mathbf{J}_k^T \mathbf{f}_k$   $\triangleright$  first Newton direction applying (7.17)
6:  $\mu \leftarrow 1$ 
7:  $iter \leftarrow 0$   $\triangleright$  iter ... number of “Newton” iterations
   MAIN LOOP
8: while ( $|v_k - v_{k-1}| > \epsilon_f$  or  $\|\mu \Delta \mathbf{x}_k\|_{\mathcal{L}_2} > \epsilon_x$ ) and ( $iter < \text{max number of } iter$ ) do
   NEWTON DIRECTION
9: if  $\mu = 1$  then
10:  $\Delta \mathbf{x}_k \leftarrow -(\mathbf{J}_k^T \mathbf{J}_k)^{-1} \mathbf{J}_k^T \mathbf{f}_k$   $\triangleright$  Newton direction applying (7.17)
11:  $s_k \leftarrow -\text{sign}(\mathbf{f}_k)^T \mathbf{f}_k$   $\triangleright$  rate of descent (7.23)
12:  $v_k \leftarrow \sum_{p=1}^{n_j n_m} |f_{k,p}|$   $\triangleright$   $\mathcal{L}_1$  norm calculation
13:  $\mathbf{f}_{k-1} \leftarrow \mathbf{f}_k, \mathbf{x}_{k-1} \leftarrow \mathbf{x}_k, v_{k-1} \leftarrow v_k$   $\triangleright$  buffer old values
14:  $iter \leftarrow iter + 1$ 
15: end if
   NEWTON STEP
16:  $\mathbf{x}_k \leftarrow \mathbf{x}_{k-1} + \mu \Delta \mathbf{x}_k$   $\triangleright$  next Newton Step (7.11)
17:  $[\mathbf{x}_k]_j = x_{k,j} \leftarrow |x_{k,j}|$  for  $j = 1, 2, \dots, n_\ell$   $\triangleright$  symmetry (1st bullet point on page 90)
18:  $[\mathbf{f}_k, \mathbf{J}_k] \leftarrow \text{FUN}(\mathbf{x}_k)$ 
19:  $v_k \leftarrow \sum_{p=1}^{n_j n_m} |f_{k,p}|$   $\triangleright$  norm calculation (7.22b)
20:  $\mu_{\text{old}} \leftarrow \mu$   $\triangleright$  buffer old step length
   STEP LENGTH CONTROL
21: if  $v_k > v_{k-1} + 10^{-4} \mu s_k$  then  $\triangleright$  criterion (7.25) with  $\alpha = 10^{-4}$ 
22: if  $\mu = 1$  then
23:  $\mu \leftarrow \frac{-s_k}{2(v_k - v_{k-1} - s_k)}$   $\triangleright$  see (7.29)
24: else
25: calculate coefficients  $a, b$  via (7.31) where
26:  $\mu^* = \mu_{\text{old}}, g(0) = v_{k-1}, g(1) = v_k, g'(0) = s_k$ 
27: if  $a = 0$  then
28:  $\mu \leftarrow -\frac{s_k}{2b}$   $\triangleright$  minimum of (7.31) if coefficient  $a = 0$ 
29: else
30:  $\mu \leftarrow \frac{-b + \sqrt{b^2 - 3as_k}}{3a}$   $\triangleright$  see (7.32)
31: end if
32:  $\mu \leftarrow \min(\mu, 0.5\mu_{\text{old}})$   $\triangleright$  maximal step length
33: end if
34:  $\mu \leftarrow \max(\mu, 0.1\mu_{\text{old}})$   $\triangleright$  minimal step length
35: else
36:  $\mu \leftarrow 1$ 
37: end if
38: end while
39: return  $[\mathbf{x}_{k-1}, \mathbf{f}_{k-1}]$ 
40: end procedure

```

Remark 7.9. *Since the argument of equation set (7.7) to be solved has two sets of components, namely $\boldsymbol{\epsilon}$ and $\mathbf{h}_N^{(i)}$, which are (at least) in the range of 3 orders of magnitude different from each other, it is advisable to scale $\mathbf{x} \in \mathbb{R}^{n_\ell + n_m(n_j - n_p)}$ (7.10) for the Newton direction calculation via (7.17c). Numerical issues become dominant with growing number of nodes n_j and pipes n_ℓ . The scaling may be accomplished with a scaling vector such as $\mathfrak{s} = \max(|\mathbf{x}_0|, 10^{-5})$ (function $\max()$ is applied componentwise)*

$$\mathcal{S} = [1 \quad 1 \quad \dots \quad 1]^T \left(\mathfrak{s}^{\odot -1} \right)^T = \mathbf{1}_{n_\ell + n_m(n_j - n_p)} \left(\mathfrak{s}^{\odot -1} \right)^T \quad (7.34)$$

such that

$$\mathbf{J}^* = \mathbf{J} \odot \mathcal{S} \quad (7.35a)$$

$$\Delta \mathbf{x}^* \stackrel{(7.17c)}{=} -(\mathbf{J}^{*T} \mathbf{J}^*)^{-1} \mathbf{J}^{*T} \mathbf{f} \quad (7.35b)$$

$$\Delta \mathbf{x} = \Delta \mathbf{x}^* \odot \mathfrak{s} \quad (7.35c)$$

resulting in far better numerical behavior.

Remark 7.10. *The scaling, in reference to Remark 7.9, was not included in Algorithm 1 in order to keep the complexity reasonable for illustrative purposes, but also because it can only be applied for the Newton direction (7.13). In the later part of this chapter, the author enhances the determination of the search direction which will require a nonlinear equation to solve.*

7.4.3 Initial Values and Range

In the sensor-noise-free case Algorithm 1 occasionally finds the real root \mathbf{x}^* of (7.7) if \mathbf{x}_0 is already close to \mathbf{x}^* . The convergence highly depends on the initial values \mathbf{x}_0 with which Algorithm 1 is launched. Thereby, (7.7) turns out to be particularly sensitive with respect to the not-measured pressures $\mathbf{h}_N^{(i)}$. In this context it is utterly important to define a physically useful range

$$h_{N,\bar{p}}^{(i)} \in [h_{N,\bar{p}}^{(i)}, \overline{h_{N,\bar{p}}^{(i)}}] \quad \forall \bar{p} \in \bar{\mathcal{P}} \wedge \forall i \in \mathfrak{M} \quad (7.36a)$$

$$\Rightarrow \mathbf{h}_N^{(i)} \in [\underline{\mathbf{h}}_N^{(i)}, \overline{\mathbf{h}}_N^{(i)}] \quad \forall i \in \mathfrak{M} \quad (7.36b)$$

$$\Rightarrow \mathbf{x}_{h_N} = [\mathbf{h}_N^{(1)T} \quad \mathbf{h}_N^{(2)T} \quad \dots \quad \mathbf{h}_N^{(n_m)T}]^T \in [\underline{\mathbf{h}}_N, \overline{\mathbf{h}}_N] \quad (7.36c)$$

and let $\mathbf{h}_N^{(i)}$ concerning \mathbf{x}_0 (the initial value) be in this range. Otherwise the solution space of $v(\mathbf{x}) = \|\mathbf{f}(\mathbf{x})\|_{\mathcal{L}_1}$ will most unlikely feature a desired convex-type form (only for $[\mathbf{x}]_i = \epsilon_i > 0 \quad \forall i \in \mathfrak{B}$) as in figure 7.2B. In analogy, the physically useful range for the roughnesses ought to be between 0% and 5% of the pipe's diameter in reference to the *Moody*-chart in figure 2.2.

In order to increase the chance of converging to the real root, the strategy to launch Algorithm 1 several times with different initial values \mathbf{x}_0 turns out successful. However, going from one initial value to another, it is useful to remember the temporarily “best” solution, i.e. \mathbf{x}^+ , meaning the one which has the smallest residual of (7.7) measured by $v(\mathbf{x}^+)$. Thereby, the $\mathbf{h}_N^{+,(i)}$ -components of the temporarily best solution, in terms of the smallest $v(\mathbf{x}^+)$, are used for the $n_m(n_j - n_p)$ components of the next initial value, i.e.

$$\mathbf{x}_0 = \left[\boldsymbol{\epsilon}_0^T \quad \mathbf{h}_N^{+,(1)T} \quad \dots \quad \mathbf{h}_N^{+,(n_m)T} \right]^T. \quad (7.37)$$

Note that yet another index for (7.37) to denote the iteration along different initial values was omitted. The selection of the (next) initial roughness $\boldsymbol{\epsilon}_0$ is done by a random number generator, assuming a uniformly distributed roughness between 0% and 5% of the corresponding pipe's diameter. In this context, it turned out effective to vary only (or more aggressively for another

modification later) those elements of ϵ_0 which are not in the physically relevant range, i.e. $\epsilon_{0,i} = \text{random}(0, 0.05d_i)$ for $[\mathbf{x}^+]_i = \epsilon_i^+ > 0.05d_i \quad \forall i \in \mathfrak{P}$.

In case Algorithm 1 does return $\mathbf{h}_N^{(i)}$ outside its considered range (7.36), the returned \mathbf{x} will not be buffered in \mathbf{x}^+ , even if $v(\mathbf{x})$ would be the smallest so far.

Algorithm 2 Launching Algorithm 1 effectively

```

1: procedure NETCALIBRATION(FUN,  $\mathbf{x}_0$ )
   INITIAL PHASE
2:    $[\mathbf{x}^+, \mathbf{f}^+] \leftarrow \text{NEWTON}(\text{FUN}, \mathbf{x}_0)$  ▷ run Algorithm 1
3:    $v^+ \leftarrow \sum_{p=1}^{n_j n_m} |f_p^+|$  ▷ norm calculation (7.22b)
4:    $\mathbf{x} \leftarrow \mathbf{x}_0$  ▷ for initialization only
5:    $iter \leftarrow 0$  ▷ iter ... number of iterations
   MAIN LOOP
6:   while ( $v^+ > \epsilon_f$  or  $\|\mathbf{x} - \mathbf{x}^+\|_{\mathcal{L}_2} > \epsilon_x$ ) and ( $iter < \text{max number of } iter$ ) do
7:      $\mathbf{x}_0 \leftarrow \mathbf{x}^+$ 
8:     determine indices  $[i_1 \ i_2 \ \dots \ i_{n_\epsilon}]$  where  $[\mathbf{x}^+]_{i \in \mathfrak{P}} = \epsilon_i > 0.05d_i \quad \forall i \in \{i_1, i_2, \dots, i_{n_\epsilon}\}$ 
9:      $[\mathbf{x}_0]_i \leftarrow \text{random}(0, 0.05d_i)$  for  $i = i_1, i_2, \dots, i_{n_\epsilon}$  ▷ random number: [0%, 5%] of  $d_i$ 
10:     $[\mathbf{x}, \mathbf{f}] \leftarrow \text{NEWTON}(\text{FUN}, \mathbf{x}_0)$ 
11:     $v \leftarrow \sum_{p=1}^{n_j n_m} |f_p|$  ▷ norm calculation (7.22b)
12:     $[\mathbf{x}_{h_N}]_l \leftarrow [\mathbf{x}]_{l+n_\ell}$  for  $l = 1, 2, \dots, n_m(n_j - n_p)$  ▷ cf. (7.36c)
    BUFFER "GOOD" SOLUTIONS
13:    if  $v \leq v^+$  and  $\underline{\mathbf{h}}_N \leq \mathbf{x}_{h_N} \leq \overline{\mathbf{h}}_N$  then
14:      |  $\mathbf{x}^+ \leftarrow \mathbf{x}, v^+ \leftarrow v, \mathbf{f}^+ \leftarrow \mathbf{f}$ 
15:    end if
16:     $iter \leftarrow iter + 1$ 
17:  end while
18:  return  $[\mathbf{x}^+, \mathbf{f}^+]$ 
19: end procedure

```

Actually, Algorithm 2 steers \mathbf{x} , provided by Algorithm 1, back to its physical range by varying roughnesses. Although Algorithm 2 requires the not-measured pressure heads to remain inside their physical relevant range, that is $\underline{\mathbf{h}}_N \leq \mathbf{x}_{h_N} \leq \overline{\mathbf{h}}_N$ (see line 13 of Algorithm 2), roughnesses $[\mathbf{x}^+]_i = \epsilon_i \quad \forall i \in \mathfrak{P}$ can, in fact, exceed the 5% mark of the pipe's diameter d_i . Variants of Algorithm 2 where roughnesses, concerning \mathbf{x}^+ , are forced to never exceed this $0.05d_i = 0.05[\mathfrak{D}]_i \quad \forall i \in \mathfrak{P}$ boundary turned out far too conservative in the solution finding.

However, even when considering no disturbances at all, the real root \mathbf{x}^* will not lead to a perfect zero, i.e. $v(\mathbf{x}^*) > 0$ due to numerics. A basic assumption for Algorithm 2 to work is that this real root \mathbf{x}^* has a clearly distinguishable (cf. with (7.36c))

$$v(\mathbf{x}^*) < v(\mathbf{x}) \quad \forall \mathbf{x} \in \left[\begin{bmatrix} \mathbf{0}_{n_\ell} \\ \underline{\mathbf{h}}_N \end{bmatrix}, \begin{bmatrix} \mathbf{0}_{n_\ell} \\ \overline{\mathbf{h}}_N \end{bmatrix} \right] \quad (7.38)$$

value in the defined range at least. This can only be the case if Assumption 7.1 holds, providing measurement-sets which are sufficiently independent from each other.

The limits for Algorithm 2 to abort, referring to ϵ_f and ϵ_x , should actually be chosen conservatively, compared to the ones used for Algorithm 1, to avoid too many iterations in this outer loop. Thereby, condition $v^+ > \epsilon_f$ (m^3/s) allows direct adjustment of the accuracy with respect to the sum of all nodal consumption-errors (heavily dependent on n_j). Also, keep in mind that

at this point one still has to select initial conditions for Algorithm 2 as well as the physically relevant range for the not-measured pressures $\mathbf{h}_N^{(i)} \forall i$, namely $\underline{\mathbf{h}}_N$ and $\overline{\mathbf{h}}_N$. With the purpose to clarify the general methodology, an example is provided in the following.

7.5 Illustrative Example

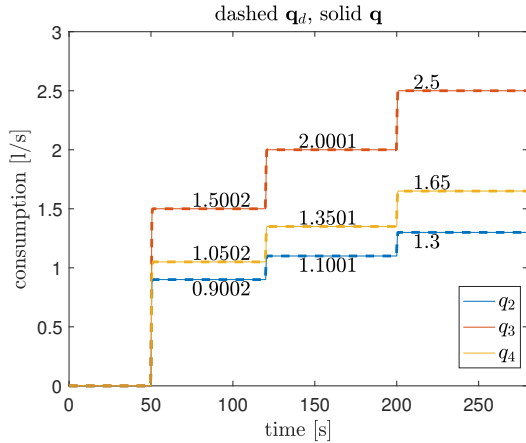
The 3-cycle network in figure 7.1 serves as illustration. First, incidence matrix

$$\mathbf{A} = \begin{bmatrix} 1 & -1 & -1 & 0 & 0 & 0 & 0 & 0 \\ 0 & 1 & 0 & -1 & -1 & 0 & 0 & 0 \\ 0 & 0 & 1 & 0 & 0 & 0 & 1 & 1 \\ 0 & 0 & 0 & 1 & 0 & 1 & -1 & 0 \\ 0 & 0 & 0 & 0 & 1 & -1 & 0 & -1 \end{bmatrix} \in \mathbb{Z}_{\{-1,0,1\}}^{n_j \times n_\ell}, \quad (7.39)$$

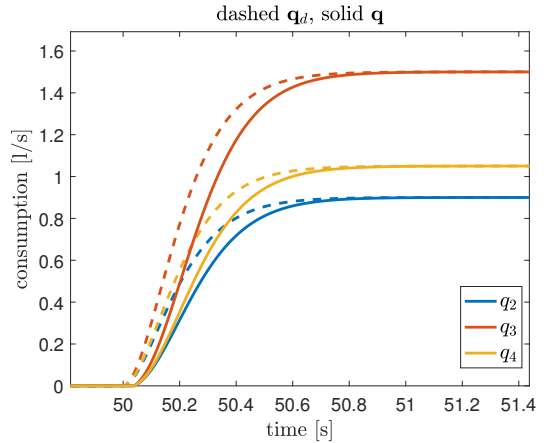
nodal elevation $\mathbf{z} = [0 \ 10 \ 5 \ 0 \ 0]^T$ (m), the pipes' diameter $\mathbf{d} = 0.04 \times \mathbf{1}_{n_\ell}$ (m) (i.e. $d_i = [\mathbf{d}]_i \forall i \in \mathfrak{P}$), their length $\mathbf{l} = [10 \ 10 \ 20 \ 15 \ 5 \ 10 \ 15 \ 5]^T$ (m), roughnesses $\boldsymbol{\epsilon} = [2 \ 1.75 \ 1.5 \ 1.25 \ 1 \ 0.75 \ 0.5 \ 0.25]^T \times 10^{-3}$ (m) are chosen, whereas minor losses are set to zero. In contrast to the illustrative 2-cycle network in figure 3.2, the *Colebrook & White* formula (2.6) is applied for the calculation of the friction factor λ_{DW} (2.4). The solving of the implicit equation is achieved by (2.29) applying the *Lambert* function, saving computational effort by avoiding an iterative solving scheme. In order to produce an independent set of steady-state configurations (“measurements”), model $\text{PD}_{\mathbf{u}}$ (see Definition 4.14) is utilized while varying the desired consumption \mathbf{q}_d . Orifice coefficients, serving as control variables for the consumption \mathbf{q} , are not in saturation $\mathbf{u} = \mathbf{r}^{\ominus -2} \in]1, \epsilon_r^{-2}[$. Eigenvalues are selected as $\boldsymbol{\lambda}_q = -15 \times \mathbf{1}_3$.

The following matrices are utilized

$$\mathbf{C}_h = \begin{bmatrix} 0 & 1 & 0 & 0 & 0 \\ 0 & 0 & 1 & 0 & 0 \\ 0 & 0 & 0 & 1 & 0 \end{bmatrix} = \mathbf{R}_q, \quad \bar{\mathbf{C}}_h = \begin{bmatrix} 1 & 0 & 0 & 0 & 0 \\ 0 & 0 & 0 & 0 & 1 \end{bmatrix} = \bar{\mathbf{R}}_q, \quad \mathbf{C}_s = [1 \ \mathbf{0}_7^T]^T. \quad (7.40)$$



(A) Comparison of $\mathbf{q}_d(t)$ and $\mathbf{q}(t)$.



(B) Zoom of figure 7.3A showing dynamics.

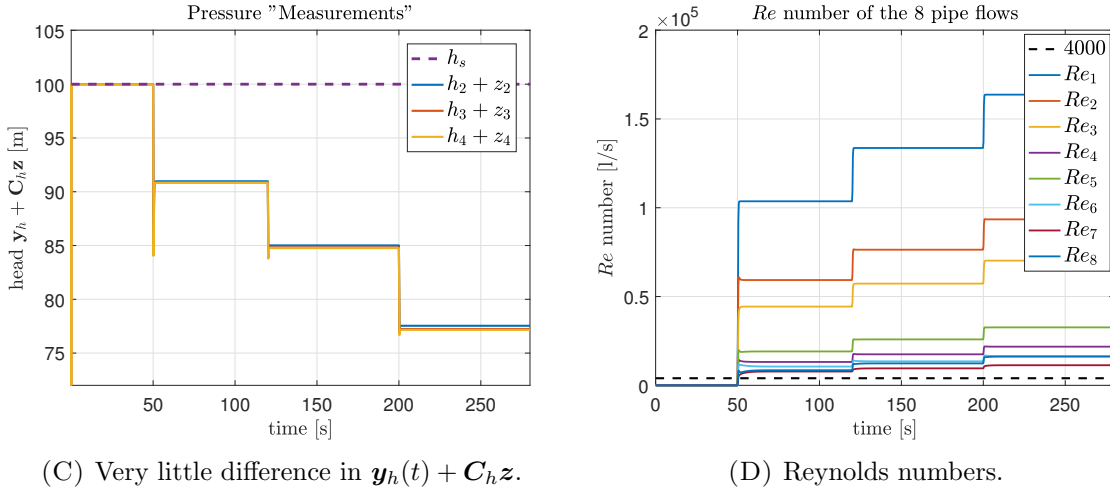


FIGURE 7.3: Figures showing $n_m = n_{m,\min} = 3$ “measurement” -sets for the roughness calibration of the 3-cycle network in figure 7.1.

Figure 7.3A shows that the real consumption follows \mathbf{q}_d appropriately along the linear differential equation (4.22), also the consumption values used for (7.7) were displayed explicitly. As a remark, all the selected references concerning $\mathbf{q}_d(t)$ were generated with a filtered step using a *Butterworth* filter which degree 2 and a cut-off angular frequency of $\omega_c = 10$ rad/s each concerning figure 7.3A.

Beforehand, the selected configuration by means of consumption $\mathbf{q}(t)$, which leads to sensed head values $\mathbf{y}_h + \mathbf{C}_h \mathbf{z}$, which can barely be distinguished among each other, was chosen on purpose for this example. Due to very little difference among the $\mathbf{y}_h + \mathbf{C}_h \mathbf{z}$, numerical inaccuracies are sufficient to cause serious difficulty to restore the roughness ϵ with \mathbf{y}_h and \mathbf{q} when applying (7.7), presumably violating Assumption 7.1. In this context it is important to emphasize that this illustrative example was configured such that all flows in all the 3 “measurement”-sets are in the turbulent regime according to Assumption 7.7, seen in figure 7.3D. The quantities to set up (7.7) as well as its *Jacobian* (7.15) are summarized in the following table.

set	1	2	3	unit
\mathbf{y}_h	90.9743	85.0087	77.5380	m
	90.8720	84.8200	77.2370	
	90.8339	84.7638	77.1594	
\mathbf{q}	0.9002	1.1001	1.3000	l/s
	1.5002	2.0001	2.5000	
	1.0502	1.3501	1.6500	
\mathbf{h}_s	100	100	100	m

TABLE 7.3: Measurement-sets.

Initial Values. The initial value for the not-measured pressure head at node 5, i.e. $h_{N_0,5}^{(i)}$, is chosen as the mean over all surrounding pressure heads (which happen to be located at pressure-nodes).

$$h_{N_0,5}^{(i)} = \frac{1}{n_j - n_p} \sum_{j=1}^{n_j - n_p} [\mathbf{y}_h]_j^{(i)} = \frac{1}{3} \sum_{j=2}^4 h_j^{(i)} \quad \forall i \quad (7.41a)$$

The initial value for the not-measured pressure head at node 1, i.e. $h_{N_0,1}^{(i)}$, is chosen analogously.

$$h_{N_0,1}^{(i)} = \frac{1}{3} \left(h_s^{(i)} + h_2^{(i)} + h_3^{(i)} \right) \quad \forall i \quad (7.41b)$$

The initial roughness value is chosen as 1% of the pipes' diameter, leading to the initial vector

$$\begin{aligned} \mathbf{x}_0 &= \left[\epsilon_0^T \quad h_{N_0,1}^{(1)} \quad h_{N_0,5}^{(1)} \quad h_{N_0,1}^{(2)} \quad h_{N_0,5}^{(2)} \quad h_{N_0,1}^{(3)} \quad h_{N_0,5}^{(3)} \right]^T \\ &= \left[0.0004 \times \mathbf{1}_{n_\epsilon}^T \quad 93.9488 \quad 90.8934 \quad 89.9429 \quad 84.8642 \quad 84.9250 \quad 77.3115 \right]^T \end{aligned} \quad (7.42)$$

for launching Algorithm 2. The minimal and maximal value of all surrounding pressure heads in the corresponding measurement-set is chosen for lower and upper boundary concerning \mathbf{h}_N and $\overline{\mathbf{h}_N}$, leading, for instance, to a maximal value of the pressure at node 1 of $h_{N,1}^{(i)} \leq \overline{h_{N,1}}^{(i)} = h_s^{(i)} = 100 \forall i$. As it will turn out that the presented \mathbf{x}_{h_N} results never leave their defined physically relevant range, these boundaries are not important for the present example. The initial values along some iterations of Algorithm 2 are presented in table 7.4.

Table 7.5 presents the solutions of Algorithm 1, which was launched with initial values in table 7.4, along some iterations of Algorithm 2. Concerning Algorithm 1, the maximal number of iterations was limited to 1000, whereas $\epsilon_f = 10^{-7}$ and $\epsilon_x = 5 \times 10^{-7}$.

iteration	1	2	3	4	5	6	7	\mathbf{x}^*
ϵ_1	0.400	0.225	1.272	1.272	0.319	1.177	1.239	2.000
ϵ_2	0.400	1.632	1.562	1.567	1.730	1.730	1.730	1.750
ϵ_3	0.400	1.410	1.227	1.083	1.496	1.496	1.496	1.500
ϵ_4	0.400	1.111	1.361	1.361	1.176	1.176	1.176	1.250
ϵ_5	0.400	1.054	0.824	0.824	1.028	1.028	1.028	1.000
ϵ_6	0.400	0.788	0.696	0.696	0.786	0.786	0.786	0.750
ϵ_7	0.400	0.499	0.471	0.471	0.505	0.505	0.505	0.500
ϵ_8	0.400	0.250	0.228	0.228	0.250	0.250	0.250	0.250
$h_{N,1}^{(1)}$	93.949	93.047	94.344	94.344	93.097	93.097	93.097	93.104
$h_{N,5}^{(1)}$	90.893	90.885	90.886	90.886	90.885	90.885	90.885	90.885
$h_{N,1}^{(2)}$	89.943	88.443	90.602	90.602	88.525	88.525	88.525	88.538
$h_{N,5}^{(2)}$	84.864	84.846	84.848	84.848	84.846	84.846	84.846	84.846
$h_{N,1}^{(3)}$	84.925	82.674	85.916	85.916	82.799	82.799	82.799	82.818
$h_{N,5}^{(3)}$	77.311	77.280	77.283	77.283	77.280	77.280	77.280	77.280

TABLE 7.4: Initial values for calibrating the 3-cycle network (figure 7.1) via Algorithm 1 along iterations of Algorithm 2. Roughnesses ϵ_i are presented in mm, whereas pressure heads are presented in m.

In reference to table 7.4 and 7.5, Algorithm 2 ran for a fixed number of iterations, namely 7 iterations in order allow visible investigation of its working principle. In this context, the accuracy limits ϵ_f and ϵ_x for the while loop in line 6 of Algorithm 2 were chosen such that Algorithm 2 does not abort until the fixed iteration-number 7 was reached.

iteration	1	2	3	4	5	6	7	\mathbf{x}^*
ϵ_1	2.036	1.272	1.986	2.005	1.340	2.031	2.036	2.000
ϵ_2	1.632	4.280	1.802	1.730	4.188	1.648	1.631	1.750
ϵ_3	1.410	3.880	1.562	1.496	3.398	1.425	1.408	1.500
ϵ_4	1.111	1.361	1.216	1.176	3.568	1.183	1.185	1.250
ϵ_5	1.054	0.824	0.990	1.028	0.393	1.019	1.019	1.000
ϵ_6	0.788	0.696	0.752	0.786	0.199	0.755	0.756	0.750
ϵ_7	0.499	0.471	0.495	0.505	0.389	0.493	0.494	0.500
ϵ_8	0.250	0.228	0.261	0.250	0.710	0.265	0.264	0.250
$h_{N,1}^{(1)}$	93.047	94.344	93.128	93.097	94.219	93.056	93.047	93.104
$h_{N,5}^{(1)}$	90.885	90.886	90.885	90.885	90.890	90.885	90.885	90.885
$h_{N,1}^{(2)}$	88.443	90.602	88.578	88.525	90.395	88.458	88.442	88.538
$h_{N,5}^{(2)}$	84.846	84.848	84.846	84.846	84.856	84.846	84.846	84.846
$h_{N,1}^{(3)}$	82.674	85.916	82.877	82.799	85.604	82.697	82.674	82.818
$h_{N,5}^{(3)}$	77.280	77.283	77.281	77.280	77.297	77.280	77.280	77.280
$v(\mathbf{x}) \times 10^5$	5.897	1.969	7.630	1.932	5014.8	5.151	5.089	0.011

TABLE 7.5: Solutions of (7.7) concerning the 3-cycle network (figure 7.1) by Algorithm 1 along iterations of Algorithm 2. The corresponding initial values can be found in table 7.4. Roughnesses ϵ_i are presented in mm, whereas pressure heads are presented in m.

Discussion. The pleasing news is that the roughness and the not-measured pressure heads in all measurement-sets could be restored with reasonable accuracy (i.e. a maximal deviation of 6% in ϵ_4^+). The intermediate best result \mathbf{x}^+ , in reference to Algorithm 2, in table 7.5 is colored in (color) olive with a residual of $v(\mathbf{x}^+) = 1.932 \times 10^{-5} \text{ m}^3/\text{s} = 1.932 \times 10^{-2} \text{ l/s}$, whereas the real root can still clearly be distinguished from all other solutions of Algorithm 1 with a residual of $v(\mathbf{x}^*) = 0.011 \times 10^{-2} \text{ l/s}$. The blue colored values in table 7.5 are those roughnesses which exceed the 5% mark of the corresponding pipe’s diameter. Those roughnesses are then selected by a random number generator applied in Algorithm 2 for the next iteration. Randomly generated roughnesses can be found in corresponding entries of table 7.4.

On the contrary, one has to pay attention to the fact that a solution was found which features an ever so slightly higher residual $v(\mathbf{x}) = 1.969 \times 10^{-2} \text{ l/s}$ in the second iteration of table 7.5 compared to $v(\mathbf{x}^+) = 1.932 \times 10^{-2} \text{ l/s}$. When also considering measurement noise, one certainly loses the capability to identify the real root by only looking at $v(\mathbf{x})$. Also, the indicator that the solution in the second iteration has two roughnesses ϵ_2, ϵ_3 which exceed their physical bounds in comparison to \mathbf{x}^+ (olive), only featuring ϵ_1 which exceeds $0.05d_1$ by a mere 0.25%, will not be sufficient. In the opinion of the author, the only possibility to deal with measurement noise and potentially non-zero minor losses (referring to Assumption 7.3 and 7.4) is by considering measurement-sets which are sufficiently independent from each other in a sense that “measured” heads $\mathbf{y}_h^{(i)} + \mathbf{C}_h \mathbf{z}$ are sufficiently different from each other. This comes on top of the requirement formulated within Assumption 7.3. In this context, it turned out particularly useful to not only consider the minimal number of required measurement-sets $n_{m,\min}$ but additional, thereby improving the number of (nodal) equations to the number of unknowns. Nevertheless, the solving becomes more delicate due to a fast growing equation-set (7.7).

7.6 Tensor Method

Recapitulating the above example, one will recognize that, in fact, the real root \mathbf{x}^* does have a considerable smaller residual $v(\mathbf{x}^*) = 0.011 \times 10^{-2}$ 1/s when compared to the other solutions of Algorithm 1 in table 7.5. Subsequently, there is potential to improve the result by two orders of magnitude in terms of the residual $v(\mathbf{x})$.

One part of Algorithm 1 to be potentially improved, involves the determination of the search direction. Generally, the search direction is determined by setting the truncated *Taylor* series, as in (7.12) to zero, whereas *Newton* proposes to truncate after the linear term. The primary idea is simple, also consider the second order term of this *Taylor* series for the calculation of the search direction with the intention to account for additional non-linearities of $\mathbf{f}(\mathbf{x})$.

$$\mathbf{f}(\mathbf{x}_k) = \mathbf{f}(\mathbf{x}_{k-1}) + \left. \frac{\partial \mathbf{f}}{\partial \mathbf{x}} \right|_{\mathbf{x}_{k-1}} \Delta \mathbf{x}_k + \frac{1}{2} \begin{bmatrix} \Delta \mathbf{x}_k^T \mathcal{H}(f_1) \Big|_{\mathbf{x}_{k-1}} \Delta \mathbf{x}_k \\ \Delta \mathbf{x}_k^T \mathcal{H}(f_2) \Big|_{\mathbf{x}_{k-1}} \Delta \mathbf{x}_k \\ \vdots \\ \Delta \mathbf{x}_k^T \mathcal{H}(f_{n_m n_j}) \Big|_{\mathbf{x}_{k-1}} \Delta \mathbf{x}_k \end{bmatrix} + \mathcal{O}(\Delta \mathbf{x}_k^3) \quad (7.43)$$

Concerning notation, $\mathcal{H}(f_i)$ denotes the *Hessian* matrix (with $n = n_\ell + n_m(n_j - n_p) = n_j n_m$ when square)

$$\mathcal{H}(f)(\mathbf{x}) = \nabla_{\mathbf{x}}^2 f = \begin{bmatrix} \frac{\partial^2 f}{\partial x_1^2} & \frac{\partial^2 f}{\partial x_1 \partial x_2} & \cdots & \frac{\partial^2 f}{\partial x_1 \partial x_n} \\ \frac{\partial^2 f}{\partial x_2 \partial x_1} & \frac{\partial^2 f}{\partial x_2^2} & \cdots & \frac{\partial^2 f}{\partial x_2 \partial x_n} \\ \vdots & \vdots & \ddots & \vdots \\ \frac{\partial^2 f}{\partial x_n \partial x_1} & \frac{\partial^2 f}{\partial x_n \partial x_2} & \cdots & \frac{\partial^2 f}{\partial x_n^2} \end{bmatrix} \quad (7.44)$$

of the i -th component of $\mathbf{f}(\mathbf{x})$. The method of taking the solution $\Delta \mathbf{x}_k$ of the equation

$$\mathbf{f}(\mathbf{x}_{k-1}) + \left. \frac{\partial \mathbf{f}}{\partial \mathbf{x}} \right|_{\mathbf{x}_{k-1}} \Delta \mathbf{x}_k + \frac{1}{2} \begin{bmatrix} \Delta \mathbf{x}_k^T \mathcal{H}(f_1) \Big|_{\mathbf{x}_{k-1}} \Delta \mathbf{x}_k \\ \Delta \mathbf{x}_k^T \mathcal{H}(f_2) \Big|_{\mathbf{x}_{k-1}} \Delta \mathbf{x}_k \\ \vdots \\ \Delta \mathbf{x}_k^T \mathcal{H}(f_{n_m n_j}) \Big|_{\mathbf{x}_{k-1}} \Delta \mathbf{x}_k \end{bmatrix} = \mathbf{0}, \quad (7.45)$$

referred to as *Tensor Equation*, for the search direction is called the *Tensor Method* [Bouaricha and B. Schnabel, 1998; Nocedal and Wright, 2006]. In practice, however, there are two particularly good reasons why the *Tensor Equation* is hardly applied for the determination of the search direction, although it is known that once (7.45) is solved, significantly less iterations are necessary for the iterative scheme to converge to \mathbf{x}^* for solving $\mathbf{f}(\mathbf{x}) = \mathbf{0}$ [Bouaricha and B. Schnabel, 1998]:

- assuming the problem has as many unknowns as equations one would need to store n^3 entries, where $n = n_m n_j$, evaluating *Hessian* $\mathcal{H}(f_1), \mathcal{H}(f_2), \dots$ in each iteration
- the *Tensor Equation* as in (7.45) is an actual hard problem to solve, especially for large problems

In this thesis it is shown that the former issue (first bullet point) can actually be completely resolved for the current application. Concerning the second bullet point, however, the author presents findings which lead to the strong presumption that the second problem may be mitigated substantially.

7.6.1 Second Turbulent Flow Derivatives

This section is supplement to section 7.4.1 and provides the appropriate second derivatives of the turbulent flow (7.5) with respect to the roughness ϵ and the not-measured pressure head \mathbf{h}_N . One receives

$$\frac{\partial^2 Q_i}{\partial \epsilon_j \partial \epsilon_k} \stackrel{(7.6)}{=} \frac{\partial^2 f_{t,i}}{\partial \epsilon_j \partial \epsilon_k} = 0 \quad \text{for } \forall i \neq j \neq k \in \mathfrak{P}, \quad \frac{\partial^2 f_{t,i}}{\partial \epsilon_j \partial h_{N,k}} = 0 \quad \text{for } \forall i \neq j \in \mathfrak{P} \wedge k \in \bar{\mathcal{P}} \quad (7.46a)$$

which holds always for all pipes, whereas one has to expect that

$$\frac{\partial^2 f_{t,i}}{\partial \epsilon_i^2} \neq 0 \quad \text{for } i \in \mathfrak{P}, \quad \frac{\partial^2 f_{t,i}}{\partial \epsilon_i \partial h_{N,j}} \neq 0 \quad \text{for } i \in \mathfrak{P} \wedge j \in \bar{\mathcal{P}}. \quad (7.46b)$$

Remark 7.11. *As the turbulent flow (7.5) is at least two times continuously differentiable (in the turbulent regime at least) with respect to ϵ and Δh , the second derivatives*

$$\frac{\partial^2 f_{t,i}}{\partial \epsilon_i \partial h_{N,j}} = \frac{\partial^2 f_{t,i}}{\partial h_{N,j} \partial \epsilon_i} \quad \forall i \in \mathfrak{P} \wedge j \in \bar{\mathcal{P}} \quad (7.47a)$$

$$\frac{\partial^2 f_{t,i}}{\partial h_{N,k} \partial h_{N,j}} = \frac{\partial^2 f_{t,i}}{\partial h_{N,j} \partial h_{N,k}} \quad \forall i \in \mathfrak{P} \wedge j, k \in \bar{\mathcal{P}} \quad (7.47b)$$

of (7.5) are symmetrical.

Suppressing indices for the sake of readability, one obtains the following derivatives while applying the chain rule $\frac{\partial f_t}{\partial \mathbf{h}_N} = \frac{\partial f_t}{\partial \Delta \mathbf{h}} \frac{\partial \Delta \mathbf{h}}{\partial \mathbf{h}_N}$ and (7.20):

$$\begin{aligned} \frac{\partial^2 f_{t,i}}{\partial \epsilon_i^2} &\hat{=} \frac{\partial^2 f_t}{\partial \epsilon^2} = \frac{\text{sign}(\Delta h) \frac{2}{\ln(10)} \sqrt{\frac{|\Delta h|}{k}} \left(\frac{1}{3.7d}\right)^2}{\ell^2(\epsilon, \Delta h)} \\ &=: [\mathbf{p}_{\epsilon^2}(\epsilon, \Delta \mathbf{h})]_i = p_{\epsilon^2,i}(\epsilon_i, \Delta h_i) \quad \forall i \in \mathfrak{P} \end{aligned} \quad (7.48a)$$

$$\begin{aligned} \frac{\partial^2 f_{t,i}}{\partial \epsilon_i \partial \Delta h_i} &\hat{=} \frac{\partial^2 f_t}{\partial \epsilon \partial \Delta h} = \frac{\partial^2 f_t}{\partial \Delta h \partial \epsilon} = -\frac{1}{\ln(10)} \left(\sqrt{\frac{1}{k|\Delta h|}} \frac{1}{3.7d \ell(\epsilon, \Delta h)} + \frac{2.51\eta A}{3.7\rho d^2} \frac{|\Delta h|^{-1}}{\ell^2(\epsilon, \Delta h)} \right) \\ &=: [\mathbf{p}_{\epsilon \Delta h}(\epsilon, \Delta \mathbf{h})]_i = p_{\epsilon \Delta h,i}(\epsilon_i, \Delta h_i) \quad \forall i \in \mathfrak{P} \end{aligned} \quad (7.48b)$$

The vector function $\mathbf{f}_t(\epsilon, \Delta \mathbf{h}) = [f_{t,1}(\epsilon_1, \Delta h_1) \dots f_{t,n_\ell}(\epsilon_{n_\ell}, \Delta h_{n_\ell})]^T$ thereby denotes function (7.5) evaluated for each pipe flow while applying abbreviation (7.18). In this context it is trivial to see that, e.g., $\frac{\partial \mathbf{f}_t}{\partial \Delta \mathbf{h}} = \text{diag}(\mathbf{p}_{\Delta h})$ is diagonal. As in section 7.4.1, note that the author assumed that $\frac{\partial}{\partial \Delta h} \text{sign}(\Delta h) = 0$, neglecting the *Dirac-Delta* $\delta(\Delta h)$ function. Applying unity vector $\mathbf{e}_i \in \mathbb{Z}_{\{0,1\}}^{n_\ell}$ when writing (7.48b) in vector notation one obtains

$$\frac{\partial^2 f_{t,i}}{\partial \epsilon \partial \mathbf{h}_N} = \frac{\partial}{\partial \Delta \mathbf{h}_N} \left(\frac{\partial f_{t,i}}{\partial \epsilon_i} \frac{\partial \epsilon_i}{\partial \epsilon} \right)^T = \left(\frac{\partial \epsilon_i}{\partial \epsilon} \right)^T \frac{\partial^2 f_{t,i}}{\partial \epsilon_i \partial \Delta h_i} \frac{\partial \Delta h_i}{\partial \mathbf{h}_N} = -\mathbf{e}_i p_{\epsilon \Delta h,i} \mathbf{e}_i^T \mathbf{A}^T \bar{\mathbf{C}}_h^T \quad \forall i \in \mathfrak{P}. \quad (7.49)$$

Regarding the second derivative with respect to \mathbf{h}_N in the scalar form

$$\frac{\partial^2 f_{t,i}}{\partial h_{N,j} \partial h_{N,k}} = \frac{\partial^2 f_{t,i}}{\partial \Delta h_i^2} \frac{\partial \Delta h_i}{\partial h_{N,j}} \frac{\partial \Delta h_i}{\partial h_{N,k}} \quad i \in \mathfrak{P} \wedge j, k \in \bar{\mathcal{P}} \quad (7.50)$$

one obtains

$$\frac{\partial^2 f_{t,i}}{\partial \Delta h_i^2} =: [\mathbf{p}_{\Delta h^2}(\boldsymbol{\epsilon}, \Delta \mathbf{h})]_i = p_{\Delta h^2,i}(\epsilon_i, \Delta h_i) \quad \forall i \in \mathfrak{P} \hat{=} \quad (7.51a)$$

$$\frac{\partial^2 f_t}{\partial \Delta h^2} = \frac{\text{sign}(\Delta h)}{2 \ln(10)} \left[\frac{|\Delta h|^{-3/2}}{\sqrt{k}} \ln(\ell(\epsilon, \Delta h)) - 2.51 \frac{\eta A}{\rho d} \frac{|\Delta h|^{-2}}{\ell(\epsilon, \Delta h)} + \left(2.51 \frac{\eta A}{\rho d} \right)^2 \frac{\sqrt{k} |\Delta h|^{-5/2}}{\ell^2(\epsilon, \Delta h)} \right] \quad (7.51b)$$

yet again suppressing indices (one would simply add, analogously to (7.48), the identical index for all pipe parameters, Δh and ϵ). Applying vector notation, (7.50) yields

$$\begin{aligned} \frac{\partial^2 f_{t,i}}{\partial \mathbf{h}_N^2} &= \frac{\partial}{\partial \mathbf{h}_N} \left(\frac{\partial f_{t,i}}{\partial \Delta h_i} \frac{\partial \Delta h_i}{\partial \mathbf{h}_N} \right)^T = \left(\frac{\partial \Delta h_i}{\partial \mathbf{h}_N} \right)^T \frac{\partial^2 f_{t,i}}{\partial \Delta h_i^2} \frac{\partial \Delta h_i}{\partial \mathbf{h}_N} \\ &= (\bar{\mathbf{C}}_h \mathbf{A} \mathbf{e}_i) p_{\Delta h^2,i} \left(\mathbf{e}_i^T \mathbf{A}^T \bar{\mathbf{C}}_h^T \right) \quad \forall i \in \mathfrak{P}. \end{aligned} \quad (7.52)$$

Finally, things become structurally more appealing by rewriting the derivatives. Denoting

$$\mathbf{A} = \begin{bmatrix} \mathbf{a}_1 & \mathbf{a}_2 & \dots & \mathbf{a}_{n_\ell} \end{bmatrix} = \begin{bmatrix} \mathbf{b}_1 & \mathbf{b}_2 & \dots & \mathbf{b}_{n_j} \end{bmatrix}^T \quad (7.53)$$

with $\mathbf{a}_i \in \mathbb{Z}_{\{-1,0,1\}}^{n_j} \forall i \in \mathfrak{P}$ and $\mathbf{b}_i \in \mathbb{Z}_{\{-1,0,1\}}^{n_\ell} \forall i \in \mathfrak{J}$ while rewriting (7.50) and (7.48), the second turbulent flow derivatives

$$\frac{\partial^2 f_{t,i}}{\partial \mathbf{h}_N^2} \stackrel{(7.51) \wedge (7.52)}{=} p_{\Delta h^2,i} \bar{\mathbf{C}}_h \mathbf{a}_i \mathbf{a}_i^T \bar{\mathbf{C}}_h^T \quad (7.54a)$$

$$\frac{\partial^2 f_{t,i}}{\partial \epsilon^2} \stackrel{(7.48a)}{=} p_{\epsilon^2,i} \mathbf{e}_i \mathbf{e}_i^T \quad (7.54b)$$

$$\frac{\partial^2 f_{t,i}}{\partial \epsilon \partial \mathbf{h}_N} = \left(\frac{\partial^2 f_{t,i}}{\partial \mathbf{h}_N \partial \epsilon} \right)^T \stackrel{(7.48b) \wedge (7.49)}{=} -p_{\epsilon \Delta h,i} \mathbf{e}_i \mathbf{e}_i^T \mathbf{A}^T \bar{\mathbf{C}}_h^T \quad (7.54c)$$

$$\forall i \in \mathfrak{P}$$

along $i = 1, 2, \dots, n_\ell$ can be presented compactly where nonlinearities are stored in vectors $\mathbf{p}_{\epsilon^2}, \mathbf{p}_{\epsilon \Delta h}$ and $\mathbf{p}_{\Delta h^2}$ which are functions on $\boldsymbol{\epsilon}$ and $\Delta \mathbf{h}$. However, the i -th component of these vector functions only depends on the i -th component of $\boldsymbol{\epsilon}$ and $\Delta \mathbf{h}$.

In analogy to the first turbulent flow derivatives in section 7.4.1, it can be recognized that the information along the different measurement-sets can be entirely stored in vector functions $\mathbf{p}_\epsilon, \mathbf{p}_{\Delta h}$ concerning (7.21) as well as $\mathbf{p}_{\epsilon^2}, \mathbf{p}_{\epsilon \Delta h}, \mathbf{p}_{\Delta h^2}$ concerning (7.54). This will be important for the next steps.

7.6.2 Tensor Equation

Lemma 7.12. *Suppose $\mathcal{H}_{k-1}(f) = \mathcal{H}(f)(\mathbf{x}_{k-1})$ for any scalar function f . Then, the Hessian term in the Tensor Equation (7.45) concerning the equation set (7.7) yields*

$$\begin{bmatrix} \Delta \mathbf{x}_k^T \mathcal{H}_{k-1}(f_1) \Delta \mathbf{x}_k \\ \Delta \mathbf{x}_k^T \mathcal{H}_{k-1}(f_2) \Delta \mathbf{x}_k \\ \vdots \\ \Delta \mathbf{x}_k^T \mathcal{H}_{k-1}(f_{n_m n_j}) \Delta \mathbf{x}_k \end{bmatrix} = \begin{bmatrix} \mathbf{A} & & & \\ & \mathbf{A} & & \\ & & \ddots & \\ & & & \mathbf{A} \end{bmatrix} \begin{bmatrix} \Delta \mathbf{x}_k^T \mathcal{H}_{k-1}(Q_1^{(1)}) \Delta \mathbf{x}_k \\ \Delta \mathbf{x}_k^T \mathcal{H}_{k-1}(Q_2^{(1)}) \Delta \mathbf{x}_k \\ \vdots \\ \Delta \mathbf{x}_k^T \mathcal{H}_{k-1}(Q_{n_\ell}^{(1)}) \Delta \mathbf{x}_k \\ \Delta \mathbf{x}_k^T \mathcal{H}_{k-1}(Q_1^{(2)}) \Delta \mathbf{x}_k \\ \vdots \\ \Delta \mathbf{x}_k^T \mathcal{H}_{k-1}(Q_{n_\ell}^{(n_m)}) \Delta \mathbf{x}_k \end{bmatrix} \quad (7.55)$$

when considering pipe flow $Q_j^{(i)} = Q(\epsilon_j, \Delta h_j^{(i)}) \forall j \in \mathfrak{P} \wedge i \in \mathfrak{M}$ which is considered to be a function on the roughness and the head loss generally.

Proof. It is sufficient to show that

$$\begin{bmatrix} \Delta \mathbf{x}_k^T \mathcal{H}_{k-1}(f_{1+(i-1)n_j}) \Delta \mathbf{x}_k \\ \Delta \mathbf{x}_k^T \mathcal{H}_{k-1}(f_{2+(i-1)n_j}) \Delta \mathbf{x}_k \\ \vdots \\ \Delta \mathbf{x}_k^T \mathcal{H}_{k-1}(f_{n_j+(i-1)n_j}) \Delta \mathbf{x}_k \end{bmatrix} \stackrel{!}{=} \mathbf{A} \begin{bmatrix} \Delta \mathbf{x}_k^T \mathcal{H}_{k-1}(Q_1^{(i)}) \Delta \mathbf{x}_k \\ \Delta \mathbf{x}_k^T \mathcal{H}_{k-1}(Q_2^{(i)}) \Delta \mathbf{x}_k \\ \vdots \\ \Delta \mathbf{x}_k^T \mathcal{H}_{k-1}(Q_{n_\ell}^{(i)}) \Delta \mathbf{x}_k \end{bmatrix} \quad (7.56)$$

for measurement-set $i = 1$. The validity of (7.56) for remaining $i = 2, 3, \dots, n_m$ measurement-sets follows subsequently. Let $a_{ij} = [\mathbf{A}]_{ij}$ and remember that $\mathbf{A} = [\mathbf{b}_1 \ \mathbf{b}_2 \ \dots \ \mathbf{b}_{n_j}]^T$ according to (7.53). Hence $\mathbf{b}_j = [a_{j,1} \ a_{j,2} \ \dots \ a_{j,n_\ell}]^T \forall j \in \mathfrak{J}$. Omitting the 1-index in $\mathbf{A} \mathbf{x}_Q^{(1)} - \mathbf{R}_Q^T \mathbf{q}^{(1)} = [f_1 \ \dots \ f_{n_j}]^T \stackrel{!}{=} \mathbf{0}$ concerning the first measurement-sets in favor of readability, one receives

$$\mathcal{H}_{k-1}(f_j) = \mathcal{H}_{k-1}(\mathbf{b}_j^T \mathbf{x}_Q) = a_{j,1} \mathcal{H}_{k-1}(Q_1) + a_{j,2} \mathcal{H}_{k-1}(Q_2) + \dots + a_{j,n_\ell} \mathcal{H}_{k-1}(Q_{n_\ell}) \quad \forall j \in \mathfrak{J} \quad (7.57)$$

exploiting linearity of the Hessian operator. Extended by the search direction from the left and right, (7.57) yields

$$\Delta \mathbf{x}_k^T \mathcal{H}_{k-1}(f_j) \Delta \mathbf{x}_k = \mathbf{b}_j^T \begin{bmatrix} \Delta \mathbf{x}_k^T \mathcal{H}_{k-1}(Q_1) \Delta \mathbf{x}_k \\ \Delta \mathbf{x}_k^T \mathcal{H}_{k-1}(Q_2) \Delta \mathbf{x}_k \\ \vdots \\ \Delta \mathbf{x}_k^T \mathcal{H}_{k-1}(Q_{n_\ell}) \Delta \mathbf{x}_k \end{bmatrix} \quad \forall j \in \mathfrak{J}. \quad (7.58)$$

By extending (7.58) for each of node $j \in \mathfrak{J}$, one obtains (7.56). Additionally, extended with the remaining measurements-sets $2, 3, \dots, n_m$, it is apparent that (7.55) is equivalent to the nonlinear term in (7.45). This completes the proof. \blacksquare

It is important to note that Lemma 7.12 does hold not only for the turbulent flow, but also for laminar and transitional flow. Nevertheless, Lemma 7.12 on its own does *not* directly resolve any of the mentioned problems involved with the *Tensor Method*.

Notation. Knowing that $[\Delta \mathbf{x}_k]_i = \Delta x_{k,i}$ for $i = 1, 2, \dots, n_\ell + n_m(n_j - n_p)$ a separation of the search direction²

$$\mathbf{d} = \left[\mathbf{d}_\epsilon^T \quad \mathbf{d}_{h_N}^{(1)T} \quad \mathbf{d}_{h_N}^{(2)T} \quad \dots \quad \mathbf{d}_{h_N}^{(n_m)T} \right]^T \quad (7.59a)$$

$$\mathbf{d}_\epsilon = \left[\Delta x_{k,1} \quad \Delta x_{k,2} \quad \dots \quad \Delta x_{k,n_\ell} \right]^T \quad (7.59b)$$

$$\mathbf{d}_{h_N}^{(i)} = \left[\Delta x_{k,n_\ell+(i-1)(n_j-n_p)+1} \quad \Delta x_{k,n_\ell+(i-1)(n_j-n_p)+2} \quad \dots \quad \Delta x_{k,n_\ell+i(n_j-n_p)} \right]^T \quad \forall i \in \mathfrak{M} \quad (7.59c)$$

between roughness and not-measured pressure heads is conducted. Analogously, function $\mathbf{f}(\mathbf{x}) = [f_1(\mathbf{x}) \quad f_2(\mathbf{x}) \quad \dots \quad f_{n_m n_j}(\mathbf{x})]^T$ (7.14) which describes the residual of set (7.7) is separated into

$$\mathbf{f}_{k-1}^{(i)} := \left[f_{1+(i-1)n_j}(\mathbf{x}_{k-1}) \quad f_{2+(i-1)n_j}(\mathbf{x}_{k-1}) \quad \dots \quad f_{n_j+(i-1)n_j}(\mathbf{x}_{k-1}) \right]^T \quad \forall i \in \mathfrak{M} \quad (7.59d)$$

concerning the *Tensor Method* iteration k and measurement-set i .

Theorem 7.13. *Let all assumptions in table 7.1 in addition to Assumption 7.7 hold. Further apply notation (7.59) as well as $\mathbf{p}_{\mathcal{X}}^{(i)} := \mathbf{p}_{\mathcal{X}}(\epsilon, \Delta \mathbf{h}^{(i)})$ for all the partial derivatives with respect to $\mathcal{X} \in \{\epsilon, \epsilon^2, \Delta h, \Delta h^2, \epsilon \Delta h\}$. Then, Tensor Equation (7.45) for set (7.7) is equivalent to*

$$\mathbf{A} \left(\overbrace{\left(\frac{1}{2} \mathbf{p}_{\epsilon^2}^{(i)} \odot \mathbf{d}_\epsilon^{\odot 2} - \mathbf{d}_\epsilon \odot \mathbf{p}_{\epsilon \Delta h}^{(i)} \odot (\mathbf{A}^T \bar{\mathbf{C}}_h^T \mathbf{d}_{h_N}^{(i)}) + \frac{1}{2} \mathbf{p}_{\Delta h^2}^{(i)} \odot (\mathbf{A}^T \bar{\mathbf{C}}_h^T \mathbf{d}_{h_N}^{(i)})^{\odot 2} \right)}^{\textcircled{III}} + \underbrace{\mathbf{p}_\epsilon^{(i)} \odot \mathbf{d}_\epsilon - \mathbf{p}_{\Delta h}^{(i)} \odot (\mathbf{A}^T \bar{\mathbf{C}}_h^T \mathbf{d}_{h_N}^{(i)})}_{\textcircled{II}} + \underbrace{\text{diag}(\mathbf{c}_l) \mathbf{A}^T \mathbf{L}^{-1} \mathbf{f}_{k-1}^{(i)}}_{\textcircled{I}} \right) =: \mathbf{A} \bar{\mathbf{m}}_k^{(i)} \quad (7.60)$$

for all of the $i \in \mathfrak{M}$ measurement-sets.

Proof. Under consideration of first turbulent flow derivatives (7.21), Jacobian (7.15) yields

$$\begin{bmatrix} \text{diag}(\mathbf{p}_\epsilon^{(1)}) & -\text{diag}(\mathbf{p}_{\Delta h}^{(1)}) \mathbf{A}^T \bar{\mathbf{C}}_h^T & \mathbf{0} & \dots & \mathbf{0} \\ \text{diag}(\mathbf{p}_\epsilon^{(2)}) & \mathbf{0} & -\text{diag}(\mathbf{p}_{\Delta h}^{(2)}) \mathbf{A}^T \bar{\mathbf{C}}_h^T & \dots & \mathbf{0} \\ \vdots & \vdots & & \ddots & \\ \text{diag}(\mathbf{p}_\epsilon^{(n_m)}) & \mathbf{0} & \mathbf{0} & \dots & -\text{diag}(\mathbf{p}_{\Delta h}^{(n_m)}) \mathbf{A}^T \bar{\mathbf{C}}_h^T \end{bmatrix} \quad (7.61)$$

leading to the following *Jacobian* term in *Tensor Equation* (7.45) when applying (7.59)

$$\mathbf{A} \left(\mathbf{p}_\epsilon^{(i)} \odot \mathbf{d}_\epsilon - \mathbf{p}_{\Delta h}^{(i)} \odot (\mathbf{A}^T \bar{\mathbf{C}}_h^T \mathbf{d}_{h_N}^{(i)}) \right) \hat{=} \mathbf{A} \textcircled{II}. \quad (7.62)$$

Compare this result with incidence matrix \mathbf{A} times the term \textcircled{II} in the second line of (7.60). Considering Lemma 7.12 concerning the *Hessian* term with respect to the $j \in \mathfrak{P}$ turbulent pipe flow (7.5) (and the k -th iteration) in *Tensor Equation* (7.45), one obtains in the first $i = 1$

²Please do not confuse the search direction \mathbf{d} with the pipes' diameter $[\mathbf{d}]_i = d_i \quad \forall i \in \mathfrak{P}$.

measurement-set

$$\Delta \mathbf{x}_k^T \mathcal{H}_{k-1}(f_{t,j}^{(1)}) \Delta \mathbf{x}_k = \begin{bmatrix} \mathbf{d}_\epsilon^T & \mathbf{d}_{h_N}^{(1)T} & \dots & \mathbf{d}_{h_N}^{(n_m)T} \end{bmatrix} \begin{bmatrix} \frac{\partial^2 f_{t,j}^{(1)}}{\partial^2 \epsilon^2} & \frac{\partial^2 f_{t,j}^{(1)}}{\partial \epsilon \partial \mathbf{h}_N^{(1)}} & \mathbf{0} & \dots \\ \frac{\partial^2 f_{t,j}^{(1)}}{\partial \mathbf{h}_N^{(1)} \partial \epsilon} & \frac{\partial^2 f_{t,j}^{(1)}}{\partial \mathbf{h}_N^{(1)2}} & \mathbf{0} & \dots \\ \mathbf{0} & \mathbf{0} & \mathbf{0} & \dots \\ \vdots & \vdots & \vdots & \ddots \end{bmatrix} \begin{bmatrix} \mathbf{d}_\epsilon \\ \mathbf{d}_{h_N}^{(1)} \\ \vdots \\ \mathbf{d}_{h_N}^{(n_m)} \end{bmatrix} \quad (7.63a)$$

$$\stackrel{(7.54)}{=} p_{\epsilon^2,j}^{(1)} \mathbf{d}_\epsilon^T \mathbf{e}_j \mathbf{e}_j^T \mathbf{d}_\epsilon - 2p_{\epsilon \Delta h,j}^{(1)} \mathbf{d}_\epsilon^T \mathbf{e}_j \mathbf{e}_j^T \mathbf{A}^T \bar{\mathbf{C}}_h^T \mathbf{d}_{h_N}^{(1)} + p_{\Delta h^2,j}^{(1)} \mathbf{d}_{h_N}^{(1)T} \bar{\mathbf{C}}_h \mathbf{a}_j \mathbf{a}_j^T \bar{\mathbf{C}}_h^T \mathbf{d}_{h_N}^{(1)} \quad (7.63b)$$

and in the second measurement-set

$$\Delta \mathbf{x}_k^T \mathcal{H}_{k-1}(f_{t,j}^{(2)}) \Delta \mathbf{x}_k = \begin{bmatrix} \mathbf{d}_\epsilon^T & \mathbf{d}_{h_N}^{(1)T} & \dots & \mathbf{d}_{h_N}^{(n_m)T} \end{bmatrix} \begin{bmatrix} \frac{\partial^2 f_{t,j}^{(2)}}{\partial^2 \epsilon^2} & \mathbf{0} & \frac{\partial^2 f_{t,j}^{(2)}}{\partial \epsilon \partial \mathbf{h}_N^{(2)}} & \mathbf{0} & \dots \\ \mathbf{0} & \mathbf{0} & \mathbf{0} & \mathbf{0} & \dots \\ \frac{\partial^2 f_{t,j}^{(2)}}{\partial \mathbf{h}_N^{(2)} \partial \epsilon} & \mathbf{0} & \frac{\partial^2 f_{t,j}^{(2)}}{\partial \mathbf{h}_N^{(2)2}} & \mathbf{0} & \dots \\ \mathbf{0} & \mathbf{0} & \mathbf{0} & \mathbf{0} & \dots \\ \vdots & \vdots & \vdots & \vdots & \ddots \end{bmatrix} \begin{bmatrix} \mathbf{d}_\epsilon \\ \mathbf{d}_{h_N}^{(1)} \\ \vdots \\ \mathbf{d}_{h_N}^{(n_m)} \end{bmatrix} \quad (7.64a)$$

$$\stackrel{(7.54)}{=} p_{\epsilon^2,j}^{(2)} \mathbf{d}_\epsilon^T \mathbf{e}_j \mathbf{e}_j^T \mathbf{d}_\epsilon - 2p_{\epsilon \Delta h,j}^{(2)} \mathbf{d}_\epsilon^T \mathbf{e}_j \mathbf{e}_j^T \mathbf{A}^T \bar{\mathbf{C}}_h^T \mathbf{d}_{h_N}^{(2)} + p_{\Delta h^2,j}^{(2)} \mathbf{d}_{h_N}^{(2)T} \bar{\mathbf{C}}_h \mathbf{a}_j \mathbf{a}_j^T \bar{\mathbf{C}}_h^T \mathbf{d}_{h_N}^{(2)} \quad (7.64b)$$

which, ultimately, results in

$$\Delta \mathbf{x}_k^T \mathcal{H}_{k-1}(f_{t,j}^{(i)}) \Delta \mathbf{x}_k = p_{\epsilon^2,j}^{(i)} \mathbf{d}_\epsilon^T \mathbf{e}_j \mathbf{e}_j^T \mathbf{d}_\epsilon - 2p_{\epsilon \Delta h,j}^{(i)} \mathbf{d}_\epsilon^T \mathbf{e}_j \mathbf{e}_j^T \mathbf{A}^T \bar{\mathbf{C}}_h^T \mathbf{d}_{h_N}^{(i)} + p_{\Delta h^2,j}^{(i)} \mathbf{d}_{h_N}^{(i)T} \bar{\mathbf{C}}_h \mathbf{a}_j \mathbf{a}_j^T \bar{\mathbf{C}}_h^T \mathbf{d}_{h_N}^{(i)} \quad \forall i \in \mathfrak{M} \wedge j \in \mathfrak{P}. \quad (7.65)$$

This is feasible as a result of Assumption 7.1 leading to

$$\frac{\partial^2 f_{t,j}^{(i)}}{\partial \epsilon \partial \mathbf{h}_N^{(l)}} = \mathbf{0}, \quad \frac{\partial^2 f_{t,j}^{(i)}}{\partial \mathbf{h}_N^{(l)2}} = \mathbf{0} \quad \forall i \in \mathfrak{M} \neq l \in \mathfrak{M} \wedge j \in \mathfrak{P}. \quad (7.66)$$

The application of the *Hadamard* operator allows a compact representation of (7.65)

$$\mathbf{p}_{\epsilon^2}^{(i)} \odot \mathbf{d}_\epsilon^{\odot 2} - 2\mathbf{d}_\epsilon \odot \mathbf{p}_{\epsilon \Delta h}^{(i)} \odot (\mathbf{A}^T \bar{\mathbf{C}}_h^T \mathbf{d}_{h_N}^{(i)}) + \mathbf{p}_{\Delta h^2}^{(i)} \odot (\mathbf{A}^T \bar{\mathbf{C}}_h^T \mathbf{d}_{h_N}^{(i)})^{\odot 2} \hat{=} \textcircled{\text{III}} \quad (7.67)$$

for all $i \in \{1, \dots, n_m\} = \mathfrak{M}$. In order for (7.65) to be equivalent to (7.67) along all $j \in \mathfrak{P}$ one has to prove that

$$\begin{bmatrix} p_{\Delta h^2,1}^{(i)} \mathbf{d}_{h_N}^{(i)T} \bar{\mathbf{C}}_h \mathbf{a}_1 \mathbf{a}_1^T \bar{\mathbf{C}}_h^T \mathbf{d}_{h_N}^{(i)} \\ p_{\Delta h^2,2}^{(i)} \mathbf{d}_{h_N}^{(i)T} \bar{\mathbf{C}}_h \mathbf{a}_2 \mathbf{a}_2^T \bar{\mathbf{C}}_h^T \mathbf{d}_{h_N}^{(i)} \\ \vdots \\ p_{\Delta h^2,n_\ell}^{(i)} \mathbf{d}_{h_N}^{(i)T} \bar{\mathbf{C}}_h \mathbf{a}_{n_\ell} \mathbf{a}_{n_\ell}^T \bar{\mathbf{C}}_h^T \mathbf{d}_{h_N}^{(i)} \end{bmatrix} = \mathbf{p}_{\Delta h^2}^{(i)} \odot (\mathbf{A}^T \bar{\mathbf{C}}_h^T \mathbf{d}_{h_N}^{(i)})^{\odot 2}. \quad (7.68)$$

Denoting $\bar{\mathbf{C}}_h^T \mathbf{d}_{h_N}^{(i)} = [c_1^{(i)} \quad c_2^{(i)} \quad \dots \quad c_{n_j}^{(i)}]^T$ and $a_{ij} = [\mathbf{A}]_{ij}$, this becomes apparent when writing

$$\mathbf{d}_{h_N}^{(i)T} \bar{\mathbf{C}}_h \mathbf{a}_j = c_1^{(i)} a_{j1} + c_2^{(i)} a_{j1} + \dots + c_2^{(i)} a_{jn_j} \quad \forall j \in \mathfrak{P} \wedge i \in \mathfrak{M} \quad (7.69a)$$

$$\Rightarrow \mathbf{d}_{h_N}^{(i)T} \bar{\mathbf{C}}_h \mathbf{a}_j \mathbf{a}_j^T \bar{\mathbf{C}}_h^T \mathbf{d}_{h_N}^{(i)} = \left(c_1^{(i)} a_{j1} + c_2^{(i)} a_{j1} + \dots + c_2^{(i)} a_{jn_j} \right)^2 = \left[(\mathbf{A}^T \bar{\mathbf{C}}_h^T \mathbf{d}_{h_N}^{(i)})^{\odot 2} \right]_j. \quad (7.69b)$$

The equivalence of the *Jacobian* (7.62) (see $\mathbf{A}^{\textcircled{II}}$) and the *Hessian* term (7.67) (see \textcircled{III}), under consideration of Lemma 7.12, to the appropriate terms of the *Tensor Equation* (7.45) has been proven. The equivalence of missing zero-order term $\mathbf{f}_{k-1}^{(i)}$ with $\mathbf{A}^{\textcircled{I}}$, i.e.

$$\mathbf{f}_{k-1}^{(i)} = \mathbf{A} \left(\text{diag}(\mathbf{c}_l) \mathbf{A}^T \mathbf{L}^{-1} \mathbf{f}_{k-1}^{(i)} \right) \quad (7.70)$$

becomes apparent when looking at Proposition 4.1. The combination of (7.62), (7.67), (7.70) under consideration of Lemma 7.12, that is $\mathbf{A} \bar{\mathbf{m}}_k^{(i)} \hat{=} \mathbf{A}(\textcircled{I} + \textcircled{II} + \textcircled{III})$, yields the *Tensor Equation* (7.45) in measurement-set i . This completes the proof. \blacksquare

In sum, Theorem 7.13 delivers the *Tensor Equation* in a compact form which completely resolves the problem to store and evaluate $n_m n_j$ *Hessians* $\mathcal{H}_{k-1}(f_1), \mathcal{H}_{k-1}(f_2), \dots$ with $(n_\ell + n_m(n_j - n_p))^2$ entries each. Effectively, only $5n_\ell n_m$ second-turbulent-flow-derivatives need to be evaluated in comparison to $n_j n_m (n_\ell + n_m(n_j - n_p))^2$. Actually, the linear *Newton* equation for the search direction (7.13) considering the *Jacobian*, already requires $n_m n_j \times (n_\ell + n_m(n_j - n_p))$ first-turbulent-flow-derivative evaluations when not directly applying (7.21). Overall, the application of the *Hardamard* operator substantially improves computational effort in this context. Nonetheless, the question how to solve it, remains.

As the *Tensor Equation* in all its derived forms, is nothing else but a set of $n_m n_j$ polynomials of degree 2 in $n_\ell + n_m(n_j - n_p)$ unknowns, the examples below will help to establish a connection between its solutions and the *Hadamard* product.

7.6.3 Motivating Examples

Consider the set of two polynomial equations with degree 2 in two unknowns x, y

$$\begin{aligned} 2x^2 + 2y^2 + 5xy - x + y - 1 &= 0 & \Leftrightarrow & \begin{array}{l} \textcircled{1a} \qquad \qquad \textcircled{1b} \\ (x + 2y - 1)(2x + y + 1) = 0 \end{array} \\ -3x^2 - 2y^2 + 5xy + 10x - 8y - 8 &= 0 & & \begin{array}{l} \textcircled{2a} \qquad \qquad \textcircled{2b} \\ (-x + y + 2)(3x - 2y - 4) = 0 \end{array} \end{aligned} \quad (7.71)$$

which can be separated into linear terms each. The solutions of (7.71) can then be obtained by solving the linear equations

$$\textcircled{1a} \wedge \textcircled{2a} \hat{=} \begin{bmatrix} 1 & 2 \\ -1 & 1 \end{bmatrix} \begin{bmatrix} x \\ y \end{bmatrix} = \begin{bmatrix} 1 \\ -2 \end{bmatrix}, \quad \textcircled{1b} \wedge \textcircled{2b} \hat{=} \begin{bmatrix} 2 & 1 \\ 3 & -2 \end{bmatrix} \begin{bmatrix} x \\ y \end{bmatrix} = \begin{bmatrix} -1 \\ 4 \end{bmatrix}, \quad (7.72a)$$

$$\textcircled{1a} \wedge \textcircled{2b} \hat{=} \begin{bmatrix} 1 & 2 \\ 3 & -2 \end{bmatrix} \begin{bmatrix} x \\ y \end{bmatrix} = \begin{bmatrix} 1 \\ 4 \end{bmatrix}, \quad \textcircled{1b} \wedge \textcircled{2a} \hat{=} \begin{bmatrix} 2 & 1 \\ -1 & 1 \end{bmatrix} \begin{bmatrix} x \\ y \end{bmatrix} = \begin{bmatrix} -1 \\ -2 \end{bmatrix} \quad (7.72b)$$

as combination of the linear terms in (7.71), effectively, leading to 4 independent solutions. This means (7.71) can be rewritten in terms of (taking “ $(\textcircled{1a} \wedge \textcircled{2a}) \odot (\textcircled{1b} \wedge \textcircled{2b})$ ”)

$$\left(\begin{bmatrix} 1 & 2 \\ -1 & 1 \end{bmatrix} \begin{bmatrix} x \\ y \end{bmatrix} - \begin{bmatrix} 1 \\ -2 \end{bmatrix} \right) \odot \left(\begin{bmatrix} 2 & 1 \\ 3 & -2 \end{bmatrix} \begin{bmatrix} x \\ y \end{bmatrix} - \begin{bmatrix} -1 \\ 4 \end{bmatrix} \right) = \mathbf{0} \quad (7.73a)$$

or (taking “ $(\textcircled{1a} \wedge \textcircled{2b}) \odot (\textcircled{1b} \wedge \textcircled{2a})$ ”)

$$\left(\begin{bmatrix} 1 & 2 \\ 3 & -2 \end{bmatrix} \begin{bmatrix} x \\ y \end{bmatrix} - \begin{bmatrix} 1 \\ 4 \end{bmatrix} \right) \odot \left(\begin{bmatrix} 2 & 1 \\ -1 & 1 \end{bmatrix} \begin{bmatrix} x \\ y \end{bmatrix} - \begin{bmatrix} -1 \\ -2 \end{bmatrix} \right) = \mathbf{0} \quad (7.73b)$$

when applying the *Hadamard* product. According to *Bézout’s* theorem [Coolidge, 2004, p. 10], it is known that a set of n polynomials $\{f_1, f_2, \dots, f_n\}$ in n unknowns has at most

$$\prod_{i=1}^n \deg(f_i) \quad (7.74)$$

(i.e. the product of the degrees of each polynomial) solutions as it is the case in the present example. This statement is, however, incomplete as there possibly exist infinitely many solutions [Coolidge, 2004, p. 10], for instance when the equations are linear dependent. However, by selecting representation (7.73a) or (7.73b) one loses 2 solutions when applying the *Hadamard* product.

The factorization into linear terms as in (7.71) is not always possible for a polynomial with more than one variable, for instance

$$f(x, y) = xy + 1 \quad (7.75)$$

is not factorizable into linear terms. For the general case, consider a general polynomial of degree 2 in two unknowns, also known as conic section

$$f(x, y) = ax^2 + 2hxy + by^2 + 2fx + 2gy + c = 0 \quad (7.76)$$

with coefficients a, h, b, f, g, c . The following properties of (7.76) are known. Property 7.14 and 7.15 were found in [Lawrence, 1972, p.63] as well as [Spain, 2007, p.40], though in both references respective authors do not concern themselves with a proof. Other mentions of Property 7.14 can be found in, for instance, Faucette [1996].

Property 7.14. *Let coefficients $a, b, h, g, f, c \in \mathbb{R}$. Then, the conic section f (7.76) is factorizable into the linear-pair*

$$f(x, y) = (Ax + By + C)(Dx + Ey + F) = 0 \quad (7.77)$$

with coefficients $A, B, C, D, E, F \in \mathbb{C}$ if and only if

$$\Delta := \begin{vmatrix} a & h & f \\ h & b & g \\ f & g & c \end{vmatrix} = 0 \quad \wedge \quad \hat{\Delta} := \begin{vmatrix} a & h \\ h & b \end{vmatrix} = ab - h^2 \leq 0 \quad (7.78)$$

the determinant $\Delta = 0$ and its sub determinant $\hat{\Delta} \leq 0$. In addition to that, these two linear factors as in (7.77) represent

- two intersecting lines if and only if $\hat{\Delta} < 0$
- two parallel lines (or a single line if $a = b = h = 0$) if and only if $\hat{\Delta} = 0$

However, in case $\Delta = 0$ and $\hat{\Delta} > 0$, only a single point concerning x, y satisfies the conic section (7.76) (interpreted graphically, it is an ellipse with zero radius).

In the general case where $\Delta = 0$, conic (7.76) is called degenerate as the coefficient matrix to build determinant Δ is singular.

Property 7.15. *As a specification of Property 7.14, the factorization of conic (7.76) in (7.77) yields real-valued A, B, C, D, E, F if and only if*

$$\Delta = 0 \quad \wedge \quad \hat{\Delta} < 0 \quad (7.79a)$$

$$\text{or } \Delta = 0 \quad \wedge \quad \hat{\Delta} = 0 \quad \wedge \quad f^2 + g^2 \geq c(a + b). \quad (7.79b)$$

Lemma 7.16. *Let $\Delta = 0$ and $\hat{\Delta} = 0$, concerning the degenerate conic $f(x, y)$ (7.76). Then,*

$$f^2 + g^2 \geq c(a + b) \quad \Leftrightarrow \quad f^2 \geq ac \wedge g^2 \geq bc \quad (7.80)$$

in reference to (7.79b).

Proof. Knowing that $\hat{\Delta} = 0 \Leftrightarrow h^2 = ab$, the determinant Δ yields

$$\Delta = abc + 2fgh - ag^2 - bf^2 - ch^2 = 0 \quad (7.81a)$$

$$= 2fgh - ag^2 - bf^2 = 0. \quad (7.81b)$$

Subsequently,

$$g = \frac{1}{-2a} \left(2fh \pm \sqrt{4(fh)^2 - 4abf^2} \right) \stackrel{\hat{\Delta}=0}{=} -\frac{fh}{a} \quad (7.81c)$$

$$g^2 = \left(\frac{fh}{a} \right)^2 = f^2 \frac{b}{a} \quad (7.81d)$$

$$f^2 = g^2 \frac{a}{b}. \quad (7.81e)$$

This means that

$$f^2 + g^2 \stackrel{(7.81d)}{=} f^2 \left(\frac{a+b}{a} \right) \geq c(a+b) \quad \Rightarrow \quad f^2 \geq ac \quad (7.81f)$$

$$f^2 + g^2 \stackrel{(7.81e)}{=} g^2 \left(\frac{a+b}{b} \right) \geq c(a+b) \quad \Rightarrow \quad g^2 \geq bc. \quad (7.81g)$$

From the other side of the argumentation, it is known that $f^2 \geq ac \wedge g^2 \geq bc$ and thus $f^2 + g^2 \geq ac + bc$. This completes the proof. \blacksquare

Plausibility Check of Property 7.14. Conducting a comparison of coefficients of (7.76) and (7.77), the six conditions

$$AD = a, \quad BE = b, \quad CF = c \quad (7.82a)$$

$$AE + DB = 2h, \quad BF + EC = 2g, \quad AF + DC = 2f \quad (7.82b)$$

must be met if $f(x, y)$ ought to be factorizable into linear terms. This is the case (necessary condition) if the set (7.82) of six equations in six unknowns is consistent. Consistency can be verified when multiplying conditions (7.82b) among each other such that

$$\begin{aligned} 8hgf &= (AE + DB)(BF + EC)(AF + DC) \\ &= 2ADBEFC + AD(B^2F^2 + E^2C^2) + BE(A^2F^2 + D^2C^2) \\ &\quad + CF(A^2E^2 + B^2D^2). \end{aligned} \quad (7.83)$$

By reformulating the square of conditions (7.82b) respectively, one obtains

$$(AE)^2 + (DB)^2 = 4h^2 - 2AEDB \stackrel{(7.82a)}{=} 4h^2 - 2ab \quad (7.84a)$$

$$(BF)^2 + (EC)^2 = 4g^2 - 2BFEC \stackrel{(7.82a)}{=} 4g^2 - 2bc \quad (7.84b)$$

$$(AF)^2 + (DC)^2 = 4f^2 - 2AFDC \stackrel{(7.82a)}{=} 4f^2 - 2ac \quad (7.84c)$$

which is inserted into the right hand side of (7.83). To conclude, consistency of set (7.82) is preserved if

$$8hgf \stackrel{(7.82a) \wedge (7.84)}{=} 2abc + a(4g^2 - 2bc) + b(4f^2 - 2ac) + c(4h^2 - 2ab) \quad (7.85)$$

holds. Bringing $8ghf$ of (7.85) on the right hand side while dividing by -4 , condition (7.85) yields

$$0 \stackrel{!}{=} 2ghf + abc - ag^2 - bf^2 - ch^2 = \Delta \quad (7.86)$$

the determinant Δ (7.78).

As a remark on polynomials of degree n , it is possible to show that if a homogeneous polynomial, that is $f(\mu\mathbf{x}) = \mu^n f(\mathbf{x})$ for any $\mathbf{x} \in \mathbb{C}^n, \mu \in \mathbb{C}$ has a factorization, then its factors must be homogeneous too. Consider, for instance, the polynomial in variables x, y, z

$$x^3 + y^3 + z^3 = (x + y + z)(x + wy + w^2z)(x + w^2y + wz) \quad \text{for } w = e^{2i\pi/3} \quad (7.87)$$

(credit to [Elenchajg]) where i denotes the imaginary unit satisfying $i^2 = -1$.

7.6.4 Degenerate Tensor Equation

Remark 7.17. Looking for a search direction \mathbf{d}_ϵ and $\mathbf{d}_{h_N}^{(i)}$ for measurement-set $i \in \mathfrak{M}$ which solves Tensor Equation (7.60), i.e. $\mathbf{A}\bar{\mathbf{m}}_k^{(i)}(\mathbf{d}_\epsilon, \mathbf{d}_{h_N}^{(i)}) = \mathbf{0} \forall i \in \mathfrak{M}$, the confinement to look for a search direction which solves $\bar{\mathbf{m}}_k^{(i)}(\mathbf{d}_\epsilon, \mathbf{d}_{h_N}^{(i)}) = \mathbf{0} \forall i \in \mathfrak{M}$ only is eligible yet far too conservative. This is the consequence of incidence matrix $\mathbf{A} \in \mathbb{Z}_{\{-1,0,1\}}^{n_j \times n_\ell}$ being fat, i.e. $n_\ell \geq n_j$ (Corollary 3.4).

To circumvent the problem that the incidence matrix \mathbf{A} can not be directly considered when solving $\bar{\mathbf{m}}_k^{(i)} = \mathbf{0}$ (which is considered to be a function on \mathbf{d}_ϵ and $\mathbf{d}_{h_N}^{(i)}$) component-wise, the problem is projected into the kernel. Knowing that $\mathbf{A}\mathbf{S}^T \equiv \mathbf{0}$ in reference to Proposition 3.6, one can write

$$\mathbf{A}\bar{\mathbf{m}}_k^{(i)}(\mathbf{d}_\epsilon, \mathbf{d}_{h_N}^{(i)}) = \mathbf{0} \quad \Leftrightarrow \quad \mathbf{m}_k := \bar{\mathbf{m}}_k^{(i)}(\mathbf{d}_\epsilon, \mathbf{d}_{h_N}^{(i)}) - \mathbf{S}^T \boldsymbol{\alpha}^{(i)} = \mathbf{0} \quad \forall i \in \mathfrak{M} \quad (7.88)$$

for some $\boldsymbol{\alpha}^{(i)} \in \mathbb{C}^{n_\ell \times n_j}$ along all measurement-set $i \in \mathfrak{M}$, where $\mathbf{m}_k^{(i)}(\mathbf{d}_\epsilon, \mathbf{d}_{h_N}^{(i)}, \boldsymbol{\alpha}^{(i)}) \forall i \in \mathfrak{M}$ is considered to be a function on $\boldsymbol{\alpha}^{(i)}$ too.

Theorem 7.18. Denoting $p_{\mathcal{X}_j}^{(i)} = [\mathbf{p}_{\mathcal{X}}^{(i)}(\boldsymbol{\epsilon}_k, \Delta \mathbf{h}_k^{(i)})]_j$ for all pipes $j \in \mathfrak{P}$ and measurement-sets $i \in \mathfrak{M}$ concerning all partial derivatives of turbulent flow (7.5) with respect to $\mathcal{X} \in \{\epsilon, \epsilon^2, \Delta h, \Delta h^2, \epsilon \Delta h\}$ in the solving-iteration k . Then, Tensor Equation (7.60) in the measurement-set $i \in \mathfrak{M}$ can be factorized into linear terms

$$\mathbf{m}_k^{(i)} = (\mathbf{B}^{(i)} \mathbf{d}_\epsilon + \mathbf{C}^{(i)} \mathbf{d}_{h_N}^{(i)} + \mathbf{v}^{(i)}) \odot (\mathbf{E}^{(i)} \mathbf{d}_\epsilon + \mathbf{F}^{(i)} \mathbf{d}_{h_N}^{(i)} + \mathbf{w}^{(i)}) \quad i \in \mathfrak{M} \quad (7.89)$$

connected via the Hadamard product if and only if $\Delta_j^{(i)}(\boldsymbol{\alpha}^{(i)}) = 0$ and $\hat{\Delta}_j^{(i)} \leq 0 \quad \forall j \in \mathfrak{P}$ for a specific $\boldsymbol{\alpha}^{(i)} \in \mathbb{C}^{n_\ell - n_c}$, same as in (7.88), concerning the determinant

$$\Delta_j^{(i)}(\boldsymbol{\alpha}^{(i)}) := \frac{1}{2} \begin{vmatrix} p_{\epsilon_j^2}^{(i)} & -p_{\epsilon \Delta h_j}^{(i)} & p_{\epsilon_j}^{(i)} \\ -p_{\epsilon \Delta h_j}^{(i)} & p_{\Delta h_j^2}^{(i)} & -p_{\Delta h_j}^{(i)} \\ p_{\epsilon_j}^{(i)} & -p_{\Delta h_j}^{(i)} & 2\bar{f}_{0,j}^{(i)}(\boldsymbol{\alpha}^{(i)}) \end{vmatrix} \quad \text{and} \quad \hat{\Delta}_j^{(i)} := \begin{vmatrix} p_{\epsilon_j^2}^{(i)} & -p_{\epsilon \Delta h_j}^{(i)} \\ -p_{\epsilon \Delta h_j}^{(i)} & p_{\Delta h_j^2}^{(i)} \end{vmatrix}. \quad (7.90)$$

Also applying

$$\bar{f}_{0,j}^{(i)}(\boldsymbol{\alpha}^{(i)}) = [\bar{\mathbf{f}}_0^{(i)}(\boldsymbol{\alpha}^{(i)})]_j := \left[\text{diag}(\mathbf{c}_l) \mathbf{A} \mathbf{L}^{-1} \mathbf{f}_{k-1}^{(i)} - \mathbf{S}^T \boldsymbol{\alpha}^{(i)} \right]_j \quad \forall j \in \mathfrak{P} \wedge i \in \mathfrak{M}, \quad (7.91)$$

matrices in (7.89) yield the diagonal forms $\mathbf{B}^{(i)} = \text{diag}(\mathbf{b}^{(i)})$, $\mathbf{E}^{(i)} = \text{diag}(\mathbf{e}^{(i)})$, whereas $\mathbf{C}^{(i)} = \text{diag}(\mathbf{c}^{(i)}) \mathbf{A}^T \bar{\mathbf{C}}_h^T$ and $\mathbf{F}^{(i)} = \text{diag}(\tilde{\mathbf{f}}^{(i)}) \mathbf{A}^T \bar{\mathbf{C}}_h^T$ with $\mathbf{b}^{(i)}, \mathbf{e}^{(i)}, \mathbf{c}^{(i)}, \tilde{\mathbf{f}}^{(i)}, \mathbf{v}^{(i)}, \mathbf{w}^{(i)} \in \mathbb{C}^{n_\ell}$ respectively

which will be referred to as Tensor Separators. Thereby, $\mathbf{v}^{(i)}, \mathbf{w}^{(i)} \in \mathbb{C}^{n_\ell}$ are functions on $\boldsymbol{\alpha}^{(i)} \in \mathbb{C}^{n_\ell - n_j}$ which lie inside the kernel of the incidence matrix \mathbf{A} .

Proof. For the sake of readability, the index (i) along the measurement-sets $i = 1, 2, \dots, n_m$ is not displayed. Comparing terms of (7.60) with the ones of (7.89) one obtains:

$$\begin{aligned}
(i) \quad & \mathbf{B}\mathbf{d}_\epsilon \odot \mathbf{E}\mathbf{d}_\epsilon \stackrel{!}{=} \frac{1}{2}\mathbf{p}_{\epsilon^2} \odot \mathbf{d}_\epsilon^{\odot 2} \\
(ii) \quad & \mathbf{C}\mathbf{d}_{h_N} \odot \mathbf{F}\mathbf{d}_{h_N} \stackrel{!}{=} \frac{1}{2}\mathbf{p}_{\Delta h^2} \odot (\mathbf{A}^T \bar{\mathbf{C}}_h^T \mathbf{d}_{h_N})^{\odot 2} \\
(iii) \quad & \mathbf{B}\mathbf{d}_\epsilon \odot \mathbf{F}\mathbf{d}_{h_N} + \mathbf{C}\mathbf{d}_{h_N} \odot \mathbf{E}\mathbf{d}_\epsilon \stackrel{!}{=} -\mathbf{d}_\epsilon \odot \mathbf{p}_{\epsilon \Delta h} \odot (\mathbf{A}^T \bar{\mathbf{C}}_h^T \mathbf{d}_{h_N}) \\
(iv) \quad & \mathbf{B}\mathbf{d}_\epsilon \odot \mathbf{w} + \mathbf{v} \odot \mathbf{E}\mathbf{d}_\epsilon \stackrel{!}{=} \mathbf{p}_\epsilon \odot \mathbf{d}_\epsilon \\
(v) \quad & \mathbf{C}\mathbf{d}_{h_N} \odot \mathbf{w} + \mathbf{v} \odot \mathbf{F}\mathbf{d}_{h_N} \stackrel{!}{=} -\mathbf{p}_{\Delta h} \odot (\mathbf{A}^T \bar{\mathbf{C}}_h^T \mathbf{d}_{h_N}) \\
(vi) \quad & \mathbf{v} \odot \mathbf{w} \stackrel{!}{=} \text{diag}(\mathbf{c}_l) \mathbf{A}^T \mathbf{L}^{-1} \mathbf{f}_{k-1} - \mathbf{S}^T \boldsymbol{\alpha} =: \bar{\mathbf{f}}_0(\boldsymbol{\alpha})
\end{aligned}$$

The simplification starts with the premise that the above conditions should hold for every \mathbf{d}_ϵ and \mathbf{d}_{h_N} , not only for ones to find. As a result, $\mathbf{B} = \text{diag}(\mathbf{b})$ and $\mathbf{E} = \text{diag}(\mathbf{e})$ in (i) are diagonal and lead to $\mathbf{b} \odot \mathbf{e} = \frac{1}{2}\mathbf{p}_{\epsilon^2}$. Subsequently, condition (iv) yields

$$(\text{diag}(\mathbf{w})\mathbf{B} + \text{diag}(\mathbf{v})\mathbf{E})\mathbf{d}_\epsilon = \mathbf{p}_\epsilon \odot \mathbf{d}_\epsilon \quad \Leftrightarrow \quad \mathbf{w} \odot \mathbf{b} + \mathbf{v} \odot \mathbf{e} = \mathbf{p}_\epsilon. \quad (7.92)$$

In analogy, (iii) yields

$$\mathbf{d}_\epsilon \odot (\text{diag}(\mathbf{b})\mathbf{F}\mathbf{d}_{h_N} + \text{diag}(\mathbf{e})\mathbf{C}\mathbf{d}_{h_N}) = -\mathbf{d}_\epsilon \odot (\text{diag}(\mathbf{p}_{\epsilon \Delta h})\mathbf{A}^T \bar{\mathbf{C}}_h^T \mathbf{d}_{h_N}) \quad (7.93a)$$

$$\Rightarrow \text{diag}(\mathbf{b})\mathbf{F} + \text{diag}(\mathbf{e})\mathbf{C} = -\text{diag}(\mathbf{p}_{\epsilon \Delta h})\mathbf{A}^T \bar{\mathbf{C}}_h^T. \quad (7.93b)$$

Considering (7.93b) and condition (v), which can be rewritten in terms of $\text{diag}(\mathbf{w})\mathbf{C} + \text{diag}(\mathbf{v})\mathbf{F} = -\text{diag}(\mathbf{p}_{\Delta h})\mathbf{A}^T \bar{\mathbf{C}}_h^T$, one can conclude that (also concerning (ii))

$$\mathbf{F} = \text{diag}(\tilde{\mathbf{f}})\mathbf{A}^T \bar{\mathbf{C}}_h^T, \quad \mathbf{C} = \text{diag}(\mathbf{c})\mathbf{A}^T \bar{\mathbf{C}}_h^T \quad (7.94)$$

is the only feasible choice for matrices \mathbf{F}, \mathbf{C} . Conditions (i), (iii), (iv), (v) and (vi) are already independent from the search direction. Under (7.94), (ii) yields $\tilde{\mathbf{f}} \odot \mathbf{c} = \frac{1}{2}\mathbf{p}_{\Delta h^2}$, also leading to $\mathbf{b} \odot \tilde{\mathbf{f}} + \mathbf{e} \odot \mathbf{c} = -\mathbf{p}_{\epsilon \Delta h}$ concerning (iii) or (7.93b). In sum, one receives

$$\begin{aligned}
(i) \quad & \mathbf{b} \odot \mathbf{e} \stackrel{!}{=} \frac{1}{2}\mathbf{p}_{\epsilon^2} \\
(ii) \quad & \mathbf{c} \odot \tilde{\mathbf{f}} \stackrel{!}{=} \frac{1}{2}\mathbf{p}_{\Delta h^2} \\
(iii) \quad & \mathbf{b} \odot \tilde{\mathbf{f}} + \mathbf{c} \odot \mathbf{e} \stackrel{!}{=} -\mathbf{p}_{\epsilon \Delta h} \\
(iv) \quad & \mathbf{b} \odot \mathbf{w} + \mathbf{v} \odot \mathbf{e} \stackrel{!}{=} \mathbf{p}_\epsilon \\
(v) \quad & \mathbf{c} \odot \mathbf{w} + \mathbf{v} \odot \tilde{\mathbf{f}} \stackrel{!}{=} -\mathbf{p}_{\Delta h} \\
(vi) \quad & \mathbf{v} \odot \mathbf{w} \stackrel{!}{=} \bar{\mathbf{f}}_0(\boldsymbol{\alpha})
\end{aligned}$$

this utterly appealing, decoupled form. Considering set (i)-(vi) componentwise, meaning for all its n_ℓ components, it is the equivalent condition-set obtained when factorizing conic (7.76) into (7.77). This can be seen when comparing set (i)-(vi) with condition-set (7.82). Therefore the same requirements for its linear factorization apply. Applying Property 7.14 completes the proof. \blacksquare

In Theorem 7.18 all $\boldsymbol{\alpha}^{(i)}$ along $i \in \mathfrak{M}$ are still unknown. However, in case $\boldsymbol{\alpha}^{(i)} = \mathbf{0} \forall i \in \mathfrak{M}$ the determinant $\Delta_j^{(i)}$ can be calculated. The case $\boldsymbol{\alpha}^{(i)} = \mathbf{0}$ presumably corresponds with $\bar{\mathbf{m}}_k^{(i)} = \mathbf{0}$.

Following Theorem 7.18, by assuming $\Delta_j^{(i)} = 0$ and $\hat{\Delta}_j^{(i)} \leq 0 \forall i \in \mathfrak{M} \wedge j \in \mathfrak{P}$, one takes a closer look on the special case where $n_m = 2 \geq n_{m,\min}$, then (7.89) yields

$$\begin{bmatrix} \mathbf{B}^{(1)} & \mathbf{C}^{(1)} \\ \mathbf{B}^{(2)} & \mathbf{C}^{(2)} \end{bmatrix} \mathbf{d} = - \begin{bmatrix} \mathbf{v}^{(1)} \\ \mathbf{v}^{(2)} \end{bmatrix}, \quad \begin{bmatrix} \mathbf{E}^{(1)} & \mathbf{F}^{(1)} \\ \mathbf{E}^{(2)} & \mathbf{F}^{(2)} \end{bmatrix} \mathbf{d} = - \begin{bmatrix} \mathbf{w}^{(1)} \\ \mathbf{w}^{(2)} \end{bmatrix} \quad (7.95a)$$

$$\begin{bmatrix} \mathbf{B}^{(1)} & \mathbf{C}^{(1)} \\ \mathbf{E}^{(2)} & \mathbf{F}^{(2)} \end{bmatrix} \mathbf{d} = - \begin{bmatrix} \mathbf{v}^{(1)} \\ \mathbf{w}^{(2)} \end{bmatrix}, \quad \begin{bmatrix} \mathbf{E}^{(1)} & \mathbf{F}^{(1)} \\ \mathbf{B}^{(2)} & \mathbf{C}^{(2)} \end{bmatrix} \mathbf{d} = - \begin{bmatrix} \mathbf{w}^{(1)} \\ \mathbf{v}^{(2)} \end{bmatrix} \quad (7.95b)$$

meaning four search directions \mathbf{d} (7.59) may be obtained. This provides that $\mathbf{B}^{(i)}, \mathbf{C}^{(i)}, \mathbf{v}^{(i)}, \mathbf{E}^{(i)}, \mathbf{F}^{(i)}, \mathbf{w}^{(i)}$, which will be referred to as *Tensor Separators*, have been found as a solution of set (i)-(vi).

Corollary 7.19. *Let all assumptions in table 7.1 in addition to Assumption 7.7 hold. Following the necessary and sufficient conditions of Property 7.14, one can deduce the following statements about the number of search directions solving Tensor-Equation (7.45) thus (7.60) for all $i \in \mathfrak{M}$ exactly or at least in approximation:*

1. if $\Delta_j^{(i)}(\boldsymbol{\alpha}^{(i)}) \neq 0$ for any $i \in \mathfrak{M}$ or $j \in \mathfrak{P}$ there exist at most $2^{n_i n_m}$ exact solutions (Bezout's Theorem).
2. if $\Delta_j^{(i)}(\boldsymbol{\alpha}^{(i)}) = 0 \forall i \in \mathfrak{M} \wedge j \in \mathfrak{P}$ there exist at most 2^{n_m} exact solutions and if (additionally)
 - (a) $\hat{\Delta}_j^{(i)} < 0 \forall i \in \mathfrak{M} \wedge j \in \mathfrak{P}$, (7.60) yields precisely 2^{n_m} different linear matrix-equations such as (7.95). As they are over-determined by nature $n_m \geq n_{m,\min}$, precisely 2^{n_m} different \mathbf{d} result when applying, e.g., the pseudo-inverse.
 - (b) $\hat{\Delta}_j^{(i)} = 0 \forall i \in \mathfrak{M} \wedge j \in \mathfrak{P}$ and $\mathbf{v}^{(i)} = \mathbf{w}^{(i)} \forall i \in \mathfrak{M}$, Tensor-Equation (7.60) yields a single linear matrix-equation (e.g. one of (7.95)) over all $i \in \mathfrak{M}$. Given $n_m \geq n_{m,\min}$, there either exists a unique or no exact solution for \mathbf{d} due to linear independency (Assumption 7.1).
 - (c) $\hat{\Delta}_j^{(i)} > 0 \forall j \in \mathfrak{P}$, one obtains \mathbf{d}_ϵ and $\mathbf{d}_{h_N}^{(i)}$ as parts of the search direction \mathbf{d} already when only considering a single measurement-set by solving one of the $i \in \mathfrak{M}$ in (7.60). However, the roughness part \mathbf{d}_ϵ may be incompatible with other measurement-sets in \mathfrak{M} concerning the satisfaction of (7.60).

Corollary 7.19 underlines the difficulty to find a supposedly unique roughness ϵ with growing number of measurements as the number of feasible search directions in each iteration step for solving set (7.7) grows exponentially with the number of measurements n_m .

Theorem 7.20. *Let all assumptions in table 7.1 in addition to Assumption 7.7 hold. Further suppose that $\Delta_j^{(i)}(\boldsymbol{\alpha}^{(i)}) = 0$ and $\hat{\Delta}_j^{(i)} \leq 0 \forall j \in \mathfrak{P}$ in measurement-set $i \in \mathfrak{M}$. Then, Tensor Separators as a solution of set (i) to (vi) appear in pairs and can be found among*

$$ec = \frac{1}{2} \left(-p_{\epsilon\Delta h} \pm_1 \sqrt{p_{\epsilon\Delta h}^2 - p_{\epsilon^2} p_{\Delta h^2}} \right) \quad (7.96a)$$

$$bw = \frac{1}{2} \left(p_{\epsilon} \pm_2 \sqrt{p_{\epsilon}^2 - 2\bar{f}_0 p_{\epsilon^2}} \right) \quad (7.96b)$$

$$\tilde{f}v = \frac{1}{2} \left(-p_{\Delta h} \pm_3 \sqrt{p_{\Delta h}^2 - 2\bar{f}_0 p_{\Delta h^2}} \right) \quad (7.96c)$$

$$b\tilde{f} = \frac{1}{2} \left(-p_{\epsilon\Delta h} \mp_1 \sqrt{p_{\epsilon\Delta h}^2 - p_{\epsilon^2} p_{\Delta h^2}} \right) = \frac{p_{\epsilon^2} p_{\Delta h^2}}{2 \left(-p_{\epsilon\Delta h} \pm_1 \sqrt{p_{\epsilon\Delta h}^2 - p_{\epsilon^2} p_{\Delta h^2}} \right)} \quad (7.96d)$$

$$ev = \frac{1}{2} \left(p_{\epsilon} \mp_2 \sqrt{p_{\epsilon}^2 - 2\bar{f}_0 p_{\epsilon^2}} \right) = \frac{p_{\epsilon^2} \bar{f}_0}{p_{\epsilon} \pm_2 \sqrt{p_{\epsilon}^2 - 2\bar{f}_0 p_{\epsilon^2}}} \quad (7.96e)$$

$$cw = \frac{1}{2} \left(-p_{\Delta h} \mp_3 \sqrt{p_{\Delta h}^2 - 2\bar{f}_0 p_{\Delta h^2}} \right) = \frac{p_{\Delta h^2} \bar{f}_0}{-p_{\Delta h} \pm_3 \sqrt{p_{\Delta h}^2 - 2\bar{f}_0 p_{\Delta h^2}}} \quad (7.96f)$$

presented in scalar form. The current measurement-set index $i \in \mathfrak{M}$ as well as the index along the pipes $j \in \mathfrak{P}$ is not displayed for the sake of readability, e.g. $ec \hat{=} [\mathbf{e}^{(i)} \odot \mathbf{c}^{(i)}]_j$ (7.96a). Solution pair (7.96) has 3 different locations of the \pm sign presented with indices which indicate that there are $2^3 = 8$ possibilities per $j \in \mathfrak{P}$ and $i \in \mathfrak{M}$.

Remark 7.21. *In reference to the solution pairs (7.96) in Theorem 7.20, only those \pm_l combinations concerning $l = 1, 2, 3$ are feasible which satisfy*

$$\begin{aligned} & \left(-p_{\epsilon\Delta h} \pm_1 \sqrt{p_{\epsilon\Delta h}^2 - p_{\epsilon^2} p_{\Delta h^2}} \right) \left(p_{\epsilon} \pm_2 \sqrt{p_{\epsilon}^2 - 2\bar{f}_0 p_{\epsilon^2}} \right) \left(-p_{\Delta h} \pm_3 \sqrt{p_{\Delta h}^2 - 2\bar{f}_0 p_{\Delta h^2}} \right) \\ & \quad = 2p_{\epsilon^2} p_{\Delta h^2} \bar{f}_0. \end{aligned} \quad (7.97)$$

Thereby (7.97) can be considered as multiplication of (i), (ii) and (vi) which subsequently has to equal the multiplication of (7.96a), (7.96b) and (7.96c). According to Theorem 7.18, there exists at least one feasible \pm_l combination per $j \in \mathfrak{P}$ and $i \in \mathfrak{M}$ with respect to $l = 1, 2, 3$ such that (7.97) holds, provided that $\Delta_j^{(i)}(\boldsymbol{\alpha}^{(i)}) = 0$ and $\hat{\Delta}_j^{(i)} \leq 0$ regarding determinants (7.90).

Proof. Analogously to (7.96), partial turbulent-flow derivatives $p_{\mathcal{X}}$ (see (7.21) and (7.54)) with respect to $\mathcal{X} \in \{\epsilon, \epsilon^2, \Delta h, \Delta h^2, \epsilon\Delta h\}$ and b, c, e, \tilde{f}, v, w as well as \bar{f}_0 (for the zero order term) are considered to be scalar temporarily. Using (i), (ii), (vi) to express e, c, v by means of b, \tilde{f}, w (or vice versa) such that

$$(i^*) \quad e = \frac{1}{2} \frac{p_{\epsilon^2}}{b}, \quad b = \frac{1}{2} \frac{p_{\epsilon^2}}{e}$$

$$(ii^*) \quad c = \frac{1}{2} \frac{p_{\Delta h^2}}{\tilde{f}}, \quad \tilde{f} = \frac{1}{2} \frac{p_{\Delta h^2}}{c}$$

$$(vi^*) \quad v = \frac{\bar{f}_0}{w}, \quad w = \frac{\bar{f}_0}{v}$$

one receives three independent quadratic equations in the context of (iii) , (iv) and (v)

$$\begin{aligned} (iii^*) \quad & (ec)^2 + p_{\epsilon\Delta h}ec + \frac{1}{4}p_{\epsilon^2}p_{\Delta h^2} = 0 \\ (iv^*) \quad & (bw)^2 - p_{\epsilon}bw + \frac{1}{2}\bar{f}_0p_{\epsilon^2} = 0 \\ (v^*) \quad & (\tilde{f}v)^2 + p_{\Delta h}\tilde{f}v + \frac{1}{2}\bar{f}_0p_{\Delta h^2} = 0. \end{aligned}$$

The set (i) to (vi) has no solution for individual b, e, \tilde{f}, e, v, w , but one can obtain the pairs

$$\begin{aligned} (iii^*) \quad & ec = \frac{-p_{\epsilon\Delta h} \pm_1 \sqrt{p_{\epsilon\Delta h}^2 - p_{\epsilon^2}p_{\Delta h^2}}}{2} \\ (iv^*) \quad & bw = \frac{p_{\epsilon} \pm_2 \sqrt{p_{\epsilon}^2 - 2\bar{f}_0p_{\epsilon^2}}}{2} \\ (v^*) \quad & \tilde{f}v = \frac{-p_{\Delta h} \pm_3 \sqrt{p_{\Delta h}^2 - 2\bar{f}_0p_{\Delta h^2}}}{2}. \end{aligned}$$

Although the diagonal elements of the *Tensor Separators* appear in pairs, it will be sufficient for the separation of the *Tensor* equation (7.60). The index $l = 1, 2, 3$ of the “ \pm_l ” symbols thereby indicates the location of different signs, resulting in $2^3 = 8$ potential possibilities for the *Tensor Separators* per pipe.

The investigation of the final solution of (7.95) for the case $n_m = 2$ will be helpful to clarify what is actually needed for the separation (7.89) of the *Tensor* equation. Applying the diagonal forms of *Tensor Separators* and (7.94) on the left hand side (7.95a) while multiplying with $\text{diag}([e^{(1)T} \quad e^{(2)T}])$

$$\begin{bmatrix} \text{diag}(e^{(1)} \odot b^{(1)}) & \text{diag}(e^{(1)} \odot c^{(1)})\mathbf{A}^T\bar{\mathbf{C}}_h^T \\ \text{diag}(e^{(2)} \odot b^{(2)}) & \text{diag}(e^{(2)} \odot c^{(2)})\mathbf{A}^T\bar{\mathbf{C}}_h^T \end{bmatrix} \mathbf{d} = - \begin{bmatrix} e^{(1)} \odot v^{(1)} \\ e^{(2)} \odot v^{(2)} \end{bmatrix} \quad (7.98a)$$

the right hand side of (7.95a) while multiplying with $\text{diag}([b^{(1)T} \quad b^{(2)T}])$

$$\begin{bmatrix} \text{diag}(b^{(1)} \odot e^{(1)}) & \text{diag}(b^{(1)} \odot \tilde{f}^{(1)})\mathbf{A}^T\bar{\mathbf{C}}_h^T \\ \text{diag}(b^{(2)} \odot e^{(2)}) & \text{diag}(b^{(2)} \odot \tilde{f}^{(2)})\mathbf{A}^T\bar{\mathbf{C}}_h^T \end{bmatrix} \mathbf{d} = - \begin{bmatrix} b^{(1)} \odot w^{(1)} \\ b^{(2)} \odot w^{(2)} \end{bmatrix} \quad (7.98b)$$

the left hand side of (7.95b) while multiplying with $\text{diag}([e^{(1)T} \quad b^{(2)T}])$

$$\begin{bmatrix} \text{diag}(e^{(1)} \odot b^{(1)}) & \text{diag}(e^{(1)} \odot c^{(1)})\mathbf{A}^T\bar{\mathbf{C}}_h^T \\ \text{diag}(b^{(2)} \odot e^{(2)}) & \text{diag}(b^{(2)} \odot \tilde{f}^{(2)})\mathbf{A}^T\bar{\mathbf{C}}_h^T \end{bmatrix} \mathbf{d} = - \begin{bmatrix} e^{(1)} \odot v^{(1)} \\ b^{(2)} \odot w^{(2)} \end{bmatrix} \quad (7.98c)$$

and the right hand side of (7.95b) while multiplying with $\text{diag}([b^{(1)T} \quad e^{(2)T}])$

$$\begin{bmatrix} \text{diag}(b^{(1)} \odot e^{(1)}) & \text{diag}(b^{(1)} \odot \tilde{f}^{(1)})\mathbf{A}^T\bar{\mathbf{C}}_h^T \\ \text{diag}(e^{(2)} \odot b^{(2)}) & \text{diag}(e^{(2)} \odot c^{(2)})\mathbf{A}^T\bar{\mathbf{C}}_h^T \end{bmatrix} \mathbf{d} = - \begin{bmatrix} e^{(1)} \odot v^{(1)} \\ b^{(2)} \odot w^{(2)} \end{bmatrix} \quad (7.98d)$$

one has to determine the “scalar” terms $eb, ec, ev, b\tilde{f}, bw$ concerning (i) to (vi) . However, as eb (see (i)), ec, bw are already known, only $ev, b\tilde{f}$ and cw need to be found to show (7.96).

Looking for $b\tilde{f}$, one makes use of the first solution of the quadratic equation from before

$e = \frac{1}{2c} \left(-p_{\epsilon\Delta h} \pm_1 \sqrt{p_{\epsilon\Delta h}^2 - p_{\epsilon^2} p_{\Delta h^2}} \right)$ where c is expressed by means of (\mathbf{ii}^*) $c = \frac{1}{2} \frac{p_{\Delta h^2}}{f}$ leading to

$$e = \frac{\tilde{f}}{p_{\Delta h^2}} \left(-p_{\epsilon\Delta h} \pm_1 \sqrt{p_{\epsilon\Delta h}^2 - p_{\epsilon^2} p_{\Delta h^2}} \right) \quad (7.99)$$

which is then inserted into (\mathbf{i}^*) $b = \frac{1}{2e} p_{\epsilon^2}$ yielding in

$$b\tilde{f} = \frac{p_{\epsilon^2} p_{\Delta h^2}}{2 \left(-p_{\epsilon\Delta h} \pm_1 \sqrt{p_{\epsilon\Delta h}^2 - p_{\epsilon^2} p_{\Delta h^2}} \right)}. \quad (7.100)$$

The same result for $b\tilde{f}$ is obtained when using $b\tilde{f} = -p_{\epsilon\Delta h} - ec$ according to (\mathbf{iii}) and applying ec as a result of (\mathbf{iii}^*) , see (7.96d).

Looking for ev , one uses (\mathbf{vi}^*) in terms of $v = \frac{\tilde{f}_0}{w}$ to be inserted in bw such that $b = \frac{v}{2\tilde{f}_0} \left(p_{\epsilon} \pm_2 \sqrt{p_{\epsilon}^2 - 2\tilde{f}_0 p_{\epsilon^2}} \right)$ which is then inserted into (\mathbf{i}^*) yielding

$$ev = \frac{p_{\epsilon^2} \tilde{f}_0}{p_{\epsilon} \pm_2 \sqrt{p_{\epsilon}^2 - 2\tilde{f}_0 p_{\epsilon^2}}}. \quad (7.101)$$

The same result for ev is obtained when using $ev = -p_{\epsilon} - bw$ according to (\mathbf{iv}) and applying bw as a result of (\mathbf{iv}^*) , see (7.96e).

The solution-pairs of equation set (\mathbf{i}) to (\mathbf{vi}) are now summarized in the scalar form (7.96) knowing that $\mathbf{b}, \mathbf{e}, \tilde{\mathbf{f}}, \mathbf{e}, \mathbf{v}, \mathbf{w}$, meaning their element-wise combinations, have length n_{ℓ} actually and have to be considered along the different measurement-sets $1, 2, \dots, n_m$. The determination of pair cw was thereby accomplished analogously to $b\tilde{f}$ and ev .

When inserting pairs (7.96) back into set (\mathbf{i}) to (\mathbf{vi}) , one will have proof that solution (7.96) is only consistent if (7.97) is satisfied. In reference to Remark 7.21, one needs to find a feasible \pm_l combination per $j \in \mathfrak{J}$ and $i \in \mathfrak{M}$ with respect to $l = 1, 2, 3$ where (7.97) holds. ■

7.6.5 The Factorization of a Conic Section as Exemplification

In this section the scalar coefficients A, B, \dots, F denote those which separate conic section (7.76) into linear terms (7.77). Following Theorem 7.20, the factorization (7.77) of the conic section (7.76) can be accomplished by the pairs

$$DB = h \pm_1 \sqrt{h^2 - ab} \quad (7.102a) \quad AE = h \mp_1 \sqrt{h^2 - ab} \quad (7.102d)$$

$$AF = f \pm_2 \sqrt{f^2 - ac} \quad (7.102b) \quad DC = f \mp_2 \sqrt{f^2 - ac} \quad (7.102e)$$

$$EC = g \pm_3 \sqrt{g^2 - bc} \quad (7.102c) \quad BF = g \mp_3 \sqrt{g^2 - bc}. \quad (7.102f)$$

The multiplication of (7.77) with D and B yields

$$\mathfrak{f}(x, y) = \nu(DAx + DBy + DC)(BDx + BEy + BF) = 0 \quad (7.103)$$

where factor $\nu = \frac{1}{DB}$. Pairs $DA = a$ and $BE = b$ are given by (7.82a). Subsequently,

$$\begin{aligned} \mathfrak{f}(x, y) = \nu & \left(ax + \left(h \pm_1 \sqrt{h^2 - ab} \right) y + f \mp_2 \sqrt{f^2 - ac} \right) \\ & \times \left(\left(h \pm_1 \sqrt{h^2 - ab} \right) x + by + g \mp_3 \sqrt{g^2 - bc} \right). \end{aligned} \quad (7.104)$$

Note that this is only possible if and only if $\Delta = 0$ and $\hat{\Delta} \leq 0$ (7.78). From representation (7.104) it is also clear that in case $\hat{\Delta} = 0$ the coefficients of the linear factorization are real if $f^2 \geq ac \wedge g^2 \geq bc$ which is equivalent to the requirement that $f^2 + g^2 \geq c(a + b)$ (Lemma 7.16).

Example. Consider the conic section

$$f(x, y) = 2x^2 + 2y^2 + 5xy - x + y - 1 = 0, \quad (7.105)$$

then one has to determine for which \pm combinations

$$\left(h \pm_1 \sqrt{h^2 - ab}\right) \left(f \pm_2 \sqrt{f^2 - ac}\right) \left(g \pm_3 \sqrt{g^2 - bc}\right) = abc \quad (7.106)$$

holds. Verifying consistency of set (7.82), (7.106) is the multiplication of (7.102a), (7.102b) and (7.102c), i.e. $(DB)(AF)(EC)$, which can also be written in terms of $(AD)(BE)(CF) = abc$ according to (7.82a) (in hindsight on (7.97) for consistency of set (i) to (vi)). In analogy, the multiplication of (7.102d), (7.102e) and (7.102f), i.e. $(AE)(DC)(BF)$, equals $(AD)(BE)(CF) = abc$ reversing all $l = 1, 2, 3$ of \pm_l in (7.106).

Referring to table 7.6, one can see that only “+ + -” and “- - +” are feasible combinations for the conic section (7.105). Note that there is a seeming conflict between Corollary 7.19 and Remark 7.21. In Corollary 7.19 it is said that there is *exactly* one linear factorization if $\Delta = 0$ and $\hat{\Delta} \leq 0$ whereas in Remark 7.21 it is said that there exist possibly more than one \pm_l combinations concerning $l = 1, 2, 3$ to be feasible in terms of (7.106) or (7.97). It will be shown by means of the present example that these combinations result in the identical factorization with different ν (7.103) (which is not always $\frac{1}{DB}$) to be determined only.

$2 \left(h \pm_1 \sqrt{h^2 - ab}\right)$	$2 \left(f \pm_2 \sqrt{f^2 - ac}\right)$	$2 \left(g \pm_3 \sqrt{g^2 - bc}\right)$	$8abc$	\pm_1	\pm_2	\pm_3
$5 \pm_1 3$	$-1 \pm_2 3$	$1 \pm_3 3$	-32			
8	2	4	64	+	+	+
8	2	-2	-32	+	+	-
8	-4	4	-128	+	-	+
8	-4	-2	64	+	-	-
2	2	4	16	-	+	+
2	2	-2	-8	-	+	-
2	-4	4	-32	-	-	+
2	-4	-2	16	-	-	-

TABLE 7.6: Combinations of \pm which factorize conic section (7.105) to preserve consistency of set (7.82).

This becomes apparent when applying the feasible combination “+ + -”

$$\begin{aligned} f(x, y) &= \nu \left(2x + \frac{1}{2}(5 + 3)y + \frac{1}{2}(-1 - 3)\right) \left(\frac{1}{2}(5 + 3)x + 2y + \frac{1}{2}(1 + 3)\right) \\ &= \frac{1}{2}(2x + 4y - 2)(4x + 2y + 2) \end{aligned} \quad (7.107a)$$

as well as the combination “- - +” obtained in table 7.6 on (7.104)

$$\begin{aligned} f(x, y) &= \nu \left(2x + \frac{1}{2}(5 - 3)y + \frac{1}{2}(-1 + 3)\right) \left(\frac{1}{2}(5 - 3)x + 2y + \frac{1}{2}(1 - 3)\right) \\ &= (2x + y + 1)(x + 2y - 1). \end{aligned} \quad (7.107b)$$

7.6.6 Final Observations

The reader shall be reminded at this point that pairs $\mathbf{b} \odot \mathbf{w}, \tilde{\mathbf{f}} \odot \mathbf{v}, \mathbf{e} \odot \mathbf{v}, \mathbf{c} \odot \mathbf{w}$, given by (7.96), comprise $\bar{\mathbf{f}}_0$ which itself is a function on $\boldsymbol{\alpha}$ in the corresponding measurement-set. Those $\boldsymbol{\alpha}^{(i)}$ for $i \in \mathfrak{M} = \{1, 2, \dots, n_m\}$ lie in the nullspace, or kernel, of incidence matrix \mathbf{A} , i.e. $\mathbf{A}\bar{\mathbf{m}}_k^{(i)} = \mathbf{0} \Leftrightarrow \bar{\mathbf{m}}_k^{(i)} - \mathbf{S}^T \boldsymbol{\alpha}^{(i)} = \mathbf{0}$. Applying the proposed solution (7.96) (also using $\mathbf{b} \odot \mathbf{e}^{(i)}$) for all the n_ℓ components of the *Tensor Separators* on the deceptively linear forms (7.98), one will actually recognize that in all 4 representations (7.98) only the right hand sides (those independent from the search direction \mathbf{d}) depend on $\boldsymbol{\alpha}^{(i)}$.

To continue the line of thought, which started with Theorem 7.18, the proposed forms (7.98), solving the degenerate *Tensor Equation* (7.60), can actually be transformed. Taking a closer look at (7.98a) comprising pairs $\mathbf{b}^{(i)} \odot \mathbf{e}^{(i)} = \frac{1}{2} \mathbf{p}_{\epsilon^2}^{(i)}(\mathbf{i})$, $\mathbf{e}^{(i)} \odot \mathbf{c}^{(i)}$ (7.96a) and $\mathbf{e}^{(i)} \odot \mathbf{v}^{(i)}$ (7.96e) in measurement-set i , the $\boldsymbol{\alpha}^{(i)}$ only appear in the numerator of the right hand side (see (7.96e)).

$$\begin{aligned} & \begin{bmatrix} \text{diag}(\mathbf{e}^{(1)} \odot \mathbf{b}^{(1)}) & \text{diag}(\mathbf{e}^{(1)} \odot \mathbf{c}^{(1)}) & & \\ & & \text{diag}(\mathbf{e}^{(2)} \odot \mathbf{b}^{(2)}) & \text{diag}(\mathbf{e}^{(2)} \odot \mathbf{c}^{(2)}) \\ & & & \\ & & & \end{bmatrix} \begin{bmatrix} \mathbf{I} & & & \\ & \mathbf{A}^T \bar{\mathbf{C}}_h^T & & \\ & & \mathbf{I} & \\ & & & \mathbf{A}^T \bar{\mathbf{C}}_h^T \end{bmatrix} \\ & \times \mathbf{d} \stackrel{(7.96e)}{=} -\frac{1}{2} \begin{bmatrix} \mathbf{p}_\epsilon^{(1)} \mp_2^{(1)} \left(\mathbf{p}_\epsilon^{(1)^2} - 2\bar{\mathbf{f}}_0^{(1)} \odot \mathbf{p}_{\epsilon^2}^{(1)} \right)^{\odot 1/2} \\ \mathbf{p}_\epsilon^{(2)} \mp_2^{(2)} \left(\mathbf{p}_\epsilon^{(2)^2} - 2\bar{\mathbf{f}}_0^{(2)} \odot \mathbf{p}_{\epsilon^2}^{(2)} \right)^{\odot 1/2} \end{bmatrix}. \end{aligned} \quad (7.108a)$$

In reference to Remark 7.21 and table 7.6, signs “ \pm ” may also vary along the measurement-sets and potentially along all \mathfrak{P} , i.e. along all components.

Remark 7.22. Please mind that “ $\pm_2^{(i)}$ ” signs utilized in (7.108) can also vary along $j \in \mathfrak{P}$, i.e. along all of the partial derivative’s $[\mathbf{p}_X]_j$ components $\forall j \in \mathfrak{P}$ with respect to $\mathcal{X} \in \{\epsilon, \epsilon^2, \Delta h, \Delta h^2, \epsilon \Delta h\}$. However, only those combinations are feasible which satisfy (7.97) in the corresponding measurement-set $i \in \mathfrak{M}$ and in $j \in \mathfrak{P}$.

Ultimately, this will turn out irrelevant for the next considerations when taking the element-wise square. One can write for the right hand side of (7.98b) (applying (7.96b))

$$-\frac{1}{2} \begin{bmatrix} \mathbf{p}_\epsilon^{(1)} \pm_2^{(1)} \left(\mathbf{p}_\epsilon^{(1)^2} - 2\bar{\mathbf{f}}_0^{(1)} \odot \mathbf{p}_{\epsilon^2}^{(1)} \right)^{\odot 1/2} \\ \mathbf{p}_\epsilon^{(2)} \pm_2^{(2)} \left(\mathbf{p}_\epsilon^{(2)^2} - 2\bar{\mathbf{f}}_0^{(2)} \odot \mathbf{p}_{\epsilon^2}^{(2)} \right)^{\odot 1/2} \end{bmatrix}. \quad (7.108b)$$

This is can be done completely analogously for the mixed terms (7.98c) and (7.98d) by simply changing the \pm_2 signs. Thereby, the $\boldsymbol{\alpha}^{(i)}$ solely appear in the numerator of the right hand side.

The following notation is applied:

$$\begin{aligned} & \mathbf{M}_1 \stackrel{(i) \wedge (7.96a)}{:=} \frac{1}{2} \begin{bmatrix} \text{diag} \left(\mathbf{p}_{\epsilon^2}^{(1)\odot -1/2} \right) & & & \\ & & & \\ & & \text{diag} \left(\mathbf{p}_{\epsilon^2}^{(2)\odot -1/2} \right) & \\ & & & \end{bmatrix} \times \quad (7.109a) \\ & \begin{bmatrix} \text{diag}(\mathbf{e}^{(1)} \odot \mathbf{b}^{(1)}) & \text{diag}(\mathbf{e}^{(1)} \odot \mathbf{c}^{(1)}) & & \\ & & \text{diag}(\mathbf{e}^{(2)} \odot \mathbf{b}^{(2)}) & \text{diag}(\mathbf{e}^{(2)} \odot \mathbf{c}^{(2)}) \\ & & & \\ & & & \end{bmatrix} \begin{bmatrix} \mathbf{I} & & & \\ & \mathbf{A}^T \bar{\mathbf{C}}_h^T & & \\ & & \mathbf{I} & \\ & & & \mathbf{A}^T \bar{\mathbf{C}}_h^T \end{bmatrix} \end{aligned}$$

$$\mathbf{M}_2 \stackrel{(i) \wedge (7.96d)}{:=} \mathbb{2} \begin{bmatrix} \text{diag} \left(\mathbf{p}_{\epsilon^2}^{(1) \odot -1/2} \right) & \\ & \text{diag} \left(\mathbf{p}_{\epsilon^2}^{(2) \odot -1/2} \right) \end{bmatrix} \times \quad (7.109b)$$

$$\begin{bmatrix} \text{diag}(\mathbf{b}^{(1)} \odot \mathbf{e}^{(1)}) & \text{diag}(\mathbf{b}^{(1)} \odot \tilde{\mathbf{f}}^{(1)}) \\ & \text{diag}(\mathbf{b}^{(2)} \odot \mathbf{e}^{(2)}) & \text{diag}(\mathbf{b}^{(2)} \odot \tilde{\mathbf{f}}^{(2)}) \end{bmatrix} \begin{bmatrix} \mathbf{I} & & \\ & \mathbf{A}^T \bar{\mathbf{C}}_h^T & \\ \mathbf{I} & & \mathbf{A}^T \bar{\mathbf{C}}_h^T \end{bmatrix}$$

$$\mathbf{M}_3 \stackrel{(i) \wedge (7.96a) \wedge (7.96d)}{:=} \mathbb{2} \begin{bmatrix} \text{diag} \left(\mathbf{p}_{\epsilon^2}^{(1) \odot -1/2} \right) & \\ & \text{diag} \left(\mathbf{p}_{\epsilon^2}^{(2) \odot -1/2} \right) \end{bmatrix} \times \quad (7.109c)$$

$$\begin{bmatrix} \text{diag}(\mathbf{e}^{(1)} \odot \mathbf{b}^{(1)}) & \text{diag}(\mathbf{e}^{(1)} \odot \mathbf{c}^{(1)}) \\ & \text{diag}(\mathbf{e}^{(2)} \odot \mathbf{b}^{(2)}) & \text{diag}(\mathbf{b}^{(2)} \odot \tilde{\mathbf{f}}^{(2)}) \end{bmatrix} \begin{bmatrix} \mathbf{I} & & \\ & \mathbf{A}^T \bar{\mathbf{C}}_h^T & \\ \mathbf{I} & & \mathbf{A}^T \bar{\mathbf{C}}_h^T \end{bmatrix}$$

$$\mathbf{M}_4 \stackrel{(i) \wedge (7.96a) \wedge (7.96d)}{:=} \mathbb{2} \begin{bmatrix} \text{diag} \left(\mathbf{p}_{\epsilon^2}^{(1) \odot -1/2} \right) & \\ & \text{diag} \left(\mathbf{p}_{\epsilon^2}^{(2) \odot -1/2} \right) \end{bmatrix} \times \quad (7.109d)$$

$$\begin{bmatrix} \text{diag}(\mathbf{b}^{(1)} \odot \mathbf{e}^{(1)}) & \text{diag}(\mathbf{b}^{(1)} \odot \tilde{\mathbf{f}}^{(1)}) \\ & \text{diag}(\mathbf{e}^{(2)} \odot \mathbf{b}^{(2)}) & \text{diag}(\mathbf{e}^{(2)} \odot \mathbf{c}^{(2)}) \end{bmatrix} \begin{bmatrix} \mathbf{I} & & \\ & \mathbf{A}^T \bar{\mathbf{C}}_h^T & \\ \mathbf{I} & & \mathbf{A}^T \bar{\mathbf{C}}_h^T \end{bmatrix}$$

$$\mathbf{s} := \begin{bmatrix} \mathbf{p}_{\epsilon}^{(1)} \odot \mathbf{p}_{\epsilon^2}^{(1) \odot -1/2} \\ \mathbf{p}_{\epsilon}^{(2)} \odot \mathbf{p}_{\epsilon^2}^{(2) \odot -1/2} \end{bmatrix} \quad (7.110)$$

Remark 7.23. The notation applied on (7.109) and (7.110) is only valid for $n_m = 2$ measurement-sets resulting in $2^{n_m} = 4$ different variants of matrix $\mathbf{M}_{\mathfrak{Y}}$ for $\mathfrak{Y} \in \{1, 2, \dots, 2^{n_m}\}$. The difference is only given by varying \pm_1 along all $j \in \mathfrak{P}$ in pairs $[\mathbf{e} \odot \mathbf{c}]_j$ and $[\mathbf{b} \odot \tilde{\mathbf{f}}]_j$. However, notation $\mathbf{M}_{\mathfrak{Y}}$ and \mathbf{s} is also applied for all other n_m considering additional measurement-sets, leading to 2^{n_m} variants concerning \mathfrak{Y} per $j \in \mathfrak{P}$.

Proposition 7.24. Let $\Delta_j^{(i)}(\boldsymbol{\alpha}^{(i)}) = 0$ and $\hat{\Delta}_j^{(i)} \leq 0 \forall j \in \mathfrak{P} \wedge i \in \mathfrak{M}$ concerning (7.90). Knowing that $\mathbf{f}_{k-1} = [\mathbf{f}_{k-1}^{(1)T} \quad \mathbf{f}_{k-1}^{(2)T} \quad \dots \quad \mathbf{f}_{k-1}^{(n_m)T}]^T$ while applying notation (7.109) and (7.110) in reference to Remark 7.23, Tensor Equation (7.60) is equivalent to

$$\frac{1}{2} \begin{bmatrix} \mathbf{A} & & \\ & \ddots & \\ & & \mathbf{A} \end{bmatrix} \left((\mathbf{M}_{\mathfrak{Y}} \mathbf{d})^{\odot 2} + 2\mathbf{M}_{\mathfrak{Y}} \mathbf{d} \odot \mathbf{s} \right) + \mathbf{f}_{k-1} = \mathbf{0} \quad (7.111)$$

for all $\mathfrak{Y} \in \{1, 2, \dots, 2^{n_m}\}$ in Tensor-Method iteration k .

Proof. (7.98) extended to arbitrary n_m can be written as

$$\mathbf{M}_{\mathfrak{y}}\mathbf{d} = - \begin{bmatrix} \mathbf{p}_{\epsilon^2}^{(1)\odot^{-1/2}} \odot \mathbf{p}_{\epsilon}^{(1)} \pm_2^{(1)} \left(\mathbf{p}_{\epsilon^2}^{(1)\odot^{-1}} \odot \mathbf{p}_{\epsilon}^{(1)^2} - 2\bar{\mathbf{f}}_0^{(1)} \right)^{\odot^{1/2}} \\ \vdots \\ \mathbf{p}_{\epsilon^2}^{(n_m)\odot^{-1/2}} \odot \mathbf{p}_{\epsilon}^{(n_m)} \pm_2^{(n_m)} \left(\mathbf{p}_{\epsilon^2}^{(n_m)\odot^{-1}} \odot \mathbf{p}_{\epsilon}^{(n_m)^2} - 2\bar{\mathbf{f}}_0^{(n_m)} \right)^{\odot^{1/2}} \end{bmatrix}. \quad (7.112)$$

whereas the $\pm_2^{(i)}$ sign is actually only valid for the pair $\mathbf{b}^{(i)} \odot \mathbf{w}^{(i)}$. Effectively, this will turn out irrelevant and thus also eligible for pair $\mathbf{e}^{(i)} \odot \mathbf{v}^{(i)}$ after bringing the $\mathbf{p}_{\epsilon^2}^{(i)\odot^{-1/2}} \odot \mathbf{p}_{\epsilon}^{(i)}$ term of (7.112) on the left hand side and then taking the element-wise square (consider Remark 7.22)

$$\left(\mathbf{M}_{\mathfrak{y}}\mathbf{d} + \underbrace{\begin{bmatrix} \mathbf{p}_{\epsilon}^{(1)} \odot \mathbf{p}_{\epsilon^2}^{(1)\odot^{-1/2}} \\ \vdots \\ \mathbf{p}_{\epsilon}^{(n_m)} \odot \mathbf{p}_{\epsilon^2}^{(n_m)\odot^{-1/2}} \end{bmatrix}}_{\mathbf{s}} \right)^{\odot^2} - \mathbf{s}^{\odot^2} = -2 \begin{bmatrix} \bar{\mathbf{f}}_0^{(1)} \\ \vdots \\ \bar{\mathbf{f}}_0^{(n_m)} \end{bmatrix} = -2 \begin{bmatrix} \text{diag}(\mathbf{c}_l) \mathbf{A}^T \mathbf{L}^{-1} \mathbf{f}_{k-1}^{(1)} - \mathbf{S}^T \boldsymbol{\alpha}^{(1)} \\ \vdots \\ \text{diag}(\mathbf{c}_l) \mathbf{A}^T \mathbf{L}^{-1} \mathbf{f}_{k-1}^{(n_m)} - \mathbf{S}^T \boldsymbol{\alpha}^{(n_m)} \end{bmatrix} \quad (7.113)$$

yielding

$$(\mathbf{M}_{\mathfrak{y}}\mathbf{d} + \mathbf{s})^{\odot^2} - \mathbf{s}^{\odot^2} + 2 \underbrace{\begin{bmatrix} \text{diag}(\mathbf{c}_l) \mathbf{A}^T \mathbf{L}^{-1} \mathbf{f}_{k-1}^{(1)} \\ \vdots \\ \text{diag}(\mathbf{c}_l) \mathbf{A}^T \mathbf{L}^{-1} \mathbf{f}_{k-1}^{(n_m)} \end{bmatrix}}_{\mathbf{r}_f} = 2 \begin{bmatrix} \mathbf{S}^T & & \\ & \ddots & \\ & & \mathbf{S}^T \end{bmatrix} \begin{bmatrix} \boldsymbol{\alpha}^{(1)} \\ \vdots \\ \boldsymbol{\alpha}^{(n_m)} \end{bmatrix} \quad (7.114)$$

which ultimately results in

$$\frac{1}{2} (\mathbf{M}_{\mathfrak{y}}\mathbf{d})^{\odot^2} + \mathbf{M}_{\mathfrak{y}}\mathbf{d} \odot \mathbf{s} + \mathbf{r}_f = \begin{bmatrix} \mathbf{S}^T & & \\ & \ddots & \\ & & \mathbf{S}^T \end{bmatrix} \begin{bmatrix} \boldsymbol{\alpha}^{(1)} \\ \vdots \\ \boldsymbol{\alpha}^{(n_m)} \end{bmatrix} \quad (7.115)$$

where all $\boldsymbol{\alpha}^{(i)}$ and the search direction \mathbf{d} are unknown. The projection in the kernel of incidence matrix \mathbf{A} conducted in Theorem 7.18 is now reversed knowing that $\mathbf{A}\mathbf{S}^T \equiv \mathbf{0}$ and that $\mathbf{A}(\text{diag}(\mathbf{c}_l) \mathbf{A}^T \mathbf{L} \mathbf{f}_{k-1}^{(i)}) = \mathbf{f}_{k-1}^{(i)}$ according to Proposition 4.1. Thus (7.115) yields (7.111). ■

Note that $\mathbf{M}_{\mathfrak{y}}$ depends on all the partial derivatives $\mathbf{p}_{\mathcal{X}}^{(i)}$ with respect to $\mathcal{X} \in \{\epsilon, \epsilon^2, \Delta h, \Delta h^2, \epsilon \Delta h\}$ ($\mathbf{b} \odot \mathbf{e}$ in (i) and pair $b\tilde{f}$ in (7.96d) in the scalar case) whereas \mathbf{s} depends on $\mathbf{p}_{\epsilon}^{(i)}$ and $\mathbf{p}_{\epsilon^2}^{(i)}$ for $i = 1, 2, \dots, n_m$.

Proposition 7.25. *Let all Assumptions in table 7.1 hold. Further suppose that $\mathbf{x}_{k-1} = \mathbf{x}^*$ one already converged to the real root \mathbf{x}^* in the previous iteration step $k-1$. Then, the zero-search direction $\mathbf{d} = \mathbf{0}$ is the only solution for (7.111) for all $\mathfrak{y} \in \{1, 2, \dots, 2^{n_m}\}$.*

Proof. As $\mathbf{x}_{k-1} = \mathbf{x}^*$, $\mathbf{f}_{k-1} = \mathbf{f}(\mathbf{x}_{k-1}) = \mathbf{f}(\mathbf{x}^*) = \mathbf{0}$ (7.14) per definition. Subsequently,

$$\begin{bmatrix} \mathbf{A} & & \\ & \ddots & \\ & & \mathbf{A} \end{bmatrix} \left(\mathbf{M}_{\mathfrak{y}}\mathbf{d} \odot (\mathbf{M}_{\mathfrak{y}}\mathbf{d} + 2\mathbf{s}) \right) = \mathbf{0} \quad (7.116)$$

meaning that the search direction $\mathbf{d} = \mathbf{0}$ is a feasible solution of (7.116). As a result, $\boldsymbol{\alpha}^{(i)} = \mathbf{0} \forall i$ in this special case in order for $\mathbf{d} = \mathbf{0}$ to be feasible in $\mathbf{M}_{\mathfrak{y}}\mathbf{d} \odot (\mathbf{M}_{\mathfrak{y}}\mathbf{d} + 2\mathbf{s}) =$

$[\boldsymbol{\alpha}^{(1)T} \mathbf{S} \ \dots \ \boldsymbol{\alpha}^{(n_m)T} \mathbf{S}]^T$ which is formally equivalent to (7.116) (Proposition 3.6). This means that the remaining solutions ought to satisfy $\mathbf{M}_{\mathfrak{Y}} \mathbf{d} = -2\mathbf{s}$ if existent. Knowing that $\mathbf{M}_{\mathfrak{Y}} \in \mathbb{C}^{n_m n_\ell \times (n_\ell + n_m n_{\bar{p}})}$ has more rows than columns which are expected to be linear independent according to Assumption 7.1 as part of table 7.1, there is no \mathbf{d} which solves $\mathbf{M}_{\mathfrak{Y}} \mathbf{d} = -2\mathbf{s}$ exactly. As a result, $\mathbf{d} = \mathbf{0}$ is the unique solution of (7.116). ■

Note that the partial derivatives $\mathbf{p}_{\mathcal{X}}^{(i)} = \mathbf{p}_{\mathcal{X}}(\boldsymbol{\epsilon}, \Delta \mathbf{h}^{(i)})$ with respect to $\mathcal{X} \in \{\epsilon, \epsilon^2, \Delta h, \Delta h^2, \epsilon \Delta h\}$ are functions on $\Delta \mathbf{h}^{(i)}$ and $\boldsymbol{\epsilon}$, whereas $\Delta \mathbf{h}^{(i)} = \mathbf{C}_s \mathbf{h}_s^{(i)} - \mathbf{A}^T (\mathbf{C}_h^T \mathbf{y}_h^{(i)} + \bar{\mathbf{C}}_h^T \mathbf{h}_N^{(i)} + \mathbf{z})$ (7.7b) is considered as a function on $\mathbf{h}_N^{(i)}$ in measurement-set $i \in \mathfrak{M}$.

Corollary 7.26. *Suppose that $[\mathbf{p}_{\mathcal{X}}^{*(i)}]_j = [\mathbf{p}_{\mathcal{X}}(\boldsymbol{\epsilon}^*, \mathbf{h}_N^{*(i)})]_j = p_{\mathcal{X},j}^{*(i)} \ \forall j \in \mathfrak{P} \wedge i \in \mathfrak{M}$ with respect to $\mathcal{X} \in \{\epsilon, \epsilon^2, \Delta h, \Delta h^2, \epsilon \Delta h\}$ in the real root $\mathbf{x}^* = [\boldsymbol{\epsilon}^{*T} \ \mathbf{h}_N^{*(1)T} \ \dots \ \mathbf{h}_N^{*(n_m)T}]^T$. Following Proposition 7.25 and Corollary 7.19 (case 2(b)), one can construct the following argumentum e contrario. As $\mathbf{d} = \mathbf{0}$ is the unique solution if $\mathbf{x}_{k-1} = \mathbf{x}^*$, the only feasible factorization (7.89) of Tensor Equation (7.60) ought to satisfy $\Delta_j^{(i)}(\mathbf{0}) = 0 \wedge \hat{\Delta}_j^{(i)} = 0$ (7.90) and $\mathbf{v}^{(i)}(\boldsymbol{\alpha}^{(i)}) = \mathbf{w}^{(i)}(\boldsymbol{\alpha}^{(i)})$ (compare with (7.95)) with $\boldsymbol{\alpha}^{(i)} = \mathbf{0} \ \forall j \in \mathfrak{P} \wedge i \in \mathfrak{M}$ in the real root \mathbf{x}^* . Hence $\bar{\mathbf{f}}_0 = \mathbf{0}$ (7.91) in \mathbf{x}^* . Subsequently, the sufficient conditions*

$$\begin{aligned} \Delta_j^{(i)} \stackrel{(7.90)}{=} 2p_{\Delta h,j}^{*(i)} p_{\epsilon \Delta h,j}^{*(i)} p_{\epsilon,j}^{*(i)} - p_{\epsilon^2,j}^{*(i)} \left(p_{\Delta h,j}^{*(i)} \right)^2 - p_{\Delta h^2,j}^{*(i)} \left(p_{\epsilon,j}^{*(i)} \right)^2 &= 0 \\ \hat{\Delta}_j^{(i)} \stackrel{(7.90)}{=} \left(p_{\epsilon \Delta h,j}^{*(i)} \right)^2 - p_{\epsilon^2,j}^{*(i)} p_{\Delta h^2,j}^{*(i)} &= 0 \end{aligned} \quad (7.117)$$

$\forall j \in \mathfrak{P} \wedge i \in \mathfrak{M}$ for \mathbf{x}^* solving (7.7) must hold.

Transformation inside of the Kernel. The block diagonal of cycle matrices is denoted by $\mathbf{S}_b = \text{diag}([\mathbf{S}^T \ \dots \ \mathbf{S}^T])$ and $\boldsymbol{\alpha} = [\boldsymbol{\alpha}^{(1)T} \ \dots \ \boldsymbol{\alpha}^{(n_m)T}]^T$, then (7.115) can be rewritten in terms of

$$\frac{1}{2} \left(\begin{bmatrix} \mathbf{M}_{\mathfrak{Y}} & \mathbf{0} \\ \mathbf{0} & \mathbf{I} \end{bmatrix} \begin{bmatrix} \mathbf{d} \\ \boldsymbol{\alpha} \end{bmatrix} \right)^{\odot 2} + \begin{bmatrix} \text{diag}(\mathbf{s}) \mathbf{M}_{\mathfrak{Y}} & -\mathbf{S}_b \end{bmatrix} \begin{bmatrix} \mathbf{d} \\ \boldsymbol{\alpha} \end{bmatrix} + \mathbf{r}_f = \mathbf{0} \quad (7.118)$$

$\forall \mathfrak{Y} \in \{1, 2, \dots, 2^{n_m}\}$ for a arbitrary number of measurement-sets when also accounting for the appropriate extensions in $\mathbf{M}_{\mathfrak{Y}}$ (7.109b) and \mathbf{s} (7.113). In this representation it is visually clear that not only the search direction \mathbf{d} but also $\boldsymbol{\alpha}$ is unknown.

Proposition 7.27. *With the assumption that there exists a perfect inversion of $\tilde{\mathbf{M}} = [\text{diag}(\mathbf{s}) \mathbf{M}_{\mathfrak{Y}} \ -\mathbf{S}_b]$ such that $\tilde{\mathbf{M}}^{\#} \tilde{\mathbf{M}} = \mathbf{I}$ with a generalized inverse $\tilde{\mathbf{M}}^{\#}$, one can transform the problem (7.118) to unknowns $\boldsymbol{\beta} = \mathbf{M}_{\mathfrak{Y}} \mathbf{d}$ solving*

$$\mathbf{W} \boldsymbol{\beta}^{\odot 2} + 2\boldsymbol{\beta} + 2\mathbf{W} \mathbf{r}_f = \mathbf{0} \quad (7.119)$$

where $\mathbf{W} = \begin{bmatrix} \mathbf{M}_{\mathfrak{Y}} & \mathbf{0} \end{bmatrix} \tilde{\mathbf{M}}^{\#}$. However, if one is able to obtain a $\boldsymbol{\beta}$ satisfying (7.119), one simultaneously solves (7.118) and thus (7.111) with

$$\begin{bmatrix} \mathbf{d} \\ \boldsymbol{\alpha} \end{bmatrix} = -\tilde{\mathbf{M}}^{\#} \left(\frac{1}{2} \boldsymbol{\beta}^{\odot 2} + \mathbf{r}_f \right). \quad (7.120)$$

Proof. Denoting $\tilde{M}[\mathbf{d}^T \ \boldsymbol{\alpha}^T]^T = \mathbf{y}$, (7.118) yields

$$\left(\underbrace{\begin{bmatrix} M_{2y} & \mathbf{0} \end{bmatrix} \tilde{M}^\# \mathbf{y}}_{\mathbf{W}} \right)^{\odot 2} + 2\mathbf{y} + 2\mathbf{r}_f = \mathbf{0}. \quad (7.121)$$

With the aim to transform the problem to unknowns $\boldsymbol{\beta} = \mathbf{W}\mathbf{y} = \begin{bmatrix} M_{2y} & \mathbf{0} \end{bmatrix} [\mathbf{d}^T \ \boldsymbol{\alpha}^T]^T = M_{2y}\mathbf{d}$, (7.121) is multiplied with \mathbf{W} from the left resulting in $\mathbf{W}\boldsymbol{\beta}^{\odot 2} + 2\boldsymbol{\beta} + 2\mathbf{W}\mathbf{r}_f = \mathbf{0}$. Matrix \mathbf{W} does certainly not have full rank in this context. Provided that a $\boldsymbol{\beta}$ satisfying (7.119) has been found, one reformulates (7.121), which is equivalent to $\boldsymbol{\beta}^{\odot 2} + 2\mathbf{y} + 2\mathbf{r}_f = \mathbf{0}$. Knowing that $\mathbf{y} = \tilde{M}[\mathbf{d}^T \ \boldsymbol{\alpha}^T]^T$ one receives (7.120). Keep in mind that this is only feasible if a transformation $\mathbf{y} = \tilde{M}[\mathbf{d}^T \ \boldsymbol{\alpha}^T]^T \Leftrightarrow [\mathbf{d}^T \ \boldsymbol{\alpha}^T]^T = \tilde{M}^\# \mathbf{y}$ satisfying $\tilde{M}^\# \tilde{M} = \mathbf{I}$ is found. ■

Conclusion and Personal Note. In conclusion to the attempt to find explicit solutions for the *Tensor Equation*, the author believes that the applied methods using the *Hadamard* product for the separation of terms, in reference to Theorem 7.18, are well suited to develop an algorithm for solving (7.7)-type problems which converges faster and more reliably than the standard *Newton-Raphson* type approach, and potentially provides multiple solutions for the search direction. For the attentive reader, algorithms solving quadratic equations, also similar to (7.111) or (7.119), filled the PhD thesis of Poloni [2010] underling the difficulty of the subject. Nevertheless, such an algorithm was not developed in the time allocated for this thesis, but the author believes the presented methodologies in sections 7.6.4 to 7.6.6 to be interesting for further analysis.

Alternatively to the *Tensor-Method*, it would be interesting to apply *Halley's* method [Cuyt and Rall, 1985] on (7.7)-type problems as it also applies second order derivatives to obtain a search direction for solving nonlinear systems of equations iteratively.

Algorithm 3 Modification of Algorithm 1 applying *Tensor Equation* (7.60)

```

procedure TENSOR(FUN,  $\mathbf{x}_0$ )
  It is identical to NEWTON(FUN,  $\mathbf{x}_0$ ) except two changes (a,b). ▷ Algorithm 1
  ▷ (a,b) REPLACE ALGORITHM-LINES 5, 10 ON PAGE 93 WITH:
   $\Delta \mathbf{x}_k \leftarrow \mathbf{d}$  ▷ (7.59) as a (approximated) solution of (7.60)
  ▷ solving (7.60) iteratively by means of, e.g., “ $\mathbf{d} = \text{fsolve}((7.60), (7.125), \mathbf{d}_0)$ ”, take
   $\mathbf{d}_0 \leftarrow -0.1 \times (\mathbf{J}_k^T \mathbf{J}_k)^{-1} \mathbf{J}_k^T \mathbf{f}_k$  ▷ as initial value
end procedure

```

Modification of Algorithm 2. A considerably small modification of Algorithm 2 turned out to be particularly well received in combination with Algorithm 3 when solving (7.7)-type problems. This modification only concerns the variation of roughness values in each iteration of Algorithm 2, where only those roughnesses which exceeding the 5% mark of the corresponding pipes’ diameter were varied.

Algorithm 4 Modification of Algorithm 2 launching Algorithm 1 or 3 effectively

```

procedure TENSORCALIBRATION(FUN,  $\mathbf{x}_0$ , TensorMethod)
  ▷ Input variable “TensorMethod” is true if the Tensor Method (section 7.6) is applied.
  It is identical to NETCALIBRATION(FUN,  $\mathbf{x}_0$ ) with one addition (a) ▷ Algorithm 2
  and one change (b).
  ▷ (a) ADD BETWEEN ALGORITHM-LINE 9 AND 10 ON PAGE 95:
  find  $[\bar{i}_1 \ \bar{i}_2 \ \dots \ \bar{i}_{\bar{n}_\epsilon}]$  such that  $[\mathbf{x}^+]_{i \in \mathfrak{P}} = \epsilon_i \leq 0.05 d_i \Rightarrow n_\epsilon + \bar{n}_\epsilon = n_\ell$ 
   $[\mathbf{x}_0]_i \leftarrow [\mathbf{x}_0]_i + \text{normal}(0, 0.0005 d_i)$  for  $i = \bar{i}_1, \bar{i}_2, \dots, \bar{i}_{\bar{n}_\epsilon}$ 
  ▷ (b) REPLACE FUNCTION CALL IN ALGORITHM-LINE 2 ON PAGE 95 with:
  if TensorMethod is true then
  |  $[\mathbf{x}^+, \mathbf{f}^+] \leftarrow \text{TENSOR}(\text{FUN}, \mathbf{x}_0)$  ▷ call Algorithm 3
  else
  |  $[\mathbf{x}^+, \mathbf{f}^+] \leftarrow \text{NEWTON}(\text{FUN}, \mathbf{x}_0)$  ▷ call Algorithm 1
  end if
end procedure

```

When also varying (although less aggressively) those roughness values in \mathbf{x}^+ , used for the initial value \mathbf{x}_0 in the next iteration, which do *not* exceed the 5% mark of the corresponding pipe’s diameter d_i ³ improvements with regard to convergence have been noticed. In this context, a normal distribution with zero mean and a standard deviation of 0.05% = 0.0005 of the pipe’s diameter is applied.

Also, one has to specify whether to use the *Tensor Method* (section 7.6) or the original *Newton-Raphson* (section 7.4) method to determine the search direction by adding an additional input variable denoted with “TensorMethod” which is either **true** or **false**.

Configuration concerning Table 7.8. The same configuration which was applied for the illustrative example in section 7.5 is used. This means that the initial values (7.42) with the physical range of the not-measured pressure heads (7.41) are used whereas loading conditions (concerning \mathbf{q} , \mathbf{y}_h and \mathbf{h}_s) can be found in table 7.3. Calibrating the 3-cycle network in figure 7.1, the author uses

- a fixed number of 13 launches of Algorithm 4 in the outer loop which-

³Please do not confuse the pipe’s diameter d_i of pipe $i \in \mathfrak{P}$ with the search direction \mathbf{d} .

- launches Algorithm 3 (i.e. “TensorMethod = **true**”) 50 times each (fixed number).

In each of these 50 calls of Algorithm 3, (7.7) is attempted to solve with the *Tensor Method*, resulting in a total of $13 \times 50 = 650$ solving attempts of (7.7) with different initial conditions each. The best (concerning the smallest $v(\mathbf{x}^+)$ (7.24)) among those 50 launches, denoted by \mathbf{x}^+ can be found in table 7.8.

Configuration concerning Table 7.9. The same initial conditions, loading parameters etc. are applied as before. The only difference concerns Algorithm 4 which now calls Algorithm 1 (i.e. input variable “TensorMethod = **false**”) 50 times. For clarification, the 3-cycle network in figure 7.1 is calibrated with

- a fixed number of 13 launches of Algorithm 4 in the outer loop which
- launches Algorithm 1 (i.e. “TensorMethod = **false**”) 50 times each (fixed number).

Important to note is that for Algorithm 1 a scaling of \mathbf{x}_k in reference to Remark 7.9 and 7.10 is conducted although not specifically indicated in Algorithm 1. This is contrary to Algorithm 3 which does not scale \mathbf{x}_k due to the necessity to solve the nonlinear *Tensor Equation*.

Row Notation. The following applies to both tables 7.8 and 7.9. The row denoted with “iter of \mathbf{x}^+ ” indicates the iteration among the 50 (calling either Algorithm 3 for table 7.8, or Algorithm 1 for table 7.9) where the intermediate best result \mathbf{x}^+ concerning Algorithm 4 was obtained.

Concerning the last row, denoted with “average # iter to \mathbf{x}^+ ”, the author took the mean along iterations of Algorithm 4 of the number of iterations needed in Algorithm 3 and 1 (algorithm-line 14 on page 93) to converge or abort until \mathbf{x}^+ is obtained. For instance, for the 3rd entry in table 7.8 in row “average # iter to \mathbf{x}^+ ” it took 5 iterations of Algorithm 4 to obtain \mathbf{x}^+ , in these 5 runs Algorithm 3 took

run	1	2	3	4	5
# Algorithm 3 iterations	4	23	14	3	1

TABLE 7.7: Number of iterations of Algorithm 3 to converge or abort concerning the 3rd column of table 7.8. Iteration variable can be found in algorithm-line 14 on page 93.

iterations respectively to converge or abort. The 3rd entry (meaning the 3rd column) in table 7.8 in row “average # iter to \mathbf{x}^+ ”, for instance, is then the mean over the values

$$9.00 = \frac{1}{5} (4 + 23 + 14 + 3 + 1). \quad (7.126)$$

The same methodology was applied for the row “average # iter to \mathbf{x}^+ ” in table 7.9.

Colored Table Entries and Range. Blue colored entries in table 7.8 and 7.9 indicate that the corresponding result left the physical relevant range. Thereby, only roughness values occasionally left the 5% mark of the corresponding pipe’s diameter. In this context all \mathbf{x}_{h_N} , meaning the subset of non-measured pressure heads in the solution, remained in their physically relevant range. The olive-colored results highlight the \mathbf{x}^+ of those launches which have the smallest $v(\mathbf{x}^+)$ in the entire table.

launch	1	2	3	4	5	6	7	8	9	10	11	12	13	\mathbf{x}^*
ϵ_1	1.969	1.977	1.946	2.091	1.955	1.943	1.925	1.954	1.963	1.988	1.974	1.375	1.923	2.000
ϵ_2	1.839	1.816	1.906	1.498	1.879	1.914	1.968	1.881	1.856	1.784	1.824	3.878	1.976	1.750
ϵ_3	1.583	1.561	1.645	1.270	1.619	1.651	1.700	1.622	1.597	1.532	1.569	3.478	1.708	1.500
ϵ_4	1.180	1.177	1.187	1.128	1.186	1.190	1.196	1.184	1.182	1.171	1.178	1.333	1.196	1.250
ϵ_5	1.037	1.041	1.028	1.111	1.029	1.023	1.016	1.032	1.034	1.049	1.040	0.864	1.016	1.000
ϵ_6	0.817	0.818	0.806	0.806	0.826	0.829	0.822	0.804	0.822	0.808	0.818	0.722	0.811	0.750
ϵ_7	0.497	0.498	0.502	0.544	0.486	0.480	0.482	0.506	0.491	0.511	0.498	0.483	0.491	0.500
ϵ_8	0.235	0.235	0.234	0.241	0.235	0.234	0.233	0.234	0.235	0.236	0.235	0.217	0.233	0.250
$h_{N,1}^{(1)}$	93.154	93.141	93.191	92.961	93.176	93.195	93.224	93.177	93.163	93.123	93.146	94.157	93.228	93.104
$h_{N,5}^{(1)}$	90.885	90.885	90.885	90.884	90.885	90.885	90.885	90.885	90.885	90.885	90.885	90.886	90.885	90.885
$h_{N,1}^{(2)}$	88.621	88.599	88.682	88.298	88.657	88.689	88.737	88.660	88.636	88.570	88.607	90.291	88.744	88.538
$h_{N,5}^{(2)}$	84.846	84.846	84.846	84.845	84.846	84.846	84.846	84.846	84.846	84.846	84.846	84.847	84.846	84.846
$h_{N,1}^{(3)}$	82.942	82.909	83.033	82.458	82.996	83.044	83.116	83.000	82.964	82.865	82.921	85.448	83.128	82.818
$h_{N,5}^{(3)}$	77.280	77.280	77.280	77.279	77.280	77.280	77.280	77.280	77.280	77.280	77.280	77.282	77.280	77.280
$v(\mathbf{x}^+) \times 10^7$	0.484	0.637	0.655	1.067	0.547	0.569	0.690	0.669	0.553	0.553	0.532	0.770	0.710	1.082
iter of \mathbf{x}^+	29	10	5	45	23	6	49	27	50	42	20	42	34	
average # iter to \mathbf{x}^+	3.79	8.30	9.00	7.16	7.91	10.67	8.55	6.37	3.90	4.31	8.25	9.55	9.97	

TABLE 7.8: TENSOR-RESULTS.

Results of Algorithm 4 along 13 launches calibrating the 3-cycle network (figure 7.1). Thereby Algorithm 4 calls Algorithm 3 (“TensorMethod=**true**”) for a fixed number of 50 times by tightening ϵ_f and ϵ_x in line 6 on page 95 (belonging to Algorithm 4) appropriately. Roughnesses $\epsilon_i \forall i \in \mathfrak{P}$ are presented in mm, whereas pressure heads $h_{N,j}^{(i)} \forall i \in \mathfrak{M} \wedge j \in \bar{\mathcal{P}}$ are presented in m. Computational duration: 1310.185976s.

launch	1	2	3	4	5	6	7	8	9	10	11	12	13	\mathbf{x}^*
ϵ_1	1.273	1.266	1.254	2.007	2.004	2.004	1.270	2.004	2.004	1.273	2.004	1.268	2.019	2.000
ϵ_2	4.277	4.302	4.329	1.723	1.734	1.732	4.294	1.732	1.733	4.277	1.732	4.300	1.677	1.750
ϵ_3	3.873	3.906	3.973	1.487	1.495	1.496	3.876	1.495	1.496	3.872	1.496	3.883	1.472	1.500
ϵ_4	1.360	1.344	1.262	1.220	1.231	1.220	1.420	1.221	1.224	1.363	1.218	1.420	1.121	1.250
ϵ_5	0.827	0.827	0.838	1.001	0.997	1.002	0.803	1.000	0.999	0.826	1.002	0.800	1.043	1.000
ϵ_6	0.698	0.724	0.792	0.761	0.759	0.761	0.670	0.760	0.761	0.697	0.761	0.670	0.865	0.750
ϵ_7	0.473	0.484	0.507	0.497	0.496	0.497	0.457	0.497	0.496	0.473	0.497	0.458	0.523	0.500
ϵ_8	0.226	0.232	0.251	0.263	0.262	0.263	0.238	0.263	0.262	0.227	0.264	0.239	0.249	0.250
$h_{N,1}^{(1)}$	94.342	94.355	94.376	93.093	93.098	93.098	94.347	93.097	93.098	94.342	93.098	94.350	93.075	93.104
$h_{N,5}^{(1)}$	90.886	90.886	90.886	90.885	90.885	90.885	90.886	90.885	90.885	90.886	90.885	90.886	90.885	90.885
$h_{N,1}^{(2)}$	90.598	90.621	90.655	88.519	88.528	88.527	90.607	88.526	88.527	90.598	88.527	90.612	88.488	88.538
$h_{N,5}^{(2)}$	84.848	84.848	84.848	84.846	84.846	84.846	84.848	84.846	84.846	84.848	84.846	84.848	84.846	84.846
$h_{N,1}^{(3)}$	85.910	85.943	85.995	82.789	82.802	82.801	85.923	82.800	82.802	85.909	82.801	85.931	82.743	82.818
$h_{N,5}^{(3)}$	77.283	77.283	77.284	77.281	77.281	77.281	77.283	77.281	77.281	77.283	77.281	77.283	77.281	77.280
$v(\mathbf{x}^+) \times 10^6$	16.361	9.826	10.342	17.003	12.034	15.932	15.785	16.376	14.440	15.690	17.275	16.439	10.889	0.108
iter of \mathbf{x}^+	15	11	36	8	15	13	5	6	22	40	44	12	8	
average # iter to \mathbf{x}^+	11.00	27.09	123.56	264.25	13.33	253.38	216.80	243.50	63.91	140.40	241.89	12.25	16.25	

TABLE 7.9: NEWTON-RESULTS.

Results of Algorithm 4 along 13 launches calibrating the 3-cycle network (figure 7.1). Thereby Algorithm 4 calls Algorithm 1 (“TensorMethod=**false**”) for a fixed number of 50 times by tightening ϵ_f and ϵ_x in line 6 on page 95 (belonging to Algorithm 4) appropriately. Roughnesses $\epsilon_i \forall i \in \mathfrak{P}$ are presented in mm, whereas pressure heads $h_{N,j}^{(i)} \forall i \in \mathfrak{M} \wedge j \in \bar{\mathcal{P}}$ are presented in m. Computational duration: 157.195594s.

Discussion. When comparing the residuals $v(\mathbf{x}^+)$ of table 7.8 and 7.9 it is abundantly clear that the *Tensor-Results* are significantly better than the *Newton-Results* in terms of $v(\mathbf{x}^+)$. This is particularly true when considering that every single result \mathbf{x}^+ in table 7.8 has a smaller residual than the actual root \mathbf{x}^* , whereas all of the results in table 7.9 have a residual $v(\mathbf{x}^+)$ which is approximately two orders of magnitude larger than $v(\mathbf{x}^*)$.

Also, the number of iterations needed for Algorithm 3 to converge or abort is on average only a fraction of the number of “*Newton steps*”, meaning the numbers of iterations needed for Algorithm 1 to converge or abort. This can be seen when comparing the row “average # iter to \mathbf{x}^+ ” of the both above tables. With that being said it should be emphasized that since the *Tensor Equation* (7.60) is solved iteratively with the MATLAB built-in *fsolve(.)* function, it takes several times longer to finish the computation of *Tensor-Results* (table 7.8) compared to the *Newton-Results* (table 7.9).

While the *Tensor-Results* are certainly superior to the *Newton-Results* in terms of the residual $v(\mathbf{x}^+)$, one will recognize that when comparing the results of, for instance, launch $\{4, 5, 6, 8, 9\}$ in table 7.9 to *Tensor-Results*, the deviation of *Newton-Results* \mathbf{x}^+ to \mathbf{x}^* is visibly smaller. In opinion of the author, there are two possible explanations for this. First, the scaling interferes with the results leading to numerical inaccuracies (Remark 7.9 and 7.10). Second, the $n_m = 3$ measurement-sets are not sufficiently independent from each other in order for the real root \mathbf{x}^* to be properly distinguished in the solution space (in reference to Assumption 7.1). The truth presumably lies somewhere in between these two explanations.

One observation is particularly eye-catching, the *Tensor-Results* tend to remain in their physical range (in terms of roughnesses) whereas *Newton-Results* tend to leave it. Interestingly, roughnesses in *Newton-Results* or even in *Tensor-Results* which exceed their physical limit are always those which are connected to pipe 1 (Q_1 in figure 7.1) which really has a chosen relative roughness of $\epsilon_1/d_1 = 5\%$ (meaning it was placed at the 5% boundary intentionally). Therefore, the results consistently locate node $k = 1$ (see figure 7.1) which is adjacent to the pipe with the highest roughness. Due to this observation, the author expects the presented roughness scheme to be eligible for leak localization and detection, although simulations and real-world test are yet to be made.

Transitional Water Flow in Steady-State

The relieve of Assumption 7.7 for the set-up of a (7.7)-like problem requires to extend the explicit flow description, as in (7.5) for the turbulent regime, to laminar and transitional flow. At this point, set (7.7) can already be extended to also consider laminar flow. However, as the transitional flow, i.e. $2000 < Re < 4000$, is unknown, one would need to identify which pipe flow in \mathfrak{P} in which measurement-set $i \in \mathfrak{M}$ is laminar or turbulent a priori. This is a supposedly impossible endeavor.

In order to let the calibration algorithm itself decide if an appropriate pipe flow has been laminar or turbulent, a continuous and smooth description in between is needed. More specific, to let this description be compatible with the numerical solving of a (7.7)-type problem by means of *Newton-Raphson's* algorithm or the *Tensor-Method*, the smoothness on both boundaries is essential. Although there exist a variety of different formulae interpolating this transitional area, none of them satisfies the turbulent boundary or gradient in terms of the *Colebrook-White* flow (7.5) to a sufficient degree of detail. Besides, the transitional pipe friction is (as far as the author is aware) exclusively expressed in terms of the head loss and not the flow. For instance, the inversion of expression (2.8) embedded in the calculation of λ_{DW} (2.4) for the transitional flow is indeed non-trivial and, perhaps, has even no unique solution.

Ultimately, the derivation of a sufficiently smooth interpolation between laminar- and the turbulent *Colebrook-White* flow will not only enable the roughness-calibration problem description to be completed, but will give useful physical insight in this mystical area which tends to “*defy theoretical treatment*”. As a remark, the content of chapter 8 was accepted for journal publication [Kaltenbacher et al., 2020] at the time of writing.

8.1 Notation

Concerning notation, the author does neglect the network numbering with regards to pipe flows \mathfrak{P} and measurement-sets \mathfrak{M} to support readability in this chapter. This means that Δh denotes the pipe head loss, d its diameter, A its cross section area, l its length, ϵ the pipe's roughness, λ the friction factor, ρ the water density, η the water viscosity and $g \approx 9.81 \text{ m/s}^2$ the gravitational acceleration.

Let Assumption 7.4 hold. Then, one receives proportionality factor $w = \frac{1}{32} \frac{\rho}{\eta} \frac{d^2 g A}{l}$ by using (2.5) and (2.4) for the laminar flow $Q = w \Delta h$. Also applying the *Colebrook-White* flow $f_t(\epsilon, \Delta h)$ (7.5), the steady-state flow through the pipe can be specified

$$Q(\epsilon, \Delta h) = \text{sign}(\Delta h) \begin{cases} w|\Delta h| & Re \leq 2000 \\ \gamma(\epsilon, |\Delta h|) & 2000 < Re < 4000 \\ f_t(\epsilon, |\Delta h|) & Re \geq 4000 \end{cases} \quad (8.1)$$

along the flow regime separation. The major contribution of this chapter is the development of γ (8.1) within laminar and turbulent boundary.

Remark 8.1. For the sake of readability the absolute sign of the head loss Δh is omitted in the sections below meaning that only non-negative Δh values are considered. This is feasible as (2.4) and thus (8.1) is an odd function with respect to Δh , i.e. $Q(\epsilon, -\Delta h) = -Q(\epsilon, \Delta h)$.

8.2 Transitional - Turbulent Boundary

Before aiming to develop a smooth interpolation γ for (8.1), a proper description of the curve at the turbulent boundary $\Delta h = q(\epsilon)$ or $\epsilon = q^{-1}(\Delta h)$ with function $q(\cdot)$ ¹ involving boundary flow $a = 4000 \frac{A\eta}{\rho d}$ such that

$$a \approx f_t(\epsilon, q(\epsilon)) = f_t(q^{-1}(\Delta h), \Delta h) \quad (8.2)$$

is needed. The exact form of the boundary curve, denoted by $\epsilon = f_a(\Delta h) \Rightarrow f_t(f_a(\Delta h), \Delta h) = a$

$$\epsilon = 3.7d \exp \left(-a \frac{\ln 10}{2} \sqrt{\frac{k}{\Delta h}} \right) - 9.287 \frac{\eta A}{\rho} \sqrt{\frac{k}{\Delta h}} =: f_a(\Delta h) \quad (8.3)$$

has no explicit representation $\Delta h = f_a^{-1}(\epsilon)$. With the purpose to approximate (8.3), the following ansatz

$$\Delta h = q(\epsilon) = (q_0(\epsilon + q_1))^{4/7} \quad (8.4)$$

with parameters q_0, q_1 turned out to be effective over the entire tested range of l, d values considering that the relative roughness ϵ/d is only specified between 0% and 5% in the *Moody-Diagram* (figure 2.2). Considering the integral mean error

$$E(1/q_0, q_1) := \frac{1}{d^2} \int_{\underline{\Delta h}}^{\overline{\Delta h}} \left(f_a(\Delta h) - \left(\frac{\Delta h^{7/4}}{q_0} - q_1 \right) \right)^2 d\Delta h \quad (8.5)$$

with lower limit $f_a(\underline{\Delta h}) = 0$ and upper limit $f_a(\overline{\Delta h}) = 0.05d$ to be calculated numerically, parameters q_0, q_1 are determined by finding a solution for

$$\frac{\partial E}{\partial(1/q_0)} = 0 \quad \frac{\partial E}{\partial q_1} = 0. \quad (8.6)$$

Proposition 8.2. Error function $E(1/q_0, q_1)$ is convex (proven in Appendix C).

By calculating n values of $\mathbf{v} = [f_a(\underline{\Delta h}) \quad f_a(\underline{\Delta h} + u) \quad f_a(\underline{\Delta h} + 2u) \quad \dots \quad f_a(\overline{\Delta h})]^T$ with $u = (\overline{\Delta h} - \underline{\Delta h})/n$ and $\mathbf{u} = [\underline{\Delta h}^{7/4} \quad (\underline{\Delta h} + u)^{7/4} \quad (\underline{\Delta h} + 2u)^{7/4} \quad \dots \quad \overline{\Delta h}^{7/4}]^T$ the discretized optimization problem

$$\min_{1/q_0, q_1} \frac{1}{d^2} \left(\mathbf{v} - \left(\frac{1}{q_0} \mathbf{u} - q_1 \mathbf{1} \right) \right)^T \left(\mathbf{v} - \left(\frac{1}{q_0} \mathbf{u} - q_1 \mathbf{1} \right) \right) = \min_{1/q_0, q_1} F(1/q_0, q_1) \quad (8.7)$$

utilizing $\mathbf{1} = [1 \quad 1 \quad \dots \quad 1]^T$ can be solved explicitly. Equation system $\frac{\partial F}{\partial(1/q_0)} = 0, \frac{\partial F}{\partial q_1} = 0$ leads to the following solution

$$\begin{bmatrix} 1/q_0 \\ q_1 \end{bmatrix} = \frac{1}{n\mathbf{u}^T \mathbf{u} - (\mathbf{u}^T \mathbf{1})^2} \begin{bmatrix} n & \mathbf{u}^T \mathbf{1} \\ \mathbf{u}^T \mathbf{1} & \mathbf{u}^T \mathbf{u} \end{bmatrix} \begin{bmatrix} \mathbf{v}^T \mathbf{u} \\ -\mathbf{v}^T \mathbf{1} \end{bmatrix} \quad \text{if } n\mathbf{u}^T \mathbf{u} \neq (\mathbf{u}^T \mathbf{1})^2. \quad (8.8)$$

¹Please do not confuse function $q(\cdot)$ or parameters q_0 and q_1 with the consumption in other chapters.

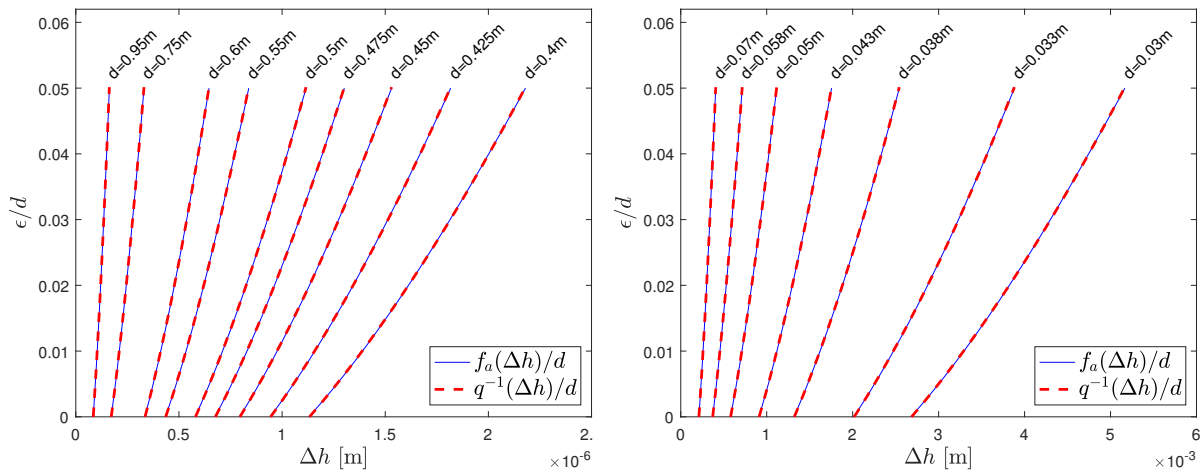


FIGURE 8.1: Curve on the transitional-turbulent boundary for a pipe length of $l = 2\text{m}$ and different pipe diameters, left for some $d \in [0.4, 0.95]\text{m}$ and right for $d \in [0.03, 0.07]\text{m}$.

Corollary 8.3. *Given Proposition 8.2 and a sufficiently large n , result (8.8) is the global minimum of optimization problem (8.7) and, effectively, the solution of (8.6) as $\lim_{n \rightarrow \infty} \frac{1}{n} F(1/q_0, q_1) = \frac{1}{(\Delta h - \underline{\Delta h})} E(1/q_0, q_1)$.*

Figure 8.1 shows that the chosen $q(\epsilon)$ manages to describe the transitional-turbulent boundary exceptionally well with no visible distinction to the exact $f_a(\Delta h)$. Thorough testing for different l, d values with particular attention to $l \in [0.1, 100]\text{m}$ and $d \in [0.001, 1]\text{m}$ suggests that this holds for all physical relevant values since the author did *not* find any parameter combination (length, diameter, temperature) where ansatz (8.4) did *not* sufficiently match $f_a(\Delta h)$.

Figure 8.2 shows the three-dimensional distribution of parameters q_0, q_1 over the pipe's diameter and length. One can see that q_1 actually solely depends on the pipe's diameter, whereas q_0 features a very steep slope over the diameter. The accuracy of the approximation $\epsilon = q^{-1}(\Delta h)$ (of $\epsilon = f_a(\Delta h)$) for all q_0, q_1 plotted in figure 8.2 thereby remains unchanged (referring to figure 8.1) regardless of l, d and, remarkably, regardless of η, ρ (not displayed).

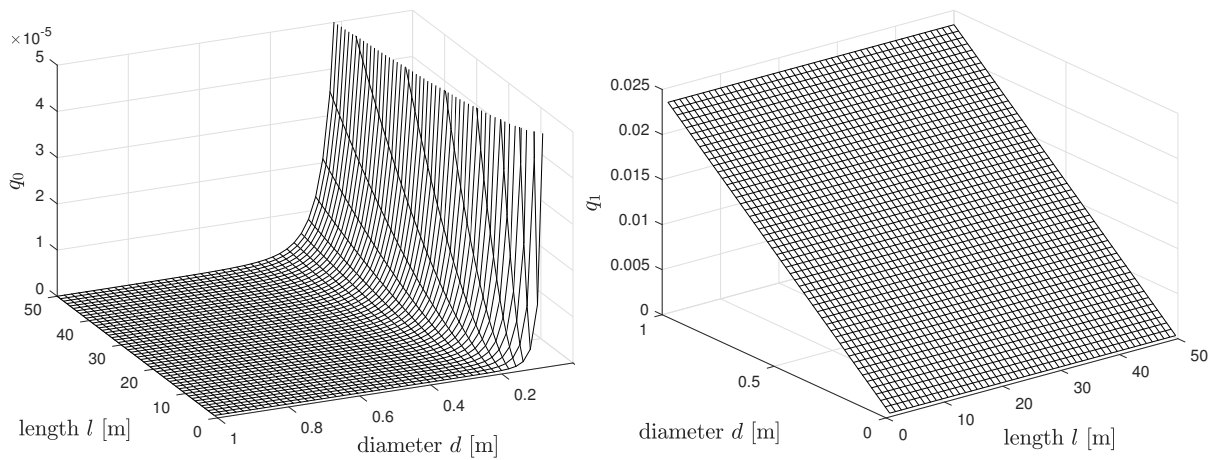


FIGURE 8.2: Parameters q_0, q_1 for $\rho = 998.5986 \text{ kg/m}^3$ and $\eta = 1.0526 \times 10^{-3} \text{ Pa}$ s plotted over the pipe's diameter and length.

8.3 Derivation of the Transitional Flow

Denoting $b = 2000 \frac{\eta A}{\rho d}$ for the laminar boundary flow, a solution for the transitional flow $\gamma(\epsilon, \Delta h)$ is developed by tackling the conditions

$$\gamma(\epsilon, b/w) \stackrel{!}{=} b \quad \forall \epsilon \quad (i)$$

$$\nabla \gamma \Big|_{(\epsilon, b/w)} \stackrel{!}{=} [w \quad 0]^T \quad \forall \epsilon \quad (ii)$$

for the laminar boundary (i) and its gradient (ii) as well as

$$\gamma(q^{-1}(\Delta h), \Delta h) \stackrel{!}{=} a \quad \forall \Delta h \in [\underline{\Delta h}, \overline{\Delta h}] \quad (iii)$$

$$\nabla \gamma \Big|_{(q^{-1}(\Delta h), \Delta h)} \stackrel{!}{=} \nabla f_t \Big|_{(f_a(\Delta h), \Delta h)} \quad \forall \Delta h \in [\underline{\Delta h}, \overline{\Delta h}] \quad (iv)$$

for the turbulent boundary (iii) and its gradient (iv). The gradient is denoted by $\nabla := [\partial/\partial\epsilon \quad \partial/\partial\Delta h]^T$ in this context. Finding a suitable function $\gamma(\epsilon, \Delta h)$ satisfying all the above conditions is remarkably tricky.

Theorem 8.4. *Let Assumption 7.4 hold. Then, the transitional flow $\gamma(\epsilon, \Delta h)$ can be expressed in terms of Δh (2.4) and ϵ (7.5) as follows:*

$$\gamma(\epsilon, \Delta h) = \gamma_1(\epsilon, \Delta h) + \gamma_2(\epsilon, \Delta h) + \gamma_3(\epsilon, \Delta h) \quad \text{with} \quad (8.9a)$$

$$\gamma_1 = c_0 + c_1 \Delta h^{-1/2} + c_2 \frac{\Delta h^{5/4}}{\epsilon + q_1} + c_3 \left(\frac{1}{\epsilon + q_1} - q_0 \Delta h^{-7/4} \right) + c_4 \frac{\Delta h^{7/4}}{\epsilon + q_1} \quad (8.9b)$$

$$\gamma_2 = \frac{(n_1 - 1)c_2}{\epsilon + q_1} \left(\frac{b}{w} \right)^{5/4} \left(\frac{b/w}{\Delta h} \right)^{\frac{5}{4(n_1-1)}} + \frac{(n_2 - 1)c_4}{\epsilon + q_1} \left(\frac{b}{w} \right)^{7/4} \left(\frac{b/w}{\Delta h} \right)^{\frac{7}{4(n_2-1)}} \quad (8.9c)$$

$$\gamma_3 = \left(\frac{1}{\epsilon + q_1} - q_0 \Delta h^{-7/4} \right) \left[c_5 \left(\Delta h^{n_3} - \left(\frac{b}{w} \right)^{n_3} \right) + c_6 \left(\Delta h^{n_4} - \left(\frac{b}{w} \right)^{n_4} \right) \right] \quad (8.9d)$$

considering parameters c_0, c_1, \dots, c_6 as well as n_1, \dots, n_4 . (8.9) thereby satisfies conditions (i),(ii) exactly and conditions (iii), (iv) in good approximation (clarification ought to be found in Remark 8.7).

The proof of Theorem 8.4 is conducted along the three separate parts of γ as shown in the sections below.

8.3.1 Choice of $\gamma_1(\epsilon, \Delta h)$

Starting with (i), γ_1 (8.9b) is expected to satisfy

$$\begin{aligned} \gamma_1(\epsilon, b/w) &= c_0 + c_1 (b/w)^{-1/2} + \frac{c_2 (b/w)^{5/4}}{\epsilon + q_1} + c_3 \left(\frac{1}{\epsilon + q_1} - q_0 (b/w)^{-7/4} \right) \\ &\quad + c_4 \frac{(b/w)^{7/4}}{\epsilon + q_1} \stackrel{!}{=} b \quad \forall \epsilon \end{aligned} \quad (8.10)$$

which leads to the conditions

$$c_0 + c_1 (b/w)^{-1/2} - c_3 q_0 (b/w)^{-7/4} \stackrel{!}{=} b \quad (8.11a)$$

$$c_2 (b/w)^{5/4} + c_3 + c_4 (b/w)^{7/4} \stackrel{!}{=} 0. \quad (8.11b)$$

From a physical standpoint the dependency of γ_1 on roughness ϵ was chosen such that increasing ϵ values lead to a decrease in the flow. As the exact boundary $f_a(\Delta h)$ (8.3) can be interpreted as a function on $\Delta h^{-1/2}$, γ_1 is developed around terms involving the head loss to the power of $-\frac{1}{2}$. When applying $q^{-1}(\Delta h) = \Delta h^{7/4}/q_0 - q_1$ on γ_1 , request (iii) results in an affine polynomial in $\Delta h^{-1/2}$

$$\gamma_1(q^{-1}(\Delta h), \Delta h) = c_0 + c_1 \Delta h^{-1/2} + c_2 q_0 \Delta h^{-1/2} + c_4 q_0 \stackrel{!}{=} a \quad \forall \Delta h \in [\underline{\Delta h}, \overline{\Delta h}]. \quad (8.12)$$

In this context, request (iii) can be fulfilled by selecting parameters c_i such that

$$c_0 + c_4 q_0 \stackrel{!}{=} a \quad (8.13a)$$

$$c_1 + c_2 q_0 \stackrel{!}{=} 0. \quad (8.13b)$$

Remark 8.5. Concerning request (ii), the partial derivative $\frac{\partial \gamma_1}{\partial \epsilon} \stackrel{!}{=} 0$ at $\Delta h = b/w$ and $\forall \epsilon$ is already satisfied implicitly through (8.11b) as a reason of request (i).

The partial derivative

$$\frac{\partial \gamma_1}{\partial \Delta h} = -1/2 c_1 \Delta h^{-3/2} + 5/4 \frac{c_2 \Delta h^{1/4}}{\epsilon + q_1} + 7/4 c_3 q_0 \Delta h^{-11/4} + 7/4 \frac{c_4 \Delta h^{3/4}}{\epsilon + q_1} \quad (8.14)$$

evaluated at $\Delta h = b/w$ and $\forall \epsilon$ leads to conditions

$$-1/2 c_1 (b/w)^{-3/2} + 7/4 c_3 q_0 (b/w)^{-11/4} \stackrel{!}{=} w \quad (8.15a)$$

$$5/4 c_2 (b/w)^{1/4} + 7/4 c_4 (b/w)^{3/4} \stackrel{!}{=} 0. \quad (8.15b)$$

Requests (8.11), (8.13) and (8.15a) yield ((8.15b) is considered later)

$$\underbrace{\begin{bmatrix} 1 & (b/w)^{-1/2} & 0 & -q_0 (b/w)^{-7/4} & 0 \\ 0 & 0 & (b/w)^{5/4} & 1 & (b/w)^{7/4} \\ 1 & 0 & 0 & 0 & q_0 \\ 0 & 1 & q_0 & 0 & 0 \\ 0 & -1/2 (b/w)^{-3/2} & 0 & 7/4 q_0 (b/w)^{-11/4} & 0 \end{bmatrix}}_{\mathcal{A}} \begin{bmatrix} c_0 \\ \vdots \\ c_4 \end{bmatrix} = \begin{bmatrix} b \\ 0 \\ a \\ 0 \\ w \end{bmatrix} \quad (8.16)$$

a system of linear equations with a rank deficiency of matrix \mathcal{A} , meaning that (i) and (iii) could not be (exactly) satisfied simultaneously. However, full rank can be restored by altering either (8.11b) or (8.13b). Altering (8.11b), the second row in \mathcal{A} , in terms of

$$n_1 c_2 (b/w)^{5/4} + c_3 + n_2 c_4 (b/w)^{7/4} = 0 \quad (8.17)$$

introducing new parameters n_1, n_2 to be determined later, (8.16) modified through (8.17) is solved. The choice to use (8.17) instead of (8.11b) in \mathcal{A} is strongly related with γ_2 . Denoting

$$C(n_1, n_2) = \frac{n_2 \left(\frac{11}{7} b - a \right) - \frac{4}{7} b}{\frac{5}{7} n_2 - n_1 + \frac{2}{7}}, \quad (8.18)$$

coefficients c_0, \dots, c_4 can be summarized:

$$\begin{aligned}
 c_0 &= \frac{11}{7}b - \frac{5}{7}C(n_1, n_2) & c_1 &= C(n_1, n_2) \left(\frac{b}{w}\right)^{1/2} \\
 c_2 &= -\frac{1}{q_0}C(n_1, n_2) \left(\frac{b}{w}\right)^{1/2} & c_3 &= \frac{2}{7} \frac{1}{q_0} \left(\frac{b}{w}\right)^{7/4} (2b + C(n_1, n_2)) \\
 c_4 &= \frac{1}{q_0} \left(a - \frac{11}{7}b + \frac{5}{7}C(n_1, n_2)\right)
 \end{aligned} \tag{8.19}$$

8.3.2 Choice of $\gamma_2(\epsilon, \Delta h)$

Thanks to special properties of γ_2 (8.9c), there is no need to explicitly fulfill request (8.15b). When considering the partial derivative

$$\begin{aligned}
 \frac{\partial \gamma_2}{\partial \Delta h} &= -\frac{5}{4} \frac{c_2}{\epsilon + q_1} \left(\frac{b}{w}\right)^{\frac{5}{4} + \frac{5}{4(n_1-1)}} \Delta h^{-\frac{5}{4(n_1-1)}-1} \\
 &\quad - \frac{7}{4} \frac{c_4}{\epsilon + q_1} \left(\frac{b}{w}\right)^{\frac{7}{4} + \frac{7}{4(n_2-1)}} \Delta h^{-\frac{7}{4(n_2-1)}-1}
 \end{aligned} \tag{8.20a}$$

at $\Delta h = b/w$ and $\forall \epsilon$ and the one of $\gamma_1 + \gamma_2$ at $\Delta h = b/w$

$$\begin{aligned}
 \frac{\partial \gamma_2}{\partial \Delta h} \Big|_{(\epsilon, b/w)} &= -\frac{5}{4} \frac{c_2}{\epsilon + q_1} \left(\frac{b}{w}\right)^{\frac{1}{4}} - \frac{7}{4} \frac{c_4}{\epsilon + q_1} \left(\frac{b}{w}\right)^{\frac{3}{4}} \\
 \Rightarrow \frac{\partial \gamma_1}{\partial \Delta h} \Big|_{(\epsilon, b/w)} + \frac{\partial \gamma_2}{\partial \Delta h} \Big|_{(\epsilon, b/w)} &= -1/2 c_1 (b/w)^{-3/2} + 7/4 c_3 q_0 (b/w)^{-11/4} \hat{=} (8.15a),
 \end{aligned} \tag{8.20b}$$

(8.15b) is satisfied implicitly. As a result, (8.15) and thus (ii) hold exactly. γ_2 's structure also helps to satisfy (8.11b) which was violated by (8.17)

$$\gamma_2(\epsilon, b/w) = \frac{(n_1 - 1)c_2}{\epsilon + q_1} \left(\frac{b}{w}\right)^{5/4} + \frac{(n_2 - 1)c_4}{\epsilon + q_1} \left(\frac{b}{w}\right)^{7/4} \tag{8.21}$$

$$\gamma_1(\epsilon, b/w) + \gamma_2(\epsilon, b/w) \stackrel{(8.17)}{=} c_0 + c_1 (b/w)^{-1/2} - c_3 q_0 (b/w)^{-7/4} \hat{=} (8.11a). \tag{8.22}$$

Consequently, (i) also holds exactly. Although the choice of γ_2 well complements γ_1 at the laminar boundary, it introduces problems at the turbulent one

$$\begin{aligned}
 \gamma_2(q^{-1}(\Delta h), \Delta h) &= \gamma_2(\Delta h^{7/4}/q_0 - q_1, \Delta h) = \\
 (n_1 - 1)c_2 q_0 \left(\frac{b}{w}\right)^{-1/2} \underbrace{\left(\frac{b/w}{\Delta h}\right)^{\frac{7n_1-2}{4(n_1-1)}}}_{<1} &+ (n_2 - 1)c_4 q_0 \underbrace{\left(\frac{b/w}{\Delta h}\right)^{\frac{7}{4} \frac{n_2}{n_2-1}}}_{<1}
 \end{aligned} \tag{8.23}$$

where the error $\gamma_2(q^{-1}(\Delta h), \Delta h)$ is expected to be sufficiently small as γ_1 already satisfies $\gamma_1(q^{-1}(\Delta h), \Delta h) = a$. From the physical context it is clear that

$$b/w < \Delta h \quad \forall \Delta h \in [\underline{\Delta h}, \overline{\Delta h}] \tag{8.24}$$

laminar and turbulent boundary do not meet. There is a clear distance between $\Delta h = b/w$ and $\Delta h = \underline{\Delta h}$ (where $\epsilon = 0$). Given (8.23) and (8.24) the aim will be to select n_1 and n_2 such that exponents $\frac{7n_1-2}{4(n_1-1)} = \frac{5}{4(n_1-1)} + \frac{7}{4}$ and $\frac{7}{4} \frac{n_2}{n_2-1}$ are large and that (see (8.18))

$$5n_2/7 - n_1 + 2/7 \neq 0 \tag{8.25}$$

to maintain solvability of (8.16) which was modified by (8.17). Additionally, the choice of n_1, n_2 also influences (iv), the gradient at the turbulent boundary.

8.3.3 Choice of $\gamma_3(\epsilon, \Delta h)$

Since γ_1 and γ_2 enable requests (i)-(iii) to be satisfied, γ_3 (8.9d) has to be chosen such that laminar and turbulent boundary remain unaffected, i.e.

$$\gamma_3(\epsilon, b/w) = 0 \quad \forall \epsilon \quad (8.26a)$$

$$\gamma_3(q^{-1}(\Delta h), \Delta h) = 0 \quad \forall \Delta h \in [\underline{\Delta h}, \overline{\Delta h}]. \quad (8.26b)$$

This explains the use of terms $(\Delta h^{n_x} - (b/w)^{n_x})$ as well as $\left(\frac{1}{\epsilon+q_1} - q_0 \Delta h^{-7/4}\right)$ while exponents $n_x \in \{n_3, n_4\}$ help to manipulate the gradient at the turbulent boundary.

Gradient at Laminar Boundary. One also has to make sure that the contribution of $\nabla \gamma_3$ to $\nabla \gamma$ at $\Delta h = b/w$ the laminar boundary is zero. Considering

$$\begin{aligned} \frac{\partial \gamma_3}{\partial \Delta h} &= c_5 n_3 \Delta h^{n_3-1} \left(\frac{1}{\epsilon+q_1} - q_0 \Delta h^{-7/4} \right) + q_0 \frac{7}{4} c_5 \Delta h^{-11/4} \left(\Delta h^{n_3} - \left(\frac{b}{w} \right)^{n_3} \right) \\ &+ c_6 n_4 \Delta h^{n_4-1} \left(\frac{1}{\epsilon+q_1} - q_0 \Delta h^{-7/4} \right) + q_0 \frac{7}{4} c_6 \Delta h^{-11/4} \left(\Delta h^{n_4} - \left(\frac{b}{w} \right)^{n_4} \right) \end{aligned} \quad (8.27)$$

the choice

$$c_5 n_3 \left(\frac{b}{w} \right)^{n_3} + c_6 n_4 \left(\frac{b}{w} \right)^{n_4} = 0 \quad \implies \quad c_6 = -c_5 \frac{n_3}{n_4} \left(\frac{b}{w} \right)^{n_3-n_4} \quad (8.28)$$

achieves the desired behavior $\left. \frac{\partial \gamma_3}{\partial \Delta h} \right|_{(\epsilon, b/w)} = 0$. Parameter c_6 is now expressed through c_5 and n_3, n_4 . γ_3 's unique form makes sure that $\left. \frac{\partial \gamma_3}{\partial \epsilon} \right|_{(\epsilon, b/w)} = 0$, hence $\nabla \gamma_3|_{(\epsilon, b/w)} \stackrel{(8.28)}{=} \mathbf{0}$.

Gradient at Turbulent Boundary. The main purpose of γ_3 as part of (8.9) is to fulfill the arguably most challenging request (iv). In sum, the parameters yet to be determined are n_1 and n_2 , which shall lead to large exponents $\frac{5}{4(n_1-1)} + \frac{7}{4}$ resp. $\frac{7}{4} \frac{n_2}{n_2-1}$ while not violating (8.25), as well as n_3, n_4 and c_5 which are free of constraints (except $n_3, n_4 \neq 0$).

Proposition 8.6. *Provided that the error between $\epsilon = q^{-1}(\Delta h)$ and $\epsilon = f_a(\Delta h)$ vanishes, i.e. $q^{-1}(\Delta h) = f_a(\Delta h) \forall \Delta h$ (see Corollary 8.3), it is sufficient to fulfill either*

$$\left. \frac{\partial \gamma}{\partial \epsilon} \right|_{(q^{-1}(\Delta h), \Delta h)} \stackrel{!}{=} \left. \frac{\partial f_t}{\partial \epsilon} \right|_{(f_a(\Delta h), \Delta h)} \quad \text{or} \quad \left. \frac{\partial \gamma}{\partial \Delta h} \right|_{(q^{-1}(\Delta h), \Delta h)} \stackrel{!}{=} \left. \frac{\partial f_t}{\partial \Delta h} \right|_{(f_a(\Delta h), \Delta h)} \quad (8.29)$$

to satisfy request (iv) (proven in Appendix D).

By setting the focus on the partial derivative concerning Δh while combining (8.9) with (8.4), (8.19) and (8.28) (writing C instead of $C(n_1, n_2)$ for better readability)

$$\left. \frac{\partial \gamma}{\partial \Delta h} \right|_{(q^{-1}(\Delta h), \Delta h)} = g_1(\Delta h) + c_5 g_2(\Delta h) \quad \text{with} \quad (8.30a)$$

$$\begin{aligned} g_1 &= -\frac{7}{4} C \left(\frac{b}{w} \right)^{1/2} \Delta h^{-3/2} + \frac{1}{2} \left(\frac{b}{w} \right)^{7/4} (2b + C) \Delta h^{-11/4} + \left(\frac{7}{4} a - \frac{11}{4} b + \frac{5}{4} C \right) \Delta h^{-1} \\ &+ \frac{5}{4} \left(\frac{b}{w} \right)^{-3/2} C \left(\frac{b/w}{\Delta h} \right)^{\frac{5}{4(n_1-1)} + \frac{11}{4}} - \left(\frac{7}{4} a - \frac{11}{4} b + \frac{5}{4} C \right) \left(\frac{b}{w} \right)^{-1} \left(\frac{b/w}{\Delta h} \right)^{\frac{7}{4(n_2-1)} + \frac{11}{4}} \end{aligned} \quad (8.30b)$$

$$g_2 = \frac{7}{4} q_0 \Delta h^{-11/4} \left[\Delta h^{n_3} - \left(\frac{b}{w}\right)^{n_3} - \frac{n_3}{n_4} \left(\frac{b}{w}\right)^{n_3-n_4} \left(\Delta h^{n_4} - \left(\frac{b}{w}\right)^{n_4} \right) \right] \quad (8.30c)$$

n_1, \dots, n_4 and c_5 are adapted to match

$$\left. \frac{\partial f_t}{\partial \Delta h} \right|_{(f_a(\Delta h), \Delta h)} = \frac{a}{2} \Delta h^{-1} + \frac{2.51}{\ln(10)} \frac{\eta A}{\rho d} \Delta h^{-1} \exp\left(a \frac{\ln(10)}{2} \sqrt{\frac{k}{\Delta h}}\right) =: p(\Delta h) \quad (8.31)$$

with the help of optimizations, minimizing the quadratic error between (8.30) and (8.31).

$$\boxed{n_1 = 5/4 \quad n_2 = 11/8 \quad n_3 = 57/31 \quad n_4 = 21/20} \quad (8.32)$$

With the help of chosen n_1, n_2 (8.32) the rational C (8.18) becomes $C(n_1, n_2) = 89b - 77a$, i.e. it has integer coefficients at boundary flows a and b .

Remark 8.7. Exponents $\frac{5}{4(n_1-1)} + \frac{7}{4} = \frac{27}{4} = 6.75$ and $\frac{7}{4} \frac{n_2}{n_2-1} = \frac{77}{12} = 6.4166$ of $1/\Delta h$ in (8.9c) are sufficiently large at the turbulent boundary such that the relative error $|(a - \gamma(q^{-1}(\Delta h), \Delta h))/a| < 0.0005 \forall \Delta h \in [\underline{\Delta h}, \overline{\Delta h}]$ remained below 0.05% for all tested l, d, ρ and η values.

Interestingly, the quality of the approximation of (8.31) by (8.30) basically remains unchanged (as seen in figure 8.3) when varying l, d (even ρ, η) with the same n_1, \dots, n_4 according to (8.32) which, effectively, represent different exponents of Δh . It is sufficient to solely adapt parameter c_5 in order for (8.30) to match (8.31) concerning different l, d, ρ and η values.

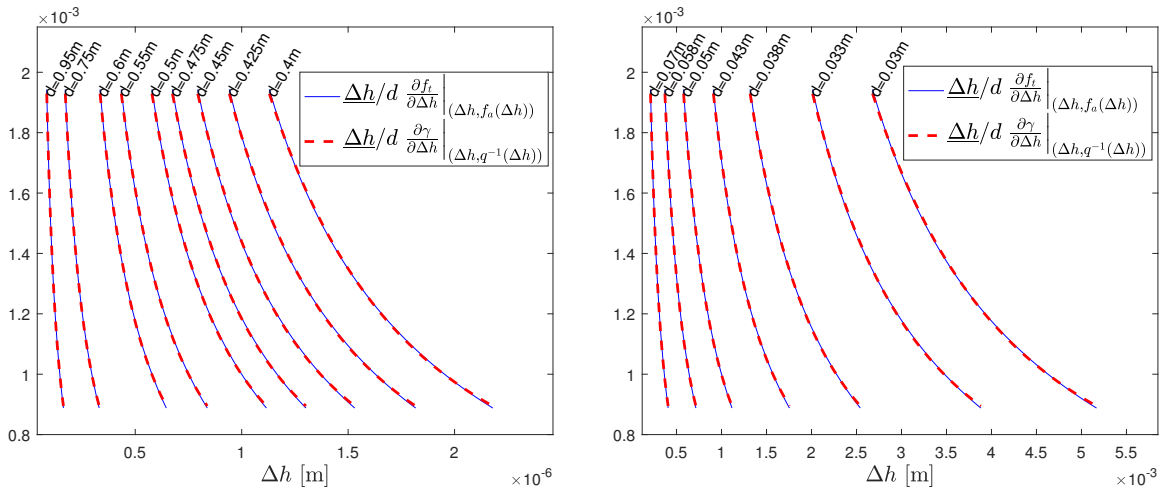


FIGURE 8.3: Partial derivative in terms of Δh on the transitional-turbulent boundary scaled by $\underline{\Delta h}/d$ for a pipe length of $l = 2\text{m}$ and different pipe diameters (same as in figure 8.1).

In this context, $\gamma_3(\epsilon, \Delta h)$ is an essential part of $\gamma(\epsilon, \Delta h)$ (8.9), it was not possible with $g_1(\Delta h)$ (8.30b), i.e. $\frac{\partial \gamma_1}{\partial \Delta h} + \frac{\partial \gamma_2}{\partial \Delta h}$ at the turbulent boundary, to reproduce (8.31) by adjusting n_1, n_2 only.

For the determination of c_5 the same equidistant step u as in (8.8) is taken and $\mathbf{p} = [p(\underline{\Delta h}) \ p(\underline{\Delta h} + u) \ p(\underline{\Delta h} + 2u) \ \dots \ p(\overline{\Delta h})]^T$ according to (8.31) as well as $\mathbf{g}_i = [g_i(\underline{\Delta h}) \ g_i(\underline{\Delta h} + u) \ \dots \ g_i(\overline{\Delta h})]^T$ for $i = 1, 2$ according to (8.30a). The corresponding discretized optimization problem

$$\min_{c_5} (\mathbf{p} - \mathbf{g}_1 - c_5 \mathbf{g}_2)^T (\mathbf{p} - \mathbf{g}_1 - c_5 \mathbf{g}_2) \quad (8.33)$$

has the optimal solution

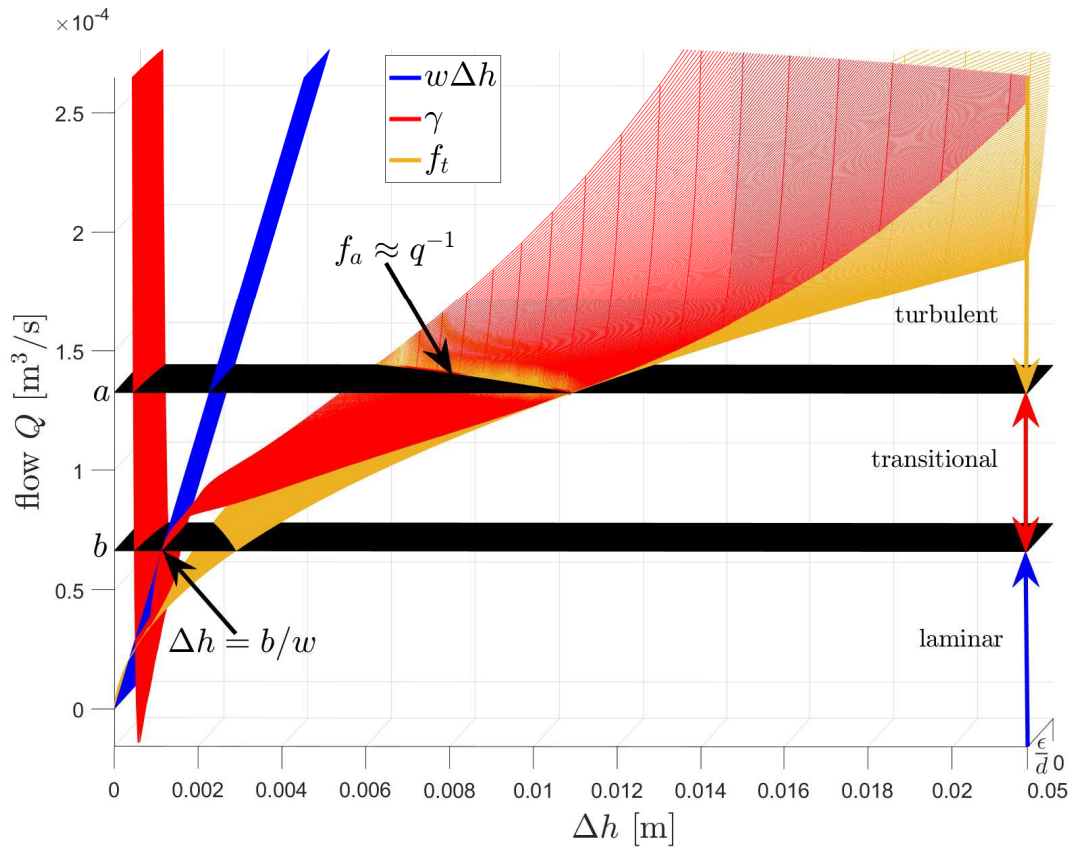
$$c_5 = \frac{\mathbf{p}^T \mathbf{g}_2 - \mathbf{g}_1^T \mathbf{g}_2}{\mathbf{g}_2^T \mathbf{g}_2}. \quad (8.34)$$

Remark 8.8. Analogous to Proposition 8.2, one can show that the integral error function

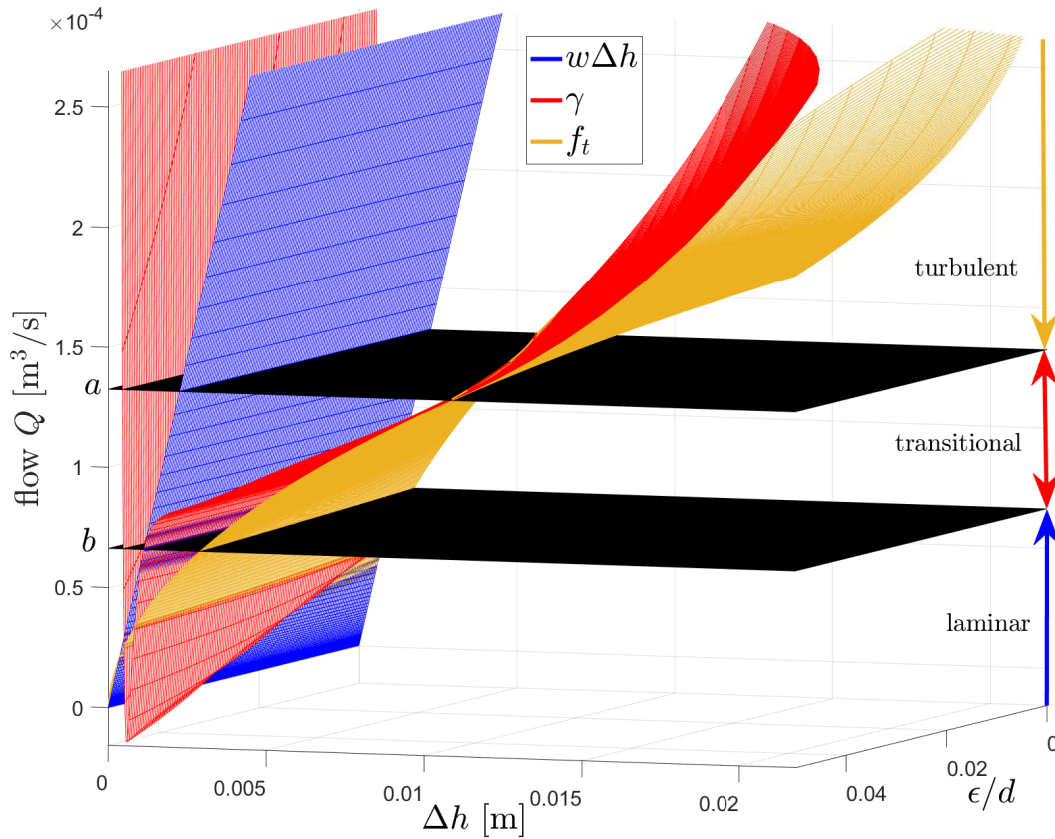
$$\tilde{E}(c_5) = \int_{\underline{\Delta h}}^{\overline{\Delta h}} (p(\Delta h) - g_1(\Delta h) - c_5 g_2(\Delta h))^2 d\Delta h \quad (8.35)$$

is convex. Subsequently, given a sufficiently large n for the discretization of $p(\Delta h)$, $g_1(\Delta h)$ and $g_2(\Delta h)$, (8.34) is solution of the problem $d\tilde{E}/dc_5 = 0$ (see Corollary 8.3).

One can see that γ (8.9) in figure 8.4 does not compromise the smoothness of Q (8.1) in any way noticeable. This holds true for all tested l, d values and, interestingly, also for different η, ρ when, for instance, adapted to other temperatures. To avoid using the flow in Re (2.3) concerning the distinction between flow regimes in Q (8.1), one specifies the laminar region in $\Delta h \leq b/w$ (instead of $Re \leq 2000$) and the turbulent region in $\Delta h \geq q(\epsilon)$ (instead of $Re \geq 4000$).



(A) First view showing the turbulent boundary curve $\epsilon = f_a(\Delta h) \approx q^{-1}(\Delta h)$ as well as the laminar boundary where $\Delta h = b/w$ for all ϵ .



(B) Second view with attention to the gradient at the turbulent boundary.

FIGURE 8.4: Comparison of laminar, transitional and turbulent flow showing γ as a smooth interpolation of $w\Delta h$ and f_t for a pipe with $l = 10\text{m}$ and $d = 0.04\text{m}$.

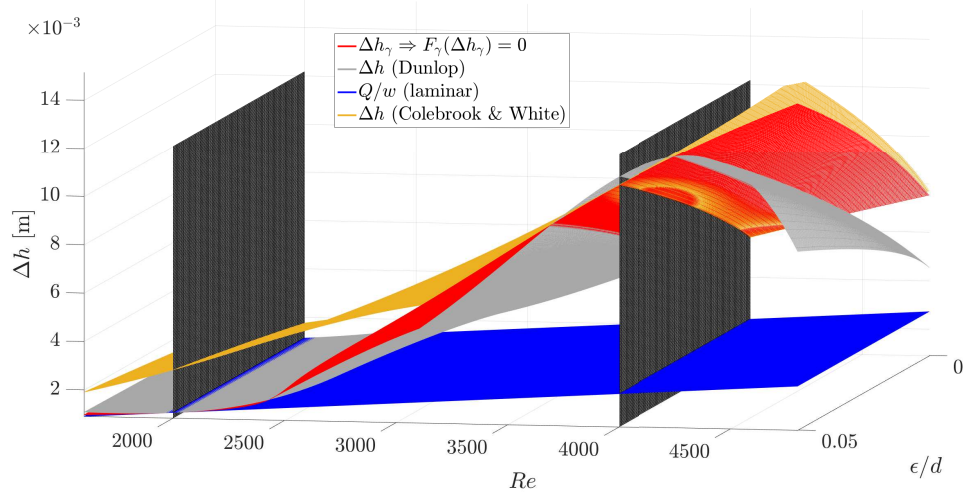
8.4 Comparison to *Dunlop's* Cubic Interpolation

In this section a brief comparison ought to clarify the differences to existing formulae describing the transitional water head loss. Thereby, the head loss as a solution of the implicit equation

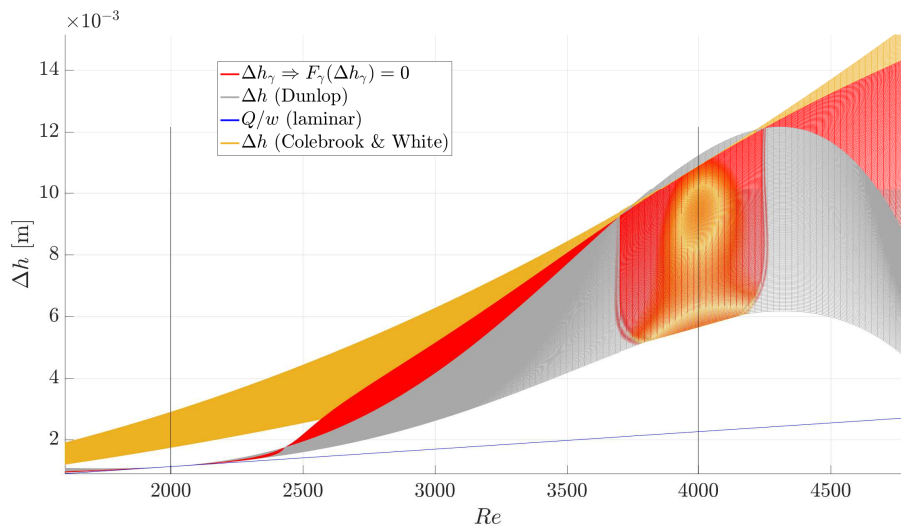
$$F_\gamma(\Delta h) = Q - \gamma(\epsilon, \Delta h) = 0 \quad (8.36)$$

is solved numerically in order to be compared to Dunlop's cubic interpolation [Dunlop, 1991] of the transitional friction factor (2.8) used within the Darcy-Weisbach head loss (2.4). This may be of particular interest since this equation is also applied in the current version of EPANET [Lewis, 2000]. This comparison can be seen in figure 8.5 showing substantial deviations between "Dunlop's formulae" and the derived γ in terms of the head loss. In figure 8.5B, the front view of 8.5A, one can see that both match the laminar boundary and gradient exactly. However, in figure 8.5C one can see that "Dunlop's head loss" shows vast deviations to Colebrook-White's head loss in terms of the turbulent gradient and somewhat minor deviations to the turbulent boundary.

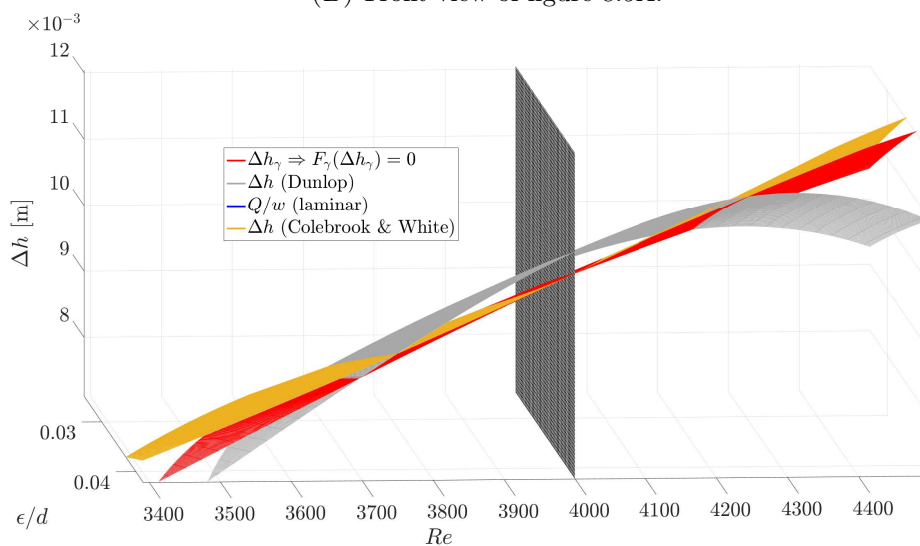
Knowing that the Dunlop-interpolation utilizes the *Swamee-Jain* formula (2.7) [Swamee and Jain, 1976] at the turbulent boundary, these deviations make sense and appear consistently when varying the pipe's length and diameter.



(A) Comparing Δh as a solution of (8.36) with the “Dunlop” [Lewis, 2000; Dunlop, 1991] formulae (see (2.8)) the Colebrook-White head loss (solved numerically) and the laminar head loss.



(B) Front view of figure 8.5A.



(C) Zoom in figure 8.5A showing the turbulent boundary.

FIGURE 8.5: Comparison of laminar, transitional and turbulent head loss showing differences to existing formulae for a pipe with $l = 10\text{m}$ and $d = 0.04\text{m}$.

8.5 Summary of Steps to Obtain γ

This section intends to clarify the process on how to obtain the final γ . Beforehand, mind that $a = 4000 \frac{A\eta}{\rho d}$, $b = 2000 \frac{\eta A}{\rho d}$ as well as $w = \frac{1}{32} \frac{\rho}{\eta} \frac{d^2 g A}{l}$. This determination of γ according to (8.9) is comprised of the following steps:

- (I) compute lower and upper limit $\underline{\Delta h}$ and $\overline{\Delta h}$ by solving $f_a(\underline{\Delta h}) = 0$ (8.3) and $f_a(\overline{\Delta h}) = 0.05d$ (8.3) numerically. Since one can show that function $\epsilon = f_a(\Delta h)$ is strictly monotone for $|\Delta h| \neq 0$ this can be done easily, also consider Remark 8.1 in this context.
- (II) take the equidistant step $u = (\overline{\Delta h} - \underline{\Delta h})/n$ for a sufficiently large n , e.g. $n = 10^4$ and calculate

$$\begin{aligned} \mathbf{u} &= [\underline{\Delta h}^{7/4} \quad (\underline{\Delta h} + u)^{7/4} \quad (\underline{\Delta h} + 2u)^{7/4} \quad \dots \quad \overline{\Delta h}^{7/4}]^T \\ \mathbf{v} &\stackrel{(8.3)}{=} [f_a(\underline{\Delta h}) \quad f_a(\underline{\Delta h} + u) \quad f_a(\underline{\Delta h} + 2u) \quad \dots \quad f_a(\overline{\Delta h})]^T \end{aligned}$$

- (III) determine q_0 and q_1 via (8.8) (pay attention to the reciprocal representation of q_0)
- (IV) take $C = 89a - 77b$ as well as (8.32) and the same equidistant step u as before and calculate

$$\begin{aligned} \mathbf{g}_i &\stackrel{(8.30)}{=} [g_i(\underline{\Delta h}) \quad g_i(\underline{\Delta h} + u) \quad g_i(\underline{\Delta h} + 2u) \quad \dots \quad g_i(\overline{\Delta h})]^T \quad \text{for } i = 1, 2 \\ \mathbf{p} &\stackrel{(8.31)}{=} [p(\underline{\Delta h}) \quad p(\underline{\Delta h} + u) \quad p(\underline{\Delta h} + 2u) \quad \dots \quad p(\overline{\Delta h})]^T \end{aligned}$$

- (V) finally coefficients c_0, \dots, c_4 (8.19) are obtained for $C = 89a - 77b$, whereas c_5 is the result of (8.34) while $c_6 \stackrel{(8.28)}{=} -c_5 \frac{n_3}{n_4} \left(\frac{b}{w}\right)^{n_3 - n_4}$ with n_3, n_4 as in (8.32)

All parameters for γ in reference to (8.9) have now been obtained, applying $C \stackrel{(8.18)}{=} 89a - 77b$ in (8.19), n_1, n_2, n_3, n_4 according to (8.32) and c_6 (8.28) yields

$$\begin{aligned} \gamma(\epsilon, \Delta h) = & \\ 55a - 62b + & \frac{89b - 77a}{\sqrt{\Delta h}} \sqrt{\frac{b}{w}} - \frac{(89b - 77a) \Delta h^{5/4}}{q_0 (\epsilon + q_1)} \sqrt{\frac{b}{w}} + \frac{26b - 22a}{q_0} \left(\frac{b}{w}\right)^{7/4} \left(\frac{1}{\epsilon + q_1} - \frac{q_0}{\Delta h^{7/4}}\right) \\ & + \frac{(-54a + 62b) \Delta h^{7/4}}{q_0 (\epsilon + q_1)} - \frac{1}{4} \frac{89b - 77a}{q_0 \Delta h^5 (\epsilon + q_1)} \left(\frac{b}{w}\right)^{27/4} + \frac{3}{8} \frac{-54a + 62b}{q_0 \Delta h^{14/3} (\epsilon + q_1)} \left(\frac{b}{w}\right)^{77/12} \\ & + c_5 \left(\frac{1}{\epsilon + q_1} - \frac{q_0}{\Delta h^{7/4}}\right) \left[\Delta h^{57/31} - \left(\frac{b}{w}\right)^{57/31} - \frac{380}{217} \left(\frac{b}{w}\right)^{489/620} \left(\Delta h^{21/20} - \left(\frac{b}{w}\right)^{21/20} \right) \right] \end{aligned} \quad (8.37)$$

with q_0, q_1 as well as c_5 as results of convex optimizations. As a side note, this process has to be done once only for a specific pipe length l , diameter d and temperature, hence ρ and η .

Roughness Identification: Consideration of All Flow Regimes

In this chapter the relieve of Assumption 7.7 is finally accomplished by merging the roughness calculation of the full turbulent case (chapter 7) with the transitional water flow (chapter 8) while also accounting for the laminar regime.

In this process it turns out that the developed methods for solving (7.7)-like problems only need slight modifications to handle the extension to all flow regimes. In this context, it is worth mentioning that the efforts put into the development of γ satisfying (i)-(iv) (on page 130) pays off when applying root-finding methods which require to find a search direction via a *Taylor* series as in (7.12) or (7.43). The satisfaction of gradients concerning (iii) and in particular (iv) (on page 130) to a sufficient degree of detail enables the (roughness) root-finding algorithm to autonomously decide if a pipe flow in the corresponding measurement-set has been laminar, turbulent or even transitional for that matter.

9.1 Complete Problem Set-Up

The following notation is applied

$$[\mathbf{f}_t(\boldsymbol{\epsilon}, \Delta \mathbf{h}^{(i)})]_j \stackrel{(7.5)}{=} f_{t,j}([\boldsymbol{\epsilon}]_j, [\Delta \mathbf{h}^{(i)}]_j) \quad (9.1a)$$

$$[\gamma(\boldsymbol{\epsilon}, \Delta \mathbf{h}^{(i)})]_j \stackrel{(8.37)}{=} \gamma_j([\boldsymbol{\epsilon}]_j, [\Delta \mathbf{h}^{(i)}]_j) \quad \forall j \in \mathfrak{P} \quad (9.1b)$$

$$[\mathbf{w}]_j = \frac{1}{32} \frac{\rho}{\eta} \frac{d_j^2 g A_j}{l_j} \quad (9.1c)$$

to specify the turbulent flow (9.1a), the transitional flow (9.1b) and the proportionality factor (9.1c) for the laminar flow for all pipes in $j \in \mathfrak{P}$. \mathbf{w} thereby involves the corresponding j -th pipe's diameter d_j , its cross section area A_j , its length l_j , the gravitational acceleration g and the water viscosity η as well as the density ρ (which, in principle, can also vary along the j -th pipe). Also γ_j and $f_{t,j}$ did receive a dedicated index in (9.1) to highlight that (7.5) and (8.37), respectively, involve parameters which also vary along \mathfrak{P} . Also note that $\gamma(\boldsymbol{\epsilon}, \Delta \mathbf{h}^{(i)})$ has to be replaced with $\text{sign}(\Delta \mathbf{h}^{(i)}) \odot \gamma(\boldsymbol{\epsilon}, |\Delta \mathbf{h}^{(i)}|)$ for negative $\Delta \mathbf{h}^{(i)}$ in reference to Remark 8.1.

Further, in order to avoid a direct case separation as in (8.1) the author introduces the following definitions:

Definition 9.1 (Flow Separation Matrices). Let $\mathbf{e}_j \in \mathbb{Z}_{\{0,1\}}^{n_\ell} \forall j \in \mathfrak{P}$. Then,

$$\mathbf{R}_t^{(i)} := \begin{bmatrix} \mathbf{e}_{t_1^{(i)}}^T \\ \mathbf{e}_{t_2^{(i)}}^T \\ \vdots \\ \mathbf{e}_{t_{n_t}^{(i)}}^T \end{bmatrix}, \quad \mathbf{R}_\gamma^{(i)} := \begin{bmatrix} \mathbf{e}_{g_1^{(i)}}^T \\ \mathbf{e}_{g_2^{(i)}}^T \\ \vdots \\ \mathbf{e}_{g_{n_\gamma}^{(i)}}^T \end{bmatrix}, \quad \mathbf{R}_l^{(i)} := \begin{bmatrix} \mathbf{e}_{l_1^{(i)}}^T \\ \mathbf{e}_{l_2^{(i)}}^T \\ \vdots \\ \mathbf{e}_{l_{n_L}^{(i)}}^T \end{bmatrix} \quad (9.2a)$$

$$\mathbf{r}_t^{(i)} := \sum_{j=t_1^{(i)}}^{t_{n_t}^{(i)}} \mathbf{e}_j, \quad \mathbf{r}_\gamma^{(i)} := \sum_{j=g_1^{(i)}}^{g_{n_\gamma}^{(i)}} \mathbf{e}_j, \quad \mathbf{r}_l^{(i)} := \sum_{j=l_1^{(i)}}^{l_{n_L}^{(i)}} \mathbf{e}_j, \quad (9.2b)$$

built from unity vectors \mathbf{e}_j with indices which belong to sets¹

$$\mathcal{T}^{(i)} \stackrel{(8.4)}{=} \left\{ j \in \mathfrak{P} \mid [|\Delta \mathbf{h}^{(i)}|]_j \geq (\mathfrak{q}_{0,j}(\epsilon_j + \mathfrak{q}_{1,j}))^{4/7} \right\} = \{t_1^{(i)}, t_2^{(i)}, \dots, t_{n_t}^{(i)}\} \quad (9.3a)$$

$$\mathcal{G}^{(i)} \stackrel{(8.4)}{=} \left\{ j \in \mathfrak{P} \mid b_j/w_j < [|\Delta \mathbf{h}^{(i)}|]_j < (\mathfrak{q}_{0,j}(\epsilon_j + \mathfrak{q}_{1,j}))^{4/7} \right\} = \{g_1^{(i)}, g_2^{(i)}, \dots, g_{n_\gamma}^{(i)}\} \quad (9.3b)$$

$$\mathcal{L}^{(i)} = \left\{ j \in \mathfrak{P} \mid [|\Delta \mathbf{h}^{(i)}|]_j \leq b_j/w_j \right\} = \{l_1^{(i)}, l_2^{(i)}, \dots, l_{n_L}^{(i)}\} \quad (9.3c)$$

and vary in each measurement-set $i \in \mathfrak{M}$ such that

$$\mathcal{T}^{(i)} \cap \mathcal{G}^{(i)} = \{\} \quad \wedge \quad \mathcal{T}^{(i)} \cap \mathcal{L}^{(i)} = \{\} \quad \wedge \quad \mathcal{G}^{(i)} \cap \mathcal{L}^{(i)} = \{\} \quad \forall i \in \mathfrak{M} \quad (9.4)$$

but $\mathcal{T}^{(i)} \cup \mathcal{G}^{(i)} \cup \mathcal{L}^{(i)} = \mathfrak{P} \forall i \in \mathfrak{M}$, effectively, separate flow vector $\mathbf{x}_Q^{(i)}$ along the flow regimes.

Finally, applying notation (9.1) and Definition 9.1 on (7.7) one receives the equation-set

$$\Psi : \left\{ \begin{array}{l} \overbrace{\mathbf{A} \left(\mathbf{R}_t^{(i)T} \mathbf{R}_t^{(i)} \mathbf{f}_t(\epsilon, \Delta \mathbf{h}^{(i)}) + \mathbf{R}_\gamma^{(i)T} \mathbf{R}_\gamma^{(i)} \gamma(\epsilon, \Delta \mathbf{h}^{(i)}) + \mathbf{R}_l^{(i)T} \mathbf{R}_l^{(i)} \text{diag}(\mathbf{w}) \Delta \mathbf{h}^{(i)} \right)}^{\mathbf{x}_Q(\epsilon, \Delta \mathbf{h}^{(i)})} = \mathbf{R}_q^T \mathbf{q}^{(i)} \\ \Delta \mathbf{h}^{(i)} = \tilde{\mathbf{C}}_s \mathbf{h}_s^{(i)} - \mathbf{A}^T \mathbf{C}_h^T \mathbf{y}_h^{(i)} - \mathbf{A}^T \bar{\mathbf{C}}_h^T \mathbf{h}_N^{(i)} - \mathbf{A}^T \mathbf{z} \end{array} \right. \quad (9.5)$$

for $i \in \{1, 2, \dots, n_m\} = \mathfrak{M}$

to be solved under the assumptions in table 7.1. To recapitulate, set (9.5) is nothing else but nodal *Kirchhoff* equations, where flows in each component of the network are expressed as functions on the roughness ϵ and the not-measured pressured heads $\mathbf{h}_N^{(i)}$ at nodes with no sensors in measurement-sets $i \in \mathfrak{M}$ which are the unknowns to be found.

Also, following Definition 9.1 it is clear that

$$\mathbf{R}_t^{(i)T} \mathbf{R}_t^{(i)} + \mathbf{R}_\gamma^{(i)T} \mathbf{R}_\gamma^{(i)} + \mathbf{R}_l^{(i)T} \mathbf{R}_l^{(i)} \equiv \mathbf{I}_{n_\ell} \quad (9.6)$$

is equivalent to the identity matrix meaning that $n_t^{(i)} + n_\gamma^{(i)} + n_L^{(i)} \equiv n_\ell$ where the lengths n_t, n_γ, n_L may also vary in each measurement-set. Please do not confuse the number of pipes n_ℓ

¹Due to the conflicting notation of the consumption $[q]_k = q_k$ for $k \in \mathcal{K}$ (Definition 4.4) with the function $\Delta \mathbf{h} = q(\epsilon)$ (8.4), describing the transitional-turbulent boundary, $q(\epsilon)$ is represented by $\mathfrak{q}(\epsilon) \leftarrow q(\epsilon)$ and thus $\mathfrak{q}(\epsilon) = (\mathfrak{q}_0(\epsilon + \mathfrak{q}_1))^{4/7}$.

with the number of laminar flows n_L in the i -th measurement-set. Similar properties as in (4.5) used to separate nodes into consumer and non-consumer nodes can certainly be derived.

Although the flow separation matrices actually depend on the variables ϵ and $\mathbf{h}_N^{(i)}$ actually, according to Definition 9.1, one can act as if they do not for the determination of first and second flow derivatives as in section 7.4.1 and section 7.6.1 for the turbulent flow. This can be attributed to the property that $\mathbf{R}_l^{(i)}, \mathbf{R}_\gamma^{(i)}, \mathbf{R}_t^{(i)}$ are only comprised of zeros and ones, i.e. their derivative always yields the zero matrix. This makes the notation applied on set (9.5) powerful in a sense that one does not have to worry about the flow-regime case-separation explicitly, the consideration of matrices $\mathbf{R}_l^{(i)}, \mathbf{R}_\gamma^{(i)}, \mathbf{R}_t^{(i)}$ or vectors $\mathbf{r}_l^{(i)}, \mathbf{r}_\gamma^{(i)}, \mathbf{r}_t^{(i)}$ is sufficient.

Another feature of equation-set Ψ has to be discussed in the context of the number of roughness variables $\epsilon \in \mathbb{R}_{\geq 0}^{n_\epsilon}$.

Remark 9.2. *The relieve of Assumption 7.7 with consideration of the transitional flow $\gamma^{(i)}$ (8.37) to allow flows $\mathbf{x}_Q^{(i)}$ to transition to the laminar regime in the solving of problem Ψ , allows individual pipe flows in \mathfrak{P} , in principle, to never become turbulent (or even transitional) in any of the $i \in \mathfrak{M}$ measurement-sets. As a result, the corresponding roughnesses in ϵ of these pipe flows among \mathfrak{P} can not be identified inherently, although one might be able to enhance Algorithms 1 and 3 to also consider a varying number of variables $\mathbf{x} = [\epsilon \ \mathbf{h}_N^{(1)} \ \dots \ \mathbf{h}_N^{(n_m)}]^T$.*

As this is not considered in this thesis, the following assumption in addition to all the ones in table 7.1 must hold for the applicability of Algorithm 1 and 3 on Ψ .

Assumption 9.3. *All individual pipe flows $\mathbf{x}_Q^{(i)}$ must at least once be in the turbulent regime in any of the $i \in \mathfrak{M}$ measurement-sets, i.e. $\exists i \in \mathfrak{M} \mid t^{(i)} \stackrel{(9.3a)}{=} j \in \mathcal{T}^{(i)} \forall j \in \mathfrak{P}$.*

Actually, it would suffice to require all pipe flows to be at least once in the turbulent or transitional regime for the solvability of Ψ via Algorithm 1 or 3. However, as the derivation of the transitional flow γ according to (8.37) was accomplished by purely mathematical considerations, the restriction to turbulent flows as in Assumption 9.3 makes sense in the opinion of the author.

9.2 Derivatives of the Combined Flow

First Derivatives. The partial derivatives of the transitional water flow γ (8.37) with respect to the roughness ϵ

$$\begin{aligned} \frac{\partial \gamma_j}{\partial \epsilon_j} \stackrel{(8.37)}{=} [\gamma_\epsilon]_j = \gamma_{\epsilon,j} \quad \forall j \in \mathfrak{P} \hat{=} \\ \frac{(89b - 77a) \Delta h^{5/4}}{q_0 (\epsilon + q_1)^2} \sqrt{\frac{b}{w}} - \frac{26b - 22a}{q_0 (\epsilon + q_1)^2} \left(\frac{b}{w}\right)^{\frac{7}{4}} - \frac{(62b - 54a) \Delta h^{7/4}}{q_0 (\epsilon + q_1)^2} \\ + \frac{1}{4} \frac{89b - 77a}{q_0 \Delta h^5 (\epsilon + q_1)^2} \left(\frac{b}{w}\right)^{\frac{27}{4}} - \frac{1}{8} \frac{-162a + 186b}{\Delta h^{14/3} q_0 (\epsilon + q_1)^2} \left(\frac{b}{w}\right)^{\frac{77}{12}} \\ - \frac{c_5}{(\epsilon + q_1)^2} \left[\Delta h^{\frac{57}{31}} - \left(\frac{b}{w}\right)^{\frac{57}{31}} - \frac{380}{217} \left(\frac{b}{w}\right)^{\frac{489}{620}} \left(\Delta h^{\frac{21}{20}} - \left(\frac{b}{w}\right)^{\frac{21}{20}} \right) \right] \end{aligned} \quad (9.7)$$

(neglecting indices in q_0, q_1, a, b, w along $\mathcal{T}^{(i)} \subseteq \mathfrak{P}$) as well as its derivative with respect to the pressure head loss

$$\begin{aligned} \frac{\partial \gamma_j}{\partial \Delta h_j} \stackrel{(8.37)}{=} [\gamma_{\Delta h}]_j = \gamma_{\Delta h, j} \quad \forall j \in \mathfrak{P} \hat{=} & -\frac{1}{2} \frac{89b - 77a}{\Delta h^{3/2}} \sqrt{\frac{b}{w}} - \frac{1}{4} \frac{(445b - 385a) \Delta h^{1/4}}{q_0 (\epsilon + q_1)} \sqrt{\frac{b}{w}} \\ & + \frac{7}{4} \frac{26b - 22a}{\Delta h^{11/4}} \left(\frac{b}{w}\right)^{7/4} + \frac{1}{4} \frac{(-378a + 434b) \Delta h^{3/4}}{q_0 (\epsilon + q_1)} + \frac{1}{4} \frac{445b - 385a}{q_0 \Delta h^6 (\epsilon + q_1)} \left(\frac{b}{w}\right)^{27/4} \\ & - \frac{1}{2} \frac{217b - 189a}{q_0 (\epsilon + q_1)} \left(\frac{b}{w}\right)^{77/12} \Delta h^{-17/3} + c_5 \frac{57}{31} \left(\frac{1}{\epsilon + q_1} - \frac{q_0}{\Delta h^{7/4}}\right) \left(\Delta h^{26/31} - \Delta h^{1/20} \left(\frac{b}{w}\right)^{489/620}\right) \\ & + \frac{7}{4} c_5 \frac{q_0}{\Delta h^{11/4}} \left[\Delta h^{57/31} - \left(\frac{b}{w}\right)^{57/31} - \frac{380}{217} \left(\frac{b}{w}\right)^{489/620} \left(\Delta h^{21/20} - \left(\frac{b}{w}\right)^{21/20}\right) \right] \end{aligned} \quad (9.8)$$

(neglecting the same indices as before) is now applied.

Remark 9.4. In reference to Remark 8.1, the partial derivatives $\gamma_\epsilon(\epsilon, \Delta \mathbf{h}^{(i)})$, $\gamma_{\Delta h}(\epsilon, \Delta \mathbf{h}^{(i)})$ have to be replaced by

$$\gamma_\epsilon(\epsilon, \Delta \mathbf{h}^{(i)}) \stackrel{(9.7)}{\leftarrow} \text{sign}(\Delta \mathbf{h}^{(i)}) \odot \gamma_\epsilon(\epsilon, |\Delta \mathbf{h}^{(i)}|) \quad (9.9a)$$

$$\gamma_{\Delta h}(\epsilon, \Delta \mathbf{h}^{(i)}) \stackrel{(9.8)}{\leftarrow} \gamma_{\Delta h}(\epsilon, |\Delta \mathbf{h}^{(i)}|) \quad (9.9b)$$

$\forall i \in \mathfrak{M}$ respectively to also consider negative head losses, i.e. $\Delta \mathbf{h}^{(i)} < \mathbf{0}$.

One can write

$$\begin{aligned} \frac{\partial \boldsymbol{\gamma}^{(i)}}{\partial \boldsymbol{\epsilon}} &= \text{diag} \left(\gamma_\epsilon(\epsilon, \Delta \mathbf{h}^{(i)}) \right) = \text{diag} \left(\gamma_\epsilon^{(i)} \right) \\ \frac{\partial \boldsymbol{\gamma}^{(i)}}{\partial \mathbf{h}_N^{(i)}} &= - \text{diag} \left(\gamma_{\Delta h}(\epsilon, \Delta \mathbf{h}^{(i)}) \right) \mathbf{A}^T \bar{\mathbf{C}}_h^T = - \text{diag} \left(\gamma_{\Delta h}^{(i)} \right) \mathbf{A}^T \bar{\mathbf{C}}_h^T \end{aligned} \quad \forall i \in \mathfrak{M} \quad (9.10)$$

for the first transitional flow derivatives where, again, the main information can be stored in vectors $\gamma_\epsilon(\epsilon, \Delta \mathbf{h})$ and $\gamma_{\Delta h}(\epsilon, \Delta \mathbf{h})$ which are functions on ϵ and $\Delta \mathbf{h}$. Concerning the *Jacobian* (7.15), one then receives

$$\begin{aligned} \frac{\partial \mathbf{x}_Q(\epsilon, \Delta \mathbf{h}^{(i)})}{\partial \boldsymbol{\epsilon}} &= \text{diag} \left(\mathbf{R}_t^{(i)T} \mathbf{R}_t^{(i)} \mathbf{p}_\epsilon^{(i)} + \mathbf{R}_\gamma^{(i)T} \mathbf{R}_\gamma^{(i)} \gamma_\epsilon^{(i)} \right) \\ &= \text{diag} \left(\mathbf{r}_t^{(i)T} \odot \mathbf{p}_\epsilon^{(i)} + \mathbf{r}_\gamma^{(i)T} \odot \gamma_\epsilon^{(i)} \right) \end{aligned} \quad \forall i \in \mathfrak{M} \quad (9.11a)$$

$$\begin{aligned} \frac{\partial \mathbf{x}_Q(\epsilon, \Delta \mathbf{h}^{(i)})}{\partial \mathbf{h}_N^{(i)}} &= - \text{diag} \left(\mathbf{R}_t^{(i)T} \mathbf{R}_t^{(i)} \mathbf{p}_{\Delta h}^{(i)} + \mathbf{R}_\gamma^{(i)T} \mathbf{R}_\gamma^{(i)} \gamma_{\Delta h}^{(i)} + \mathbf{R}_l^{(i)T} \mathbf{R}_l^{(i)} \mathbf{w} \right) \mathbf{A}^T \bar{\mathbf{C}}_h^T \\ &= - \text{diag} \left(\mathbf{r}_t^{(i)T} \odot \mathbf{p}_{\Delta h}^{(i)} + \mathbf{r}_\gamma^{(i)T} \odot \gamma_{\Delta h}^{(i)} + \mathbf{r}_l^{(i)T} \odot \mathbf{w} \right) \mathbf{A}^T \bar{\mathbf{C}}_h^T \end{aligned} \quad \forall i \in \mathfrak{M} \quad (9.11b)$$

under the relieve of Assumption 7.7 in comparison to (7.21).

Second Derivatives. For the application of the *Tensor Method* (section 7.6) the second-transitional-flow derivatives would need to be determined. As the contribution of the laminar, thus linear, flow vanishes, only the second derivatives $\gamma_{\epsilon^2,j}^{(i)}$, $\gamma_{\Delta h^2,j}^{(i)}$ and $\gamma_{\epsilon\Delta h,j}^{(i)}$ concerning

$$\frac{\partial^2 \gamma_j^{(i)}}{\partial \epsilon^2} = \gamma_{\epsilon^2,j}^{(i)} \mathbf{e}_j \mathbf{e}_j^T \quad (9.12a)$$

$$\frac{\partial^2 \gamma_j^{(i)}}{\partial \mathbf{h}_N^{(i)2}} = \gamma_{\Delta h^2,j}^{(i)} \bar{\mathbf{C}}_h^T \mathbf{a}_j \mathbf{a}_j^T \bar{\mathbf{C}}_h^T \quad (9.12b)$$

$$\frac{\partial^2 \gamma_j^{(i)}}{\partial \epsilon \partial \mathbf{h}_N^{(i)}} = \frac{\partial^2 \gamma_j^{(i)}}{\partial \mathbf{h}_N^{(i)} \partial \epsilon} = -\gamma_{\epsilon\Delta h,j}^{(i)} \mathbf{A}^T \bar{\mathbf{C}}_h^T \quad (9.12c)$$

$\forall j \in \mathcal{G}^{(i)} \subseteq \mathfrak{P} \wedge i \in \mathfrak{M}$, in analogy to (7.54), would need to be determined. Mind that $\mathbf{A} = [\mathbf{a}_1 \ \mathbf{a}_2 \ \dots \ \mathbf{a}_{n_t}]$ in this context. As first-order γ -derivatives (9.7) and (9.8) are already complex, the second-order γ -derivatives, i.e. $\gamma_{\mathcal{X},j}^{(i)}$ for $\mathcal{X} \in \{\epsilon^2, \epsilon\Delta h, \Delta h^2\}$, have been neglected in this thesis.

Remark 9.5. *All results derived in section 7.6.2 to 7.6.6 concerning the Tensor Equation/Method are applicable to Ψ (9.5) by replacing partial turbulent-flow-derivatives $\mathbf{p}_{\mathcal{X}}^{(i)}$ with respect to $\mathcal{X} \in \{\epsilon, \Delta h, \epsilon^2, \epsilon\Delta h, \Delta h^2\}$ with*

$$\mathbf{p}_{\Delta h}^{(i)} \leftarrow \mathbf{r}_t^{(i)T} \odot \mathbf{p}_{\Delta h}^{(i)} + \mathbf{r}_{\gamma}^{(i)T} \odot \gamma_{\Delta h}^{(i)} + \mathbf{r}_l^{(i)T} \odot \mathbf{w} \quad (9.13a)$$

$$\mathbf{p}_{\mathcal{X}}^{(i)} \leftarrow \mathbf{r}_t^{(i)T} \odot \mathbf{p}_{\mathcal{X}}^{(i)} + \mathbf{r}_{\gamma}^{(i)T} \odot \gamma_{\mathcal{X}}^{(i)} \quad \text{with respect to } \mathcal{X} \in \{\epsilon, \epsilon\Delta h, \Delta h^2, \epsilon^2\} \quad (9.13b)$$

respectively. This particularly applies to Lemma 7.12, Theorem 7.13, Remark 7.17, Theorem 7.18, Corollary 7.19, Theorem 7.20, Remark 7.21, Remark 7.23, Proposition 7.24 and 7.25, Corollary 7.26 as well as Proposition 7.27.

Remark 9.6. *The neglect of $\gamma_{\mathcal{X},j}^{(i)}$ regarding the partial derivatives $\mathcal{X} \in \{\epsilon^2, \epsilon\Delta h, \Delta h^2\}$, pipes $j \in \mathcal{G}^{(i)} \subseteq \mathfrak{P}$ in measurement-set $i \in \mathfrak{M}$ for the Tensor-Method may actually have adverse effects in a sense that this may **mistakenly** lead to the violation of $\Delta_j^{(i)}(\boldsymbol{\alpha}^{(i)}) = 0 \wedge \hat{\Delta}_j^{(i)} \leq 0 \quad \forall j \in \mathfrak{P}$ (7.90) concerning the applicability of Theorem 7.18. In other words, one may lose separability of the Tensor Equation (7.45) (in the combined-flow case) into linear terms (as in (7.89)) when neglecting the second-transitional-flow derivatives (9.12).*

9.3 3-Cycle Network Example

Solving Ψ (9.5) for identification of the pipes' roughness, flows are allowed to become laminar in the measurement-sets while also adding measurement noise (mean-free white noise) to pressure sensors and the consumption-data (e.g. records of *fireflows*). In continuation of the 3-cycle network (figure 7.1) example, which originally started on page 83, one is finally able to draw conclusions about the real-world applicability of the developed methods.

9.3.1 Configuration

First, in order to produce sufficient head-loss to also be able to account for measurement-noise (see Assumption 7.3) and still maintain linear independency among measurement-sets \mathfrak{M} , roughnesses were reversed (in comparison to section 7.5) such that $\epsilon = [0.25 \ 0.5 \ 0.75 \ 1 \ 1.25 \ 1.5 \ 1.75 \ 2]^T$ mm.

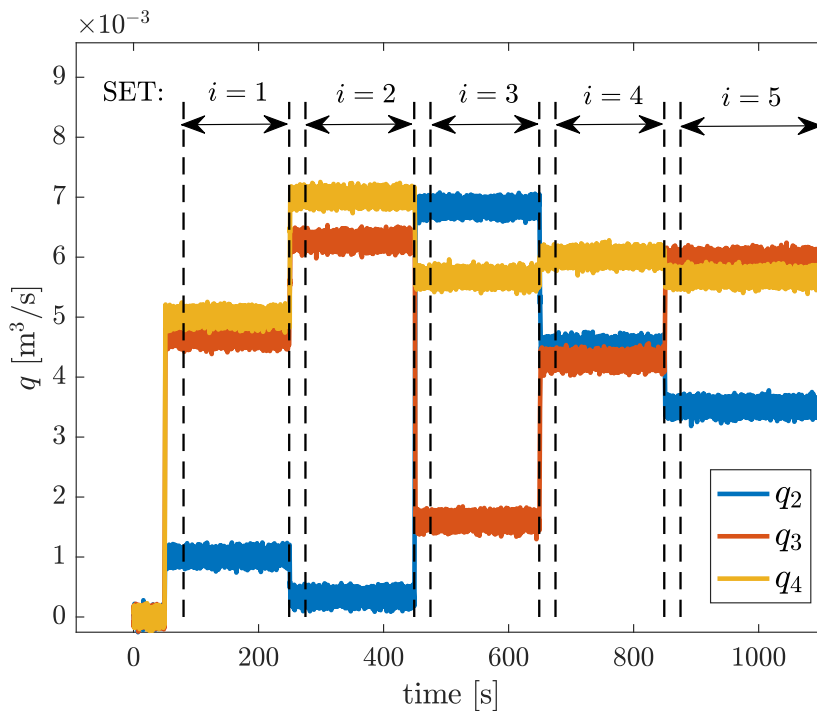
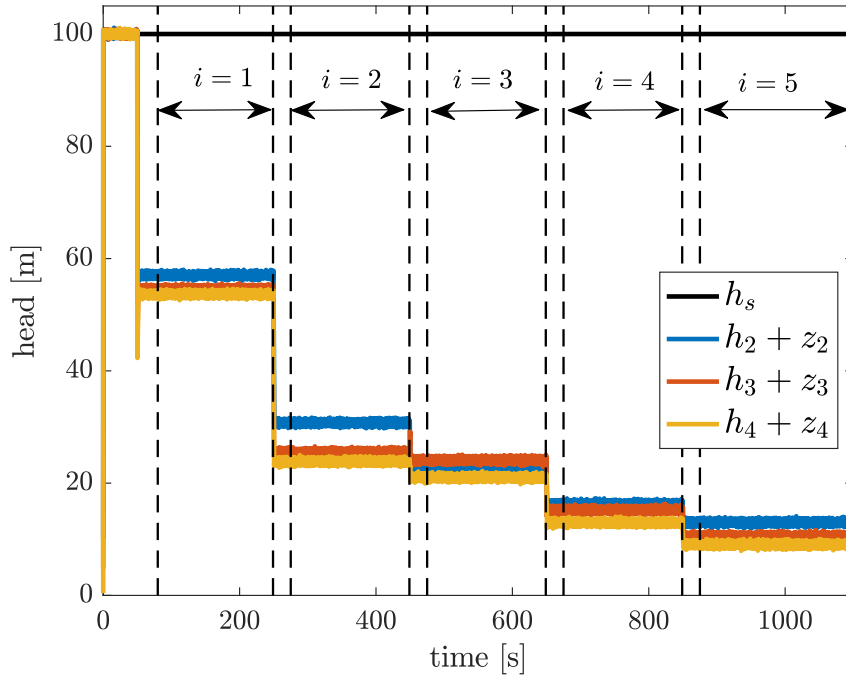
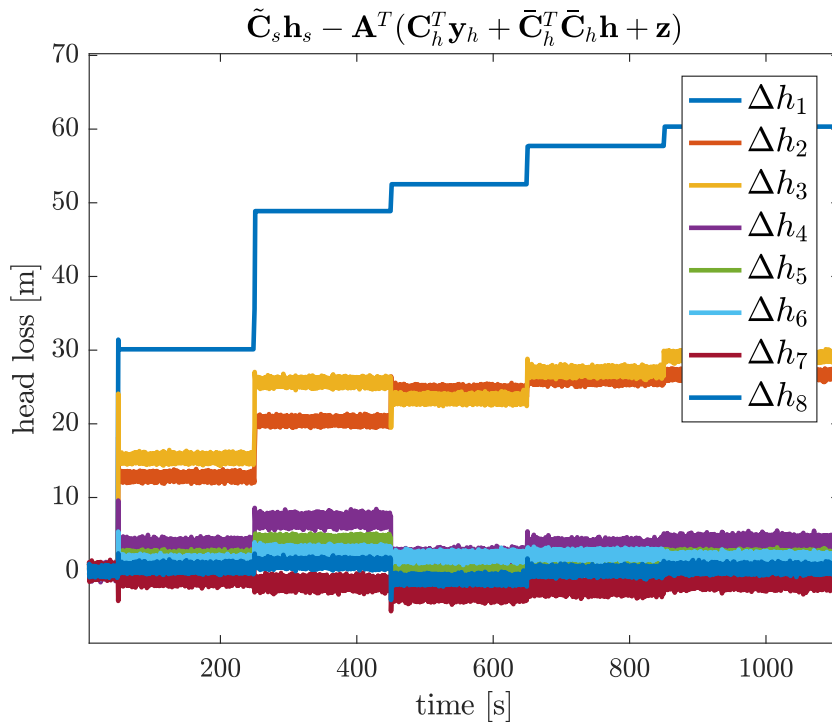


FIGURE 9.1: Consumption pattern to produce 5 independent measurement-sets.

As flow Q_1 , connected to the reservoir, will naturally have the highest flow (sum of the consumption in this case) it would also have the highest head-loss. If selecting $\epsilon_1 = 2$ mm instead of $\epsilon_1 = 0.25$ mm (the value used in this section) all the pressure head provided by the source $h_s = 100$ m is already lost before reaching consumers. This means one would need unrealistically high source pressure h_s to serve consumption values shown in figure 9.1. For analysis purposes, two measurement-sets additional to $n_{m,\min} = 3$ sets were produced to investigate performance improvements by accounting for more than $n_{m,\min}$ measurement-sets.

FIGURE 9.2: “Measured” nodal heads $\mathbf{y}_h + \mathbf{C}_h \mathbf{z}$ and source \mathbf{h}_s .FIGURE 9.3: Head losses built from the noisy \mathbf{y}_h and the not-measured \mathbf{h}_N .

Considering figure 9.2, one can already recognize that the white noise in the measured pressure heads causes some overlaps, best seen in figure 9.3 showing $\tilde{\mathbf{C}}_s \mathbf{h}_s - \mathbf{A}^T (\mathbf{C}_h^T \mathbf{y}_h + \bar{\mathbf{C}}_h^T \bar{\mathbf{C}}_h \mathbf{h} + \mathbf{z})$ which portrays head losses built from the noisy \mathbf{y}_h and the not (a-priori) known pressure heads $\mathbf{h}_N = \bar{\mathbf{C}}_h \mathbf{h}$. From figure 9.3 it is also clear that although the source pipe has the smallest roughness $\epsilon_1 = 0.25\text{mm}$, it has by far the highest head loss ($\geq 30\text{m}$) due the nonlinear friction relations. It should be emphasized that the displayed head losses in figure 9.3 are certainly not available a-priori and were provided for analysis purposes only. In this context, one can

recognize that there is particularly strong overlapping among the five inner pipes (inner cycles which are most distant from the source in figure 7.1) in terms of head losses, clearly violating Assumption 7.3. The intended violation of Assumption 7.3 is conducted to investigate negative effects on the solution finding of Ψ . This also highlights that with growing number of pipes and nodes, multiple distributed sources are necessary in a real network to maintain the supply pressure during peak-consumption events.

The quantities needed for the calibration-launch (\mathbf{q} and \mathbf{y}_h) concerning figure 9.1 and 9.2 were produced with the dynamic model PD_u (Definition 4.14) analogously to section 7.5. However, the set of “measured” values in the steady-state time-frames indicated in figure 9.1 and 9.2 were utilized for simple averaging with the aim to mitigate noise-effects (noise which was added intentionally). In this context, it is advisable to also measure real-world values with high sampling frequency, a simple measure to improve the averaging.

set	1	2	3	4	5	unit
\mathbf{h}_s	100	100	100	100	100	m
\mathbf{y}_h	47.0448	20.7637	12.9736	6.2638	2.9981	m
	49.5626	20.4885	19.1015	10.2186	5.5117	
	53.6419	23.8439	20.9840	12.9755	9.0646	
\mathbf{q}	0.9998	0.3348	6.8327	4.5018	3.5016	l/s
	4.6661	6.2667	1.6016	4.2852	5.9522	
	4.9997	6.9986	5.6647	6.0012	5.6690	
$\text{var}(\mathbf{y}_h)$	0.0825	0.0779	0.0840	0.0829	0.0815	m
	0.0799	0.0834	0.0791	0.0814	0.0813	
	0.0763	0.0817	0.0802	0.0791	0.0814	
$\text{var}(\mathbf{q}) \times 10^3$	0.5159	0.4871	0.5247	0.5179	0.5096	l/s
	0.4997	0.5212	0.4941	0.5089	0.5084	
	0.4932	0.5228	0.5246	0.4908	0.5034	
# values for averaging	1696	1740	1740	1740	2240	

TABLE 9.1: \mathbf{y}_h and \mathbf{q} values along measurement-sets after averaging whereas no noise was added to the source pressure \mathbf{h}_s . The variances of \mathbf{y}_h and \mathbf{q} have been estimated in the corresponding time-frames shown in figure 9.1 and 9.2.

set	1	2	3	4	5	unit
\mathbf{y}_h	47.0495	20.7618	12.9802	6.2606	2.9955	m
	49.5689	20.4924	19.0992	10.2152	5.5067	
	53.6446	23.8368	20.9924	12.9720	9.0648	
\mathbf{q}	1.0010	0.3343	6.8343	4.5010	3.5010	l/s
	4.6677	6.2677	1.6010	4.2843	5.9510	
	5.0010	7.0010	5.6677	6.0010	5.6677	

TABLE 9.2: Original noise-free \mathbf{y}_h and \mathbf{q} values along measurement-sets.

In view of table 9.1 and 9.2 respectively figure 9.1 and 9.2 one can recognize that the averaging turns out effective in a sense that the error in the “measurement-data” could be reduced significantly. Comparing measured pressure values \mathbf{y}_h in the current configuration (figure 9.2) with the one in the previous configuration (figure 7.3C on page 97), there are also clear indications that the current consumption configuration in this section is superior in producing independent measurement-sets as the differences in \mathbf{y}_h are vastly higher (see Assumption 7.1).

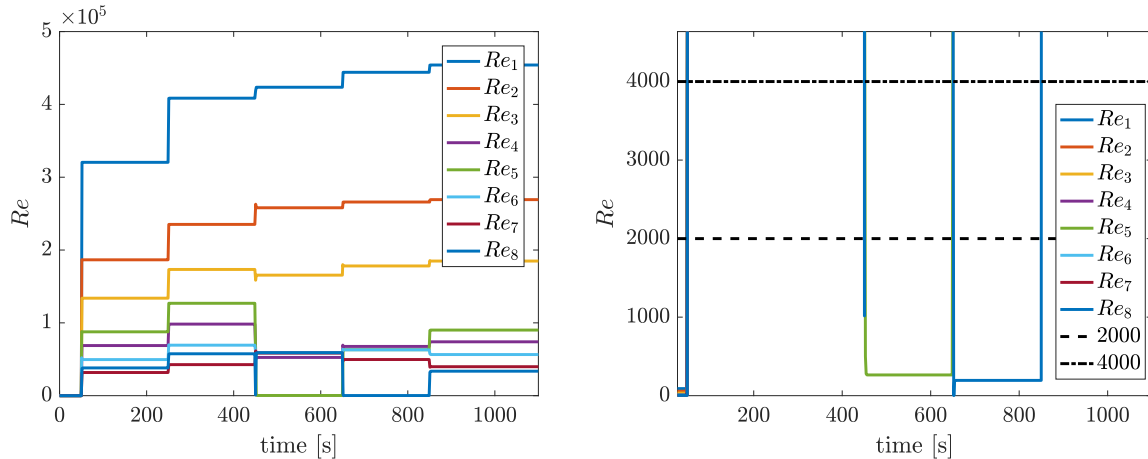


FIGURE 9.4: Reynolds numbers over time showing laminar steady-state flows $Q_5^{(3)}$ and $Q_8^{(4)}$ in set $i = 3, 4$ and no transitional (steady-state) flows.

Steady-state pipe flow 5 in measurement-set 3, i.e. $Q_5^{(3)}$, as well as steady-state pipe flow 8 in measurement-set 4, i.e. $Q_8^{(4)}$, is laminar seen in figure 9.4. Since the simulation used to produce this configuration still applies the *Dunlop* formulae (2.8) for the transitional friction factor via the Darcy-Weisbach head-loss (2.4), the consumption were varied such that no (steady-state) transitional flow results. However, as the Colebrook-White friction factor (2.6) instead of the Swamee-Jain one (2.7) is utilized for the turbulent regime, it actually does make sense to also adopt the derived transitional head loss which is given by (8.36) requiring an implicit equation to solve. This remains open for future improvements.

Two particular reasons shall be highlighted which makes this current configuration interesting. First, it will decide if the derived transitional flow γ (8.37) is eligible to provide the transition from turbulent to laminar flow in the solving of Ψ (9.5). Second, it will give insight to which extent mean-free measurement-noise in \mathbf{y}_h and \mathbf{q} interferes with the roughness-calibration.

9.3.2 Results

The following tables represent the results of the roughness-calibration (trying to solve Ψ) in the same manner as in section 7.7 whereas the same tolerances as in section 7.5 are used. This means Algorithm 4 is called for a fixed number 13 times in the outer loop which itself launches Algorithm 3 (i.e. “TensorMethod = **true**”) or Algorithm 1 (i.e. “TensorMethod = **false**”) 50 times each (fixed number). The intermediate best result in terms of $v(\mathbf{x}^+)$ is then shown in the below tables. The following initial value and range is used:

$$\begin{aligned} \mathbf{x}_0 &= \left[\epsilon_0^T \quad h_{N_0,1}^{(1)} \quad h_{N_0,5}^{(1)} \quad h_{N_0,1}^{(2)} \quad h_{N_0,5}^{(2)} \quad h_{N_0,1}^{(3)} \quad h_{N_0,5}^{(3)} \quad h_{N_0,1}^{(4)} \quad h_{N_0,5}^{(4)} \quad h_{N_0,1}^{(5)} \quad h_{N_0,5}^{(5)} \right]^T \\ &= \left[0.0004 \times \mathbf{1}_{n_\epsilon}^T \quad 70.53 \quad 55.08 \quad 52.08 \quad 26.69 \quad 49.02 \quad 22.68 \quad 43.82 \quad 14.81 \quad 41.16 \quad 10.85 \right]^T \end{aligned} \quad (9.14)$$

$$\mathbf{x}_{h_N} \stackrel{(7.36)}{=} \begin{bmatrix} 54.56 & 53.64 & 25.49 & 23.84 & 22.97 & 20.984 & 15.22 & 12.98 & 10.51 & 9.06 \\ 100 & 57.04 & 100 & 30.76 & 100 & 24.1 & 100 & 16.26 & 100 & 12.99 \end{bmatrix}^T \quad (9.15)$$

launch	1	2	3	4	5	6	7	8	9	10	11	12	13	\mathbf{x}^*
ϵ_1	0.206	0.206	0.206	0.206	0.205	0.206	0.207	0.205	0.206	0.214	0.205	0.205	0.205	0.250
ϵ_2	0.682	0.684	0.684	0.684	0.687	0.682	0.676	0.689	0.684	0.649	0.688	0.686	0.686	0.500
ϵ_3	1.047	1.050	1.050	1.049	1.056	1.047	1.037	1.058	1.050	0.991	1.057	1.054	1.052	0.750
ϵ_4	1.049	1.049	1.049	1.049	1.050	1.049	1.049	1.050	1.049	1.046	1.050	1.050	1.050	1.000
ϵ_5	1.111	1.110	1.111	1.111	1.110	1.111	1.112	1.110	1.111	1.116	1.110	1.110	1.110	1.250
ϵ_6	1.293	1.290	1.289	1.290	1.283	1.293	1.304	1.280	1.290	1.359	1.281	1.285	1.287	1.500
ϵ_7	1.983	1.987	1.987	1.987	1.996	1.983	1.968	2.001	1.987	1.894	1.999	1.994	1.991	1.750
ϵ_8	1.919	1.915	1.915	1.916	1.909	1.918	1.930	1.906	1.916	1.986	1.907	1.910	1.912	2.000
$h_{N,1}^{(1)}$	71.592	71.608	71.608	71.606	71.640	71.594	71.540	71.654	71.607	71.290	71.647	71.630	71.622	69.883
$h_{N,5}^{(1)}$	55.035	55.035	55.035	55.035	55.034	55.035	55.037	55.034	55.035	55.044	55.034	55.034	55.034	55.038
$h_{N,1}^{(2)}$	53.920	53.946	53.947	53.944	53.999	53.924	53.836	54.022	53.945	53.429	54.011	53.983	53.970	51.130
$h_{N,5}^{(2)}$	26.564	26.563	26.563	26.563	26.561	26.564	26.567	26.561	26.563	26.584	26.561	26.562	26.562	26.558
$h_{N,1}^{(3)}$	50.476	50.504	50.506	50.502	50.561	50.480	50.387	50.586	50.503	49.949	50.574	50.544	50.530	47.482
$h_{N,5}^{(3)}$	22.973	22.973	22.973	22.973	22.973	22.973	22.973	22.973	22.973	22.973	22.973	22.973	22.973	22.980
$v(\mathbf{x}^+) \times 10^7$	2.843	2.842	2.874	2.873	2.848	2.857	2.839	2.842	2.844	2.830	2.791	2.819	2.836	410.753
iter of \mathbf{x}^+	17	5	18	39	7	4	22	31	9	22	36	17	37	
average # iter to converge	4.41	20.60	18.61	18.90	24.71	8.25	3.32	48.13	19.56	9.41	33.58	22.65	15.73	

TABLE 9.3: Tensor-Results for $n_m = 3$ of Algorithm 4 along 13 launches calibrating the 3-cycle network (figure 7.1). Thereby Algorithm 4 calls Algorithm 3 (“TensorMethod=true”) for a fixed number of 50 times by tightening ϵ_f and ϵ_x in line 6 on page 95 (belonging to Algorithm 4) appropriately. Roughnesses $\epsilon_i \forall i \in \mathfrak{P}$ are presented in mm, whereas pressure heads $h_{N,j}^{(i)} \forall i \in \mathfrak{M} \wedge j \in \bar{\mathcal{P}}$ are presented in m. Computational duration: 280.004028s

launch	1	2	3	4	5	6	7	8	9	10	11	12	13	\mathbf{x}^*
ϵ_1	0.206	0.207	0.206	0.208	0.206	0.206	0.206	0.206	0.206	0.206	0.206	0.206	0.207	0.250
ϵ_2	0.681	0.680	0.682	0.672	0.682	0.682	0.682	0.682	0.682	0.682	0.681	0.682	0.680	0.500
ϵ_3	1.045	1.044	1.047	1.029	1.047	1.046	1.047	1.047	1.047	1.047	1.046	1.046	1.043	0.750
ϵ_4	1.049	1.049	1.049	1.048	1.049	1.049	1.049	1.049	1.049	1.049	1.049	1.049	1.049	1.000
ϵ_5	1.111	1.111	1.111	1.113	1.111	1.111	1.111	1.111	1.111	1.111	1.111	1.111	1.111	1.250
ϵ_6	1.295	1.296	1.292	1.312	1.292	1.293	1.292	1.292	1.292	1.293	1.294	1.294	1.297	1.500
ϵ_7	1.980	1.978	1.983	1.955	1.983	1.982	1.983	1.983	1.983	1.982	1.981	1.981	1.976	1.750
ϵ_8	1.921	1.922	1.918	1.939	1.918	1.919	1.918	1.918	1.918	1.919	1.920	1.920	1.923	2.000
$h_{N,1}^{(1)}$	71.583	71.577	71.594	71.499	71.594	71.589	71.594	71.594	71.594	71.591	71.586	71.587	71.572	69.883
$h_{N,5}^{(1)}$	55.036	55.036	55.035	55.038	55.035	55.035	55.035	55.035	55.035	55.035	55.035	55.035	55.036	55.038
$h_{N,1}^{(2)}$	53.906	53.896	53.925	53.769	53.924	53.916	53.924	53.924	53.924	53.919	53.910	53.913	53.888	51.130
$h_{N,5}^{(2)}$	26.565	26.565	26.564	26.570	26.564	26.564	26.564	26.564	26.564	26.564	26.565	26.565	26.565	26.558
$h_{N,1}^{(3)}$	50.462	50.451	50.481	50.315	50.481	50.472	50.480	50.481	50.481	50.475	50.466	50.469	50.441	47.482
$h_{N,5}^{(3)}$	22.973	22.973	22.973	22.973	22.973	22.973	22.973	22.973	22.973	22.973	22.973	22.973	22.973	22.980
$v(\mathbf{x}^+) \times 10^7$	2.898	2.899	2.902	2.882	2.902	2.901	2.902	2.902	2.902	2.901	2.900	2.902	2.896	410.753
iter of \mathbf{x}^+	44	22	21	46	42	39	46	20	31	44	43	33	27	
average # iter to converge	9.27	10.45	10.95	9.07	8.48	9.31	9.33	10.90	10.03	9.34	9.93	9.79	9.56	

TABLE 9.4: Newton-Results for $n_m = 3$ of Algorithm 4 along 13 launches calibrating the 3-cycle network (figure 7.1). Thereby Algorithm 4 calls Algorithm 1 (“TensorMethod=false”) for a fixed number of 50 times by tightening ϵ_f and ϵ_x in line 6 on page 95 (belonging to Algorithm 4) appropriately. Roughnesses $\epsilon_i \forall i \in \mathfrak{P}$ are presented in mm, whereas pressure heads $h_{N,j}^{(i)} \forall i \in \mathfrak{M} \wedge j \in \bar{\mathcal{P}}$ are presented in m. Computational duration 7.254637s

launch	1	2	3	4	5	6	7	8	9	10	11	12	13	\mathbf{x}^*
ϵ_1	0.220	0.220	0.219	0.220	0.219	0.220	0.219	0.219	0.219	0.220	0.220	0.220	0.219	0.250
ϵ_2	0.624	0.624	0.624	0.624	0.624	0.624	0.624	0.625	0.625	0.624	0.624	0.624	0.624	0.500
ϵ_3	0.943	0.943	0.944	0.943	0.944	0.943	0.944	0.945	0.944	0.943	0.943	0.944	0.944	0.750
ϵ_4	1.002	1.002	1.002	1.002	1.002	1.002	1.002	1.002	1.002	1.002	1.002	1.002	1.002	1.000
ϵ_5	1.188	1.188	1.187	1.188	1.187	1.188	1.187	1.187	1.187	1.188	1.188	1.187	1.187	1.250
ϵ_6	1.406	1.406	1.405	1.406	1.406	1.406	1.405	1.405	1.405	1.406	1.406	1.406	1.405	1.500
ϵ_7	1.894	1.894	1.894	1.894	1.894	1.894	1.894	1.894	1.894	1.894	1.894	1.894	1.894	1.750
ϵ_8	1.952	1.952	1.951	1.952	1.951	1.951	1.951	1.951	1.951	1.952	1.951	1.951	1.951	2.000
$h_{N,1}^{(1)}$	71.047	71.048	71.053	71.048	71.052	71.049	71.053	71.057	71.054	71.048	71.049	71.050	71.054	69.883
$h_{N,5}^{(1)}$	55.033	55.033	55.033	55.033	55.033	55.033	55.033	55.033	55.033	55.033	55.033	55.033	55.033	55.038
$h_{N,1}^{(2)}$	53.032	53.033	53.042	53.034	53.041	53.035	53.042	53.049	53.044	53.034	53.035	53.037	53.044	51.130
$h_{N,5}^{(2)}$	26.559	26.559	26.559	26.559	26.559	26.559	26.559	26.559	26.559	26.559	26.559	26.559	26.559	26.558
$h_{N,1}^{(3)}$	49.524	49.526	49.535	49.527	49.534	49.528	49.535	49.542	49.537	49.526	49.527	49.530	49.537	47.482
$h_{N,5}^{(3)}$	22.973	22.973	22.973	22.973	22.973	22.973	22.973	22.973	22.973	22.973	22.973	22.973	22.973	22.980
$h_{N,1}^{(4)}$	44.540	44.542	44.552	44.543	44.550	44.544	44.551	44.560	44.554	44.542	44.543	44.546	44.554	42.286
$h_{N,5}^{(4)}$	15.219	15.219	15.219	15.219	15.219	15.219	15.219	15.219	15.219	15.219	15.219	15.219	15.219	15.215
$v(\mathbf{x}^+) \times 10^7$	10.385	10.179	10.102	10.252	10.264	10.224	10.285	10.213	9.916	10.200	10.227	10.277	10.264	652.087
iter of \mathbf{x}^+	29	35	25	37	30	15	19	29	19	26	42	28	42	
average # iter to converge	9.21	9.14	5.16	7.08	12.33	9.00	5.95	3.79	7.68	7.38	8.67	9.07	9.60	

TABLE 9.5: Tensor-Results for $n_m = 4$ of Algorithm 4 along 13 launches calibrating the 3-cycle network (figure 7.1). Thereby Algorithm 4 calls Algorithm 3 (“TensorMethod=true”) for a fixed number of 50 times by tightening ϵ_f and ϵ_x in line 6 on page 95 (belonging to Algorithm 4) appropriately. Roughnesses $\epsilon_i \forall i \in \mathfrak{P}$ are presented in mm, whereas pressure heads $h_{N,j}^{(i)} \forall i \in \mathfrak{M} \wedge j \in \bar{\mathcal{P}}$ are presented in m. Computational duration: 143.616633s.

launch	1	2	3	4	5	6	7	8	9	10	11	12	13	\mathbf{x}^*
ϵ_1	0.220	0.220	0.220	0.220	0.220	0.220	0.220	0.220	0.220	0.220	0.220	0.220	0.220	0.250
ϵ_2	0.623	0.623	0.623	0.623	0.623	0.623	0.623	0.623	0.623	0.623	0.623	0.623	0.623	0.500
ϵ_3	0.943	0.943	0.943	0.943	0.943	0.943	0.943	0.943	0.943	0.943	0.943	0.943	0.943	0.750
ϵ_4	1.002	1.002	1.002	1.002	1.002	1.002	1.002	1.002	1.002	1.002	1.002	1.002	1.002	1.000
ϵ_5	1.188	1.188	1.188	1.188	1.188	1.188	1.188	1.188	1.188	1.188	1.188	1.188	1.188	1.250
ϵ_6	1.406	1.406	1.406	1.406	1.406	1.406	1.406	1.406	1.406	1.406	1.406	1.406	1.406	1.500
ϵ_7	1.894	1.894	1.894	1.894	1.894	1.894	1.894	1.894	1.894	1.894	1.894	1.894	1.894	1.750
ϵ_8	1.952	1.952	1.952	1.952	1.952	1.952	1.952	1.952	1.952	1.952	1.952	1.952	1.952	2.000
$h_{N,1}^{(1)}$	71.044	71.044	71.044	71.043	71.043	71.044	71.044	71.044	71.044	71.044	71.044	71.044	71.044	69.883
$h_{N,5}^{(1)}$	55.033	55.033	55.033	55.033	55.033	55.033	55.033	55.033	55.033	55.033	55.033	55.033	55.033	55.038
$h_{N,1}^{(2)}$	53.027	53.027	53.027	53.026	53.026	53.027	53.027	53.027	53.027	53.027	53.027	53.027	53.027	51.130
$h_{N,5}^{(2)}$	26.559	26.559	26.559	26.559	26.559	26.559	26.559	26.559	26.559	26.559	26.559	26.559	26.559	26.558
$h_{N,1}^{(3)}$	49.519	49.519	49.519	49.518	49.518	49.519	49.519	49.519	49.519	49.519	49.519	49.519	49.519	47.482
$h_{N,5}^{(3)}$	22.973	22.973	22.973	22.973	22.973	22.973	22.973	22.973	22.973	22.973	22.973	22.973	22.973	22.980
$h_{N,1}^{(4)}$	44.534	44.534	44.534	44.533	44.533	44.534	44.534	44.534	44.534	44.534	44.534	44.534	44.535	42.286
$h_{N,5}^{(4)}$	15.219	15.219	15.219	15.219	15.219	15.219	15.219	15.219	15.219	15.219	15.219	15.219	15.219	15.215
$v(\mathbf{x}^+) \times 10^7$	10.510	10.510	10.509	10.510	10.510	10.510	10.509	10.509	10.510	10.510	10.510	10.509	10.510	652.087
iter of \mathbf{x}^+	27	15	27	42	44	50	10	17	18	4	38	26	23	
average # iter to converge	4.56	5.07	4.26	4.31	4.66	4.64	5.00	4.94	4.56	8.50	4.61	4.77	4.83	

TABLE 9.6: Newton-Results for $n_m = 4$ of Algorithm 4 along 13 launches calibrating the 3-cycle network (figure 7.1). Thereby Algorithm 4 calls Algorithm 1 (“TensorMethod=false”) for a fixed number of 50 times by tightening ϵ_f and ϵ_x in line 6 on page 95 (belonging to Algorithm 4) appropriately. Roughnesses $\epsilon_i \forall i \in \mathfrak{P}$ are presented in mm, whereas pressure heads $h_{N,j}^{(i)} \forall i \in \mathfrak{M} \wedge j \in \bar{\mathcal{P}}$ are presented in m. Computational duration: 4.429753s.

launch	1	2	3	4	5	6	7	8	9	10	11	12	13	\mathbf{x}^*
ϵ_1	0.194	0.195	0.195	0.194	0.195	0.195	0.195	0.195	0.195	0.195	0.194	0.195	0.195	0.250
ϵ_2	0.742	0.741	0.741	0.742	0.741	0.741	0.741	0.741	0.741	0.741	0.742	0.741	0.741	0.500
ϵ_3	1.121	1.119	1.119	1.121	1.119	1.119	1.119	1.119	1.119	1.119	1.121	1.120	1.119	0.750
ϵ_4	1.059	1.059	1.059	1.059	1.059	1.059	1.059	1.059	1.059	1.059	1.060	1.059	1.059	1.000
ϵ_5	1.092	1.092	1.092	1.092	1.092	1.092	1.092	1.092	1.092	1.092	1.091	1.092	1.092	1.250
ϵ_6	1.308	1.308	1.308	1.308	1.308	1.308	1.308	1.308	1.308	1.308	1.307	1.308	1.309	1.500
ϵ_7	1.943	1.942	1.942	1.943	1.943	1.943	1.943	1.943	1.942	1.942	1.943	1.943	1.942	1.750
ϵ_8	1.919	1.919	1.919	1.919	1.919	1.919	1.919	1.919	1.919	1.919	1.919	1.919	1.919	2.000
$h_{N,1}^{(1)}$	72.064	72.056	72.056	72.063	72.057	72.057	72.057	72.057	72.056	72.055	72.067	72.058	72.054	69.883
$h_{N,5}^{(1)}$	55.040	55.040	55.040	55.040	55.040	55.040	55.040	55.040	55.040	55.040	55.040	55.040	55.040	55.038
$h_{N,1}^{(2)}$	54.688	54.675	54.675	54.687	54.677	54.677	54.677	54.677	54.674	54.674	54.692	54.678	54.673	51.130
$h_{N,5}^{(2)}$	26.575	26.575	26.575	26.575	26.575	26.575	26.575	26.575	26.575	26.575	26.575	26.575	26.575	26.558
$h_{N,1}^{(3)}$	51.307	51.292	51.293	51.305	51.295	51.295	51.294	51.294	51.292	51.291	51.311	51.296	51.290	47.482
$h_{N,5}^{(3)}$	22.973	22.973	22.973	22.973	22.973	22.973	22.973	22.973	22.973	22.973	22.973	22.973	22.973	22.980
$h_{N,1}^{(4)}$	46.500	46.483	46.484	46.498	46.486	46.486	46.486	46.486	46.483	46.482	46.505	46.488	46.481	42.286
$h_{N,5}^{(4)}$	15.219	15.219	15.219	15.219	15.219	15.219	15.219	15.219	15.219	15.219	15.219	15.219	15.219	15.215
$h_{N,1}^{(5)}$	44.075	44.058	44.059	44.073	44.061	44.061	44.061	44.060	44.058	44.057	44.080	44.063	44.055	39.662
$h_{N,5}^{(5)}$	10.882	10.882	10.882	10.882	10.882	10.882	10.882	10.882	10.882	10.882	10.882	10.882	10.882	10.872
$v(\mathbf{x}^+) \times 10^7$	30.309	30.419	30.352	30.348	30.359	30.356	30.377	30.168	30.360	30.324	30.349	30.324	30.416	679.963
iter of \mathbf{x}^+	30	36	44	38	49	24	40	22	11	45	35	19	20	
average # iter to converge	5.60	9.72	10.36	3.47	4.78	6.58	5.60	6.05	8.64	6.24	4.34	6.89	12.20	

TABLE 9.7: Tensor-Results for $n_m = 5$ of Algorithm 4 along 13 launches calibrating the 3-cycle network (figure 7.1). Thereby Algorithm 4 calls Algorithm 3 (“TensorMethod=true”) for a fixed number of 50 times by tightening ϵ_f and ϵ_x in line 6 on page 95 (belonging to Algorithm 4) appropriately. Roughnesses $\epsilon_i \forall i \in \mathfrak{P}$ are presented in mm, whereas pressure heads $h_{N,j}^{(i)} \forall i \in \mathfrak{M} \wedge j \in \bar{\mathcal{P}}$ are presented in m. Computational duration: 164.804157s.

launch	1	2	3	4	5	6	7	8	9	10	11	12	13	\mathbf{x}^*
ϵ_1	0.195	0.195	0.195	0.195	0.195	0.195	0.195	0.195	0.195	0.195	0.195	0.195	0.195	0.250
ϵ_2	0.740	0.740	0.741	0.740	0.740	0.741	0.740	0.740	0.741	0.741	0.741	0.741	0.741	0.500
ϵ_3	1.118	1.118	1.119	1.118	1.118	1.118	1.118	1.118	1.119	1.119	1.119	1.118	1.119	0.750
ϵ_4	1.058	1.057	1.058	1.058	1.058	1.059	1.058	1.058	1.059	1.059	1.058	1.059	1.058	1.000
ϵ_5	1.093	1.093	1.092	1.093	1.093	1.092	1.092	1.093	1.092	1.092	1.093	1.093	1.092	1.250
ϵ_6	1.309	1.309	1.309	1.309	1.309	1.308	1.309	1.309	1.308	1.308	1.309	1.309	1.308	1.500
ϵ_7	1.942	1.942	1.942	1.942	1.942	1.942	1.942	1.942	1.942	1.942	1.942	1.942	1.942	1.750
ϵ_8	1.919	1.919	1.919	1.919	1.919	1.919	1.919	1.919	1.919	1.919	1.919	1.919	1.919	2.000
$h_{N,1}^{(1)}$	72.049	72.050	72.053	72.051	72.051	72.054	72.051	72.050	72.055	72.055	72.054	72.052	72.054	69.883
$h_{N,5}^{(1)}$	55.040	55.040	55.040	55.040	55.040	55.040	55.040	55.040	55.040	55.040	55.040	55.040	55.040	55.038
$h_{N,1}^{(2)}$	54.664	54.665	54.671	54.667	54.667	54.672	54.667	54.666	54.673	54.673	54.671	54.668	54.672	51.130
$h_{N,5}^{(2)}$	26.575	26.575	26.575	26.575	26.575	26.575	26.575	26.575	26.575	26.575	26.575	26.575	26.575	26.558
$h_{N,1}^{(3)}$	51.281	51.282	51.288	51.284	51.284	51.289	51.284	51.283	51.291	51.291	51.289	51.286	51.290	47.482
$h_{N,5}^{(3)}$	22.973	22.973	22.973	22.973	22.973	22.973	22.973	22.973	22.973	22.973	22.973	22.973	22.973	22.980
$h_{N,1}^{(4)}$	46.472	46.473	46.479	46.475	46.475	46.480	46.475	46.473	46.482	46.482	46.480	46.476	46.481	42.286
$h_{N,5}^{(4)}$	15.219	15.219	15.219	15.219	15.219	15.219	15.219	15.219	15.219	15.219	15.219	15.219	15.219	15.215
$h_{N,1}^{(5)}$	44.046	44.047	44.053	44.049	44.049	44.054	44.049	44.047	44.057	44.056	44.054	44.050	44.055	39.662
$h_{N,5}^{(5)}$	10.882	10.882	10.882	10.882	10.882	10.882	10.882	10.882	10.882	10.882	10.882	10.882	10.882	10.872
$v(\mathbf{x}^+) \times 10^7$	29.876	29.345	29.571	29.802	30.400	29.596	30.055	29.790	30.685	30.108	29.773	30.372	30.524	679.963
iter of \mathbf{x}^+	30	41	33	12	4	9	9	37	18	10	22	12	19	
average # iter to converge	4.40	4.15	4.42	5.00	6.25	5.00	5.11	4.03	4.94	6.50	4.77	5.00	4.47	

TABLE 9.8: Newton-Results for $n_m = 5$ of Algorithm 4 along 13 launches calibrating the 3-cycle network (figure 7.1). Thereby Algorithm 4 calls Algorithm 1 (“TensorMethod=false”) for a fixed number of 50 times by tightening ϵ_f and ϵ_x in line 6 on page 95 (belonging to Algorithm 4) appropriately. Roughnesses $\epsilon_i \forall i \in \mathfrak{P}$ are presented in mm, whereas pressure heads $h_{N,j}^{(i)} \forall i \in \mathfrak{M} \wedge j \in \bar{\mathcal{P}}$ are presented in m. Computational duration: 7.027230s.

9.3.3 Discussion

In comparison to the previous simulation results in section 7.7 one can see that the results in tables 9.3 to 9.8 of Algorithm 4 either calling Algorithm 1 or Algorithm 3 are noticeably consistent. Conducting more intensive computations with different initial values and more iterations/launches (beyond the ones indicated), the author is confident to claim that the presented results can be considered global in a sense that no (significantly different) solution was found with a noticeably smaller residual $v(\mathbf{x})$. The consistency among the presented results can presumably be explained by the fact that the presented results better suffice Assumption 7.1, meaning that independency among measurement-sets of this configuration is superior to the one in section 7.7 concerning the variation of \mathbf{q} . In this context, one can see that the residual of the results is approximately two orders of magnitude smaller than the one of the real root $v(\mathbf{x}^*)$ (especially in table 9.3 and 9.4).

Concerning the regime-case-separation, the *Tensor* as well as *Newton* method managed to successfully identify $Q_5^{(3)}$ (in case $n_m = 3$) as well as $Q_5^{(3)} \wedge Q_8^{(4)}$ (in case $n_m = 4, 5$) as laminar and all other steady-state flows as turbulent. Although remarkable, this is presumably only accomplished due to Reynolds numbers of laminar flows $Q_5^{(3)} \wedge Q_8^{(4)}$ being sufficiently distant to the boundary $Re = 2000$ (seen in figure 9.4). This proves the applicability of γ (8.37) for the complete roughness calibration problem Ψ (9.5). Not only that, the consideration of laminar flows improves reconstructability of original roughnesses as the known linear (laminar) terms indeed facilitate the solving of Ψ . This can be seen when comparing tables considering $n_m = 4$ with ones considering $n_m = 5$ measurement-sets as the results in former ones are much closer to the original root. The fact that it took approximately ten times longer to compute results in table 7.8 and 7.9 (the full-turbulent case) compared to the computational duration of the results in the above tables applying the same tolerances of Algorithm 1 & 3, also underlines the facilitation of the Ψ -solving. In other words, the inclusion of measurement-set $i = 5$ in the problem set-up aggravates the solution finding as uncertainties additionally disguise the desired residual $v(\mathbf{x}^*)$ in the solution space.

Comparing *Tensor* with *Newton* results for all n_m no significant improvements could be achieved when considering the second order derivatives concerning the *Tensor-Method*. Actually, a slightly smaller residual was found by the *Newton-Method* for $n_m = 5$ comparing table 9.7 with table 9.8. Why is that? First, it has to be expected that the neglect of the second derivatives of γ (see Remark 9.6) is problematic in the solution finding of the search direction via the *Tensor-Equation* (7.60). Second, trying to solve (7.60) iteratively with the MATLAB built-in *fsolve*(.) function, it occasionally happens that a search direction is taken which has a comparably high residual of $\mathbf{m}_k^{(i)} \neq 0$ (7.60) in solving iteration k of Ψ . In this context, one can also see that the *Tensor-Method* indeed takes more iterations on average (rows: “average # iter to converge”) to converge or abort. Third, as long as measurement-sets are sufficiently independent, the application of the *Newton-Method* might presumably suffice in combination with Algorithm 4 to obtain a solution which features an even smaller residual $v(\mathbf{x}^+)$ than the original root $v(\mathbf{x}^*)$.

In view of the results in the above tables, the comparably high deviation in the solution of the not-measured pressure head at node 1, i.e. $h_{N,1}^{(i)} \forall i \in \mathfrak{M}$, is also noteworthy. The deviation in $h_{N,1}^{(i)}$ is inherently connected with the deviation in the roughness of the first pipe. Although the estimated roughness of the first pipe, i.e. ϵ_1 , is arguably close to the original one ϵ_1^* in all the above tables (particularly when $n_m = 4$) the error in $h_{N,1}^{(i)} \forall i \in \mathfrak{M}$ is eye-catching. The major reason for this can again be found in the non-linear friction relation, where comparably small differences in roughness lead to a substantial deviation in the head-loss and thus in the nodal head due to the high flow in pipe 1.

In sum, the collection of suitable measurement-sets is key for the reconstruction of the pipes’

roughness. The arguably best indicator for the quality of the measurement-sets is given by the differences among $\mathbf{y}_h + \mathbf{C}_h \mathbf{z}$ and the differences in the consumption \mathbf{q} . However, when considering minor-losses (violating Assumption 7.4), i.e. non-zero parameters $\mathbf{k}_m \neq \mathbf{0}$, and measurement-noise which features a non-zero mean, the solving of Ψ becomes substantially more delicate in a sense that one commonly receives estimated roughnesses outside their physical range (above 5% of the pipe's diameter). These solutions, which lie outside the considered physical range, sometimes indeed have a comparably low residual, due to the aggressive search by Algorithm 4 which has some global convergence properties. Nevertheless, in the opinion of the author, the solving of problem Ψ (9.5) offers the best chance to reconstruct individual roughnesses per pipe. However, it is very common to group pipes' roughnesses for the solution finding, meaning to assign a single roughness value to multiple pipes in order to compensate for additional unknowns. This procedure may potentially hinder the parameter-identifiability and therefore the ability to locate/detect leakages.

In short, the above example gives valuable insights about the applicability of the presented roughness-calibration scheme as:

- adverse effects due to measurement-noise have been studied
- the consideration of laminar flows turns out to facilitate the solving of Ψ
- the functionality of γ (8.37) to allow a transition from turbulent to laminar flow (or vice versa) in the solution-finding of Ψ has been demonstrated
- the analysis of considering more than $n_{m,\min}$ measurement-sets reveals, that it does not always facilitate the solving of Ψ , but a careful selection of measurement-sets may be necessary

Roughness Identification on a Real Network

The application of the roughness-identification, as it was presented in chapter 7 and 9, on the drinking-water-distribution-network of Graz-Ragnitz will clarify the legitimacy of the assumptions of table 7.1 and Assumption 9.3 in real-world scenarios. The measurements used for this analysis were conducted *prior* to the involvement of the author with the help of the local water-utility in the course of a project with the *Institute of Urban Water Management* (Graz University of Technology). The author expresses special thanks to *Daniela Fuchs-Hanusch* who provided these data.

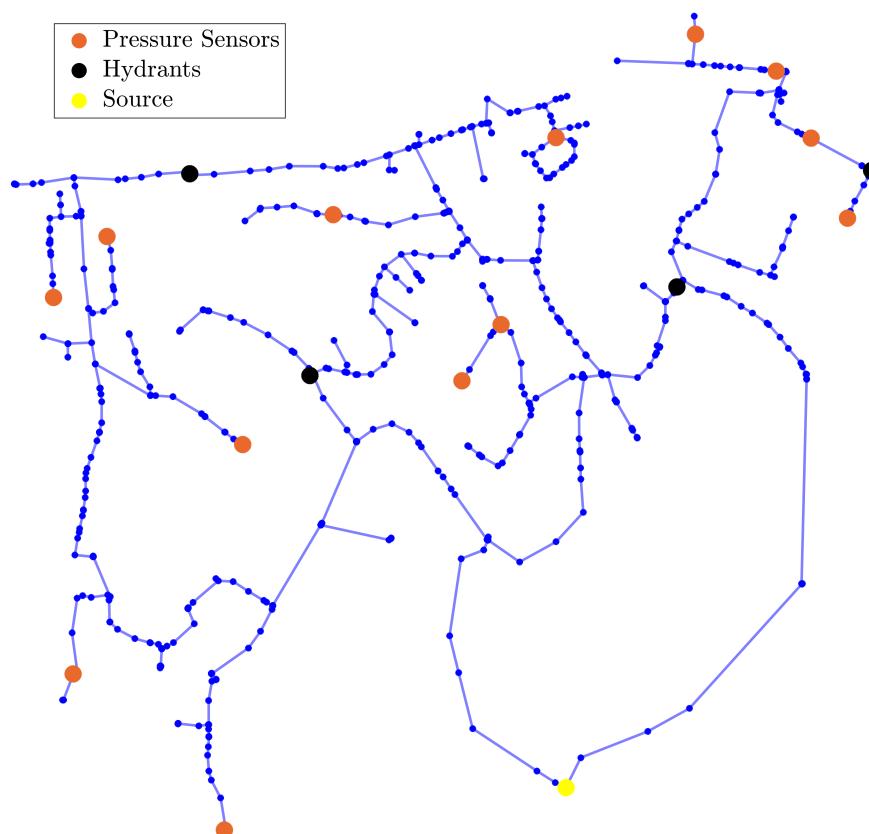


FIGURE 10.1: Original graph representing the water-distribution network of Graz-Ragnitz with about 10.17km of total pipe length. Nodes with pressure sensors, hydrants and the source (a reservoir-like water-basin) are highlighted.

10.1 Topology Simplification

During the time-frame where measurements have been recorded, the network according to figure 10.1 was isolated by valves from other parts connecting itself to a larger distribution network. The topology of this isolated network (part) as presented in figure 10.1 features:

# pipes	$n_\ell = 654$
# inner nodes	$n_j = 650$
# cycles	$n_c = n_\ell - n_j = 4$
# sources	$n_s = 1$
# hydrants	$n_q = 4$
# pressure-nodes	$n_p = 13$

TABLE 10.1: Characterization of the original topology according to figure 10.1.

The fact that only $n_c = 4$ cycles are present to provide redundancy to the water-supply is relativized when those valves, which were closed for the isolation of the presented network part in figure 10.1, are reopened. Nevertheless, given the number of pipes $n_\ell = 654$ and pressure-sensors $n_p = 13$, one would need to produce at least $\lceil n_\ell/n_p \rceil = 51$ independent measurement-sets with only $n_q = 4$ fireflows. It is reasonable to assume that there is no way to produce so many independent measurement-sets, especially on a high fireflow-level necessary to produce enough head-loss (in reference to Assumption 7.3). The only chance is to simplify the topology to the highest extent possible and thereby reduce the number of pipes and nodes in order to result in a sufficiently small $n_{m,\min} = \lceil n_\ell/n_p \rceil$.

Dead-Ends. The first step of the topology-simplification involves the removal of dead-ends which have been colored in green in figure 10.2. These dead-ends also include nodes which represent real consumer (not hydrants) in the original topology. However, as it has to be assumed that they do not retrieve water during the calibration-measurements (at night), they have to be removed as no corresponding roughness values can be identified.

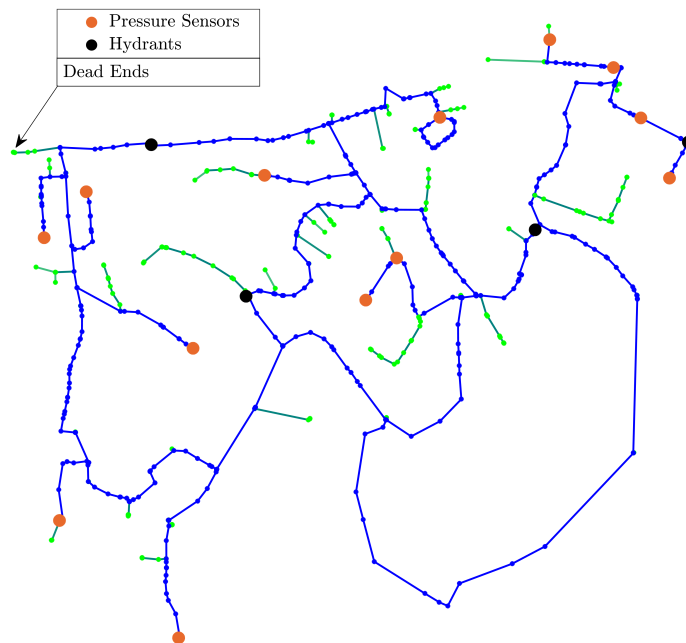


FIGURE 10.2: Dead-Ends.

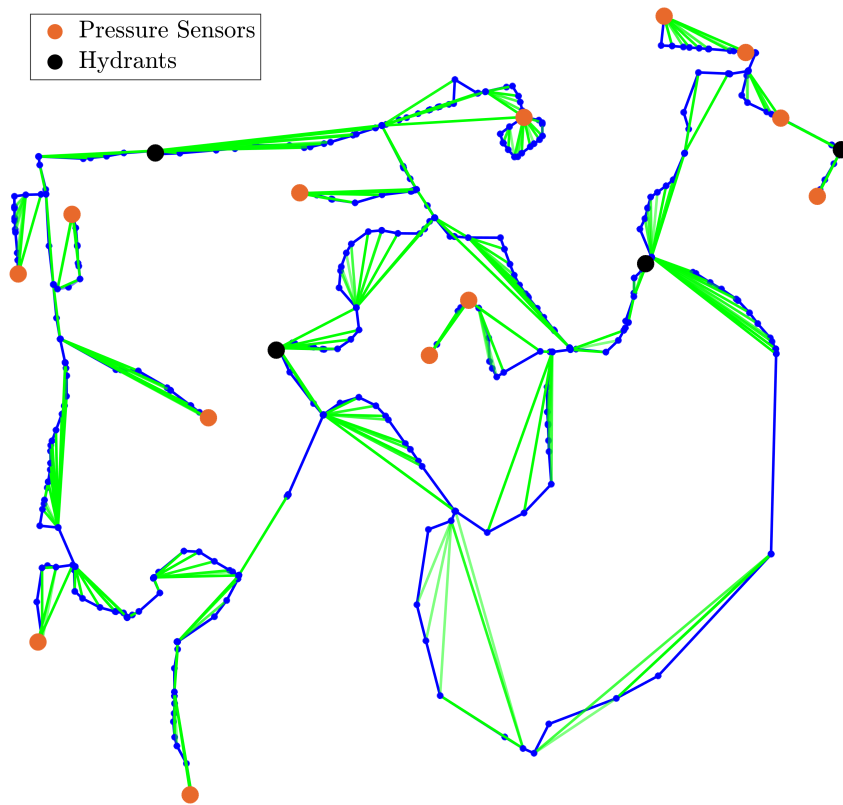


FIGURE 10.3: Combining adjoining pipes with same diameter iteratively.

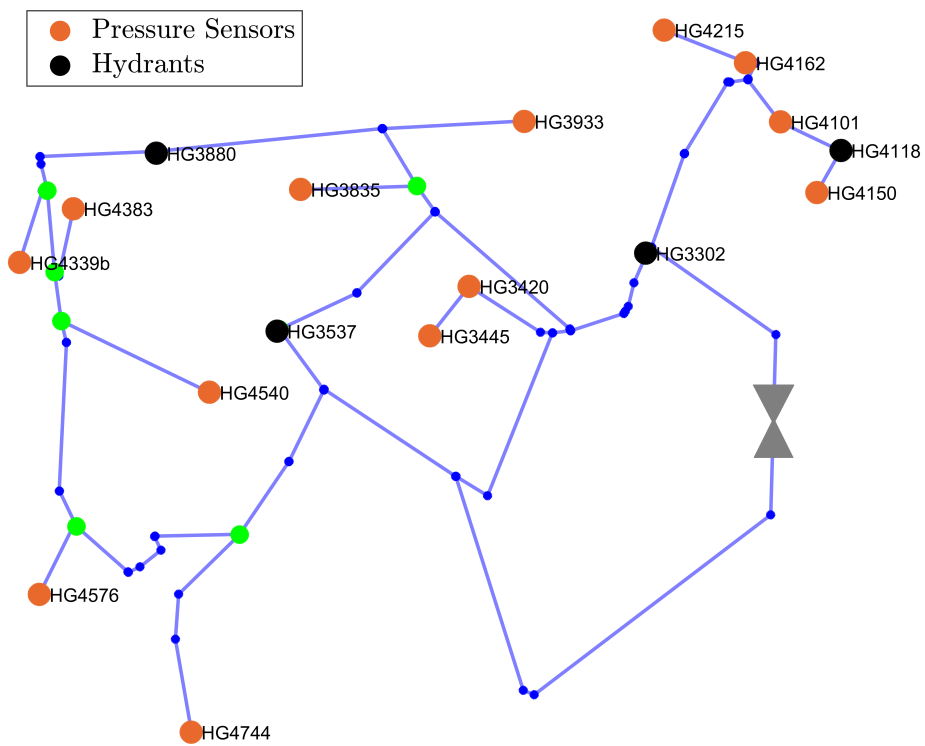


FIGURE 10.4: Result of combining adjoining pipes with same diameter also highlighting some nodes with more than two connections (yellow) and a valve (gray).

Combine Adjoining Pipes with Same Diameter. The next step involves the detection and then combination of adjoining pipes with the same diameter by removing the node in between, i.e. the new combined pipe’s length has to be adjusted. Pressure- and hydrant-nodes do certainly have to be excluded from this removal.

In figure 10.4 one can see the result of the iterative rejoining of pipes with the same diameter, seen in figure 10.3. In this process the x, y -coordinates of the original nodes have been preserved which causes, for instance, the small cycle at ‘HG3933’ seen in figure 10.3 to seemingly disappear in figure 10.4. The reader shall be assured that this cycle is still present in the graph of figure 10.4 at this point of simplification, however, one would have to zoom in substantially.

Remapping Pressure-Nodes and Hydrant-Nodes. This paragraph lists 4 measures, denoted by (a)-(d), to simplify the graph’s topology. First (a), as pressure-nodes with no hydrants on the same link do not have any head-loss along this link, it is feasible to remap the pressure-nodes to the next respective junction (more than two connections). In the course of this process, one has to carefully consider the difference in elevation between the pressure-node and the final junction node (where it is intended to be moved) as the height-difference has to be considered in the corresponding pressure-readings. When looking at figure 10.4, for instance, the pressure-nodes (nodes with pressure-sensor, Definition 7.8) are moved to the yellow-colored junctions.

Second (b), it turned out that two deployed pressure sensors, namely ‘HG3445’ and ‘HG4215’ are redundant for all measurements-sets, i.e. ‘HG3420’ and ‘HG3445’ or ‘HG4162’ and ‘HG4215’ have to have the same pressure-readings as there should be no flow in the links of these two sensor-pairs. As the head-readings shown in figure 10.5 of these respective sensors confirm their redundancy, corresponding nodes are removed from the graph. This then enables to move pressure-nodes ‘HG3420’ and ‘HG4215’ to the next higher junction (more than two connections), thereby also taking care of the nodes’ elevation-difference.

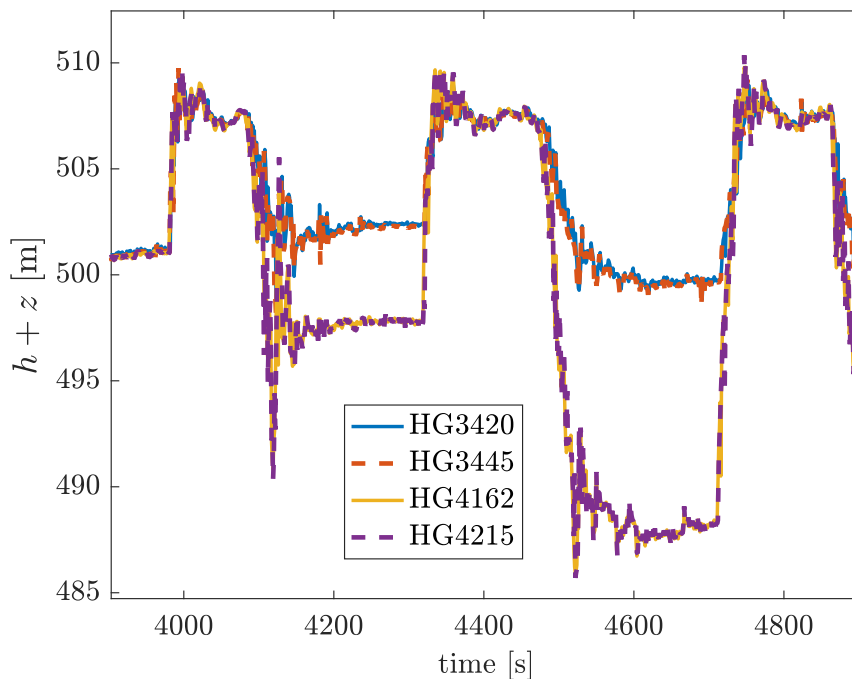


FIGURE 10.5: Time-frame of head readings during high fireflows showing redundant sensors ‘HG3445’ and ‘HG4215’.

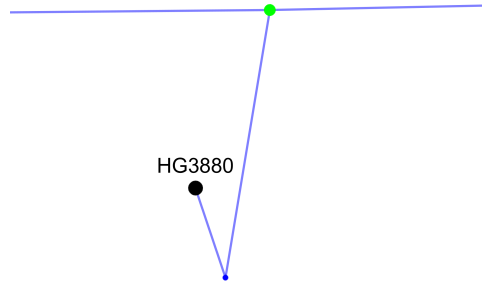


FIGURE 10.6: Zoom into figure 10.4.

Third (c), in analogy to (b), the cycle (seen in figure 10.3) enclosing pressure-node ‘HG3933’ (according to figure 10.4) does not have any hydrant to cause water to flow into this network part. As a result, there should be no head-loss in this entire cycle, leading to a uniform head-distribution up to the next junction. As side note, this is of course only feasible if no background consumption/leakage occurs there. Effectively, the pressure-readings of ‘HG3933’ are moved to the next higher junction also accounting for differences in nodal elevation.

Fourth (d), similar to (a), as hydrants are also located on dead-end-like links as shown in figure 10.6, they are moved to the next higher junction which is colored in yellow. This is only feasible due to Assumption 7.2, assuming to measure in steady-state only. As, for instance, in figure 10.6, it is irrelevant to the rest of the network if the fireflow is subtracted from the yellow instead of the black node.

Closed Valves. Finally (e), in retrospect to the conducted measurements, it turned out that a valve located between the source (seen in figure 10.1) and the hydrant ‘HG3302’, highlighted in gray in figure 10.4) was closed. As a consequence, the corresponding pipes and nodes also have been removed thereby breaking the cycle enclosing the source.

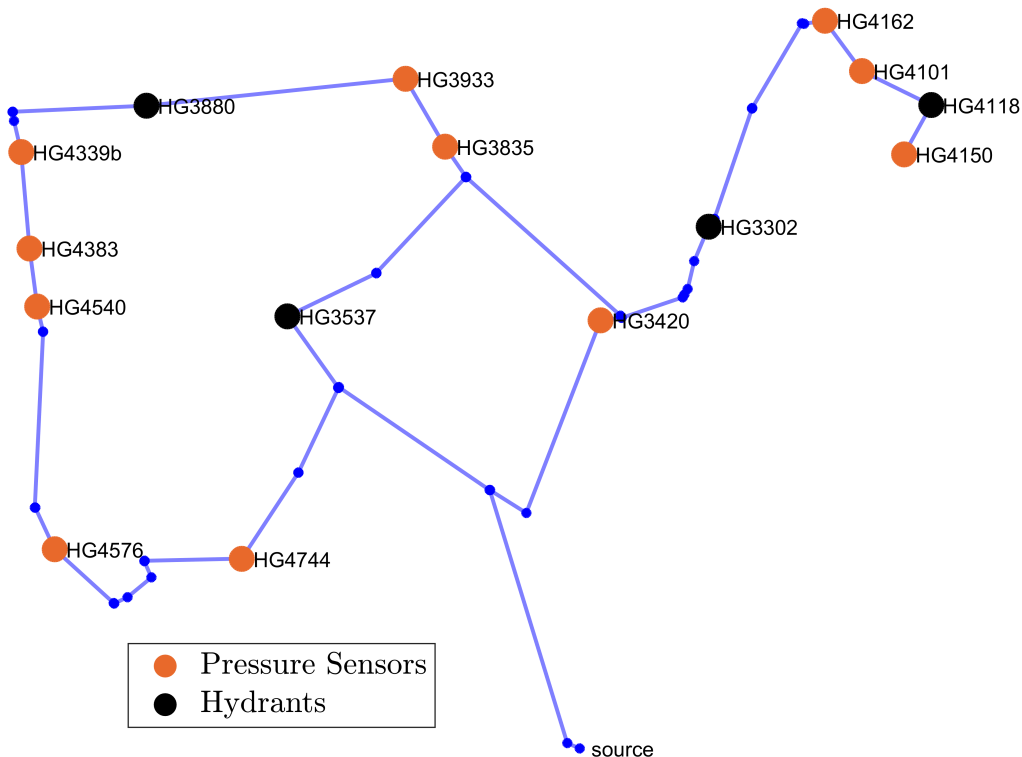


FIGURE 10.7: Final graph obtained by applying measures (a)-(e) on the graph of figure 10.4.

Final Graph. The final graph’s topology used for the attempt of the roughness-identification is presented in figure 10.7. Mind that the identifiers (IDs), e.g. ‘HG3537’, are actually used to denote individual nodes of the original graph in figure 10.1, meaning that the highlighted pressure- and hydrant-nodes of the final graph in figure 10.7 do have different names, i.e. IDs, internally. However, in order to not confuse the reader, the original IDs have been preserved to support identifiability with the corresponding sensors. Effectively, one can see that the graph has been simplified substantially in comparison to the original one in figure 10.1.

# pipes	$n_\ell = 74$
# inner nodes	$n_j = 72$
# cycles	$n_c = n_\ell - n_j = 2$
# sources	$n_s = 1$
# hydrants	$n_q = 4$
# pressure-nodes	$n_p = 11$

TABLE 10.2: Characterization of the final topology according to figure 10.7.

Given the simplified graph, at least $\lceil n_\ell/n_p \rceil = 7$ independent measurement-sets are needed to possibly reconstruct suitable roughness values for $n_\ell = 74$ (combined) pipes in the drinking-water-distribution-network of Graz Ragnitz. This is a significant improvement to the previous $n_{m,\min} = 51$ when considering the original topology in figure 10.1. Nonetheless, it will turn out questionable if $n_q = 4$ hydrants, which are treated as consumers, are sufficient to really achieve independency among measurement-sets.

10.2 Sensor Readings and First Assessments

Generally, hydrants are equipped with flow-sensors to record the fireflow, treated as “consumption” \mathbf{q} , while the pressure-sensors record the nodal pressure heads \mathbf{y}_h during the minimum-night-flow where the real, unknown consumption (also including losses) is lowest.

In figure 10.8 one can see the individual fireflow measurements at the $n_q = 4$ hydrants whereas figure 10.9 compares the sum of all fireflows (of the 4 hydrants) with the total network’s inflow which was measured separately at the link where the source connects to the rest of the network (cf. topology in figure 10.7). Counting the peaks in figure 10.8, one can see that there are potentially 15 measurement-sets available. However, it will turn out that approximately half of these sets is certainly not suitable for calibration.

In figure 10.10 one can see all relevant head-readings of pressure-sensors with respect to the IDs found in the graph of figure 10.7. Considering figures 10.8 to 10.10, observations and the applied approaches are summarized in reference to the taken assumptions (as in table 7.1 and others):

1. Assumptions 3.2, 3.10 and 6.12 do not pose any problem to the current application.
2. It is, in principle, possible to cause sufficiently large head-loss by fireflows to satisfy Assumption 7.3 and thereby provide sufficiently independent-sets concerning Assumption 7.1. Mind that this was not possible on the experimental-network in figure 5.1. Compare heads in figure 5.4 with the ones of figure 10.10 in this context.
3. Specifically referring to head-readings, the assumption (concerning Assumption 7.2) to only measure in steady-state does seem legitimate yet in very small time frames only. The numerous occurrences of oscillating heads and peaks indicate frequent transient events.
4. No assessment can be made about the validity of Assumption 7.4 or 9.3 at this point.

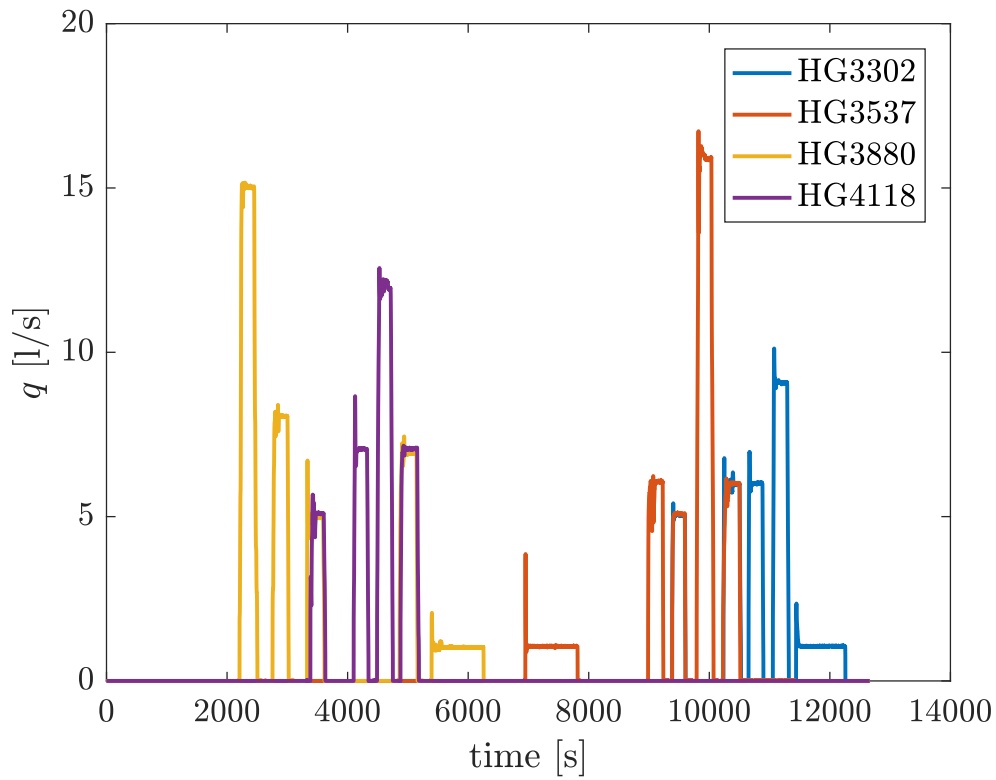


FIGURE 10.8: Fireflow-readings over all measurement-sets.

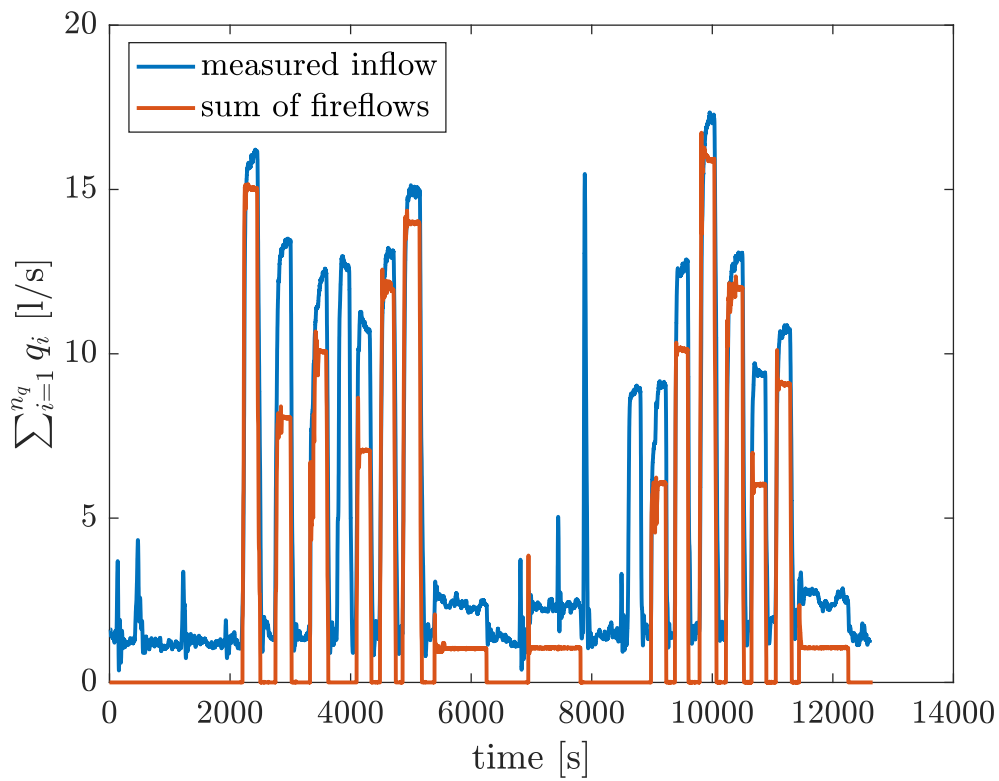


FIGURE 10.9: Comparison of the measured inflow via the source pipe and the sum of all fireflows.

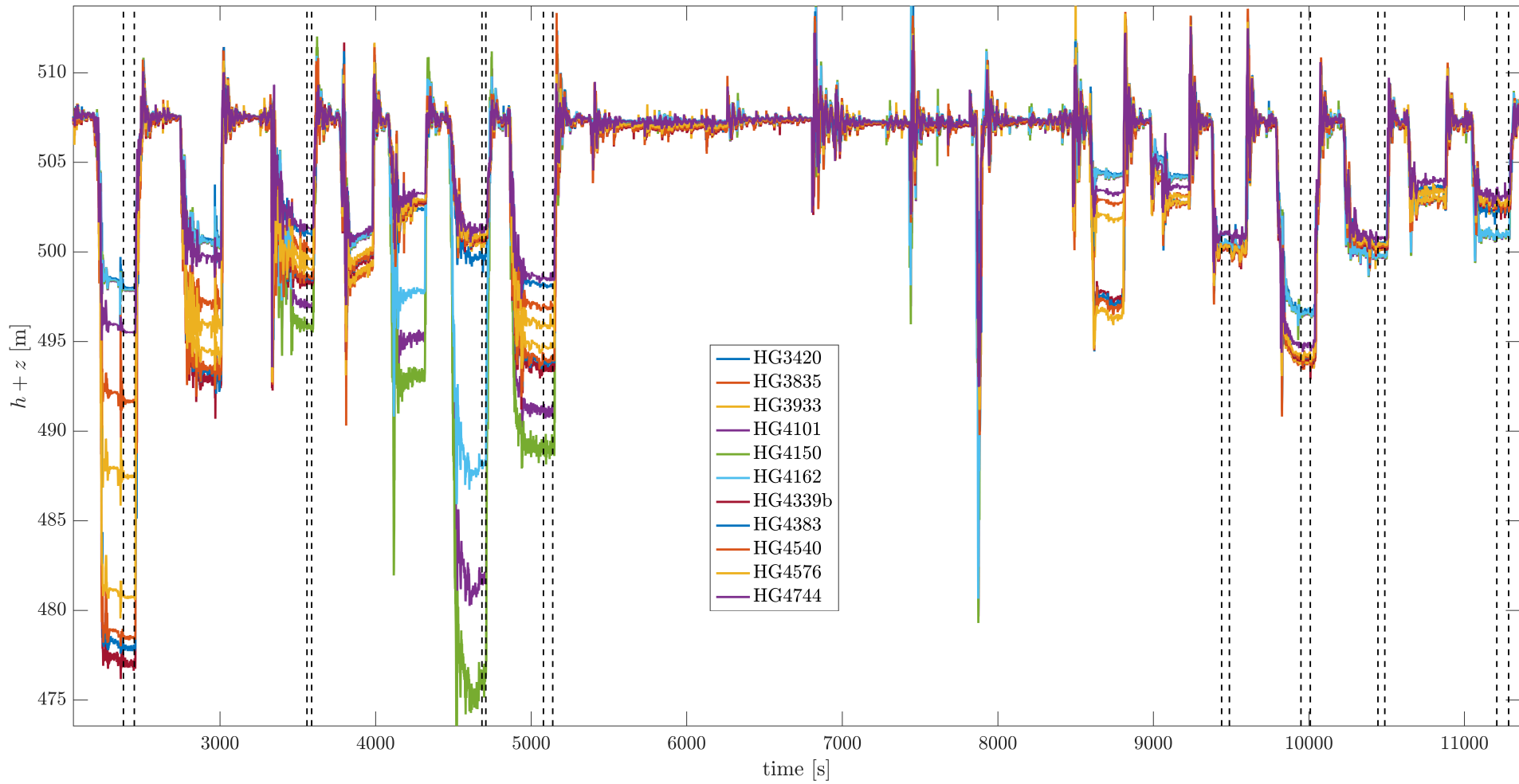


FIGURE 10.10: Head-readings of all (relevant) pressure-sensors according to the graph in figure 10.7. The steady-state time-frames used for averaging are highlighted with black dashed lines at the starting- and end-points respectively. For instance, the fourth time-frame can be found between $t \in [5080, 5140]$ s.

5. Figure 10.9 demonstrates the presumably major problem of these measurements as the unknown background-consumption (difference between blue and green curve) makes up to approximately 40% (between $t \approx [2900, 2960]$ s) of the total consumption in the corresponding measurement-set. The only possibility to circumvent this is to avoid high-erroneous measurement-sets, with respect to the background-consumption, from Ψ (9.5) and to take only those where the error is smallest, e.g. in the first time-frame (compare figure 10.9 with 10.10) where $t \approx [2380, 2450]$ s.
6. Three time-frames of comparably small fireflows around $t \approx 6000, 7000, 12000$ s at a level of 1 l/s in figure 10.8 actually do not cause any notable head-loss, seen in figure 10.10, and are therefore completely unsuitable for the consideration in Ψ .
7. The chosen $n_m = 8$ time-frames (see figure 10.10),

set i	1	2	3	4	5	6	7	8	unit
start $t \approx$	2380	3560	4685	5080	9440	9950	10445	11209	s
end $t \approx$	2450	3590	4710	5140	9490	10010	10489	11285	s

TABLE 10.3: Time-frames for averaging, visible in figure 10.10.

- i.e. measurement-sets, for the averaging of measurements had to be chosen considerably small to avoid any possibly transient events. With a sampling time of about 1s (it actually varied according to the data received), the number of single measurements eligible for averaging is comparably small (below 100 for most sets). As a result, the compensation of mean-free noise through averaging as it was achieved in section 9.3 is far less aggressive.
8. The minimum-night-flow, which gives a good estimate about the total water loss, can be identified in the range of 1.2 l/s according to figure 10.9. This background-losses are potentially very problematic for the developed calibration scheme as it is based on the satisfaction of nodal *Kirchhoff* equations, see Ψ (9.5). However, this is a general problem with all sorts of roughness-calibration algorithms as these background-losses at the time of the calibration-measurements ultimately lead to mistakenly increased friction parameters. To put it bluntly, one can hardly detect and localize leakages in an uncalibrated hydraulic network, meaning all leakages prior to the calibration (identification of friction parameters) are likely to remain invisible to the observer. This certainly depends on the size of the leakage nonetheless. If it exceeds a critical size, the detection and localization becomes feasible at some point.

10.3 Initial Values

A crucial point in the course of the measurement preparations is the choice of useful initial values for the launch of the roughness calibration concerning Ψ (9.5). In particular, the selection of suitable nodal pressure-head values at nodes with no sensors concerning $\mathbf{h}_N^{(i)} \in \mathbb{R}_{\geq 0}^{n_j - n_p}$ for all $i \in \mathfrak{M} = \{1, 2, \dots, 8\}$ is challenging and leaves a lot of potential variables to be adjusted. However, the stochastic variation of initial values as in Algorithm 2 and 4 helps to relax the requirement of already starting with values close to the ones to find.

Effectively, the very same approach as in section 9.3 is taken where initial values for \mathbf{h}_N are chosen by means of simple averaging of heads between pressure-nodes. For instance, when looking at the lower left corner of figure 10.11, which shows the steady-state network in the 1st measurement-set, the two heads between the orange pressure-nodes ‘HG4576’ and ‘HG4540’ with $y_{h, \text{HG4576}}^{(1)} + z_{\text{HG4576}} = 480.7406\text{m}$ and $y_{h, \text{HG4540}}^{(1)} + z_{\text{HG4540}} = 478.4789\text{m}$,

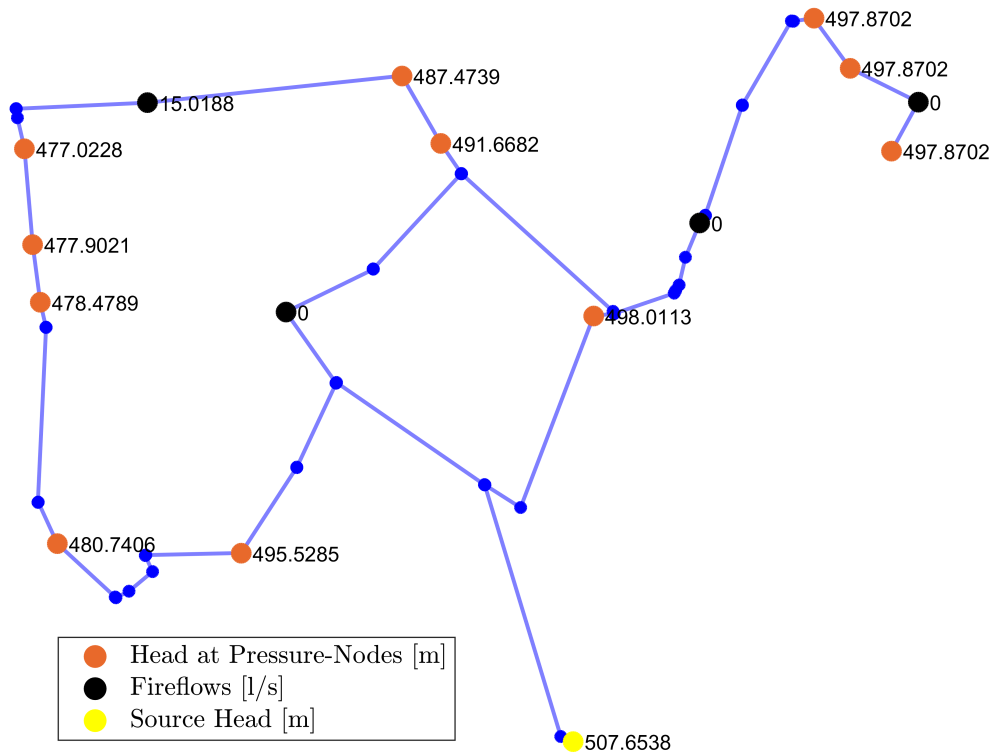


FIGURE 10.11: Network in 1st measurement-set.

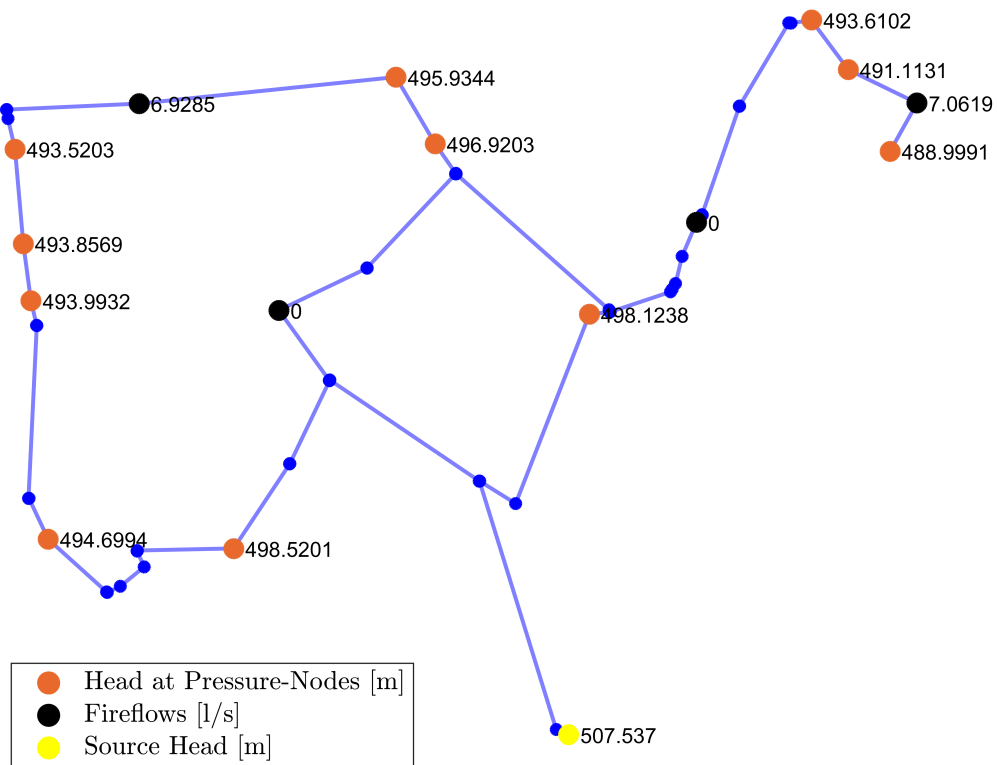


FIGURE 10.12: Network in 4th measurement-set.

are assigned with $h_{N,0}^{(1)} + z = 479.2328\text{m}$ and $h_{N,0}^{(1)} + z = 479.9867\text{m}$ respectively. Pressured head limits $\underline{h}_N, \overline{h}_N$ (7.36) are chosen analogously as the minimum respectively maximum of closest-surrounding head-readings, with respect to the corresponding non-pressure node, minus the elevation. For details have a look at section 7.5, in particular on (7.41).

This procedure is repeated analogously to all other network parts which leaves the question on how to deal with junctions. The problem becomes clear when looking at figure 10.13 where different paths between pressure-nodes (orange) via the junctions of the simplified graph are highlighted. One consistent possibility to determine the initial \mathbf{h}_N is to first take the average of heads along all those junction-paths respectively which then yields, for instance, several possible head values for some nodes according to figure (10.13). Then, in a second step, the simple average along the remaining possibilities could be taken as initial value for the respective non-pressure node. This procedure has to be done for each measurement-set respectively and remains open for future improvements.

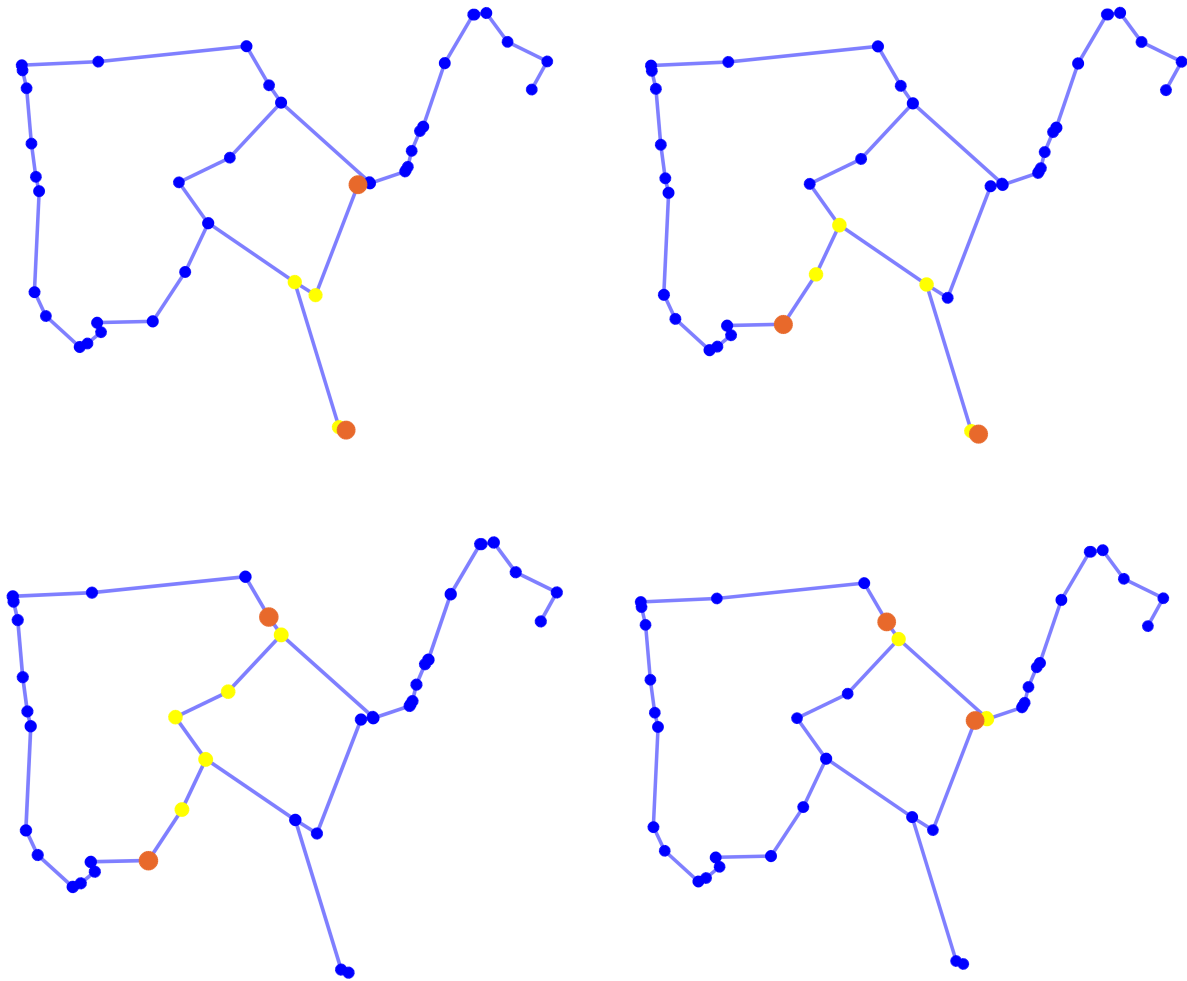


FIGURE 10.13: Different paths between pressure-nodes via junctions.

As in the previous examples, the initial roughness values for launching the calibration are selected as 1% of the corresponding pipe's diameter. Mind that according to Algorithm 4 these initial roughnesses are already varied slightly within a normal distribution before launching Algorithm 1 or 3.

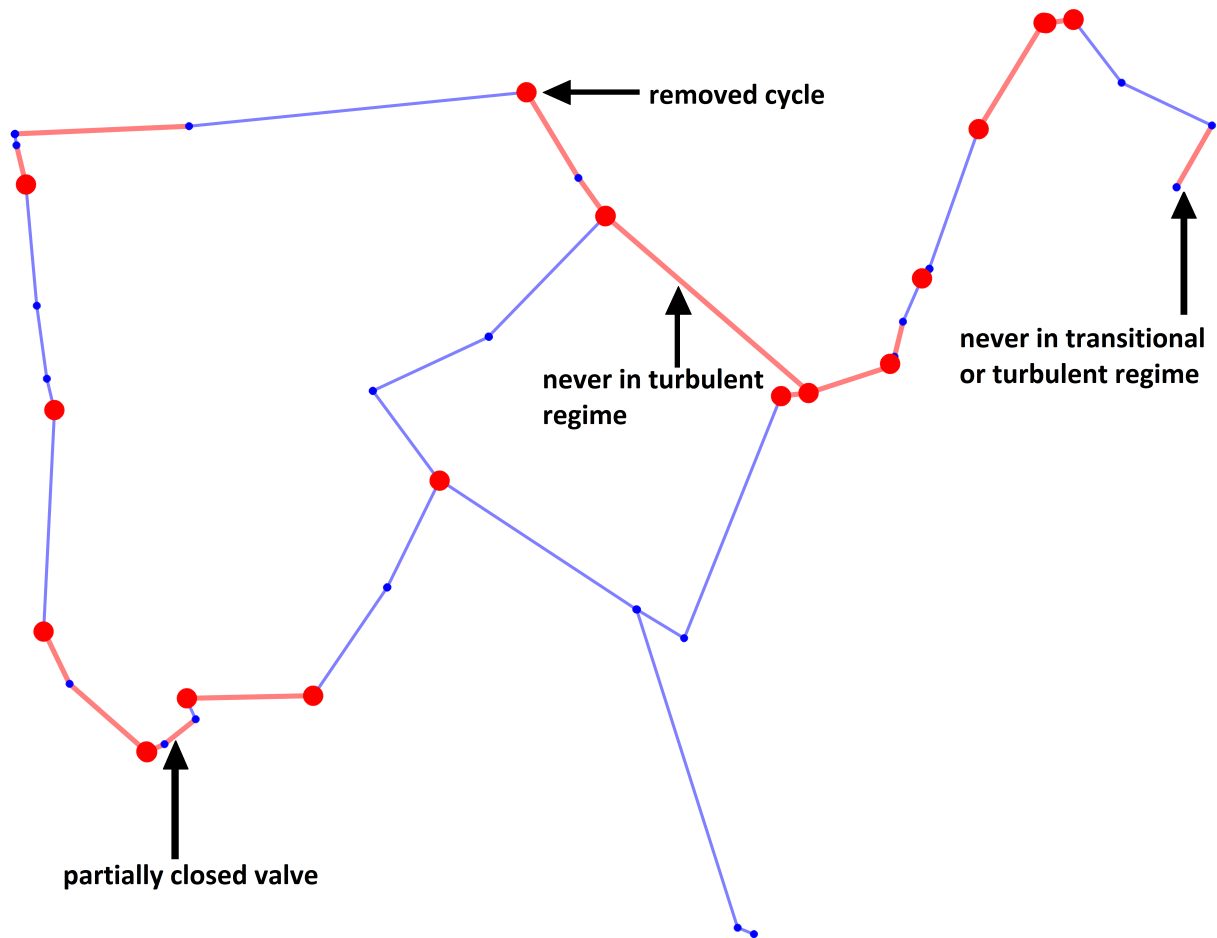


FIGURE 10.15: Corresponding to the results in figure 10.14, nodes with an error greater or equal than 10 l/s in one of the 8 measurement-sets are highlighted in red. The same red-colored pipes as in figure 10.14 with unrealistically high roughnesses are also displayed.

Figure 10.15 highlights nodes with an error greater or equal than 10 l/s in one of the 8 measurement-set and also displays the same pipes with unrealistically high roughness values. One can clearly see that there is a correlation between high-erroneous nodes and unrealistically high roughness values. Effectively, the author expects that 2 major issues hinder the solving of Ψ to result in a smaller, more realistic residual. First, the occurrence of the comparably high background consumption/leakage seen in figure 10.9 causes higher than actual roughnesses inherently. Again, due to the nonlinear friction relations an unrealistically high roughness might be necessary to compensate for the unaccounted flow at respective nodes. Second, it turned out that the data is erroneous as the author was informed that apart from the background leakage, a valve in the lower left corner, as in figure 10.15, was closed partially during the measurement night. From the information received it was not clear if this valve is located inside the presented network only or if it intends to isolate the presented network from the larger distribution network. Interestingly however, one can actually see that the exact area of the partially closed valve was identified with the presented roughness-identification scheme.

This is actually one of the major reasons why this real world example was included in this thesis, to demonstrate that the developed approach to identify roughness may also be suitable to identify network parts inconsistent with the measurement-data, i.e. leakages for instance. In this context, the author believes that the reason why the area close to pressure sensor ‘HG3933’ happens to be red-colored is not mere chance, but hints that there is significant background

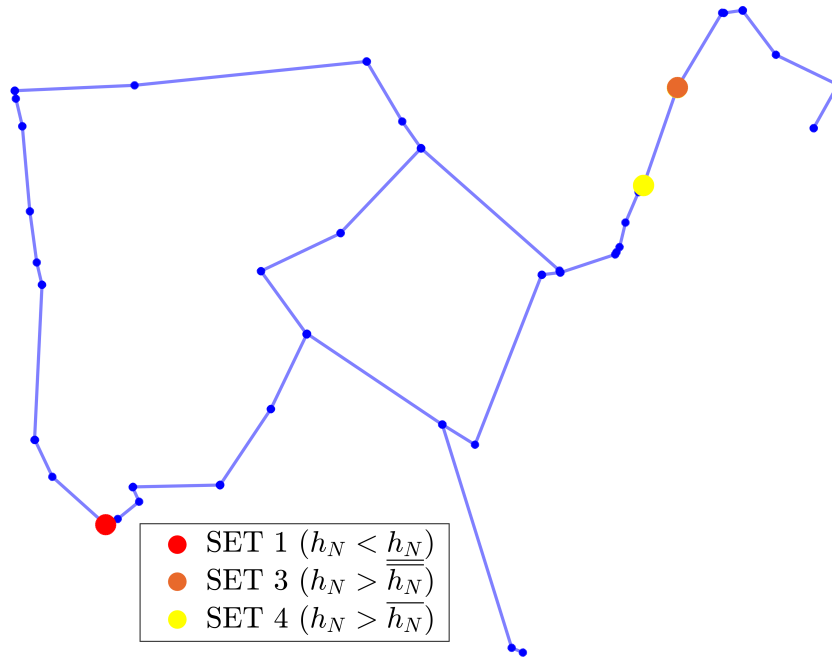


FIGURE 10.16: Highlighting non-pressure nodes whose head values are not inside their considered range in the respective measurement-set (cf. figure 10.10).

leakage/consumption in the removed cycle (last seen in the graph of figure 10.3). Nevertheless, this cycle had to be removed as no hydrant was opened in this cycle during the measurements.

Concerning the h_N results, they remain in their physical range, except at nodes which are highlighted in figure 10.16 in the respective measurement-set. This range violation is very minor for the yellow and orange colored nodes, for instance, the orange colored non-pressure node results in $h_N + z = 497.9588\text{m}$ which exceeds the identified upper limit $\overline{h_N} + z = 497.9061\text{m}$ by a mere 5.27cm. Also regarding the orange and yellow non-pressure nodes of figure 10.16, heads h_N tend to leave their intended range at exactly those nodes adjacent to pipes with ridiculously high roughness values. There also seems to be a correlation on this front. Things become interesting when considering the red-colored node of figure 10.16 which has $h_N + z = 476.3744\text{m}$ but should actually be above $h_N + z = 480.7406\text{m}$. Knowing that there was a partially closed-valve as indicated in figure 10.15, the developed calibration algorithm seems to confidently find discrepancies in the measurement-data.

When taking the results as initial value for the next iteration of, e.g., Algorithm 4 and relax the requirement for the not-measured pressure heads h_N to remain inside their selected limits $\mathbf{x}_{h_N} \in [\overline{h_N}, \underline{h_N}]$ (see code-line 13 on page 95 of Algorithm 4), one indeed manages to obtain smaller residuals. However, the roughnesses exceedingly leave their physical range and therefore do not represent results which can be seriously applied. The effect of non-zero minor losses thereby violating Assumption 7.4 may be of particular interest in this context.

Flow Regimes. Beforehand, there are $n_\ell n_m = 592$ pipe flows to be categorized among the three flow regimes. Thereby only 238 pipe flows have been identified to be in turbulent regime, 219 in the transitional regime and hence 135 in the laminar regime. This result underlines the importance to distinguish among the three flow regimes in the solving of Ψ .

Violating Assumption 9.3, 8 pipes have flows which *never* reach the turbulent regime in any of the 8 measurement-sets. Theoretically, it is sufficient to have flows in the transitional or turbulent area to identify the roughness, although the derivation of γ as in chapter 8 was

motivated by purely mathematical considerations. According to the results of the roughness-identification, there only is a single pipe whose flows never become turbulent nor transitional in any of the measurement-sets. Seen in figure 10.15, the obtained roughness of this pipe then also exceeds the physical limitation, as the variation of this roughness value has no effect on the residual of Ψ in the solving process. Looking at figure 10.7 for instance, it is clear why this pipe can neither have turbulent nor transitional flow as there can not be any flow between ‘HG4118’ (a hydrant) and ‘HG4150’ (a pressure-sensor) according to the hydrant-configuration. This is a remarkable result nonetheless and proves the applicability of γ (8.37) on the solving of Ψ to properly distinguish among flow regimes.

In analogy, the pipe whose flow never reaches the turbulent regime in figure 10.15 has a ridiculously high relative roughness of 43.3% according to figure 10.14. At this point a problem reveals which was not yet mentioned. Knowing that the smoothness and validity of γ is only preserved in the range of $\epsilon/d \in [0, 5]\%$ of the pipe’s diameter (see requirements (iii), (iv) on page 130), the root-finding algorithm for Ψ particularly struggles to handle roughness values greater 5% when being in the transitional regime. Once in the transitional regime and outside the physical limitation, the algorithm can not again converge to the turbulent regime due the violation of (iii) and (iv) on page 130.

Linear Independency. Recall at this point that $n_m \geq n_{m,\min} = \lceil n_\ell/n_p \rceil$ is only a necessary condition to satisfy Assumption 7.1. Apart from that, the best indication about the linear independency is given by the rank of *Jacobian* (7.15) which is function of the solution in iteration step k , i.e. $\mathbf{J}(\mathbf{x}_k)$. This *Jacobian* has size $\mathbf{J} \in \mathbb{R}^{576 \times 562}$ for the 8 measurement-sets. Without considering any scaling in reference to Remark 7.9 and 7.10, one obtains $\text{rank}(\mathbf{J}(\mathbf{x}_0)) = 545$ in \mathbf{x}_0 and in the solution corresponding to the roughness values in figure 10.14 it reaches $\text{rank}(\mathbf{J}(\mathbf{x}^+)) = 549$, i.e. its deficiency concerns at least 13 variables among $n_\ell + n_m(n_j - n_p) = 562$.

Why is it deficient? First, as discussed in the previous paragraph, there are pipes whose flows are never in the turbulent regime (violating Assumption 9.3) making it impossible to find corresponding roughnesses. Second, although there is, in principle, enough head loss along some pipes according to the final graph in figure 10.7, this presumably does not apply to all $n_\ell = 74$ when inspecting figure 10.10. Mind Assumption 7.3 in this context. The only possibility to improve on this is to consider further and/or different measurement-sets with other fireflow configurations, whereas additional fireflows provided by other than the n_q hydrants may be particular valuable in this regard.

10.5 Conclusions

In this chapter the basic applicability of the developed roughness-calibration on a real drinking water distribution network was demonstrated. The difficulties and uncertainties when considering real-world data were discussed, whereas the problems in the solution-finding and results could, at least in part, be traced back to inconsistencies in the data and, for instance, background consumption. The legitimacy of the assumptions in table 7.1 and Assumption 9.3 have been studied and turn out to be attainable to a large extent. Nevertheless, the validity of the neglect of minor losses concerning Assumption 7.4 has yet to be verified in greater detail. In short, the author believes the developed calibration scheme not only to be eligible for roughness-identification but for the detection and localization of leakages. Although the complexity of the presented scheme outweighs the one of comparable approaches on the basis of optimization problems, there potentially are performance gains which make this effort worthwhile.

The following list provides a range of topics which may demand further research and evaluation with measurement data.

- more detailed investigation on how to select eigenvalues $\lambda_q \in \mathbb{R}_{<0}^{n_q}$ of linear consumption dynamics as in (4.22) (see section 4.4.1) of model $\text{PD}_{\mathbf{u}}$ and LCD (see table 4.1 concerning Definition 4.12 and table 4.2 concerning Definition 4.14)
 - the detailed example in section 4.3.1 may serve as starting point
- further model evaluation with measurements beyond the scope of chapter 5 considering
 - slow transient effects excited through other than rapid valve operations
 - the coupling of air vessels and tanks as described in chapter 4.7
- further evaluation of the developed roughness identification algorithms (e.g. Algorithm 1 and 3 in cooperation with Algorithm 4) solving problem Ψ (9.5) on real-world networks
 - compliance with all the assumptions in table 7.1 and Assumption 9.3
 - investigation of the extent to which these assumptions may be violated while still being able identify roughnesses
- usage of the findings in section 7.6.3 to 7.6.6 to develop an algorithm on the basis of the *Tensor-Method* aiming to provide a search direction for the solving of Ψ (9.5) (by solving the *Tensor-Equation* (7.60)) which does *not* require an iterative thus computationally intensive scheme (as e.g. applied in section (7.7))
- enhancement of the solving of problem Ψ by considering the second *transitional* flow derivatives (9.12) in the determination of the search direction in reference to Remark 9.5
- application of the derived explicit flow γ in chapter 8 as implicit description of the *transitional* head loss (as in (8.36)) in the steady-state hydraulic network equations Γ (3.23) or Γ_h (3.24) and comparison of simulation result when applying the conventional “*Dunlop*” formulae (2.8) for the friction factor λ in (2.4) when $2000 < Re < 4000$
 - same comparison for the dynamic models
 - verification of the results of the example in chapter (9.3) when considering γ for the *transitional* head loss via (8.36) in the creation of measurement-sets (concerning section 9.3.1)



Proof of Proposition 3.6

Concerning notation, set \mathcal{N}_k (associated with the k -th row of \mathbf{A})

$$\begin{aligned} \mathcal{N}_k &= \{i : [\mathbf{A}]_{ki} \neq 0, i \in \mathfrak{P}\} \quad \forall k \in \mathfrak{J} \\ &\hat{=} \{\text{set of all flow indices in } \mathfrak{P} \text{ which are connected to node } k\} \end{aligned} \quad (\text{A.1})$$

and set \mathcal{S}_j (associated with the j -th row of \mathbf{S})

$$\begin{aligned} \mathcal{S}_j &= \{i : [\mathbf{S}]_{ji} \neq 0, i \in \mathfrak{P}\} \quad \forall j \in \{1, \dots, n_c\} \\ &\hat{=} \{\text{set of all flow indices in } \mathfrak{P} \text{ which are part of cycle/loop } j\} \end{aligned} \quad (\text{A.2})$$

are defined while Q_i for $i \in \{1, \dots, n_\ell\} = \mathfrak{P}$ denotes (directed) flows. Further, a_{ki} denotes the ki -th element of \mathbf{A} while s_{ji} denotes the ji -th element of \mathbf{S} . Then,

$$\left[\mathbf{S} \mathbf{A}^T \right]_{jk} = \sum_{i=1}^{n_\ell} [\mathbf{S}]_{ji} [\mathbf{A}^T]_{ik} = \sum_{i=1}^{n_\ell} [\mathbf{S}]_{ji} [\mathbf{A}]_{ki} = \sum_{i=1}^{n_\ell} s_{ji} a_{ki}. \quad (\text{A.3})$$

The following cases have to be considered

- (i) $i \in \mathcal{N}_k \quad \wedge \quad i \notin \mathcal{S}_j \quad \Rightarrow \quad s_{ji} = 0 \quad \Rightarrow \quad s_{ji} a_{ki} = 0$
- (ii) $i \in \mathcal{N}_k \quad \wedge \quad i \in \mathcal{S}_j \quad \Rightarrow \quad s_{ji} a_{ki} \neq 0$
- (iii) $i \notin \mathcal{N}_k \quad \wedge \quad i \in \mathcal{S}_j \quad \Rightarrow \quad a_{ki} = 0 \quad \Rightarrow \quad s_{ji} a_{ki} = 0$
- (iv) $i \notin \mathcal{N}_k \quad \wedge \quad i \notin \mathcal{S}_j \quad \Rightarrow \quad s_{ji} a_{ki} = 0$

meaning that only case (ii), where flow Q_i is part of node k and loop j needs to be further investigated as all the other cases do not contribute to $\mathbf{S} \mathbf{A}^T$ (A.3). Since the network is represented by means of a directed graph, the cases (a) to (d) displayed in figure A.1 actually cover all the possible contributions of $\mathbf{S} \mathbf{A}^T$ where $s_{ji} a_{ki} \neq 0$. This also utilizes the property that exactly two flow connections Q_{i_1} and Q_{i_2} of node k have to be considered as it is also part of loop j , referring to case (ii).



FIGURE A.1: Cases of different directions of flows Q_{i_1} and Q_{i_2} of node k which is also part of loop j .

Considering figure A.1, flows influent to node k are counted positively and effluent of node k are counted negatively as mentioned in section 3.1.1. However, entries of loop j are counted positively if the direction of the flow is in line with the loop direction and negatively otherwise.

case	a_{ki_1}	a_{ki_2}	s_{ji_1}	s_{ji_2}
(a)	1	-1	1	1
(b)	-1	-1	-1	1
(c)	1	1	1	-1
(d)	-1	1	-1	-1

TABLE A.1: Entry values of \mathbf{A}^T and \mathbf{S} according to cases in figure A.1.

Then, the contribution of node k to loop j equals

$$a_{ki_1}s_{ji_1} + a_{ki_2}s_{ji_2} = 1 - 1 = 0 \tag{A.4}$$

for all possibilities according to table A.1. The same applies when reversing the direction of loop j or even the count direction of flows (cf. figure A.1) which simply reverts the sign in (A.4). Since this procedure applies for all $i \in \{1, \dots, n_\ell\} = \mathfrak{P}$, $k \in \{1, \dots, n_j\} = \mathfrak{J}$ and $j \in \{1, \dots, n_c\}$, Proposition 3.6 holds. ■



Proof of Proposition 3.11

First, considering λ_{DW} (2.6) as a solution of the *Lambert* function $W(x)$ (2.12)

$$\lambda_{\text{DW}} = \left(W \frac{2}{\ln(10)} - \frac{\epsilon_{\text{DW}}}{3.7d} \frac{Re}{2.51} \right)^{-2} > 0, \quad (\text{B.1})$$

it is clear that the friction factor is always positive (given Property 2.1). Differentiating Δh_{DW} (2.4)

$$\frac{d\Delta h_{\text{DW}}}{dQ} = k_{\text{DW}} \left(\lambda_{\text{DW}} |Q| + \lambda_{\text{DW}} \text{sign}(Q)Q + \frac{d\lambda_{\text{DW}}}{dQ} |Q| Q \right) = k_{\text{DW}} |Q| \left(2\lambda_{\text{DW}} + \frac{d\lambda_{\text{DW}}}{dQ} Q \right), \quad (\text{B.2})$$

one takes a closer look at the derivative of λ_{DW} , where $F_{cw}(\lambda_{\text{DW}}) = 0$.

$$\frac{\partial F_{cw}}{\partial Q} + \frac{\partial F_{cw}}{\partial \lambda_{\text{DW}}} \frac{\partial \lambda_{\text{DW}}}{\partial Q} = 0 \quad \Rightarrow \quad \frac{\partial \lambda_{\text{DW}}}{\partial Q} = -\frac{\partial F_{cw}}{\partial Q} \left(\frac{\partial F_{cw}}{\partial \lambda_{\text{DW}}} \right)^{-1} \quad (\text{B.3})$$

Taking the appropriate derivatives

$$\frac{\partial F_{cw}}{\partial Q} = -\frac{2}{\ln 10} \frac{\frac{2.51}{Re\sqrt{\lambda_{\text{DW}}}}}{\frac{\epsilon_{\text{DW}}}{3.7d} + \frac{2.51}{Re\sqrt{\lambda_{\text{DW}}}}} \frac{1}{Q} \quad \text{and} \quad \frac{\partial F_{cw}}{\partial \lambda_{\text{DW}}} = -\frac{1}{2\lambda_{\text{DW}}} \left(\frac{1}{\sqrt{\lambda_{\text{DW}}}} + \frac{2}{\ln 10} \frac{\frac{2.51}{Re\sqrt{\lambda_{\text{DW}}}}}{\frac{\epsilon_{\text{DW}}}{3.7d} + \frac{2.51}{Re\sqrt{\lambda_{\text{DW}}}}} \right) \quad (\text{B.4})$$

one receives

$$\frac{\partial \lambda_{\text{DW}}}{\partial Q} = \frac{d\lambda_{\text{DW}}}{dQ} = -2\lambda_{\text{DW}} \frac{\sqrt{\lambda_{\text{DW}}}}{\sqrt{\lambda_{\text{DW}}} + \frac{\ln 10}{2} \frac{\frac{2.51}{Re\sqrt{\lambda_{\text{DW}}}} + \frac{\epsilon_{\text{DW}}}{3.7d}}{\frac{2.51}{Re\sqrt{\lambda_{\text{DW}}}}}} \frac{1}{Q} \quad (\text{B.5})$$

which leads to

$$\frac{d\Delta h_{\text{DW}}}{dQ} = \underbrace{2\lambda_{\text{DW}} k_{\text{DW}} |Q|}_{>0 \text{ for } Re > 0} \left(1 - \frac{\sqrt{\lambda_{\text{DW}}}}{\sqrt{\lambda_{\text{DW}}} + \frac{\ln 10}{2} \frac{\frac{2.51}{Re\sqrt{\lambda_{\text{DW}}}} + \frac{\epsilon_{\text{DW}}}{3.7d}}{\frac{2.51}{Re\sqrt{\lambda_{\text{DW}}}}}} \right) > 0 \quad \forall Q \neq 0, \lambda_{\text{DW}}, \frac{\epsilon_{\text{DW}}}{d} \quad (\text{B.6})$$

an expression which is always greater zero, as result of the remaining term

$$1 - \frac{\sqrt{\lambda_{\text{DW}}}}{\underbrace{\sqrt{\lambda_{\text{DW}}} + \frac{\ln 10}{2} \frac{2.51}{\underbrace{Re\sqrt{\lambda_{\text{DW}}}}_{\geq 1}} + \frac{\epsilon_{\text{DW}}}{3.7d}}_{\geq 1}} \geq 1 - \underbrace{\frac{\sqrt{\lambda_{\text{DW}}}}{\sqrt{\lambda_{\text{DW}}} + \frac{\ln 10}{2}}}_{<1} > 0 \quad (\text{B.7})$$

being always greater zero too. This provides that $Re > 0$ (2.3) which implies $2\lambda_{\text{DW}}k_{\text{DW}}|Q| > 0$, whereas $\epsilon_{\text{DW}}/d > 0$ due to the physical relation. Actually, $\Delta h_{\text{DW}}(Q)$ is strictly monotonically increasing except in the zero point $Q = 0$ where its slope equals zero. ■



Proof of Proposition 8.2

Denoting $\mathbf{q} = [1/q_0 \quad q_1]^T$, where $q_0 \neq 0$ (8.8) and $E(1/q_0, q_1) = E(\mathbf{q})$, one has to show that $E(\mu\mathbf{q}_1 + (1 - \mu)\mathbf{q}_2) \leq \mu E(\mathbf{q}_1) + (1 - \mu)E(\mathbf{q}_2) \forall \mu \in [0, 1]$ and different $\mathbf{q}_1, \mathbf{q}_2$ as a result of (8.8).

$$\begin{aligned} \int_{\underline{\Delta h}}^{\overline{\Delta h}} \left(f_a(\Delta h) + [-\Delta h^{7/4} \quad 1](\mu\mathbf{q}_1 + (1 - \mu)\mathbf{q}_2) \right)^2 d\Delta h \leq & \quad (C.1) \\ \mu \int_{\underline{\Delta h}}^{\overline{\Delta h}} \left(f_a(\Delta h) + [-\Delta h^{7/4} \quad 1]\mathbf{q}_1 \right)^2 d\Delta h \\ + (1 - \mu) \int_{\underline{\Delta h}}^{\overline{\Delta h}} \left(f_a(\Delta h) + [-\Delta h^{7/4} \quad 1]\mathbf{q}_2 \right)^2 d\Delta h \end{aligned}$$

Positive factor $1/d^2$ was already canceled from the left and right hand side of (C.1). Considering the left hand side of (C.1)

$$\begin{aligned} \int_{\underline{\Delta h}}^{\overline{\Delta h}} \left(f_a^2(\Delta h) + 2f_a(\Delta h)[- \Delta h^{7/4} \quad 1](\mu\mathbf{q}_1 + (1 - \mu)\mathbf{q}_2) + \mu^2([- \Delta h^{7/4} \quad 1]\mathbf{q}_1)^2 \right. \\ \left. + 2\mu(1 - \mu)([- \Delta h^{7/4} \quad 1]\mathbf{q}_1)([- \Delta h^{7/4} \quad 1]\mathbf{q}_2) + (1 - \mu)^2([- \Delta h^{7/4} \quad 1]\mathbf{q}_2)^2 \right) d\Delta h \end{aligned} \quad (C.2)$$

as well as the right hand side of (C.1)

$$\begin{aligned} \mu \int_{\underline{\Delta h}}^{\overline{\Delta h}} \left(f_a^2(\Delta h) + 2f_a(\Delta h)[- \Delta h^{7/4} \quad 1]\mathbf{q}_1 + ([- \Delta h^{7/4} \quad 1]\mathbf{q}_1)^2 \right) d\Delta h \\ + (1 - \mu) \int_{\underline{\Delta h}}^{\overline{\Delta h}} \left(f_a^2(\Delta h) + 2f_a(\Delta h)[- \Delta h^{7/4} \quad 1]\mathbf{q}_2 + ([- \Delta h^{7/4} \quad 1]\mathbf{q}_2)^2 \right) d\Delta h, \end{aligned} \quad (C.3)$$

terms are canceled successively. This results in

$$\begin{aligned} \int_{\underline{\Delta h}}^{\overline{\Delta h}} \left(\mu^2([- \Delta h^{7/4} \quad 1]\mathbf{q}_1)^2 + 2\mu(1 - \mu)([- \Delta h^{7/4} \quad 1]\mathbf{q}_1)([- \Delta h^{7/4} \quad 1]\mathbf{q}_2) \right. \\ \left. + (1 - \mu)^2([- \Delta h^{7/4} \quad 1]\mathbf{q}_2)^2 \right) d\Delta h \leq \\ \int_{\underline{\Delta h}}^{\overline{\Delta h}} \mu([- \Delta h^{7/4} \quad 1]\mathbf{q}_1)^2 + (1 - \mu)([- \Delta h^{7/4} \quad 1]\mathbf{q}_2)^2 d\Delta h. \end{aligned} \quad (C.4)$$

As $1 - \mu - (1 - \mu)^2 = \mu(1 - \mu)$ and $\mu - \mu^2 = \mu(1 - \mu)$, one brings terms of the left hand side of (C.4) to its right hand side while canceling $\mu(1 - \mu)$. This yields

$$0 \leq \int_{\underline{\Delta h}}^{\overline{\Delta h}} \left([-\Delta h^{7/4} \quad 1] \mathbf{q}_1 - [-\Delta h^{7/4} \quad 1] \mathbf{q}_2 \right)^2 d\Delta h, \quad (\text{C.5})$$

which holds for all \mathbf{q}_1 and \mathbf{q}_2 . ■



Proof of Proposition 8.6

When considering the total derivative of $f_t(\epsilon, \Delta h) = a$ in terms of Δh at $\epsilon = f_a(\Delta h)$

$$\left. \frac{df_t(\Delta h, \epsilon)}{d\Delta h} \right|_{(f_a(\Delta h), \Delta h)} = \left. \frac{\partial f_t}{\partial \Delta h} \right|_{(f_a(\Delta h), \Delta h)} + \left. \frac{\partial f_t}{\partial \epsilon} \frac{d\epsilon}{d\Delta h} \right|_{(f_a(\Delta h), \Delta h)} \equiv 0 \quad (\text{D.1})$$

while applying the chain rule to the left hand side, the right hand side becomes identical to zero. In analogy, the same applies for $\gamma(\epsilon, \Delta h) \approx a$ at least in the considered range $\Delta h \in [\underline{\Delta h}, \overline{\Delta h}]$, when taking the total derivative in terms of Δh at $\epsilon = q^{-1}(\Delta h)$.

$$\begin{aligned} & \left. \frac{d\gamma(\Delta h)}{d\Delta h} \right|_{(q^{-1}(\Delta h), \Delta h)} = \\ & \left. \frac{\partial \gamma}{\partial \Delta h} \right|_{(q^{-1}(\Delta h), \Delta h)} + \left. \frac{\partial \gamma}{\partial \epsilon} \frac{d\epsilon}{d\Delta h} \right|_{(q^{-1}(\Delta h), \Delta h)} \approx 0 \quad \forall \Delta h \in [\underline{\Delta h}, \overline{\Delta h}] \end{aligned} \quad (\text{D.2})$$

This is an indirect consequence of Corollary 8.3, providing parameters q_0, q_1 for which turbulent boundary curves are basically indistinguishable $q^{-1}(\Delta h) \approx f_a(\Delta h) \quad \forall \Delta h \in [\underline{\Delta h}, \overline{\Delta h}]$ (see figure 8.1). As a result,

$$\begin{aligned} & \frac{dq^{-1}}{d\Delta h} \approx \frac{df_a}{d\Delta h} \quad \forall \Delta h \in [\underline{\Delta h}, \overline{\Delta h}] \\ \Rightarrow & \left. \frac{d\epsilon}{d\Delta h} \right|_{(q^{-1}(\Delta h), \Delta h)} \approx \left. \frac{d\epsilon}{d\Delta h} \right|_{(f_a(\Delta h), \Delta h)} \quad \forall \Delta h \in [\underline{\Delta h}, \overline{\Delta h}]. \end{aligned} \quad (\text{D.3})$$

also the slopes of the turbulent boundary curves equal to a sufficient degree of accuracy.

By reformulating (D.1) and (D.2), request (iv) can be modified with regard to (in the range $\Delta h \in [\underline{\Delta h}, \overline{\Delta h}]$)

$$\left[\begin{array}{c} \left. \frac{\partial \gamma}{\partial \epsilon} \right|_{(q^{-1}(\Delta h), \Delta h)} \\ \left. \frac{\partial \gamma}{\partial \epsilon} \frac{d\epsilon}{d\Delta h} \right|_{(q^{-1}(\Delta h), \Delta h)} \end{array} \right] \stackrel{!}{=} \left[\begin{array}{c} \left. \frac{\partial f_t}{\partial \epsilon} \right|_{(f_a(\Delta h), \Delta h)} \\ \left. \frac{\partial f_t}{\partial \epsilon} \frac{d\epsilon}{d\Delta h} \right|_{(f_a(\Delta h), \Delta h)} \end{array} \right] \quad (\text{D.4a})$$

or

$$\left[\begin{array}{c} \left. \frac{\partial \gamma}{\partial \Delta h} \right|_{(q^{-1}(\Delta h), \Delta h)} \\ \left. \frac{\partial \gamma}{\partial \Delta h} \right|_{(q^{-1}(\Delta h), \Delta h)} \left(\left. \frac{d\epsilon}{d\Delta h} \right|_{(q^{-1}(\Delta h), \Delta h)} \right)^{-1} \end{array} \right] \stackrel{!}{=} \left[\begin{array}{c} \left. \frac{\partial f_t}{\partial \Delta h} \right|_{(f_a(\Delta h), \Delta h)} \\ \left. \frac{\partial f_t}{\partial \Delta h} \right|_{(f_a(\Delta h), \Delta h)} \left(\left. \frac{d\epsilon}{d\Delta h} \right|_{(f_a(\Delta h), \Delta h)} \right)^{-1} \end{array} \right]. \quad (\text{D.4b})$$

Applying (D.3), the derivative $\frac{d\epsilon}{d\Delta h}$ at the turbulent boundary is cancelled in (D.4). This is feasible as $\frac{df_a}{d\Delta h} \neq 0$ and $\frac{dq^{-1}}{d\Delta h} \neq 0$ for all $\Delta h \in [\underline{\Delta h}, \overline{\Delta h}]$ which applies for all manufacturable pipes. This completes the proof. ■



Bibliography

- «*International Water Association, Water Losses*». <https://iwa-network.org/reduction-of-non-revenue-water-around-the-world/>. Accessed: 2019-24-05.
- Adamy, J. «*Nichtlineare Systeme und Regelungen*». Springer Vieweg, Berlin Heidelberg, Darmstadt, Deutschland, 2nd edition, 2014. ISBN: 978-3-642-45012-9.
- Afzal, N. «*Friction Factor Directly From Transitional Roughness in a Turbulent Pipe Flow*». *Journal of Fluids Engineering*, 129(10):1255–1267, May 2007.
- Axworthy, D. H. «*Water Distribution Network Modelling: From Steady-State to Waterhammer*». University of Toronto, 1997. URL: <https://tspace.library.utoronto.ca/bitstream/1807/10579/1/NQ27600.pdf>.
- Axworthy, D. H. and Karney, B. W. «*Valve Closure in Graph-Theoretical Models for Slow Transient Network Analysis*». *Journal of Hydraulic Engineering*, 126(4):304–309, 2000.
- Bapat, R. B. «*Graphs and Matrices*». Universitext. Springer-Verlag London, 2nd edition, 2014. ISBN: 978-1-4471-6568-2.
- Beck, A. «*Introduction to Nonlinear Optimization: Theory, Algorithms, and Applications with MATLAB*». Society for Industrial and Applied Mathematics, Philadelphia, PA, USA, 2014. ISBN: 1611973643, 9781611973648.
- Bellman, R. and Cooke, K. «*Essential Maple*». Academic Press, 1963.
- Bhave, P. R. «*Calibrating Water Distribution Network Models*». *Journal of Environmental Engineering*, 114(1):120–136, 1988.
- Bhave, R. P. «*Analysis of Flow in Water Distribution Networks*». Technomic Publishing Co. Inc., 1991.
- Botros, K. K. «*Experimental Investigation Into the Relationship Between the Roughness Height in Use With Nikuradse or Colebrook Roughness Functions and the Internal Wall Roughness Profile for Commercial Steel Pipes*». *Journal of Fluids Engineering*, 138(081202), 2016.
- Bouaricha, A. and Schnabel, R. «*Tensor Methods for Large Sparse Systems of Nonlinear Equations*». *Mathematical Programming*, 82:377–400, Jan 1998.
- Boulos, P. F. and Wood, D. J. «*Explicit Calculation of Pipe & Network Parameters*». *Journal of Hydraulic Engineering*, 116(11):1329–1344, 1990.

- Boulos, P. F., Lansey, K. E., and Karney, B. W. «*Comprehensive Water Distribution Systems Analysis Handbook for Engineers and Planners*». Amer Water Works Assn, 2006.
- Brown, G. O. «*The History of the Darcy-Weisbach Equation for Pipe Flow Resistance*». Environmental and Water Resources History, 2002.
- Cattani, M., Boano, C. A., Steffelbauer, D., Kaltenbacher, S., Günther, M., Römer, K., Fuchshanusch, D., and Horn, M. «*Adige: An Efficient Smart Water Network Based on Long-range Wireless Technology*». CySWATER '17, pages 3–6, New York, NY, USA, 2017. ACM. ISBN: 978-1-4503-4975-8. doi: 10.1145/3055366.3055367. URL: <http://doi.acm.org/10.1145/3055366.3055367>.
- Chaudhry, M. H. «*Applied Hydraulic Transients*». Springer New York Heidelberg Dordrecht London, third edition, 2014.
- Cho, C.-H., Jacob, U., Singh, S., Seung, P. C., and Wilse, R. G. «*Pressure Effect on the Density of Water*». The Journal of Physical Chemistry, 72:7557–7561, 7 2002.
- Colebrook, C. F. and White, C. M. «*Experiments With Fluid Friction in Roughened Pipes*». Proceedings of the Royal Society of London A: Mathematical, Physical and Engineering Sciences, 161:367–381, 1937.
- Collins, M., Cooper, L., Helgason, R., Kennington, J., and LeBlanc, L. «*Solving the Pipe Network Analysis Problem Using Optimization Techniques*». Management Science, 24(7): 747–760, 1978.
- Coolidge, J. L. «*A Treatise on Algebraic Plane Curves*». Dover phoenix editions. Dover Publications, 2004. ISBN: 9780486495767,0486495760.
- Corless, R. «*Differential-Difference Equations*». 1994.
- Corless, R. M., Gonnet, G. H., Hare, D. E. G., Jeffrey, D. J., and Knuth, D. E. «*On the Lambert W Function*». Computational Mathematics, 5:329–359, 1996.
- Covas, D. and Ramos, H. «*Hydraulic Transients used for Leakage Detection in Water Distribution Systems*». Ambient Journal, pages 227–241, 2001.
- Covas, D., Stoianov, I., Mano, J. F., Ramos, H., Graham, N., and Maksimovic, C. «*The Dynamic Effect of Pipe-Wall Viscoelasticity in Hydraulic Transients. Part II—Model Development, Calibration and Verification*». Journal of Hydraulic Research, 43(1):56–70, 2005.
- Cutnell, J. D. and Johnson, K. W. «*Physics*». John Wiley and Sons, 9th edition, 2012.
- Cuyt, A. and Rall, L. B. «*Computational Implementation of the Multivariate Halley Method for Solving Nonlinear Systems of Equations*». ACM Trans. Math. Softw., 11:20–36, 3 1985.
- Dunlop, E. J. «*WADI Users Manual*». Local Government Computer Services Board, 1991.
- Elencwajg, G. «*Do polynomials in two variables always factor in linear terms?*». Mathematics Stack Exchange. URL: <https://math.stackexchange.com/q/1463638>. URL:<https://math.stackexchange.com/q/1463638> (version: 2015-10-05).
- Eliades, D. G., Kyriakou, M., Vrachimis, S., and Polycarpou, M. M. «*EPANET-MATLAB Toolkit: An Open-Source Software for Interfacing EPANET with MATLAB*». page 8, The Netherlands, Nov 2016. doi: 10.5281/zenodo.831493.

- Faucette, W. M. «*A Geometric Interpretation of the Solution of the General Quartic Polynomial*». The American Mathematical Monthly, 103(1):51–57, 1996.
- Fox, J. A. «*Hydraulic Analysis of Unsteady Flow in Pipe Networks*». The MacMillan Press LTD, 1977.
- Fujiwara, O. and Li, J. «*Reliability Analysis of Water Distribution Networks in Consideration of Equity, Redistribution and Pressure Dependent Demand*». Water Resource Research, 34: 1843–1850, 1998.
- Fung, Y. C. «*Biomechanics – Motion, Flow, Stress and Growth*». Springer Verlag, 1990.
- Gascón, L., de la Cruz, F. A., Jordán, R. C., and Rochera, E. C. «*Urban Water Demand in Spanish Cities by Measuring end Uses Consumption Patterns*». Water Sources Conference, 2004.
- Genić, S., Arandjelović, I., Kolendić, P., Jarić, M., Budimir, N., and Genić, V. «*A Review of Explicit Approximations of Colebrook’s Equation*». FME Transactions, 39(2):67–71, 2011.
- Giustolisi, O., Savic, D., and Z., K. «*pressure-driven demand and leakage simulation for water distribution networks*». Journal of Hydraulic Engineering:pp. 626–635, 2008.
- Günther, M., Steffelbauer, D. B., and Fuchs-Hanusch, D. «*fault detection data creation using an experimental water distribution system*». 3rd Conference on Control and Fault-Tolerant Systems (SysTol), Barcelona, Spain, 2016.
- Hautus, M. «*Strong Detectability and Observers*». Linear Algebra and its Applications, 50: 353–368, 04 1983.
- Ivanov, K. P. and Bournaski, E. G. «*Combined Distributed and Lumped Parameters Model for Transient Flow Analysis in Complex Pipe Networks*». Computer methods in applied mechanics and engineering, 1996.
- Jelali, M. and Kroll, A. «*Hydraulic Servo-Systems: Modelling, Identification and Control*». Springer-Verlag London Ltd., 2003.
- Jung, B. S., Boulos, P. F., and Wood, D. J. «*Effect of Pressure-Sensitive Demand on Surge Analysis*». Journal American Water Works Association, 2009.
- Kaltenbacher, S., Steffelbauer, D., Cattani, M., Fuchs-Hanusch, D., Horn, M., and Roemer, K. «*A Dynamic Model for Smart Water Distribution Networks*». Computing and Control for the Water Industry, Sheffield, 2017.
- Kaltenbacher, S., Steinberger, M., and Horn, M. «*Modeling Hydraulic Networks for Control: How to Deal With Consumption?*». IEEE Control Systems Letters, 2(4):671–676, Oct 2018.
- Kaltenbacher, S., Steinberger, M., and Horn, M. «*Transitional water flow in steady-state*». Applied Mathematical Modelling, 77:478 – 490, 2020.
- Kapelan, Z. «*Calibration of Water Distribution System Hydraulic Models*». PhD Thesis, University of Exeter, 2002.
- Kell, G. S. «*Density, Thermal Expansion, and Compressibility of Liquid Water from 0° to 150° C: Corrections and Tables for Atmospheric Pressure and Saturation Reviewed and Expressed on 1968 Temperature Scale*». Journal of Chemical and Engineering Data, 73(1):34–39, 1969.

- Khalil, H. K. «*Nonlinear Systems*». Pearson Education. Prentice Hall, 2002. ISBN: 9780130673893.
- Korson, L., Drost-Hansen, W., and Millero, F. J. «*Viscosity of Water at Various Temperatures*». The Journal of Physical Chemistry, 20(1):97–105, 1975.
- Kumar, Prasanna, M., and Mohan, M. «*Comparative Study of Three Types of Controllers for Water Distribution Networks*». Journal of American Water Works Association, 101(1):74–86, 2009.
- Kun, D., Ding, R., Wang, Z., Song, Z., Xu, B., Zhou, M., Bai, Y., and Zhang, J. «*Direct Inversion Algorithm for Pipe Resistance Coefficient Calibration of Water Distribution Systems*». Journal of Water Resources Planning and Management, 144, Jan 2018.
- Lansey, K. E. and Basnet, C. «*Parameter Estimation for Water Distribution Networks*». Journal of Water Resources Planning and Management, 117(1):126–144, 1991.
- Larock, B. E., Jeppson, R. W., and Watters, G. Z. «*Hydraulics of Pipeline Systems*». CRC Press, 1 edition, 1999.
- Lawrence, J. «*A Catalog of Special Plane Curves*». Dover books on advanced mathematics. Dover Publications, 1972. ISBN: 9780486602882.
- Levine, W. «*The Control Handbook: Control System Applications, Second Edition*». Electrical Engineering Handbook. CRC Press, 2010. ISBN: 9781420073614. URL: <https://books.google.at/books?id=mTX4NRtGNhIC>.
- Lewis, R. A. «*EPANET 2 User Manual*». United States Environmental Protection Agency (EPA), 2000.
- Million, E. «*The Hadamard Product*». Creative Commons, 2007.
- Mohsenabadi, S. K., Biglari, M. R., and Moharrampour, M. «*Comparison of Explicit Relations of Darcy Friction Measurement with Colebrook-White Equation*». Ambient Journal, 2(4): 570–578, 2014.
- Muranho, J., Ferreira, A., Sousa, J., Gomes, A., , and Sá, M. A. «*Pressure-Dependent Demand and Leakage Modelling With an EPANET Extension - WaterNetGen*». Procedia Engineering, 89:632 – 639, 2014.
- Nault, J. D. and Karney, B. W. «*Improved Rigid Water Column Formulation for Simulating Slow Transients and Controlled Operations*». Journal of Hydraulic Engineering, 142(9): 04016025, 2016.
- Nikuradse, J. «*Strömungsgestze in Rauhen Röhren*». Technical Report 361, VDI-Verlag, 1933. (English translation: NACA Tech. Memo. 1292, National Advisory Commission for Aeronautics, Washington D.C., 1950).
- Nocedal, J. and Wright, S. J. «*Numerical Optimization*». Springer, New York, NY, USA, second edition, 2006.
- Onizuka, K. «*System Dynamics Approach to Pipe Network Analysis*». Journal of Hydraulic Engineering, 1986.
- Ormsbee, L. and Walski, T. «*Darcy-Weisbach versus Hazen-Williams: No Calm in West Palm*». World Environmental and Water Resources Congress, 2016.

- Ormsbee, L. E. «*Implicit Network Calibration*». Journal of Water Resources Planning and Management, 115(2):243–257, 1989.
- Ormsbee, L. E. and Wood, D. J. «*Explicit Pipe Network Calibration*». Journal of Water Resources Planning and Management, 112(2):166–182, 1986.
- Ostfeld, A., Salomons, E., Ormsbee, L., Uber, J. G., Bros, C. M., Kalungi, P., Burd, R., Zazula-Coetzee, B., Belrain, T., Kang, D., Lansey, K., Shen, H., McBean, E., Wu, Z. Y., Walski, T., Alvisi, S., Franchini, M., Johnson, J. P., Ghimire, S. R., Barkdoll, B. D., Koppel, T., Vassiljev, A., Kim, J. H., Chung, G., Yoo, D. G., Diao, K., Zhou, Y., Li, J., Liu, Z., Chang, K., Gao, J., Qu, S., Yuan, Y., Prasad, T. D., Laucelli, D., Lyroudia, L. S. V., Kapelan, Z., Savic, D., Berardi, L., Barbaro, G., Giustolisi, O., Asadzadeh, M., Tolson, B. A., and McKillop, R. «*Battle of the Water Calibration Networks*». Journal of Water Resources Planning and Management, 138(5):523–532, 2012.
- Pilati, S. and Todini, E. «*La Verifica Delle Reti Idrauliche in Pressione*». Istituto di Costruzioni Idrauliche, Facolta di Ingegneria dell' Universita Bologna, 1984.
- Piller, O. «*Modeling the Behavior of a Network - Hydraulic Analysis and Sampling Procedures for Parameter Estimation*». PhD Thesis, 02 1995.
- Piller, O. and Propato, M. «*Slow Transient Pressure Driven Modeling in Water Distribution Networks*». 2006. doi: 10.1061/40941(247)38.
- Piller, O., Bremond, B., and Poulton, M. «*Least Action Principles Appropriate to Pressure Driven Models of Pipe Networks*». 2003. doi: 10.1061/40685(2003)113.
- Poloni, F. «*Algorithms for Quadratic Matrix and Vector Equations*». PhD Thesis, University of Pisa, 2010.
- Press, W. H., Teukolsky, S. A., Vetterling, W. T., and Flannery, B. P. «*Numerical Recipes in C: The Art of Scientific Computing*». Cambridge University Press, New York, NY, USA, 2nd edition, 1992. ISBN: 0-521-43108-5.
- Savic, D. A. and Walters, G. A. «*Genetic Algorithm Techniques For Calibrating Network Models*». Technical report, University of Exeter, 1995.
- Savic, D. A., Kapelan, Z. S., and Jonkergouw, P. M. «*Quo vadis water distribution model calibration?*». Urban Water Journal, 6(1):3–22, 2009.
- Schneider, T. M. «*State Space Properties of Transitional Pipe Flow*». Universität Mahrburg/Lahn, PhD Thesis in Physics, 2007.
- Shimada, M. «*Graph-Theoretical Model for Slow Transient Analysis of Pipe Networks*». Journal of Hydraulic Engineering, 115(9):1165–1183, 1989.
- Shimada, M. «*State-Space Analysis and Control of Slow Transients in Pipes*». Journal of Hydraulic Engineering, 1993.
- Shockling, M. A., Allen, J. J., and Smits, A. J. «*Roughness Effects in Turbulent Pipe Flow*». Journal of Fluid Mechanics, 564:267–285, 2006.
- Sontag, E. «*Input to State Stability: Basic Concepts and Results*». Nonlinear and Optimal Control Theory, 01 2004.
- Spain, B. «*Analytical Conics*». Dover Books on Mathematics. Dover Publications, 2007. ISBN: 9780486457734.

- Steffelbauer, D. B. «*Model-Based Leak Localization in Water Distribution Systems*». PhD Thesis, Graz University of Technology, 2018.
- Swamee, P. and Jain, A. K. «*Explicit Equations for Pipe-Flow Problems*». ASCE Journal Hydraulic Div., 102:657–664, 1976.
- Terra, M. H., Reis, J. A. T., Chaundry, F. H., and de Souza, R. S. «*Control of Transients in Water Distribution Networks by H_∞ Control*». Journal of the Brazilian Society of Mechanical Sciences, 24:286 – 292, 11 2002.
- Todini, E. and Pilati, S. «*A Gradient Algorithm for the Analysis of Pipe Networks*». Computer Applications in Water Supply, 1987.
- Todini, E. and Rossman, L. A. «*Unified Framework for Deriving Simultaneous Equation Algorithms for Water Distribution Networks*». Journal of Hydraulic Engineering, 139(5):511–526, 2013.
- Walski, T. «*Technique for Calibrating Network Models*». Journal of Water Resources Planning and Management - ASCE, 109, 10 1983.
- Walski, T., Chase, D., Savic, D., Grayman, W., Beckwith, S., and Koelle, E. «*Advanced Water Distribution Modeling and Management*». Haested Press, 2003.
- Watters, G. Z. «*Modern Analysis and Control of Unsteady Flow in Pipelines*». Ann Arbor Science, 1979.
- White, F. M. «*Fluid Mechanics*». Mc Graw Hill, New York, 8th edition, 2016.
- Wright, E. «*The Linear Difference-Differential Equation With Constant Coefficients*». Proc. Royal Soc. Edinburgh, 62(A):387–393, 1949.
- Wylie, E. B. and Streeter, V. L. «*Fluid Transients*». McGraw-Hill Inc., 1978.
- Zhang, F. «*The Schur Complement and its Applications, Numerical Methods and Algorithms*», volume 4. Springer-Verlag, 2005.